

**The Use of Three-Dimensional Inkjet Printing in Conjunction
with Thermal Phase Change Inks as a Technological Platform
to Fabricate Sacrificial Microvascular Facsimiles**

Leonard Grant Edney

Reg: 110228529

Resubmitted in accordance with the requirements for the degree of
Doctor of Philosophy in Tissue Engineering and Regenerative Medicine

The University of Sheffield
Faculty of Engineering
Department of Mechanical Engineering

August 2019

The candidate confirms that the work submitted is his own and that appropriate credit has been given where reference has been made to the work of others.

This copy has been supplied on the understanding that it is copyright material and that no quotation from the thesis may be published without proper acknowledgement.

The right of Leonard Grant Edney to be identified as Author of this work has been asserted by him in accordance with the Copyright, Designs and Patents Act 1988.

© 2019 The University of Sheffield and Leonard Grant Edney

Acknowledgements

First and foremost, I would like to express my heartfelt appreciation to my supervisor, Dr. Patrick Smith, for the quality of his character and for the care and attention he has shown in his supervisory capacity. Furthermore, I would like to express my gratitude for his friendship and support during the inevitable 'challenging times', which I am sure are part of all PhD's.

I would also like to thank my co-supervisor Prof. Paul Hatton, in both his role as my co-supervisor and in his capacity as leader of the Doctoral Training Centre for Tissue Engineering and Regenerative Medicine for the University of Sheffield. I am always impressed by the warmth, wit and kindness with which he discharges his duties and I greatly appreciate the pivotal role that he has played during my PhD.

Further afield, I would like to convey my appreciation to Prof. Jo Tipper at the University of Leeds, for the efforts in her role as head of the Doctoral Training Centre for Tissue Engineering and Regenerative Medicine, not simply for giving me this great opportunity to further my education and personal development, but also for her support over the course of the PhD. I must also offer a more general 'thank you' to the many academics who form the 'DTCTERM', who have always been interesting and supportive people to work with and learn from.

On a more personal level, I would like to thank Dr. Jonathan Stringer, Dr. Anna van Doorn, Dr. Chris Tse, Dr. Kelly Davidge, Dr. Malcolm Wilkinson, Dr. Cecile Perrault and Kirsty Franklin amongst the many at the University of Sheffield (and beyond), who succeeded in ensuring that this PhD journey was the intellectually stimulating period in my life, which I had hoped that it would be.

Finally, I would like to thank my family; my Father for his inspiration and sense of adventure (may you rest in peace), my Mother for her conscientiousness, prudence, steadfast love and support, my wonderful daughters, Emma and Alex, for always making me a proud Dad (long may it continue), and last but certainly not least, Caron, for her long-suffering love and support over so many years, as well as Jo and Luke for being the being the best 'non-step step-kids' that a man could be blessed with.

Abstract

The disadvantages of surgical repair or medical management of diseased/damaged organs and tissue have inspired increasing research within Tissue Engineering. 'Tissue Replacement Technologies' are sought to enable like-for-like replacement of such organs/tissue. Providing perfusion through an engineered tissue to enable diffusion of oxygen to the cells is a demanding challenge. Replication, co-fabrication and scalability were advanced as key criteria for evaluating an Additive Manufacturing (AM) technology's capacity to fabricate the physiologically relevant structures needed to provide perfusion and diffusion to tissues engineered in a clinically relevant volume.

Inkjet printing stood out as a candidate 'indirect fabrication' technology. Inkjet output is circular, which replicates the cross section of the microvascular lumen. 3D Inkjet printing of thermal phase change inks was selected and investigated as a novel combination of AM technology, method and material for the fabrication of sacrificial 3D microvascular facsimiles. To ensure 'replication' the principles underpinning Inkjet droplet actuation and deposition were examined. This demanding new purpose meant that revisions to 'settled' Inkjet theory were found and new principles revealed. These findings are of great significance to this research and to the wider Inkjet Printing community.

'First of a kind' 3D sacrificial microvascular facsimiles were fabricated. The fundamental technological capacity of Inkjet printing is therefore well suited to the task of creating physiologically relevant microvascular systems. Full technical feasibility is required to guarantee consistency and repeatability in the microvascular facsimiles. A series of technical upgrades for the 3D Inkjet printer setup have been recommended. An assessment of the scalability of the technology demonstrated that fabrication of a facsimile of the vascular/microvascular network of a small organ could now be completed within realistic timeframes.

Advances are also needed in associated 'enabling technologies' to accelerate translation of lab-based discoveries into clinical applications. Prototypes of novel experimental devices to assist 'enabling technologies' have been produced. An experimental study into the 'co-fabrication' of the microvascular scaffold with a compatible biomaterial for a primary engineered tissue scaffold showed that further research into this aspect is required. As Bioprinting has a complimentary expertise in the rapid deposition of scaffolds and cells for the primary engineered tissue, collaboration with a bioprinting group appears to be an inviting method for taking this research forward.

Table of Contents

Acknowledgements	3
Abstract	4
Table of Contents.....	5
List of Tables.....	9
List of Figures	11
Chapter 1 Vascularised Tissue for Organ Repair and Replacement	1
1.1 Tissue Engineering and the Importance of Tissue Replacement Technologies.	1
1.2 Primary Criteria for Evaluating Tissue Replacement Technologies	2
1.2.1 Precise Replication of a Functional 3D Microvascular System	2
1.2.2 Co-Fabrication of the 3D Microvascular Scaffold with the Primary Engineered Tissue	6
1.2.3 Scalability from Laboratory to Clinic.....	7
1.2.4 Summary of the Primary Evaluative Criteria	8
1.3 Current Strategies for Engineering Complex Vascularised Tissue.....	9
1.3.1 Cell Based Strategies.....	10
1.3.2 Scaffold Based Strategies.....	12
1.3.3 Bio-fabrication/Bio-printing.....	16
1.4 Indirect Fabrication as an Alternative to Direct Fabrication	18
1.4.1 Indirect Fabrication and AM Technologies	18
1.4.2 Novelty	20
1.4.3 Research Aims and Objectives	21
Chapter 2 An Introduction to Inkjet Printing in Three Dimensions	23
2.1 IJP as a 2D AM Technology	23
2.2 The Use of IJP as a 3D AM Technology	24
2.2.1 Introduction	24
2.2.2 Binder Jetting	25
2.2.3 Material Jetting	26
2.2.4 Electrohydrodynamic Printing.....	27
2.2.5 Conclusion	28
2.3 Technical Considerations	29
2.3.1 The Working Principle of Piezoelectric Printhead Actuation	29

2.3.2	Fundamental Aspects of Inkjet Printing with Thermal Phase Change Inks.....	32
2.3.3	Application of Inkjet Printing Principles in Three-Dimensions.....	36
Chapter 3	Materials and Apparatus	41
3.1	Materials	41
3.1.1	Ink Selection.....	41
3.1.2	Ink Preparation	43
3.1.3	Viscosity Tests – Methods and results.....	44
3.2	Apparatus.....	45
3.2.1	Jetlab 4 Inkjet Printer - Standard Setup	45
3.2.2	Jetlab 4 Inkjet Printer - Bespoke Setup	46
3.2.3	Temperature Gradient Tests.....	49
3.2.4	Comparison of Thermal Gradients	50
3.2.5	Measurement of Actual Reservoir and Print Head Temperatures.	51
3.2.6	Imaging	52
Chapter 4	Enhanced Control of Droplet Actuation by Waveform Manipulation and Optimisation	54
4.1	Introduction	54
4.2	Acceleration and Velocity of a Droplet over the Course of its Flightpath	57
4.2.1	Method, Results and Discussion	57
4.3	The Sensitivity of Jetting Pulse Amplitude to Backpressure Modification and its effect on Droplet Velocity and Volume.	60
4.3.1	Methods, Results Discussion	61
4.4	Establishing the Fundamental Resonance Period of the Printhead and the Optimal Jetting Pulse by Varying Dwell Time	64
4.4.1	Methods, Results and Discussion	66
4.5	The Effect of Varying Rise Times on Droplet Actuation.....	75
4.5.1	Method, Results and Discussion	75
4.6	The Use of Extended Dwell Times to Increase Droplet Volume.....	82
4.6.1	Methods, Results and Discussion	84
4.7	The Effect of the Transition from Unipolar Single Pulse Waveforms to Bipolar Dual Pulse Waveforms on Droplet Actuation.....	91
4.7.1	Negative Unipolar Waveforms contribute to Droplet Volume and Velocity.....	93
4.7.2	The Effect of Amplitude and Amplitude Split on Bipolar Waveforms.....	94

4.7.3	Reduction in Echo Duration.....	95
4.7.4	Discussion.....	96
4.8	Summary.....	97
Chapter 5 The Control of Droplet Deposition and the Fabrication of 3D Sacrificial Microvascular Facsimiles..... 98		
5.1	Introduction.....	98
5.2	Frequency of Droplet Deposition.....	100
5.3	Offsets and Frequencies Consistent with Accurate Droplet Deposition.....	104
5.3.1	The Effect of Droplet Deposition Frequency on Consistent Column Formation.....	104
5.3.2	The Effect of Offset Distances on Consistent Column Formation.....	105
5.4	'Multi-Droplet' Layered Columns for Higher Diameter Lumen-like Column Diameter Dimensions.....	108
5.5	Fabrication of Biomimetic Bifurcating Capillary Structures.....	116
5.5.1	Fabrication of Bifurcating Microstructures.....	117
5.6	Fabrication of Arches to Join Bifurcating Microstructures.....	120
5.7	Column Spacing.....	122
5.8	Column Height and Aspect Ratio.....	124
5.9	Summary.....	125
Chapter 6 Benchmarking the IJP Apparatus and Assessing the Scalability of 3D IJP as a Technological Platform..... 126		
6.1	Introduction.....	126
6.2	The Performance Gaps of the Apparatus as a Platform for 3D IJP.....	127
6.2.1	Hardware Limitations.....	127
6.2.2	Software.....	129
6.2.3	Know How.....	134
6.3	Apparatus Performance Gaps: Summary.....	136
6.4	The Viability of 3D IJP as a Technological Platform.....	138
6.4.1	Fabrication Times for the Current Deposition Method.....	140
6.4.2	Fabrication Times for 'On the Fly' Layer-by-Layer Printing.....	140
6.4.3	Fabrication Times for a Hybrid 'On the Fly' Layer-by-Layer Solution.....	141
6.4.4	Fabrication Times for '3D Vector-Motion' Printing.....	144
6.5	The Viability of 3D IJP: Summary.....	145

Chapter 7 Applications of 3D IJP to Aid Enabling Technologies	147
7.1 Fabricating Three Dimensional Microvascular Networks within Microfluidic Devices for use in the Validation of ' <i>in silico</i> ' Models.....	147
7.1.1 Introduction	147
7.1.2 Fabrication Procedure	151
7.1.3 Conclusion	153
7.2 Co-fabrication of a Primary Engineered Tissue Scaffold in Conjunction with a Microvascular Scaffold	155
7.2.1 Introduction	155
7.2.2 Apparatus, Materials and Methods.....	157
7.2.3 Results and Discussion.....	163
7.2.4 Interim Conclusion.....	165
7.2.5 Further Research Opportunities	165
7.3 Enhancing Cellularisation in Microvasculature	167
7.3.1 Adaptation of the Bioreactor	169
7.3.2 Fabrication of the 'Capillary Membrane'	171
7.3.3 Interim Conclusion.....	172
Chapter 8 Conclusion	173
8.1 Primary Aims and Objectives.....	174
8.2 Ancillary Aims and Objectives.....	177
8.3 Further Research and Development.....	179

List of Tables

Table 1 Characteristics of AM Technologies (Melchels et al., 2012)	14
Table 2 Melting Point of Waxes Used and Indication of Undercooling Achieved.....	42
Table 3 Measurements of the reservoir and printhead temperatures.	51
Table 4 Droplet velocities within a range of backpressure settings measured at -8 mbar.....	62
Table 5 Nomenclature for ‘fundamental resonance’ period equations.....	65
Table 6 Comparison of actual meniscus displacement times with anticipated meniscus displacement times as per Morita et al and the posited revision.....	72
Table 7 Comparison of actual meniscus displacement times and revised meniscus displacement times in view of a correction for backpressure.	73
Table 8 The effect of varied rise times within an optimised jetting pulse period on droplet velocity for a jetting pulse amplitude of 33 V.	75
Table 9 Jetting pulse amplitudes adjusted against jetting pulses with rise times of 3, 6, 9, 12,15 and 18 μs (with dwell times adjusted to achieve an optimum jetting pulse duration of 29.5 μs , i.e. $t_{rj} + t_{dj} = T_f/2$) to achieve a constant droplet velocity of 0 m/s.	77
Table 10 Jetting pulse amplitudes adjusted against jetting pulses with rise times of 3, 6, 9, 12,15 and 18 μs (with dwell times adjusted to achieve an optimum jetting pulse duration of 29.5 μs , i.e. $t_{rj} + t_{dj} = T_f/2$) to achieve a constant droplet velocity of 1.53 m/s.....	78
Table 11 A Comparison of the Change in Threshold and Constant Droplet Velocity Voltage Values for Rise Times of 3, 6, 9, 12,15 and 18 μs	79
Table 12 Comparison of the actual timing of peaks and troughs in droplet volume and jetting pulse amplitude from Figure 33 with those anticipated by the waveform propagation theory advanced in Figure 32.	86
Table 13 Comparison of the actual timing of peaks and troughs in droplet volume and jetting pulse amplitude from Figure 33 with those anticipated by the waveform propagation theory advanced in Figure 32 incorporating the proposed revisions to fundamental acoustic period theory (for extended dwell times).	89
Table 14 Jetting pulse amplitudes – split between ‘dwell’ amplitude (the positive portion of the bipolar waveform) and echo amplitude (the negative portion of the bipolar waveform) required to achieve a constant droplet velocity of 1.92 m/s.	94
Table 15 The sequence of experiments and objectives for Chapter 5.	99
Table 16 Calculation of flight time at the offsets shown in Figure 43 above....	106

Table 17 Calculation of Effective Wait Time between Burst Deposition	111
Table 18 Column diameters fabricated using a 40 micron aperture’ diameter printhead using waveform control of droplet volume and ‘multi-droplet’ fabrication techniques.....	114
Table 19 Levels of Bifurcation in Microvasculature	116
Table 20 Comparison of the theoretical script execution time with the actual script execution time.....	130
Table 21 Comparison of reported script execution times with actual execution times by the Inkjet printer.	131
Table 22 Isolation of the ‘trigger start’ command delay.....	132
Table 23 Isolation of ‘moveto’/ ‘moveby’ command delays.	132
Table 24 Revised comparison of the theoretical script execution time with the actual script execution time.....	133
Table 25 An evaluation of fabrication strategies to produce the sacrificial microvascular facsimiles required for a hypothetical small organ.	145

List of Figures

Figure 1 The architectural features of the capillary network within the dermis (Capillaroscopy image from www.the-rheumatologist.org , August 2015).....	3
Figure 2 ‘Capillary Exchange’. The dynamic displacement of materials between the blood and interstitial fluid (Wikipedia Commons File: 2108).....	6
Figure 3 Tissue Engineering: The approaches to vascularisation and their inherent advantages and disadvantages (Novosel et al., 2011).	9
Figure 4 ‘In Vitro Engineering of Vascularized Tissue Surrogates’ from Nature Scientific Reports (Sakaguchi et al., 2013).....	11
Figure 5 Branched tubular structures fabricated by two-photon polymerisation of PTHF-PA 1. Height 160 μm , internal diameter 18 μm and wall thickness 3 μm (Meyer et al. 2012).	15
Figure 6 ‘Formation of microvascular networks in vitro’ (from Nature Protocols) provides a step-by-step guide to the formation of microfluidic conduits in a collagen hydrogel for subsequent endothelialisation (Morgan et al., 2013).	17
Figure 7 Cross section of the MJ-AT-01 Print head (MicroFab Inc. U.S.A.). Overall Dimensions: Length 26 mm, Diameter 4 mm	29
Figure 8 Printhead and Piezo Actuation via the Waveform.....	30
Figure 9 ‘Printhead Actuation’ Continued	31
Figure 10: The Practicality of Inkjet Printing for Fluids (Derby and Reis 2003)	34
Figure 11 Thermal behaviour of deposited phase change droplets during three-dimensional IJP	37
Figure 12 The formation of a blended interface between deposited droplets during phase change on the formation of columns (Gao and Sonin)	40
Figure 13 JetLab 4 c/w high temperature reservoir and printhead	45
Figure 14 The thermal mass of the high temperature printhead.	46
Figure 15 Fisnar 3 ml reservoir with PTFE connector to MJ-A printhead. Ceramic tubular heating rod also shown.	47
Figure 16 Exploded ‘Solidworks’ assembly of the reservoir’s encasing thermal jacket and relevant connecting fittings.	48
Figure 17 JetLab 4 c/w bespoke heated reservoir and printhead assembly.	49
Figure 18 Measurement of the thermal gradient from substrate (at 5 $^{\circ}\text{C}$) to printhead (at 40 $^{\circ}\text{C}$), comparing the MicroFab heated dispensing device to the bespoke dispensing device.	50

Figure 19 The image capture system for dispensed droplets (Kwon & Lee, 2013).....	52
Figure 20 Inputs and outputs in the droplet creation process (Rensch, 2006).....	55
Figure 21 A dispensed droplet showing the formation of a ligand and the break in the ligand as the initially dispensed single droplet separates into two droplets. ROI = Region of Interest. (Kwon & Lee, 2013).....	57
Figure 22 The incremental and average velocities of two droplets ejected at amplitudes of 30 V and 32 V respectively.	58
Figure 23 The relationship between jetting pulse amplitude and droplet velocity and volume (Microfab Technologies Inc., 1999).....	60
Figure 24 The droplet velocity generated by a jetting pulse amplitude of 32 V (with rise and fall times of 6 μ s with dwell time adjusted to achieve an optimum jetting pulse duration of 29.5 μ s, i.e. $t_{rj} + t_{dj} = T_f / 2$) at a range of backpressures from -2 mbar to -16 mbar.....	61
Figure 25 Droplet's average velocity at 600 μ s after droplet ejection, for a jetting pulse of 32 V, rise and fall times both set to 6 μ s, dwell times varied from 15 to 30 μ s.	67
Figure 26 The timing of meniscus displacement for a 32 V amplitude jetting pulse with rise and fall times set at 6 μ s and an optimised dwell time of 22.5 μ s.	68
Figure 27 The positions of the leading and trailing edge of the pressure wave during printhead actuation relative to the fundamental resonance period.....	69
Figure 28 Droplet's average velocity at 600 μ s after droplet ejection, for a jetting pulses of a, 30 V amplitude and 3 μ s rise and fall times, then b, 32 V and 6 μ s, c, 34 V and 9 μ s and d, 36 V and 12 μ s. Dwell times varied from 15 to 30 μ s.	70
Figure 29 Average droplet velocity at 600 μ s after droplet ejection, for a jetting pulses of a, 30 V amplitude and 3 μ s rise and fall times, then b, 32 V and 6 μ s, c, 34 V and 9 μ s and d, 36 V and 12 μ s. Dwell times varied from 15 to 30 μ s.	71
Figure 30 Droplet velocities of jetting pulses with rise times of 3, 6, 9, 12, 15 and 18 μ s (with dwell times adjusted to achieve an optimum jetting pulse duration of 29.5 μ s, i.e. $t_{rj} + t_{dj} = T_f / 2$) at a jetting pulse amplitude of 33 V are compared with the rate of increase in the jetting pulse amplitude (i.e. the steepness of the 'ramp up' in applied voltage).....	76
Figure 31 The figure from Gerhauser et al shows droplet volumes generated by jetting pulse amplitudes that have been adjusted against extended dwell times to achieve a constant droplet velocity of 3 m/s (Gerhauser et al., 1983).	82

Figure 32 The propagation of pressure waves in the printhead capillary during extended dwell time periods. Negative pressure wave = blue arrow. Positive pressure wave = red arrow.	83
Figure 33 The droplet volumes generated by jetting pulse amplitudes that have been adjusted against extended dwell times to achieve a constant droplet velocity of 1.47 m/s	85
Figure 34 The bipolar double-pulse trapezoidal waveform of the JetLab 4 (Microfab Technologies Inc., 1999).....	91
Figure 35 Comparison of the unipolar waveform (6 μ s rise/fall time and 23.5 μ s dwell time, dwell voltage of 32 V), with the bipolar waveform (in accordance with MicroFab's suggested bipolar waveform) having additional settings of 47 μ s for the echo time (second dwell time) and 6 μ s for the second rise time. Echo amplitude mimicked dwell amplitude at -32 V.	92
Figure 36 Droplet formation generated by a negative unipolar waveform (replicating the negative portion of the previous bipolar waveform	93
Figure 37 Total jetting pulse amplitudes – combining 'dwell' amplitude (the positive portion of the bipolar waveform) and echo amplitude (the negative portion of the bipolar waveform) required to achieve a constant droplet velocity of 1.92 m/s.	95
Figure 38; 7 30-droplet columns, fabricated at 1, 2, 4, 8, 16, 32 and 64 Hz, at an offset between printhead and substrate of 5 mm.	100
Figure 39; 7 30-droplet columns, fabricated at 9, 10, 11, 12, 13, 14 and 15 Hz, at an offset between printhead and substrate of 5 mm, using a 60 μ m printhead.	101
Figure 40; 7 30-droplet columns, fabricated at 9, 10, 11, 12, 13, 14 and 15 Hz, at an offset between printhead and substrate of 5 mm, using a 40 μ m printhead	101
Figure 41 Inset of the 12, 13 and 14 Hz columns fabricated in Figure 39	101
Figure 42; 7 10-droplet columns, fabricated at 1, 2, 4, 8, 16, 32 and 64 Hz, at an offset between printhead and substrate of 5 mm showing the effect of micro turbulence (created by adjacent Peltier cooling module).....	105
Figure 43; 7 50-droplet columns, fabricated at 12 Hz, at a range of offsets between printhead and substrate from 5 mm to 11 mm – increasing in 1 mm increments - showing the effect of micro turbulence (created by the adjacent Peltier cooling module)	106
Figure 44; 9 30-layer columns, each layer consisting of four droplets deposited in a 'burst' at 512 Hz, with a delay between the deposition of each layer ranging from 0.001 s to 5 s (0.001 s, 0.01 s, 0.02 s, 0.025 s, 0.033 s, 0.05 s, 0.1 s, 1 s and 5s). Offset between substrate and printhead of 7.5 mm. Print head 80 micron.....	109

Figure 45 Four 30-layer columns, each layer consisting of three droplets deposited in a 'burst' at 512 Hz, with a delay between the deposition of each layer ranging from 0 s to 0.75 s. Offset between substrate and printhead of 7.5 mm	110
Figure 46; 4 30-layer columns, each layer consisting of nine droplets deposited in a 'burst' at 1024 Hz, with a delay between the deposition of each layer ranging from 0 s to 0.3 s. The substrate temperature set at 30° C with an offset between substrate and printhead of 7.5 mm.	112
Figure 47; 4 30-layer columns, each layer consisting of nine droplets (increased droplet diameter of 75 µm) deposited in a 'burst' at 1024 Hz, with a delay between the deposition of each layer ranging from 0 s to 0.3 s. The substrate temperature was set at 30° C with an offset between substrate and printhead of 7.5 mm.	113
Figure 48; Two 30-layer multi-droplet columns supporting four 15-droplet angled columns. Multi-droplet columns consist of 30 layers of 2 droplets deposited in a burst at 1024 Hz, with an effective delay between droplet bursts of 0.25 s. Angled columns consist of 15 droplets deposited in accordance with the speed of the substrate movement (moving in 10 micron increments per deposited droplet from the point of bifurcation).	118
Figure 49 Two 30-layer multi-droplet columns, positioned with 300 micron between column' centres, supporting four 15-droplet angled columns. Multi-droplet columns consist of 30 layers of 2 droplets, deposited in a burst at 1024 Hz, with an effective delay between droplet bursts of 0.25 s. Angled columns: consist of 15 droplets deposited in accordance with the speed of the substrate movement (moving in 10 micron increments per deposited droplet from the point of bifurcation). Arch: decrease gap between the uppermost point of each column from 300 micron to 30 micron, in increments of 10 - 20-micron, then add 'keystone'.	120
Figure 50; 30-droplet columns at 12 Hz. Spacing between individual columns increasing from 100 micron to 150 micron (in 10 micron intervals). Clusters of columns centred at 1 mm intervals.	122
Figure 51; 2 1280-droplet columns fabricated at a frequency of 12 Hz.....	124
Figure 52 An assessment of the upgrades required to extend the capabilities of the Jetlab 4, in order to be able to fabricate consistent and repeatable sacrificial microvascular facsimiles.	137
Figure 53 'On the fly' layer-by-layer fabrication of arch-like features: A 4 x 4 Array. Two 30-droplet columns with a 250-micron spacing between centres. Arch: decrease gap to 0.075 mm in increments of 10 - 20-micron, then add 'keystone'.	141
Figure 54 The use of the lateral movement of the substrate to enhance the fabrication quality of 3D microstructures.	142

Figure 55 Model of cerebral vasculature prior to encapsulation in PDMS, (Wetzel et al., 2005).....	150
Figure 56 Schematic representation of an Inkjet printed 3D microfluidic device	151
Figure 57 2.5D vinyl microfluidic channels cut using the ‘Graphtec Craft Robo Pro’ and applied to a glass slide (channel cross-sectional area of 3500 μm^2)	152
Figure 58 The 3D sacrificial facsimile printed to connect the terminals of the 2.5D microfluidic channels.....	152
Figure 59 The 3D microfluidic device encapsulated in PDMS.....	153
Figure 60 Completed microfluidic device.....	153
Figure 61 The relationships between material selection and fabrication method for a ‘coproduced scaffold’ for complex vascularised tissue	156
Figure 62 SEM of decellularised dermis (Wessels, 2014)	156
Figure 63 SEM of a freeze dried collagen scaffold (Wessels, 2014).....	158
Figure 64 SEM comparison of freeze-dried collagen - elastin ratios with Matriderm and the decellularised dermis	163
Figure 65 The ultimate tensile strength of Matriderm measured using the Bose Electro force 3000 with 2 – 40 N load cell.	164
Figure 66 The ultimate tensile strength of four layers of hydrated Matriderm as measured by Bose Electro force using 2 – 40 N load cell.....	164
Figure 67 Left, Collagen–elastin solution applied to freeze dried gelatin and subsequently freeze dried. Right, gelatin solution applied to freeze dried collagen and subsequently freeze dried.....	166
Figure 68 The ‘Dual flow’ bioreactor – utilising flow to produce a pressure differential across an epithelial membrane (Giusti et al., 2014).....	168
Figure 69 Adaptation kit for the QV 600 air –liquid interface bioreactor (Kirkstall Ltd, Sheffield U.K.). From left: 1, Acrylic tube (13 mm internal diameter 1 mm wall thickness) laser cut to shape. 2, Nitrile ‘o’ ring (13 mm internal diameter) Millicell 0.4. micron semi permeable membrane (EMD Millipore Ltd U.K.) prior to reduction in height by milling 4, QV 600 air – liquid interface bioreactor (empty) 5, Complete assembly.	170
Figure 70 QV 600 air – liquid interface bioreactor (Kirkstall Ltd, Sheffield U.K.) adapted to a ‘dual flow’ and ‘dual pressure’ bioreactor.....	170
Figure 71 Paraffin wax microstructures encapsulated in PDMS.....	172
Figure 72 ‘Microfab’ Delivery Note for Print heads; showing the variety of optimum jetting pulse widths and amplitudes for printheads with the same diameter capillary aperture	189

Chapter 1 Vascularised Tissue for Organ Repair and Replacement

1.1 Tissue Engineering and the Importance of Tissue Replacement Technologies.

Tissue Engineering and Regenerative Medicine (TERM) is an emerging discipline that seeks to provide superior in vitro resources and solutions for clinical needs. The repair, or replacement, of diseased and damaged organs and tissues by surgical repair, or organ transplantation, has improved or saved the lives of many patients. However, surgical repair and reconstruction demand invasive surgical techniques, which can create long-term weakness in the very tissues that the surgery seeks to repair. Furthermore, transplantation opportunities are limited by the number of organ donors and entail a lifetime commitment to immunosuppressant drug therapies to prevent organ rejection. Such treatments are costly and can compromise the ability of the immune system to maintain good health. Other treatments, that seek to manage rather than resolve medical conditions e.g. the use of kidney dialyzers, may entail the use of expensive technologies and place heavy burdens on the patient's time and restrict the patient's ability to function freely. The disadvantages of these existing techniques combined with an ever-increasing clinical need have inspired and driven increasing research in the fields of Tissue Engineering and Regenerative Medicine (TERM).

In their seminal paper, Langer and Vacanti defined the term 'Tissue Engineering' as, *"an interdisciplinary field that applies the principles of engineering and life sciences toward the development of biological substitutes that restore, maintain, or improve tissue function or a whole organ"* (Langer & Vacanti, 1993).

'TERM' incorporates a wide range of technologies. The terms Regenerative Medicine and Tissue Engineering are often (and somewhat confusingly) used interchangeably. For clarity it is useful to distinguish between 'Tissue Regeneration and Repair' – technologies relying on the body as an 'in vivo bioreactor' for cellular proliferation and migration – and 'Tissue Replacement' – technologies relying on a (ex vivo/in vitro) bioreactor for cellular proliferation and migration and engineered to enable like for like replacement of tissue (Xi, Chen, & Wang, 2013).

There has been steady progress toward clinical and near clinical applications for ‘Tissue Regeneration and Repair’ technologies such as cell therapy or the use of surgically implanted scaffolds whilst there has been little progress toward the clinical application of ‘Tissue Replacement’ technologies. To date, applications for Tissue Replacement solutions have been limited to tissues in thin, sheet-like formats for endothelia/epithelia applications such as the cornea, or avascular tissues and near avascular tissues such as cartilage and bone. Engineering thicker soft vascular tissues requires the delivery of oxygen and nutrients to the cells in the engineered construct by means of a microvascular network in order to prevent cell death. In the first instance, ‘perfusion’ is needed to deliver these vital supplies through a vascular network to a microvascular network within the tissue engineered construct and then, the oxygen and nutrients must be able to diffuse through the capillary walls in order to reach the individual cells.

Novel ‘Tissue Replacement’ solutions are required in the following fields:

- Organ Regeneration and Replacement: focusing on degenerative conditions or injury to the: liver, pancreas and pancreatic islets, kidney, small intestine, and lungs
- Cardiovascular Repair and Replacement: focusing on heart valves, myocardial tissues, coronary arteries and peripheral vascular elements
- Wound Management: focusing on reconstructive surgeries, repair of chronic wounds (ulcers), hernia and soft tissue repair.

In light of the importance and size of these clinical sectors, it is clear that without a method to provide perfusion within an engineered tissue, the potential promise that Tissue Engineering holds will remain unfulfilled (Novosel, Kleinhans, & Kluger, 2011).

1.2 Primary Criteria for Evaluating Tissue Replacement Technologies

1.2.1 Precise Replication of a Functional 3D Microvascular System

The human vascular network is an inherently complex 3D system, developed by organic responses to a wide range of physical, bio-chemical and genetic factors over a lifetime. The three-dimensional nature of the system, although obvious is stressed, because current imaging limitations mean that a considerable amount of tissue replacement research is undertaken in 2 or 2.5D.

The key processes an engineered vascular/ microvascular network aims to mimic, in order to be physiologically relevant, are ‘perfusion’ and ‘diffusion’. Commencing with the aorta, the hierarchical nature of the cardiovascular system immediately becomes

apparent. A parent artery will divide (bifurcate) into two daughter arteries, enabling the total cross-sectional area of the conduits to increase, thus reducing both the velocity and pressure of the blood flow despite the increased resistance offered by these narrowing conduits. This repeated and progressive process of bifurcation is critical to the vascular system, ensuring the velocity of blood reduces from 2,000 cm/min at the aorta to 2 cm/min at the capillary whilst pressure drops from 120 mm/hg to 35 mm/hg. At this pressure and velocity, blood can transit through the capillaries of the microvascular network, leaving the delicate single cell walls of the capillary unharmed, while allowing the process of diffusion to take place (Berne & Levy, 1972). Microvascular networks are the arrangements of arterioles, capillaries and venules that bring supplies of oxygen and nutrients (via blood or serum) to within 100-200 micron of all cells in the engineered tissue, sufficiently close for 'diffusion' of those supplies to the surrounding cells and then allow for the removal of waste (Folkman, 1973). This means that additional spatial complexity is found within the tissue as the arrangement of the microvascular components corresponds to and is driven by the diffusion limitation of oxygen.

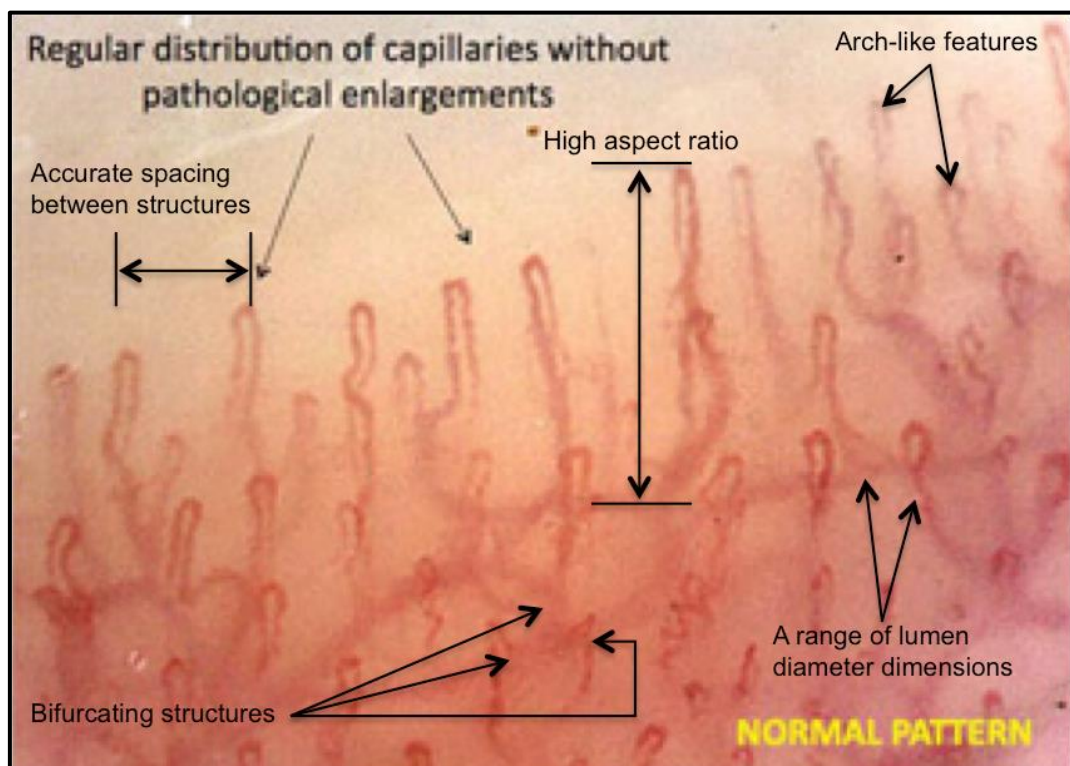


Figure 1 The architectural features of the capillary network within the dermis (Capillaroscopy image from www.the-rheumatologist.org, August 2015)

Any candidate Tissue Replacement technology must be able to fabricate the components and features of a vascular/microvascular network (tubular structures with lumen-like dimensions, bifurcations and capillary arches) at a density that is similar to that of the human body (as shown in Figure 1).

Lumen-like dimensions

Arterioles are in the range of 10 to 50 micron in diameter with wall thicknesses ranging from three cell layers to 3 micron; structural support is offered by the surrounding extra cellular matrix (ECM). Additional bifurcation then takes place within the arteriole network, further slowing blood velocity and reducing blood pressure. The inner wall of an arteriole is lined with a confluent layer of endothelial cells, which are then covered with layer/s of smooth muscle cells, which contract and dilate to provide a final mechanism by which to regulate blood flow and pressure to the capillary. This contraction/dilation process provides the final mechanism enabling the process of diffusion to take place through the capillary wall (Aird, 2007).

The diameter of the lumen of a capillary is in the range of 5 - 10 micron and is comprised of a delicate single cell wall thickness of endothelial cells (Braverman, 1997). Venules are generally 10 to 100 micron in diameter and act to collect fluid and waste from the capillary bed. The wall of the venule consists of an internal layer of endothelial cells, a middle layer of smooth muscle cells and an external layer of connective fibrous tissue. Multiple venules will connect to form veins and return blood to the vascular system.

Ideally the lumen diameters that should be reproduced to illustrate perfusion and diffusion in the microvascular network would be from 5-10 micron to 100 micron. However, there is little point in producing a scaffold for a lumen dimension that is below the limits of endothelialisation. The techniques for seeding endothelial cells in micro-conduits below a 30 micron diameter are not well advanced but it has been indicated that a less rigorous specification of 50 micron diameter for direct cell seeding of microvascular conduits is achievable (Liu, Markov, Wikswo, & McCawley, 2011). Whilst reproducing the larger features of the vascular network is unnecessary e.g. the aorta, it would be essential to construct minimum lumen diameters above 300 micron - the current lower limit for super micro-surgical connection of microvascular vessels, so a 500 micron target is chosen (Olivares et al., 2014).

Capillary Density

The spatial arrangement of capillaries corresponds to and is driven by the diffusion limitation of oxygen. If diffusion is absent, cells enter an oxygen-deprived state (hypoxia) and then begin to die (necrosis) (Folkman, 1973). By calculation, it can be estimated that approximately 25 m of capillaries will be required to ensure diffusion to all cells within 1 cm³ of tissue (capillaries located within 100 micron of all cells).

A spacing between fabricated capillary facsimiles of approximately 200 micron is required to maintain sufficient density to enable adequate mass transfer of oxygen and nutrients to the surrounding cells. However, from closer examination of Figure 1 it is clear that the spacing between the individual components of the capillary in the dermis is significantly less than 200 micron since the arterial component of the capillary is almost immediately next to the venule component of the capillary.

Bifurcating Structures and Arch-like Features

To replicate the hierarchical nature of the microvascular network it is necessary to fabricate bifurcating structures incorporating a reduction in lumen dimensions from the single parent incoming arteriole to the dual daughter outgoing capillaries. Furthermore, arch-like features that represent capillary loops – the critical vascular return mechanism, must be able to be fabricated to ensure a functional microvascular network.

High Aspect Ratio of Capillaries

William Aird has described the diffusion and transport characteristics of different types of endothelium in detail (Aird, 2007). The process optimises the potential 'mass transfer' of oxygen and nutrients from the blood cells in the diffusion zone to the cells in the extra cellular matrix (Janakiraman, Mathur, & Baskaran, 2007b) and is illustrated in Figure 2 overleaf. The spatial restriction of the lumen forces the red blood cells (6 – 8 micron in diameter) of the perfusing blood supply into single file progress through these narrow capillary conduits. The single cell wall thickness allows gases and small molecules from the blood stream to diffuse through the small gaps that occur between individual cells, whilst larger (bio) molecules are processed through the endothelium and can be altered by intercellular processes on the way. It should also be noted that capillaries exhibit a 'high aspect ratio', that is, their length is significantly greater than that of their diameter, ensuring that blood cells have a sufficiently long pathway for diffusion and subsequent reabsorption.

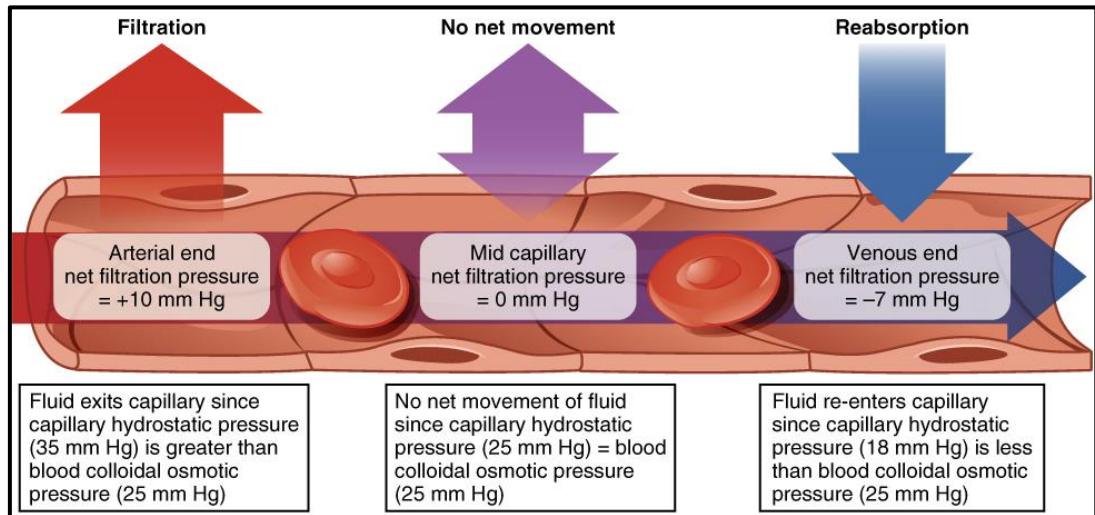


Figure 2 ‘Capillary Exchange’. The dynamic displacement of materials between the blood and interstitial fluid (Wikipedia Commons File: 2108).

It is readily apparent that the specification that must be met by a tissue replacement technology is exceptionally demanding. A bifurcating hierarchical network with decreasing lumen diameters is needed to make the engineered construct physiologically relevant. Micro-dimensioned conduits are needed and must be positioned at microscale intervals to ensure perfusion. The wall thicknesses (and material) of those conduits must be permeable to allow diffusion in order to prevent cell death. Therefore within Tissue Replacement, one of the greatest challenges is providing an engineered tissue with nutrients and oxygen via blood or serum (Auger, Gibot, & Lacroix, 2013).

1.2.2 Co-Fabrication of the 3D Microvascular Scaffold with the Primary Engineered Tissue

Vascular/microvascular networks have a symbiotic relationship with surrounding tissues (the extracellular matrix or ECM), relying on those tissues for physical support whilst providing the tissues with biological support. It is not currently feasible to insert or ‘retrofit’ a three-dimensional vascular/microvascular network into a primary engineered tissue, nor is it possible to engineer a tissue around an unsupported (but fully functional) 3D vascular-microvascular network. This symbiotic relationship means that co-fabrication of the vascular/microvascular scaffold and the primary engineered tissue must be considered.

As the vascular/microvascular network is inside the primary engineered tissue it is logical that the scaffold for the vascular components will be fabricated first in any sequence of build operations. It is therefore desirable for the vascular scaffold to be sufficiently rigid to be free standing. Furthermore, it is preferable for the fabrication

of overhanging structures to be able to be undertaken without the use of support materials in order reduce the number and complexity of processing steps.

1.2.3 Scalability from Laboratory to Clinic

From a clinical perspective, optimal 'Tissue Replacement' solutions (or constructs for organ regeneration and replacement) must be delivered in clinically relevant dimensions and volumes to be considered meaningful i.e. enabling like-for-like replacement of the existing tissue or organ that is being removed or repaired. Clinically relevant volumes for some organs that may be considered candidates in the field of 'Organ regeneration and replacement' are: the liver (1500 cm³), lungs (1300 cm³), kidneys (260 cm³), spleen (175 cm³), pancreas (70 cm³) and the thyroid (20 cm³). (Calculated from the average weights of organs at the midpoint of the range of densities for human organs, which is typically between 0.95 - 1.05 g/cm).

As discussed, it can be estimated that to enable efficient diffusion to all cells within 1 cm³ of tissue approximately 25 m of capillaries will be required, furthermore an allowance must be made for arterioles and veinules to perfuse the capillaries. A relatively small organ such as the thyroid (20 cm³ of tissue) would therefore require a vascular/microvascular network of approximately 500 m to ensure effective diffusion to all cells.

Scaling from the laboratory bench top, where the need for diffusion is typically considered within the context of cells being used in microliter quantities, to the diffusion required to sustain clinically meaningful volumes of tissue is therefore in the region of three orders of magnitude. Within engineering, scalability is often thought of as a relatively simple issue, that may be resolved by multiplying, repeating, enlarging and/or accelerating the basic production process employed (or a combination thereof). However, each of these simple tactics is challenged by the reality of fabricating a precise 'non-modular' or organic construct from sensitive biological materials.

As the volume of tissue increases from laboratory size to clinical size, the hierarchy of microvascular and indeed vascular components required to perfuse the capillaries becomes increasingly complex and extensive, which in turn ensures that a biomimetic construct cannot be fabricated on a modular basis then pieced together. The absence of modularity in a clinical meaningful volume of tissue (with a complex hierarchical vascular and microvascular network) means that the utility of the scaling principles of repeating or multiplying the number of 'diffusion modules' is restricted.

Cells are sensitive to time out of culture and the shear forces of deposition, which means that it is difficult to increase process times or accelerate deposition rates (Hoch, Tovar, & Borchers, 2014). The use of enlarged cellular deposition tools to increase the volume of cells deposited is excluded by the fact that microvascular lumen requires picolitre quantities of cells deposited at micron levels of precision.

It is therefore readily apparent that reliance on the usual methods of scaling to address the three orders of magnitude increase in diffusion needed to move from the laboratory to the clinic will be difficult. This in turn implies that an optimal tissue replacement technology should be able to engineer whole organ size scaffolds and support their functionalisation.

1.2.4 Summary of the Primary Evaluative Criteria

From a Tissue Replacement perspective, a successful tissue engineering technology will need to incorporate the following key characteristics for a physiologically relevant vascular/microvascular system to be engineered:

Biomimetic 3D Vascular/Microvascular Scaffolds

- Hierarchical bifurcations from arteriole to capillary to ensure reductions in pressure and flow
- Micro scale lumen diameters
- Replicate the exacting spatial arrangement and complexity of the vascular and microvascular network
- Micro/Nano scale capillary wall thicknesses
- Use of scaffold materials that allow/optimize mass transfer from capillary to cells

Co-fabrication of the Vascular/Microvascular Network and Primary Engineered Tissue Scaffold

- Freestanding vascular/microvascular scaffold preferable
- Fabrication of overhanging structures without support materials to reduce subsequent processing steps.

Scalability from Laboratory to Clinic

- 'Non-modularity' implies that an optimal tissue replacement technology should be able to engineer whole organ size scaffolds and support their functionalisation.

1.3 Current Strategies for Engineering Complex Vascularised Tissue

Two discernible trends have emerged amongst the many different approaches to accelerating vascularisation in tissue engineered constructs; these range from ‘cell-based strategies’ to ‘scaffold-based strategies’ as shown in Figure 3 below. While the figure presents the approaches to vascularisation as two polarities effectively book-ended by the capacities of biochemistry on the one end and bioengineering on the other, the reality is that TE research is a continuum between the two approaches (Novosel et al., 2011). The figure usefully highlights the key advantages and disadvantages of the various strategies from a Tissue Replacement perspective.

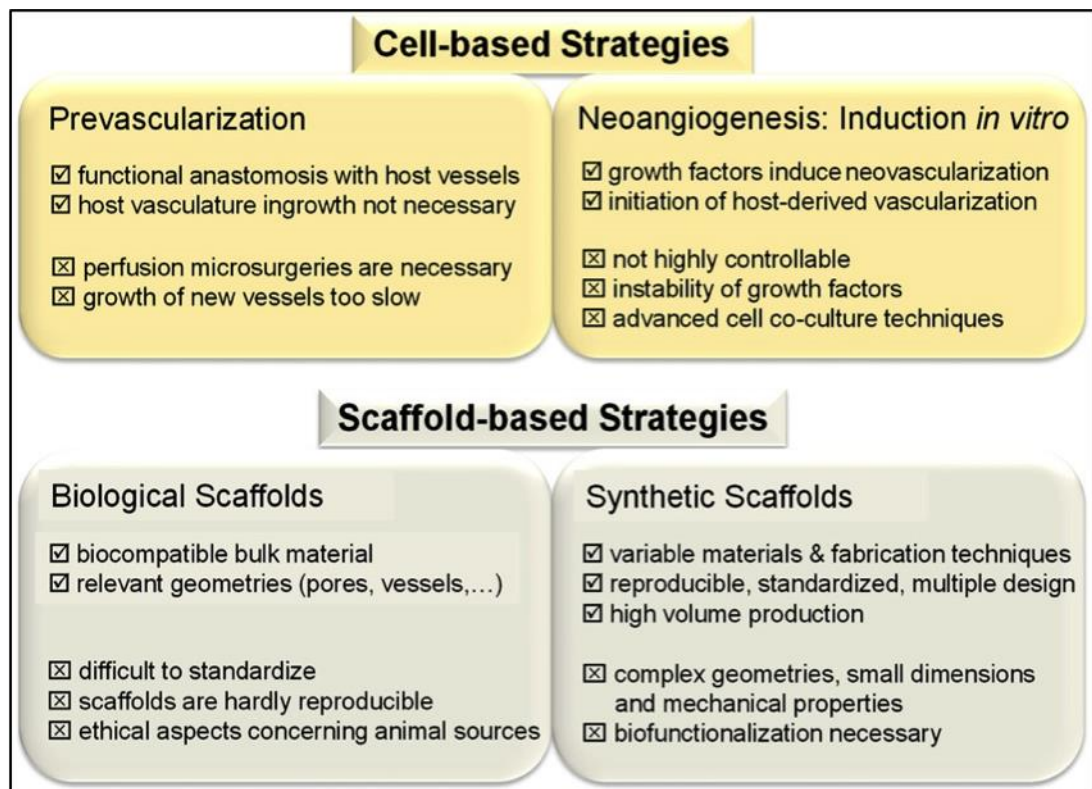


Figure 3 Tissue Engineering: The approaches to vascularisation and their inherent advantages and disadvantages (Novosel et al., 2011).

‘Bio-fabrication/Bio-printing’ is an emerging technology for the rapid deposition of both cells and scaffold for the primary engineered tissue. At present, research is being conducted into methods for the perfusion of the resulting engineered tissue. As the main focus of Bioprinting is engineering the primary tissue it is discussed separately in Section 1.3.3.

1.3.1 Cell Based Strategies

It can be seen from Figure 3, that cell-based strategies are divided into two broad categories i.e. neoangiogenesis and pre-vascularisation.

Neoangiogenesis

Neoangiogenesis relies on the ability of existing vasculature to respond to biochemical cues that induce spontaneous budding and growth of new capillaries and then in turn directs capillary proliferation into the implanted engineered scaffold or tissue construct (Patan, 2001). The research goal is usually to identify, sequence and quantify the angiogenic cellular interactions and then reconstruct that process within in vitro TE constructs, using combinations of cells and growth factors that provide the base materials and stimulation required to initiate, support and then stop angiogenesis once complete (Laschke et al., 2006). However, the fact that research in this clinical sector is focused on the inhibition of growth factors rather than stimulation (in order to manage tumour growth) illustrates the lack of control that can be exercised over the process of angiogenesis.

In addition to the disadvantages of the cell-based strategies shown in Figure 3, a more pragmatic limitation must also be noted. Despite intense research activity and expenditure, only two angiogenic growth factors to induce enhanced wound healing have received U.S. Food and Drug Administration approval at present. More significantly, others have failed to gain approval, thereby effectively placing regulatory and commercial restrictions on the range of potential solutions that may be developed and applied in the clinic (Barrientos, Stojadinovic, Golinko, Brem, & Tomic-Canic, 2008).

Pre-vascularisation

Pre-vascularisation of a tissue construct with a network of capillaries is undertaken with the aim of accelerating functional anastomosis or integration with the host tissue upon implantation. The research goal is usually to create cellular structures or tissue that can be transplanted, from either in vitro or in vivo locations, with the vascular features intact. Recent research from Sakaguchi et al aimed at providing 'patch repairs' for damaged myocardial tissue is shown overleaf, in Figure 4, as an exemplar of the prevascularisation approach (Sakaguchi et al., 2013). It also neatly highlights some of the more general strengths and limitations of cell-based approaches as noted by Novosel (Figure 3).

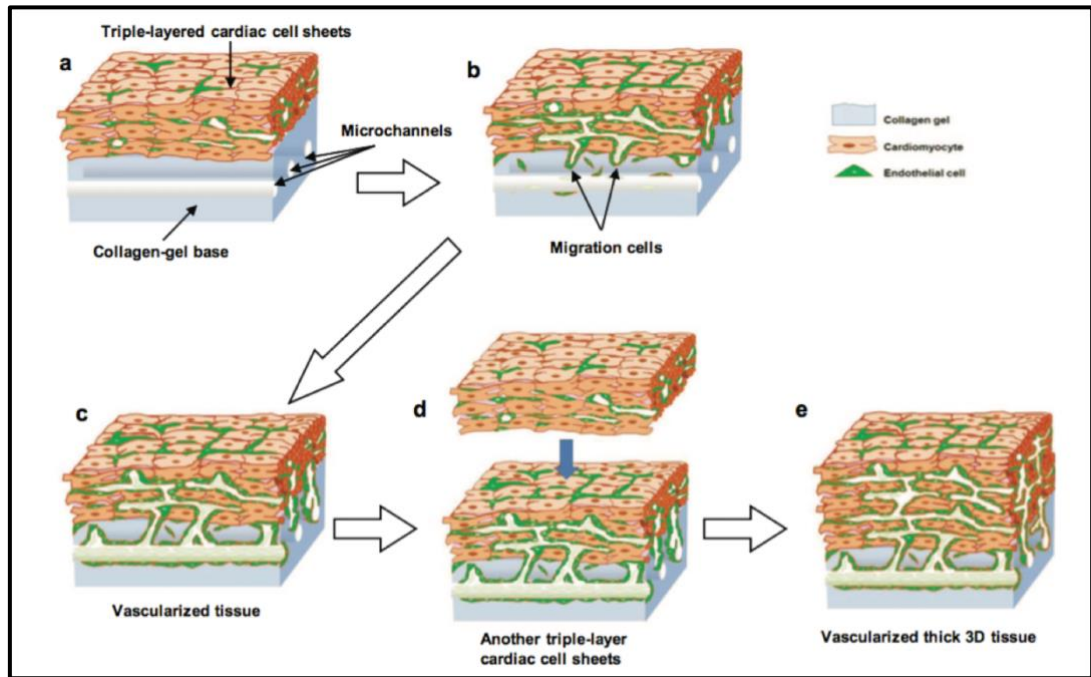


Figure 4 ‘In Vitro Engineering of Vascularized Tissue Surrogates’ from Nature Scientific Reports (Sakaguchi et al., 2013).

Sakaguchi et al took a triple layered sheet of previously incubated cardiomyocyte cells (the maximum thickness the cells could be allowed to proliferate to, before the inner most cells became hypoxic), then placed it onto a collagen base that had been artificially endothelialised via a series of microchannels through which growth serum circulated. The oxygen deprived cells naturally stimulated angiogenic activity in the endothelialised microchannels and capillaries formed with assistance from endothelial growth factors. An incubation period of five days was sufficient for endothelial cells to migrate from the microchannels into the triple layered cardiac cell sheet, self-organising to form budding micro-vessels, thereby allowing delivery of oxygen and nutrients to the previously oxygen deprived cells. Once angiogenic activity was complete in this triple layer of cells, another triple layer cell sheet would then be added on to the surface of the existing vascularised sheet. It was found that the process could be repeated every five days until the desired thickness of engineered tissue (120 micron) had been achieved over a period of 20 days.

The technique illustrates how the evaluative criterion of ‘co-fabrication’ is met because both microvasculature and engineered tissue are fabricated together. Sakaguchi et al’s choice of clinical need for their ‘in-vitro micro vascularisation’ approach neatly sidesteps the first drawback noted by Novosel (Figure 3), as extensive perfusion microsurgeries aren’t needed to create functional anastomoses between engineered tissue and host tissue in this instance. Instead, the anastomoses rely on the phenomenon of ‘inosculation’, whereby the patients existing

microvascular network 'finds and joins' with the implanted tissue's microvascular network in order to restore perfusion (Tremblay, Hudon, Berthod, Germain, & Auger, 2005).

It is often the case that 'time is of the essence' for restorative medical procedures. If the chosen TE method for vascularisation of the engineered construct means excessive delays in patient' treatment, then that choice may prejudice the final clinical outcome. The approach clearly illustrates the excessive time taken for clinically relevant tissue' thicknesses to be produced (e.g. 120 micron in 20 days in the above example) when contrasted with known endothelialisation rates of fabricated microvascular scaffolds of 0.5 mm per day. Such rates are achieved by simple cell migration within vascular scaffolds that have been subjected to optimised rates of pressure and flow (Linville, Boland, Covarrubias, Price, & Tien, 2016) and the higher rates that can be achieved by direct cell seeding.

1.3.2 Scaffold Based Strategies

In the context of vascularisation, scaffold-based strategies focus on creating a spatial framework for endothelial cells (EC) to attach to, proliferate in and to guide their migration in order to create a microvascular network (Liu et al., 2011). The scaffolds rely on the morphogenic behaviour of endothelial cells to attach to smooth continuous surfaces and create flat, single cell thickness, sheet-like structures that form cylindrical conduits (C. Xu, Yang, Wang, & Ramakrishna, 2004). Two methods are used to create these microvascular scaffolds; a, by utilising existing biological networks of branched tubular structures or b, manufacturing the microstructures from biopolymers or biocompatible synthetic polymers.

Biological Scaffolds

Avoiding the task of synthetically mimicking organic structures by reusing existing biological structures presents an interesting interim step toward achieving the goal of in vitro vascularisation. Selecting similar tissues from mammalian sources (xenograft) or human cadaveric sources (allograft) and then decellularizing those tissues reveals an extracellular matrix (ECM) of collagen and other useful biomolecules, whilst the vascular conduits remain intact but cell free. This residual structure provides an effective microvascular template for recellularization with the seeding, proliferation and migration of ECs recreating a complete vascular network. An additional benefit is that the remaining ECM is structurally superior to synthetically produced collagen matrices from current fabrication methods e.g. freeze-drying and electro-spinning (Silver, Freeman, & DeVore, 2001).

However, the broad acceptance of the method is limited by the physiological relevance of the grafted tissues, issues over quantity and consistency of supply, as well as important considerations regarding clinician and patient acceptance of reconstituted tissue from certain sources.

Synthetic Scaffolds

The fabrication of microvascular scaffolds creates the possibility that optimised microvascular structures may be designed and then uniformly reproduced in an automated or semi-automated way. Synthetic scaffolds offer the prospect of both consistency and repeatability in the final scaffold as well as scalability, which in turn raises the probability of widespread clinical acceptance and long-term commercial viability.

Additive Manufacturing (AM) technologies are a natural choice because of microvascular scaffolds' complexity and micro-scale proportions, as well as the need for frequent design changes and small experimental production runs. Additive Manufacturing (AM) is a term used to describe a set of manufacturing technologies where the fabricated item is the result of material being added together (in any of a number of ways). AM contrasts with 'subtractive manufacturing', a term that encompasses the large group of machining processes whereby the fabricated item results from material being removed or subtracted from a larger block of material.

The successful selection of an appropriate AM technology and a suitable material is primarily dependent on ensuring that the characteristics of the processing method (and any ancillary materials that may be used in it) and any properties it should impart to the chosen material during the process are consistent with the requirements for the final finished biomimetic microvascular scaffold. Further considerations such as cost, convenience, waste etc. then influence the final choice of the ideal fabrication process-material combination.

However, attempting to directly fabricate a microvascular scaffold with its exacting spatial requirements (discussed Section 1.2.1) directly confronts additive manufacturing's technological limitations in terms of resolution and accuracy (see Table 1, following page). These challenges are further compounded by the need to select a material that is both appropriate to the chosen AM technology, but also offers the permeability/post-endothelialisation degradation rate and cytocompatibility needed for a microvascular scaffold (Salacinski et al., 2016).

Table 1 Characteristics of AM Technologies (Melchels et al., 2012)

Technique	Minimum Feature Resolution (micron)	Materials	Advantages	Disadvantages
Inkjet Printing	10-100	Liquids, Hydrogels	Inexpensive technology, multiple compositions	Low viscosity materials detract from 3D capabilities
3D Printing	50	Polymers, Ceramics	Multiple compositions	Methods and materials are cell unfriendly
Stereo-lithography (inc. two photon polymerisation)	0.5 – 50	Hydrogels, Polymers, Ceramic composites	High accuracy	Single composition and requires photo curing
Laser Induced Forward Transfer (LIFT)	20	Polyelectrolytes	Single cell manipulation	No structural support for cells
Direct Writing	1	Thermoplastics, Composites	High accuracy	Methods and materials are cell unfriendly
Melt Extrusion	100	Thermoplastics, Composites	Technologically simple	Requires strong filament and high temperatures
Robotic Dispensing	100	Hydrogels, Polymers, Ceramic-composites	Multiple compositions	Relatively low accuracy
Selective Laser Sintering	50	Polymers, Ceramics	Suitable for some scaffold materials	Methods and materials are cell unfriendly
Biolaserprinting	10	Liquids	High accuracy, high speed	Low viscosity hampers 3D capabilities
Robotic Assembly	5	Rigid Solids	No heat or light required	Expensive setup costs

Relating the capabilities of the AM technologies outlined in Table 1, to the need for the precise replication of a functional 3D microvascular system discussed in Section 1.2.1., the first criterion for the elimination of candidate technologies for consideration is resolution.

Ideally, the chosen AM technology/material combination would be able to directly fabricate branching cylindrical vessels with a minimum internal diameter of between 10 micron and 1 mm, with corresponding wall thicknesses ranging from one to twenty micron. This breadth of capability is required so that biomimetic structures can be fabricated from capillary level to a size and diameter that is suitable for easy manipulation through post- fabrication processing stages (e.g. sterilisation), and subsequent attachment and perfusion, either at the laboratory or clinical level. This spatial requirement eliminates all AM technologies with the exception of Micro stereolithography (which includes two or multi-photon polymerisation) and Direct Writing. Direct Writing requires the use of cytotoxic solvents, which are likely to harm the biocompatibility of the final finished structure.

This indicates that Micro-stereolithography, particularly two-photon polymerisation (as its highest resolution derivative) is the only AM candidate suitable for investigation. Indeed, the approach has recently been the subject of an intense research effort by the 'ArtiVasc' consortium led by the Fraunhofer Institute in Germany (financed by a 10.5 M euro grant) (Fraunhofer, n.d.). Recent refinements to the two-photon polymerisation technique and associated processes and (in particular) the materials have shown that this technique now has the capacity to meet the spatial demands required for the fabrication of pseudo-capillary structures. Figure 5 below is reproduced as an exemplar of the two-photon polymerisation technique (Meyer et al., 2012).

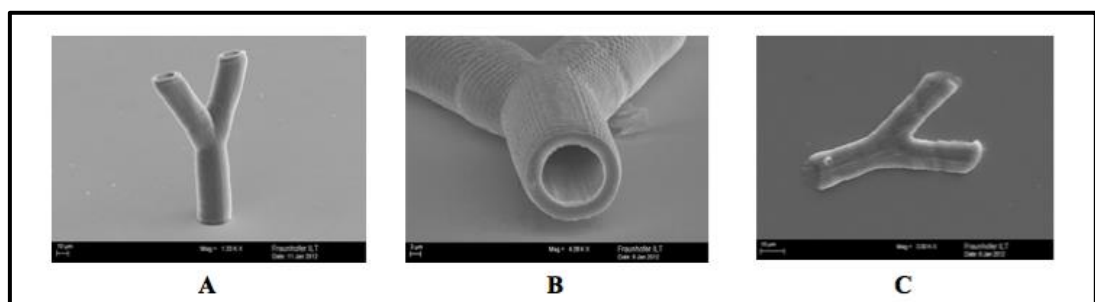


Figure 5 Branched tubular structures fabricated by two-photon polymerisation of PTHF-PA 1. Height 160 μm , internal diameter 18 μm and wall thickness 3 μm (Meyer et al. 2012).

The polymer is biocompatible and has similar mechanical properties to the human microvascular system. However, the microstructure shown in Figure 5 does not allow the process of mass transfer to take place, as the material is impermeable.

Although permeability may be produced by fabricating a structure with suitably located voids whether by direct or indirect fabrication means (Hoch et al., 2014) or induced by the degradability of the material over time (i.e. it dissolves to leave an unsupported but endothelialised structure) neither of these pathways toward a biomimetic synthetic capillary is without difficulty, in spite of the considerable investment and intense research activity already expended.

1.3.3 Bio-fabrication/Bio-printing

Bio-fabrication/bio-printing research groups focus on the fabrication of scaffolds and rapid deposition of cells for primary engineered tissue. Novel methods for ensuring interim perfusion to the deposited cells have been sought, since physiologically relevant microvascular networks are beyond the grasp of T.E. at present. In general, these methods gravitate toward the formation of ‘microchannels’ within the scaffold for the primary engineered tissue. Although these microchannels lack many features that define microvascular biomimicry (e.g. bifurcating hierarchy, lumen-like dimensions, capillary-like spacing and vascular return mechanisms) they are sufficient to prolong the lifespan of the deposited cells. Datta et al provides a comprehensive review of the methods by which microchannels may be formed (Datta, Ayan, & Ozbolat, 2017)).

The ‘Nature’ protocol for the ‘Formation of microvascular networks in vitro’ (Morgan et al., 2013) as shown in Figure 6 (overleaf) provides an exemplar of the aforementioned approach. Here, ‘soft lithography’ has been used to create a dual component master mould (i.e. top and bottom) incorporating a pseudo-capillary structure on a two-dimensional plane. Polydimethylsiloxane (PDMS) production moulds have then been used to capture and transfer the master mould’s detail into a collagen solution, which is then allowed to gel. Once gelation is complete, the mould is removed, and the two component parts are combined. The result is a network of microchannels neatly encased in a collagen gel, which can be seeded with endothelial cells, before being perfused with serum.

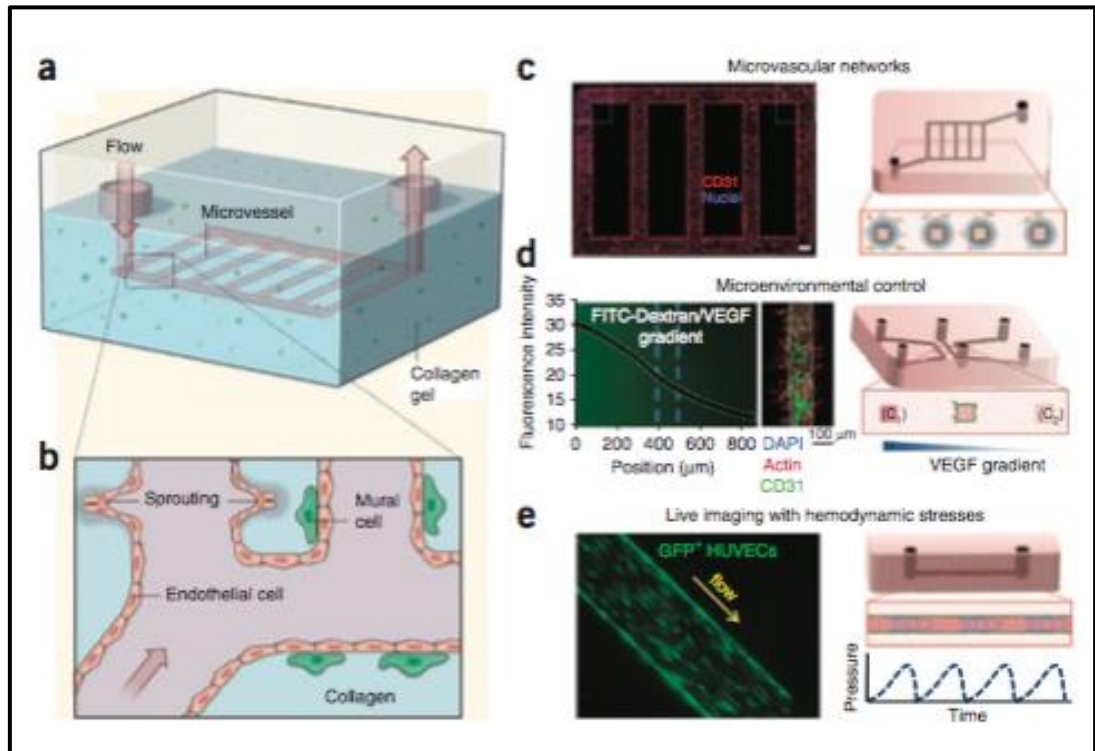


Figure 6 'Formation of microvascular networks in vitro' (from Nature Protocols) provides a step-by-step guide to the formation of microfluidic conduits in a collagen hydrogel for subsequent endothelialisation (Morgan et al., 2013).

The smooth surface of the collagen hydrogel provides a biocompatible material with a biomimetic surface, which facilitates cell attachment, proliferation and migration. The combination of a perfusing bioreactor and hydrogel scaffold nurtures the endothelial cells, as well as provides interim biological support to cells around the microchannels.

Bio-fabrication may provide useful insights into the challenges of co-fabricating a microvascular network in conjunction with the primary engineered tissue. Further research work is being undertaken toward promoting the spontaneous formation of capillaries (neoangiogenesis) from the microchannels into the engineered tissue so that more efficient perfusion and subsequent diffusion may occur. However, such methods are unlikely to provide either the biomimicry or scalability requirements required for tissue replacement technology in the immediate future.

1.4 Indirect Fabrication as an Alternative to Direct Fabrication

1.4.1 Indirect Fabrication and AM Technologies

In Section 1.3.2, it was established that AM technologies using direct fabrication methods are challenged by the criteria (replication, co-fabrication and scalability) developed to evaluate Tissue Replacement Technologies. However, indirect fabrication methods (also known as sacrificial methods) present an alternative avenue for exploration.

Indirect fabrication, such as investment casting and lost wax/mold casting describes the process of producing a sacrificial mold that is a replica of the desired final form of the item to be produced. The sacrificial mold is then either surrounded by or filled by the material that will form the finished item, which is then allowed to harden or cure. Once that material is cured, the sacrificial mold is then removed by a suitable process, leaving the finished item with the dimensions and detail of the sacrificial mold. Naturally, 'indirect' fabrication methods introduce an additional material (the sacrificial material) and additional processing steps (e.g. to remove that material) to the total fabrication sequence (compared with direct fabrication). It should also be noted that direct fabrication methods often incorporate support materials in order to fabricate overhanging structures, which function in a similar way to the materials used in a sacrificial structure. Considerable care must be exercised in the selection of the *appropriate* sacrificial material and its subsequent removal method to ensure that the physical characteristics and biocompatibility of the final TE scaffold are maintained.

Indirect fabrication methods e.g. particulate leaching and freeze drying, are commonplace in the construction of TE scaffolds, but appear to have gone largely untested in the search for a combination of AM technology and fabrication method to produce microvascular scaffolds. Returning to Table 1 and reconsidering AM technologies with indirect fabrication methods in order to produce what would now be sacrificial facsimiles of microvascular structures, it can be seen that whilst Micro-stereolithography/ two-photon polymerisation remains a candidate technology, Robotic Assembly, and Inkjet Printing may now be added to this list.

At the lower resolutions needed for fabricating sacrificial microvascular facsimiles (approx. 10 micron) lower but faster derivatives of Micro-stereolithography than two photon polymerisation might be used in conjunction with biodegradable polymers such as PLA although support materials would be required for the overhanging structures necessary in a microvascular structure (see Figure 1). The combination of two sacrificial materials in one microstructure may complicate the fabrication

process. Indeed, Raman et al describe a novel method for high resolution projection micro-stereolithography with a feature resolution of less than 5 micron. However, the advance in resolution was hindered by a layer thickness of 100 micron, although it was not evident if optimisation of the layer thickness had been attempted (Raman et al., 2015).

Robotic Assembly poses the immediate question of 'precisely what is being assembled?' i.e. what methods and materials are being used to fabricate the sacrificial components that are then to be assembled into microstructures, and thus fails to advance the discussion. A potential synergy is readily apparent between Micro-stereolithography and Robotic Assembly i.e. Micro-stereolithography might be used to fabricate the sacrificial components of a microstructure (stopping short of the point that support materials would be required), Robotic Assembly could then be used to piece those component parts together to form a complete sacrificial microvascular structure. Although the concept is undemanding, it is easy to imagine that a considerable research program, perhaps in the order of that of the ArtiVasc consortium, might be needed to bring the concept to fruition.

In some respects, Inkjet printing (IJP) stands out as a candidate technology. IJP output is circular, which replicates the cross section of the microvascular lumen. The readily available range for Inkjet printhead apertures (10 - 100 micron diameter) also corresponds well with the lumen sizes present in the arteriole-capillary-venule structure. In Table 1 it is noted that the need to use low viscosity materials as the printing 'ink' detracts from Inkjet Printing's 3D capabilities. This disadvantage may be able to be overcome if thermal phase change materials (relying on temperature change for solidification) were to be used as inks, enabling the fabrication of solid, but thermally reversible sacrificial three-dimensional lumen-like structures. Therefore, if the IJP output (i.e. individual deposited droplets) can be assembled in 3D, then solid facsimiles of microvascular structures could be fabricated without the need for support structures. Furthermore, the very ubiquity of Inkjet Printing demonstrates its track record of scalability.

The use of thermal phase change inks has been documented in IJP literature, albeit for direct 3D fabrication (Gao & Sonin, 1994). Thermal phase change materials are often ideal candidates for use in 'indirect' fabrication processes, as the phase reversal of an *appropriate* thermal phase change material (in order to facilitate the removal of the sacrificial structure) rarely damages the TE scaffold that has been formed around it. The fabricated sacrificial structures could then be either set in, dipped in or coated with a suitable biocompatible polymer before being sacrificed, thus leaving appropriately dimensioned, lumen shaped voids within a biocompatible scaffold.

IJP has been documented as an indirect fabrication method for TE scaffolds. Sachlos et al advanced the method of using IJP to deposit proprietary build and support materials, using a 2.5D 'layer-by-layer' method to fabricate microstructures with conduits in the shape of rectangular microchannels, at a minimum feature resolution of approximately 100 micron (Sachlos, 2003). Similar research was undertaken by Yeong et al, albeit with fewer processing steps (Yeong, Chua, Leong, Chandrasekaran, & Lee, 2006).

1.4.2 Novelty

The noteworthy aspects or 'inventive steps' of this proposed use of IJP as the AM technology are:

- a) the recognition that if the 2D circular microscale IJP output were to be stacked or arranged spatially in 3 dimensions it would replicate the external dimensions of microvasculature and
- b) if a phase change material were used as the ink, then once encased in a suitable biomaterial that solid 3D replica of microvasculature could then be removed or sacrificed, then
- c) lumen like conduits would be left in the biomaterial, which can serve as a scaffold for endothelialisation.

It may be argued that previous research impinges on the novelty of this thesis. However both Sachlos et al and Yeong et al did not recognise and explore the method by which the fundamental geometry of 2D IJP output might be best matched to the fundamental geometry of a 3D microvascular structure in order to fabricate microvascular facsimiles i.e. their output is a microstructure with a rectangular cross-section microchannel, which although exhibiting a lumen-like width, cannot be considered to be a facsimile of the microvasculature that occurs in the human body.

Meanwhile, whilst Gao and Sonin explored the basic use of IJP in 3D, they did not realise that the 3D microstructures that they had created could be further developed, and given the appropriate choice of sacrificial ink, then be used as sacrificial microvascular facsimiles.

The core novelty of this thesis is therefore: it is the first to investigate this combination of technology (IJP), method (3D assembly) and material (thermal phase change inks) for the purpose of fabricating sacrificial microstructures that replicate microvascular structures (a novel output), which may subsequently be used in the indirect fabrication of microvascular scaffolds.

1.4.3 Research Aims and Objectives

1.4.3.1 Primary Aims and Objectives

In order to unlock the potential of Tissue Engineering, a method for providing perfusion to thicker engineered tissue via vascular/microvascular networks is required. The primary aim of this research is therefore to test and assess the suitability of 3D IJP in conjunction with thermal phase change inks as a novel method to fabricate sacrificial vascular/microvascular facsimiles against the key evaluative criteria of replication, co-fabrication and scalability.

Objectives

- To identify a suitable set of Inkjet droplet actuation and deposition parameters.
- To optimise a set of three-dimensional droplet fabrication techniques that enable the consistent deposition of sacrificial microvascular facsimiles, focusing on lumen diameters, bifurcation of lumen, connection of bifurcating structures with arches and biomimetic spacing of microstructures.
- To fabricate these microstructures so that they are freestanding at an 'aspect ratio' (ratio of a structure's height to its diameter) similar to that of microvascular networks. Furthermore, to fabricate the previously mentioned overhanging features without the use of support materials.
- To investigate the development pathway required to overcome performance gaps between the current IJP apparatus and a hypothetical ideal apparatus that is able to deliver consistency and repeatability in the fabricated microstructures i.e. an IJP platform that ensures that fabrication is technologically feasible. Then to assess the viability (can deliver vascularisation for clinically meaningful volumes of tissue) of 3D IJP as a technological platform.

1.4.3.2 Ancillary Aims and Objectives - Aiding 'Enabling Technologies' for Tissue Replacement

Whilst the primary focus of the thesis is on the fabrication of sacrificial microvascular facsimiles it is important to note that the solution to engineering Tissue Replacement constructs will be advanced but not resolved by fabricating a biomimetic scaffold for a microvascular network. A complete solution to this multi-faceted problem can only be arrived at by considering the broader challenges to engineering complex tissue. Development of three key 'enabling technologies' is essential.

At present 3D 'in silico' research in the field of hemodynamics is dominated by a top down modelling approach, in part because of the absence of any suitable 3D microfluidic platforms, which are essential to provide validation for 3D in silico

microvascular models. Validated *in silico* models are in turn needed to design the spatial arrangement of the microvascular network in tissue engineered constructs.

Also, it is not currently feasible to insert or 'retrofit' a three-dimensional microvascular network into the primary engineered tissue, nor is it possible to engineer a tissue around an unsupported (but fully functional) microvascular network. This means that (near) simultaneous coproduction of the two scaffolds should be considered.

Finally, endothelializing a complex branching 3D microvascular network by direct cell seeding techniques also presents significant difficulties, because endothelial cells have a diameter of approximately 10 – 15 micron, which means that even the most minor agglomeration of two or three cells can cause a blockage in conduits that are approaching capillary-like dimensions.

Ancillary Objectives

- The fabrication of 3D lost wax 'micro-phantoms' in PDMS using 3D IJP, to act as microfluidic devices may provide a suitable platform for 'in silico' models of microvascular networks to be validated 'in vitro' and is demonstrated in Section 7.1.
- To produce a microvascular scaffold, and then fabricate the primary engineered tissue scaffold (the partner in the symbiotic relationship) around the previously engineered microvascular scaffold to provide mechanical support until the complex vascularised tissue matures, which is further discussed and tested in Section 7.2.
- To design a bioreactor capable of maintain low seeding densities for extended periods of time at physiologically relevant pressures and (reversible) flows for capillaries, the frequency of agglomerations might be minimised. This conceptual overview is demonstrated in greater detail in Section 7.3.

Chapter 2 An Introduction to Inkjet Printing in Three Dimensions

2.1 IJP as a 2D AM Technology

IJP technology found initial commercial acceptance as a means to increase the efficiency of small print runs of text and graphics by digital printing and was essentially 2D in nature. Although traditional IJP technologies can all be characterised as ‘push’ processes i.e. a droplet is ejected from the printhead, the mode of ejection distinguishes the three main technologies used in IJP. Whilst ‘continuous inkjet printing’ (CIJ) is more widely used in commercial printing processes, greater resolution control means that ‘drop on demand’ (DOD) is the more commonly known research grade IJP technology. Within the DOD category, there are two main methods used to affect the formation of the droplet and its subsequent ejection:

- Thermal
- Piezoelectric

Thermal printers use a compact thin film resistive heater to rapidly heat a small portion of the ink in the droplet chamber, which leads to the brief formation of a small pocket of gas. The pocket of gas then collapses once the process of heating has ceased. The formation and collapse provide the pulse (mechanical actuation) required to eject the droplet.

Thermal technology is less expensive than Piezoelectric technology, but the thermal character of the process requires that the properties of the inks are conducive to thermal printing i.e. the ink does not undergo an undesirable phase or viscosity change as a result of thermal actuation. Generally, the use of thermal actuation is not well suited to TE needs, where thermally sensitive materials such as biocompatible polymers, proteins and cells may all be used as ‘bio-inks’.

Piezoelectric printers rely on the mechanical action of the piezoelectric crystal as the principle for actuation of the droplet. Application of an electrical current to the piezoelectric crystal causes wall deformation in the droplet chamber setting up a negative pressure wave. Once wall deformation stops, the return of the chamber wall to its original position sets up a positive pressure wave. The timely combination of the pressure waves creates a pulse, which serves as mechanical actuation for ejection of the droplet.

2.2 The Use of IJP as a 3D AM Technology

2.2.1 Introduction

While IJP had proven its effectiveness in reproducing arbitrary 2D patterns on 2D surfaces its development into an equivalent 3D technology was more difficult because 'printer' ink requires a substantial amount of solvent, which once evaporated leaves only a correspondingly small amount of solid material (T. Wang, Patel, & Derby, 2008). Continuous overprinting (i.e. layer by layer) to achieve any sort of meaningful 3D structure is therefore time consuming and requires precise droplet deposition. In an attempt to resolve this issue phase change inks with negligible solvent loadings were used where solidification of the ink was induced by chemical or thermal reaction.

For chemically reactive systems, premixing of the chemicals for ejection through a single printhead ran the risk of the ink solidifying in the printhead prior to deposition. The alternative method of using multiple printheads to deposit alternate droplets of the reactive components in the same location was reliant on the degree to which the two reactive components mixed when deposited on the substrate. For effective mixing to occur it has been found that the first deposited droplet had to be larger than the incoming droplet so that a reactive 'vortex ring' of base around catalyst was formed (J. R. Castrejón-Pita, Kubiak, Castrejón-Pita, Wilson, & Hutchings, 2013). Despite this limitation, chemically reactive IJP had been applied to biomaterials, pattern polymers and other reactive materials.

Reactive IJP has been successfully utilised by Pataky et al for directly depositing alginate 'bio-inks' (biocompatible hydrogels with highly controlled spreading and setting behaviour) to form TE scaffolds, which included a network of bifurcating lumen-like voids, for the subsequent perfusion of the hydrogel (Pataky et al., 2011). The minimum feature dimension for the lumen like voids was also approximately 100 micron. Christensen et al fabricated alginate structures using calcium chloride both as a cross-linking agent and a buoyant support material (to enable IJP of overhanging structures) (Christensen et al., 2015). Although the minimum feature resolution achieved was one millimetre (wall thickness) and lumen diameters ranged from 3 mm to 5 mm, the construct was successfully seeded with fibroblasts and cell viability was reported as 92% after 24 hours.

For thermally reactive systems, the phase change material is typically a solid at room temperature which is heated to a liquid prior to printing. Upon deposition the droplet cools and solidifies at room temperature. If the phase change is liquid at room temperature, then the process is reliant on a cooled substrate to lower the temperature of the deposited droplet to effect phase change. Wax presented an obvious initial choice as a thermal phase change material, as it was already widely used in a variety of moulding processes and might naturally lend itself to the investment casting process. Later research led to the suspension of a variety of particles within the wax that are small enough to pass through the printhead. Considerable research was devoted to the use of ceramic particles in order to solidly freeform ceramic objects for use in their own right or for use in ceramic shell investment casting (Derby, 2011). The use of metallic nanofluids was also assessed in an attempt to fabricate 3D printed micro-wires and other electrical components (Kullmann et al., 2012).

As the expansion of AM has accelerated two approaches 'Binder Jetting' and 'Material Jetting' have formed the backbone of IJP's use in the growing 'rapid prototyping' sector (so much so that the name of the application became synonymous with the field of additive manufacturing).

2.2.2 Binder Jetting

'Binder Jetting' is the process of inkjet printing a binder onto a layer of powder (also known as the powder bed) whereby the powder is solidified by the deposited droplet. The process is repeated as subsequent layers of powder are spread across the powder bed and further binder is printed until the desired 3D structure is formed. The completed object is removed from the powder bed and the unbound powder eliminated. Although the binder jetting method has the advantage of the powder automatically acting as support material for any overhanging printed structures, the fabricated structures are usually porous and typically benefit from a powder/binder dependant post-processing step such as annealing (Ben Utela, Storti, Anderson, & Ganter, 2008) to reduce porosity and improve mechanical properties. However, while the post-processing step improves mechanical properties it can also cause a dimensional change in the printed structure (Shirazi et al., 2013). Licensed by M.I.T. as 3DP™ to Z Corp (subsequently taken over by 3D Systems) the method has not only been used to fabricate prototypes but also ceramic based polymer composites and more recently for time dependant drug delivery (Aprecia Pharmaceuticals - (Katstra, Palazzolo, controlled, 2000, 2000)).

Wang et al. have repurposed the concept of a printed photopolymer (used in the 'material jetting' method discussed below) to replace the traditional printed binder, which is subsequently cross linked by UV light, in order to create parts that are relatively pore free (T. Wang et al., 2008).

Generally, Binder Jetting can now produce batches of smaller parts and prototypes at a lower cost than Material Jetting, but the porosity of the finished item tends to effect mechanical properties thus limiting the parts suitability to lower end uses. The companies serving the commercial market can be coarsely divided by the material used as the powder in the binder jetting process. 3D Systems is associated with ceramics using the term 'ColorJet Printing', Voxeljet AG with thermoplastics, ExOne with metals and sand casting. More recently HP have entered the market with their MultiJet Fusion nylon powder printer, incorporating what previously may have been considered a post-processing operation (described as fusion but akin to sintering) into the fabrication process. Previously Fathi et al. had demonstrated printing nylon using a material jetting approach that included the fusion step within the fabrication process (Fathi, Dickens, & Hague, 2011).

2.2.3 Material Jetting

'Material Jetting' is an IJP method that directly jets the entirety of the material to be solidified in a layer by layer fashion. Although photopolymers are currently a popular choice of material (with each layer of material cured by the application of UV light beams), commercially the origins of the method can be traced back to the formation of 'Solidscape' in 1994 (then called Sanders Prototype Inc.) who released the first 3D wax printers for prototyping and making master moulds for investment casting. Although the company formation superficially aligns well with Gao and Sonin's - also M.I.T. - publication in 1994, this appears to be a case of commercial innovation arousing academic interest, rather than academic research spurring subsequent commercialisation. The use of photopolymers as the jetted material emerged in 1998 via an Israeli company 'Objet Geometries' (later merging with Stratasys Inc.). The range of jetted materials increased to include thermo-polymers with the arrival of 3D systems ThermoJet in 1999. Unlike 'binder jetting', 'material jetting' relies on the use of additional jetted materials to form support structures during the fabrication of overhanging structures. These materials are typically wax based, or water based materials that are either melted or dissolved away from the main fabricated structure as a post processing step.

The commercial market for Material Jetting platforms is dominated by Stratasys (PolyJet 3D printers) using a water soluble photopolymer as a support material and

3D Systems (ProJet 3D printers) using a wax material for support structures. While Solidscape has now been incorporated into the Prodways group, which previously focused on SLS printers, it maintains its offer of 3D wax pattern printers. 3D Systems and Solidscape both claim to offer high performance wax jetting on advanced commercial grade platforms specifically targeted at specialist jewellery designers and manufacturers. While 3D Systems fail to clearly list resolution and accuracy on their website (<https://uk.3dsystems.com/3d-printers/jewelry>), Solidscape S300 is described as having a resolution of 197 x 197 dpmm and an accuracy of +/-127 micron for the first 25 mm and +/-25.4 micron for each subsequent 25 mm. While the resolution is indicative of a fairly advanced substrate, the initial droplet deposition accuracy of +/- 127 micron is obviously insufficient for microstructures with absolute dimensions that are less than the S300's margin of error (<https://www.solidscape.com/s300-series-3d-printer/>).

Within TE, Sachlos et al used the material jetting method to deposit proprietary build and support materials, using a 2.5D 'layer-by-layer' method to fabricate microstructures with conduits in the shape of rectangular microchannels, at a minimum feature resolution of approximately 100 micron (Sachlos, 2003). Once formed the construct was placed in a mould, which was then filled with a concentrated collagen solution and frozen. The frozen construct was removed from the mould and immersed in ethanol, which dissolved the build and support materials, whilst also displacing the water from the collagen solution. The remaining construct was treated by 'critical point drying' in order to remove the ethanol from the construct, thereby leaving a porous collagen scaffold that could be perfused by means of the microchannels. Similar research was undertaken by Yeong et al, albeit with fewer processing steps (Yeong et al., 2006).

2.2.4 Electrohydrodynamic Printing

More recently 'electrohydrodynamic printing' (EHDP) is developing as a high potential micro/nanoscale fabrication technology. While EDHP has demonstrated its ability to fabricate 2D micropatterns, research has quickly ventured into 3D layer by layer fabrication. EHDP can be characterised as a 'pull' process because the ink is subjected to an electrostatic field to form a Taylor-cone and produce a fine jet or droplet from that cone. EHDP is predated by electrospinning, which evolved into near field electrospinning (NFES) in 2006 (Sun, Chang, Li, & Lin, 2006) mainly by reducing the nozzle to collector distance and narrowing the material deposition tip. Consequently, EHDP can overcome the resolution limitation of the nozzle size found in traditional 3D printing (Y. Han, Wei, & Dong, 2015). Furthermore, both melt materials and solution based materials can be used, whilst the process also has three

modes of ejection, described as electro-spraying, electrospinning and drop on demand modes (E-jet printing), thus enabling a multi-faceted build approach to 3D micro/nanostructures. Further refinement of process parameters, increased resolution of the movement of the collector stage and dynamic control of the distance between the nozzle will enable 3D EHDP to be a candidate technology for a computer controlled automated nanoscale 3D printing process (B. Zhang, He, Li, Xu, & Li, 2016).

2.2.5 Conclusion

This investigation into the fabrication of sacrificial microvascular facsimiles favours a material jetting approach using the traditional IJP piezoelectric DOD technology with a thermal phase change material. The probable porosity resulting from a binder jetting approach would clearly be detrimental to microstructures with a diameter equivalent to that of a single jetted droplet. It is also a more mature technology than EHDP, offers greater precision and smaller droplet formation than CIJ, while avoiding the possible complications that may be found with the use of thermal phase change inks with a thermally activated printhead.

Saunders & Derby considered that piezoelectric IJP was generally capable of generating droplets with the following properties:

- Droplet volume 1 - 100 pL
- Droplet diameter 10 - 60 micron
- Frequency 1 Hz – 30 kHz
- Velocity at ejection 1 - 10 m/s
- Distance between substrate and printhead of 1 - 3 mm

When considered collectively, IJP demonstrates a wide range of characteristics and competencies that are of particular relevance to TE. Boland et al have shown that IJP has the capacity for the accurate deposition of multiple cell lines, proteins, biomaterials and crosslinking agents (T. Boland, Mironov, Gutowska, Roth, & Markwald, 2003; T. Boland et al., 2007; C. C. Chang, Boland, Williams, & Hoying, 2011; Roth et al., 2004; W. C. Wilson Jr & Boland, 2003). The piezoelectric method is therefore well suited to the DOD requirements of bio-medical applications, ranging from the least complex such as the surface patterning of materials, to the most complex i.e. the full three-dimensional construction of a tissue analogue structure (Saunders & Derby, 2014).

2.3 Technical Considerations

2.3.1 The Working Principle of Piezoelectric Printhead Actuation

The typical electrical pulse applied to the piezoelectric actuator is a trapezoidal waveform. The transitions from one voltage level to the other first increase then reduce the cross-sectional area of the tube capillary as shown in Figure 7 below. The change in cross sectional area produces pressure variations (with respect to resting conditions) of the fluid enclosed in the tube.

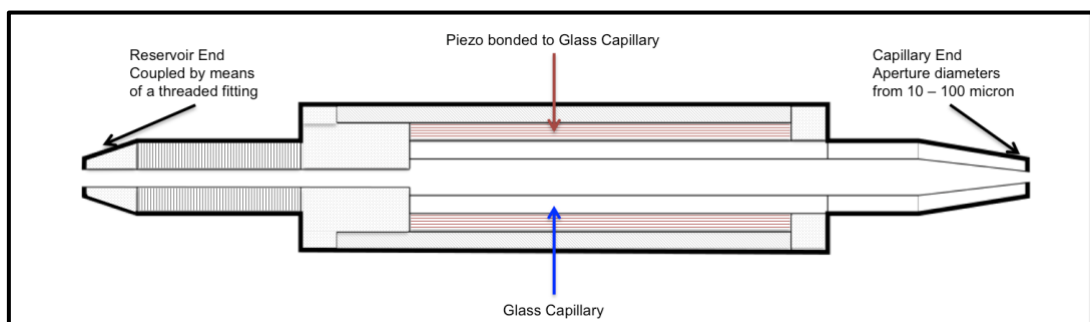


Figure 7 Cross section of the MJ-AT-01 Print head (MicroFab Inc. U.S.A.). Overall Dimensions: Length 26 mm, Diameter 4 mm

‘Ramping up’ from low to high voltage levels produces an expansion of the cross-sectional area of the capillary resulting in a lower pressure within the capillary. During the ramp up or “rise time” the inner surface of the glass tube moves outward and a negative pressure (expansion) wave is generated and starts to move towards both the supply (or reservoir) end and the aperture end of the capillary, as is shown in Figure 8 and 9 overleaf (double page figure)

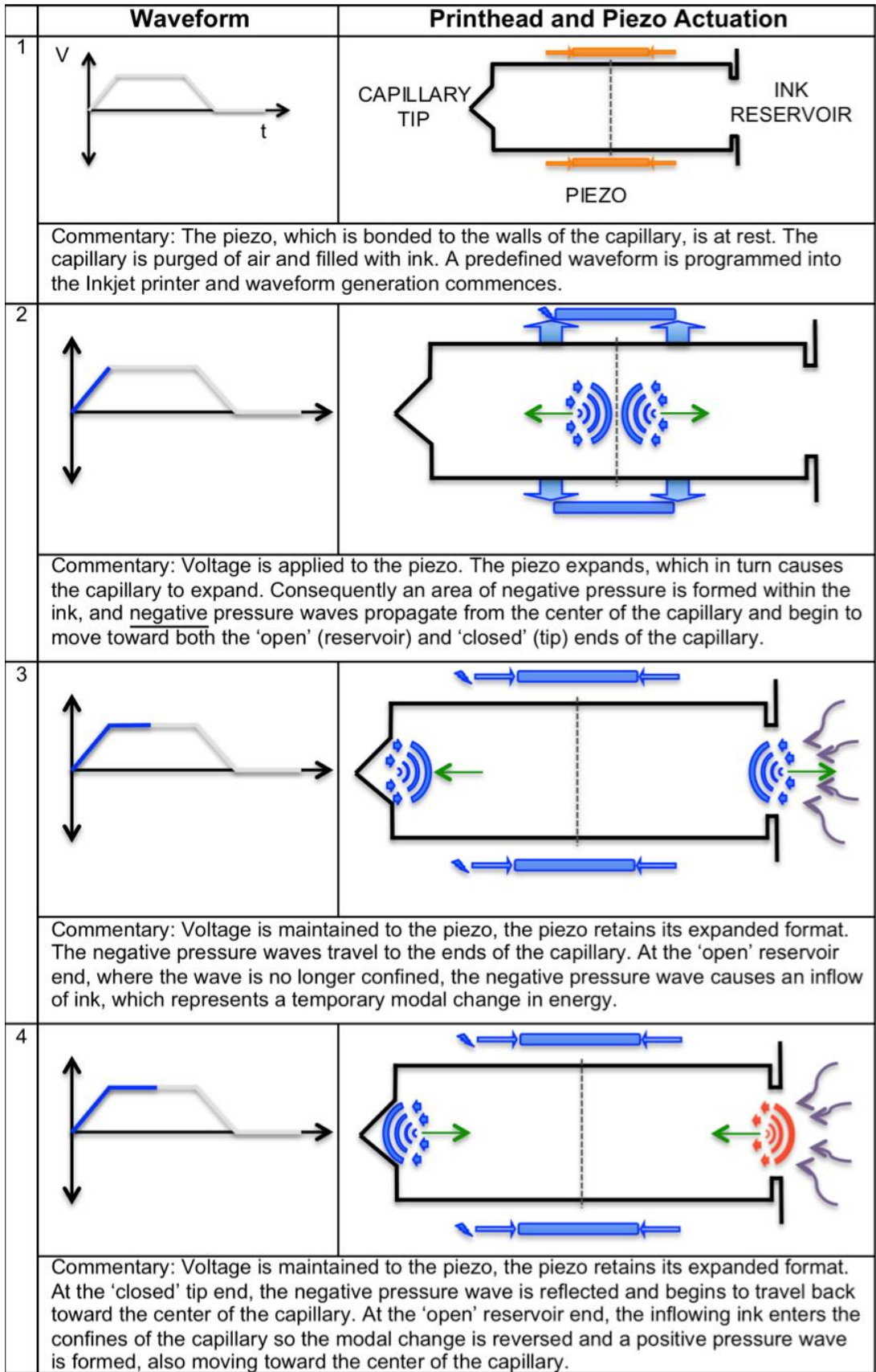


Figure 8 Printhead and Piezo Actuation via the Waveform

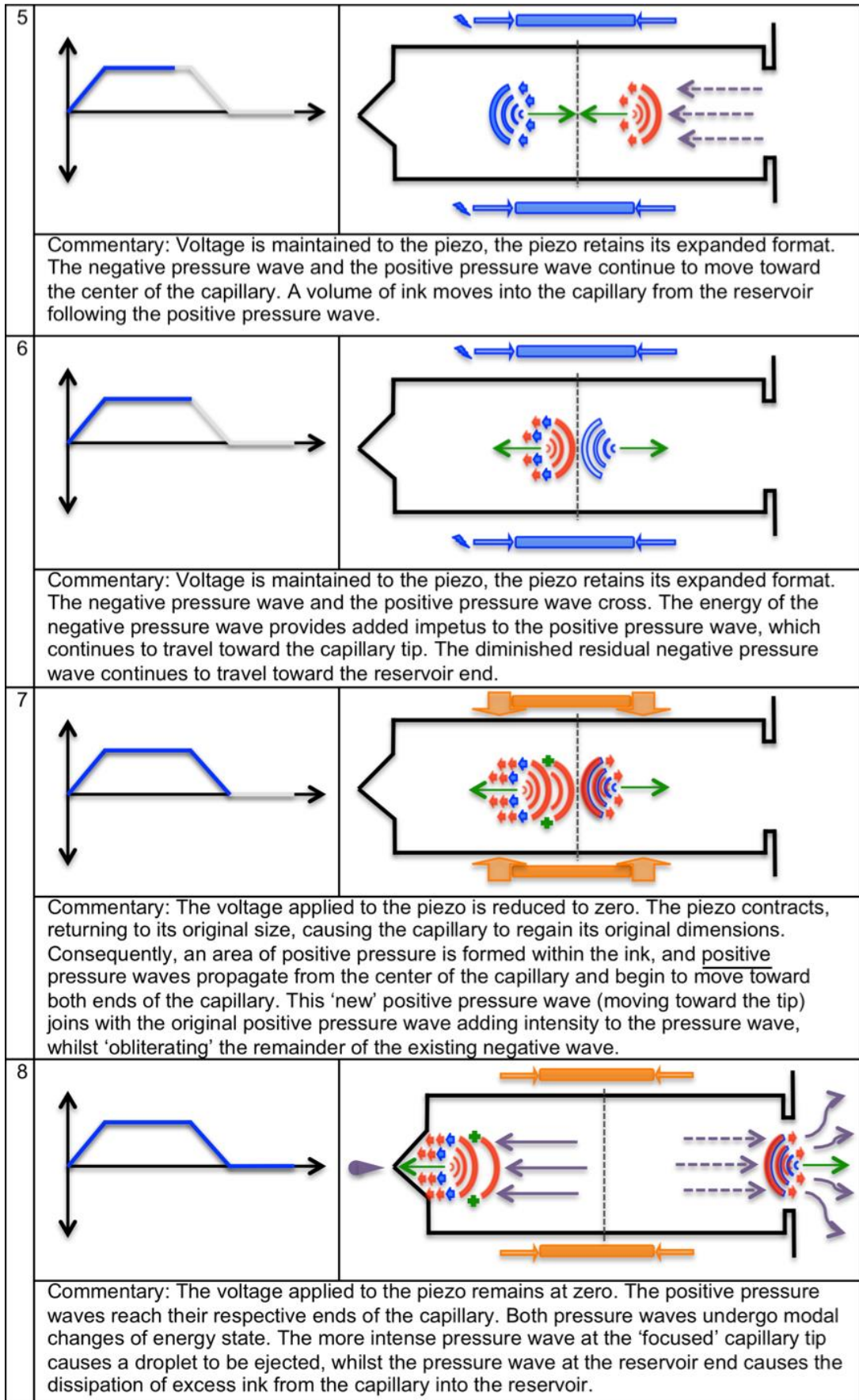


Figure 9 'Printhead Actuation' Continued

At the reservoir end the negative pressure wave reflects back as a positive pressure (compression) wave. The reflection phenomenon represents an ‘intramodal’ change as the negative pressure wave is satiated in the open reservoir as the pressure wave displaces a mass of fluid within the reservoir, pulling a volume of fluid at velocity toward the centre of the capillary. As this additional fluid mass enters the restrictions of the capillary, its volume and velocity produce a second modal change creating a positive pressure wave. At the aperture end of the capillary, the negative pressure wave is simply reflected back toward the centre of the capillary.

The “dwell time” (the time at high voltage when the capillary cross section does not change) is selected such that the ramp down or “fall time” of the voltage level starts when the reflected (now) positive pressure wave and the reflected negative pressure wave reach the middle of the capillary.

The voltage “fall” corresponds to a compression of the fluid (inward motion of the capillary as it returns to its original diameter) and thus reinforces the positive reflected pressure wave, which is travelling toward the aperture end of the capillary. The compression of the fluid also satiates the negative pressure wave, which is now travelling toward the reservoir end of the capillary. Furthermore, a residual positive pressure wave may be generated that travels toward the reservoir end of the capillary.

When the reinforced positive compression wave reaches the aperture of the capillary, the acoustic energy of the positive pressure wave is converted into kinetic energy due to the impedance mismatch (constant pressure boundary condition), which causes the fluid to start emerging from the aperture at high velocity.

2.3.2 Fundamental Aspects of Inkjet Printing with Thermal Phase Change Inks

The characteristics of the final printed droplet on the substrate can be assessed as two distinct processes:

- The formation of the individual droplet and the mode of ejection from the Inkjet printer
- The interaction between the droplet, substrate and other environmental conditions from droplet impact to solidification.

2.3.2.1 Droplet Formation and Ejection

The first condition that must be satisfied for an ink to be successfully printed is that the interaction of droplet size, surface tension and density of the ink are balanced in

relation to the ink's dynamic viscosity. This phenomena was captured by Fromm in the following equation (Fromm, 1983):

$$Z = \frac{\sqrt{\gamma \rho l}}{\eta}$$

Equation 1 The printability of an ink

Where γ is surface tension, ρ is density, η is the dynamic viscosity of the ink and l is the characteristic length of the droplet, which is considered to be equivalent to the diameter of the aperture of the printhead. Z is a dimensionless number that is easily related to other common dimensionless terms in fluid physics, where We is the Weber number, Re is the Reynolds Number and Oh is the Ohnesorge number.

$$Z = \frac{\sqrt{\gamma \rho l}}{\eta} = \frac{\sqrt{We}}{Re} = \frac{1}{Oh}$$

Equation 2 Relationship of dimensionless numbers

For the purposes of IJP, a low Z typically indicates that there is too much viscous dissipation of the energy generated (by chamber expansion and subsequent contraction) within the 'ink' for a droplet to; a, be ejected from the chamber or b, maintain sufficient velocity to generate a consistent trajectory from the printhead to the substrate. Conversely, a high Z shows insufficient surface tension in the droplet to prevent the formation of satellite droplets away from the body of the main droplet upon ejection (Smith & Stringer, 2015).

Fromm initially posited that the choice of ink and aperture diameter must give rise to a value of $Z > 4$ for IJP to be feasible. Following research initially extended the parameters to $1 < Z < 10$ (Reis & Derby, 2000) that is illustrated in Figure 10 on the following page. More recent experimental work proposes a larger range $1 < Z < 14$ (Derby, 2011; Jang, Kim, & Moon, 2009). However, in practise if satellite droplets are able to 'catch up and re-join' with the primary droplet, then inks with Z values greater than 14 may be printed (Tekin, Smith, & Schubert, 2008). Indeed, Tekin et al report printing of Z values up to $Z = 91$.

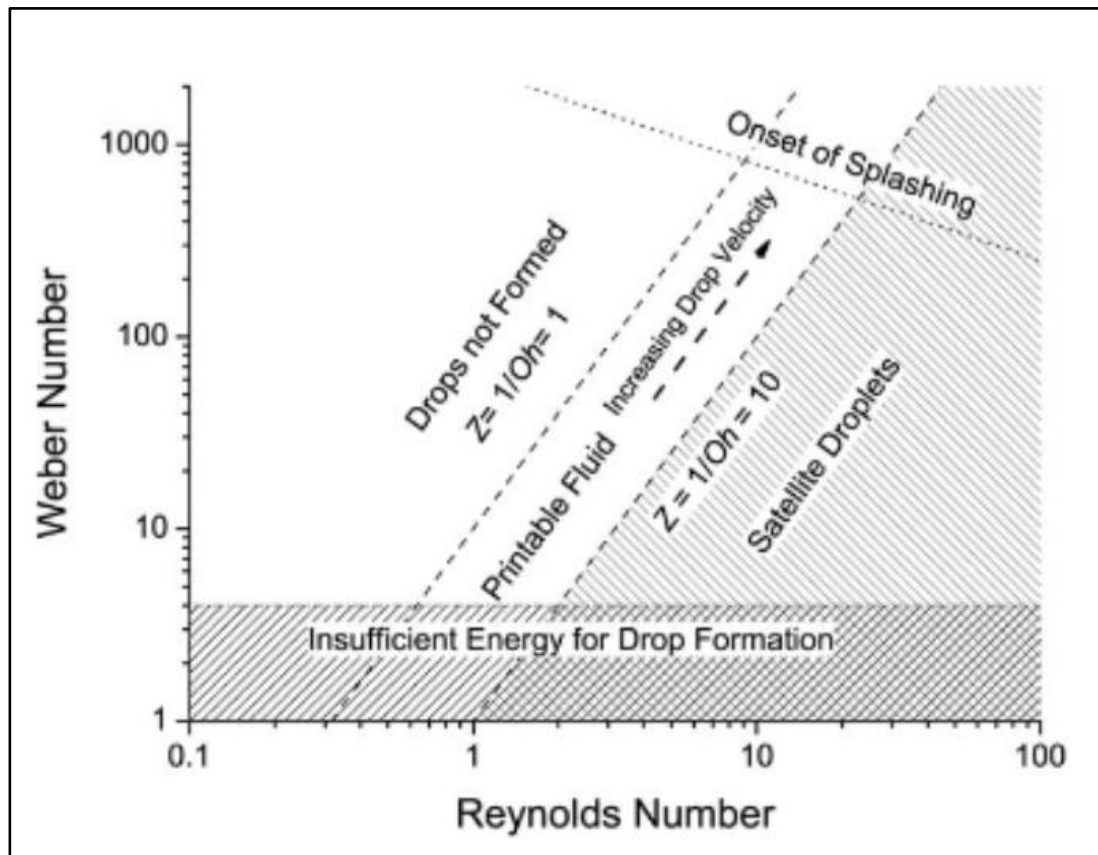


Figure 10: The Practicality of Inkjet Printing for Fluids (Derby and Reis 2003)

While it is convenient to separate droplet formation and ejection from surface impact and substrate interaction, there is naturally a linking factor between the two conditions. The velocity with which the droplet is ejected from the IJP printhead directly affects the impact energy of the droplet upon the substrate. Whilst the parameters of Z indicate a minimum velocity is needed to ensure droplet ejection (Khatavkar, Anderson, Duineveld, & Meijer, 2007), a maximum velocity is also required to prevent the droplet splashing on impact (Derby & Reis, 2003).

2.3.2.2 Droplet Behaviour of Thermal Phase Change Inks on Impact with the Substrate.

The development of IJP has mainly focussed on the technological needs of IJP manufacturers to produce ever-improving products for print consumers. For this reason, research into the behaviour of droplet interaction with the substrate has generally been concerned with printing inks, where phase change behaviour is typically reliant on solvent evaporation. While the focus of this thesis is on thermal phase change inks, both types of ink exhibit similar behaviour on immediate impact with the substrate. The main difference in the two types of inks is exhibited by their spreading behaviour on the substrate, subsequent to impact.

On impact with a flat substrate, the droplet deforms in accordance with its ejection velocity from the printhead and begins to spread. The initial force quickly reduces due to viscous dissipation of the force within the fluid droplet. In droplets with low values of We (low droplet inertia relative to its surface tension), capillary forces, i.e. the adhesive force between ink and substrate, then take over to drive the spread of the droplet over the substrate. The Ohnesorge number is useful in predicting droplet spreading behaviour in this situation, as it measures the ratio of the viscous forces that slow spreading against the inertial forces that aid spreading (Smith & Stringer, 2015).

At this point the behaviour of the two types of inks diverges. Inks relying on the (relatively) slow process of solvent evaporation will spread to an equilibrium shape defined by the liquid ink's contact angle with the substrate. In the case of thermal phase change inks, the issue of importance is that the spreading of a thermal phase change ink can slow and eventually cease, in correlation with the transfer of sensible and latent heat energy, before an equilibrium shape has been reached.

After the period between droplet impact and viscous dissipation of droplet momentum, spreading of the droplet due to capillary forces begins. At the interface between the substrate and the molten ink droplet, the viscosity of the ink progressively increases as transfer of the latent heat to the substrate begins. This, in turn, increases the resistance of the ink droplet to the capillary forces, slowing the droplet's spreading rate. As equilibrium between the capillary forces and the resistance due to the changing viscosity is reached, spreading slows. The slow spreading of the cooling ink allows phase change completion at the contact line (the droplet perimeter) and thereby effectively 'pins' or stops the spreading. The transfer of the remaining latent heat to the substrate continues until phase change is complete throughout the droplet.

A number of other dynamics exist in the interrelationship between spreading driven by capillary force and the phase change driven resistance to spreading. Two important considerations are:

- The increasing contact area between the droplet and the substrate. Initially, during the period between droplet impact and viscous dissipation of droplet momentum, the contact area between droplet and substrate is small and limits the transfer of energy from the droplet to the substrate. As spreading occurs, the contact area increases, hastening the transfer of energy between droplet and substrate, accelerating the progress of the ink droplet toward phase change.

- The reducing rate of heat transfer per unit of surface contact area. The acceleration toward phase change behaviour related to increasing surface contact area is counteracted by a reduction in the rate of heat transfer per unit of surface contact area. This ‘rate reduction’ is due to the reducing temperature differential between the cooling ink droplet and the substrate.

While the principles of droplet phase change behaviour are easily understood, the complex interplay between those principles (due to the dynamic elements outlined above) makes accurate prediction of a droplet’s final spread difficult within the context of day-to-day IJP research.

2.3.3 Application of Inkjet Printing Principles in Three-Dimensions

The use of thermal phase change inks has mainly been investigated in relation to the creation of two-dimensional lines and thin films that may be used in such items as printed circuitry components. An underlying assumption of the theory developed from two-dimensional experimental work is that *the substrate temperature remains constant* as phase change occurs in an ink droplet, and in all subsequent droplets that are deposited thereafter.

Figure 11 (following page), illustrates that this is not a valid assumption when utilising IJP in three-dimensions for the following reasons. Three-dimensional IJP entails the deposition of the first droplet of phase change ink onto the ‘initial’ substrate, the droplet spreads and freezing occurs.

As previously noted, the spread of a thermal phase change droplet in two dimensions is governed by:

- The volume of the droplet.
- The viscosity of the ink.
- The degree of undercooling provided by conduction to the substrate and convection to the surrounding microenvironment.
- The velocity of the droplet at impact.
- An underlying assumption of a flat initial substrate.

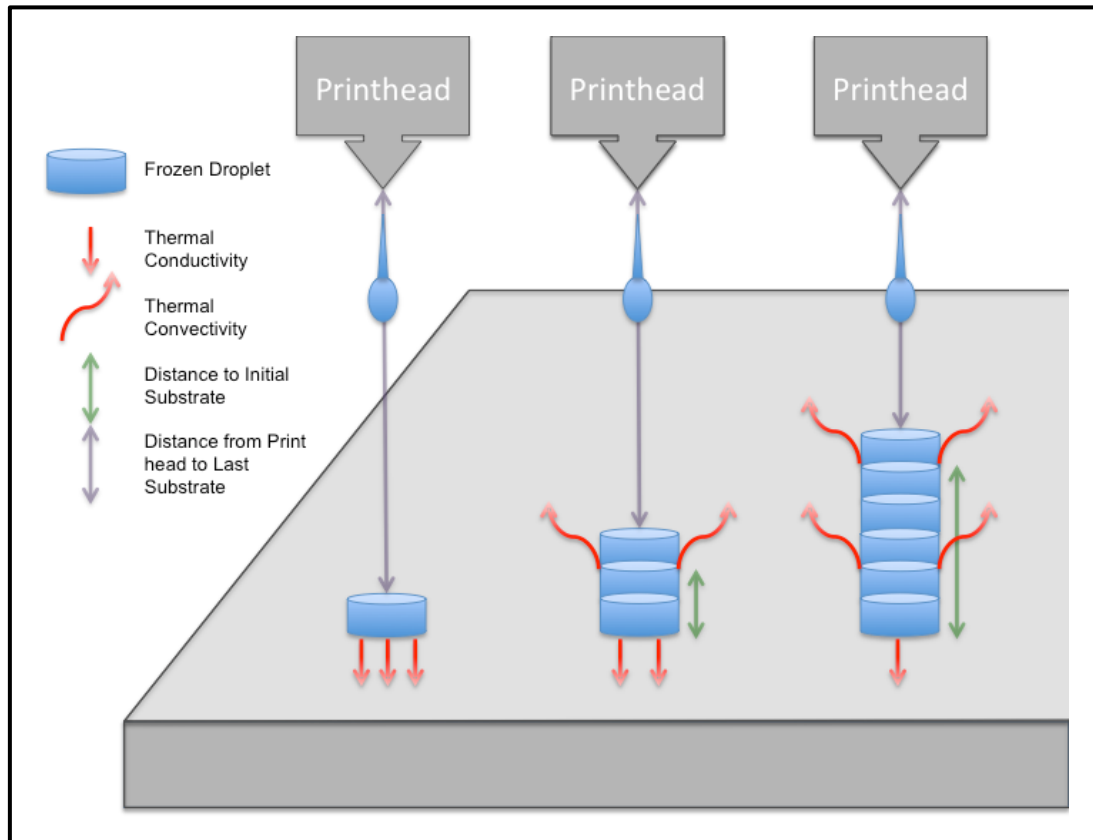


Figure 11 Thermal behaviour of deposited phase change droplets during three-dimensional IJP

The second droplet is then deposited onto the first droplet, which means that the first droplet (now frozen) must then be considered as the ‘new substrate’. As the process is repeated and each arriving molten droplet in turn becomes the substrate for the next droplet, a column will be fabricated as shown in Figure 11, and a number of additional changes occur in droplet behaviour will occur, which can be divided into the three categories that follow:

- Major determinants of energy transfer from the deposited droplet.
- Minor determinants of droplet spreading and freezing behaviour.
- Formation of a blended interface between droplets.

2.3.3.1 Major Determinants of Energy Transfer

Thermal Conductivity

It can be seen from Figure 10, that as printing progresses a column is formed and the distance from the initial substrate to the ‘new’ substrate increases. This means that the energy transferred to the emerging column, has an increasing distance to be conducted to the original substrate level. As the thermal conductivity between droplet and substrate is the first order determinant of a droplet’s phase change

behaviour, it then follows that the degree of undercooling applied to the droplet from the substrate will change; a, due to the changing thermal conductivity properties of the two different substrate materials (the 'initial' substrate and the 'new' substrate), b, the increasing distance over which that energy is to be conducted between the new and the initial substrate and c, the changing temperatures of these substrates. In practise, the speed of phase change is fastest at the initial substrate level where material conductivity is greatest and distance is lowest, it then slows as the new substrate becomes further and further removed from the initial substrate and the distance that the thermal energy has to be conducted increases.

Thermal Convectivity

The emerging fabricated column develops its own set of thermodynamic properties, transferring heat by convection to the surrounding environment. Indeed, as the total surface area of the column increases during the fabrication process and the distance between the initial substrate and the last deposited droplet increases, the heat transfer by convection from the column may supersede the importance of heat transfer by conduction between the first and last substrates of the column. The degree of convection between the growing printed structure and the surrounding microenvironment can be further complicated by the thermal gradient that will exist between printhead (heated to keep the ink liquid) and substrate (comparatively cool to ensure phase change). The combination of thermal gradient and convective forces may lead to micro turbulence around the fabricated structure, which can in turn lead to unpredictable thermal convective interaction between the column and the surrounding microenvironment.

2.3.3.2 Minor Determinants of Droplet Spreading and Freezing Behaviour

Droplet flight time

The distance from the printhead to the substrate reduces as the height of the printed structure increases (presuming the printhead is fixed at a certain offset above the substrate), which decreases the droplet flight time between printhead and substrate. This decrease means that the droplet has less time to dissipate heat to the surrounding microenvironment and therefore arrives at the substrate with more latent energy intact as compared to the preceding droplet. However, Gao and Sonin describe this as a small or nominal effect in their experiments, attributing only a 'few' degrees of the total heat loss of the droplet, to the droplet flight time (Gao & Sonin, 1994). The decrease in flight time also means that the droplet has less time to decelerate so the velocity at impact is higher, thereby increasing the inertial forces that drive the spreading of the droplet.

Change in substrate profile

The 'new' substrate (i.e. the frozen previous droplet) is now a domed surface, so on impact the initial spreading behaviour of the droplet is now driven not just by its simple momentum, but those inertial forces are enhanced by the slope of the domed substrate (and the resultant gravitational force on the spreading droplet).

These enhanced inertial forces may be offset by the fact that the distance from the centre point of the new substrate to the theoretical perimeter of the column has increased over that of the corresponding distance on a flat substrate, which would mean that the spreading droplet has further to travel and more time to dissipate the inertial forces.

Droplet spreading behaviour is 'pinned' at the new substrate perimeter

Finally, as the spreading droplet reaches the perimeter of the previous solidified droplet, the spreading slows, and it can be observed that the droplet is then spatially 'pinned' at or near the boundaries of the previous frozen droplet. A possible explanation for this behaviour, is that the capillary forces driving the final moments of spreading behaviour are momentarily lowered at the boundary (since the remaining potential contact area on that new substrate level to generate capillary forces has decreased to zero) and at this point surface tension forces momentarily overcome the diminished capillary forces, allowing time for thermal energy to be dissipated and phase change to occur.

2.3.3.3 Formation of a 'Blended Interface' between Droplets

If the arriving droplet is sufficiently 'superheated' (i.e. heated in excess of melting point) and the temperature of the new substrate is below but close to melting point, the transfer of 'super' heat from the arriving droplet to the previous solidified droplet may reverse the phase change at the surface of the solidified droplet, which allows the new droplet to mix with the now molten substrate droplet and then fuse together once phase change is complete.

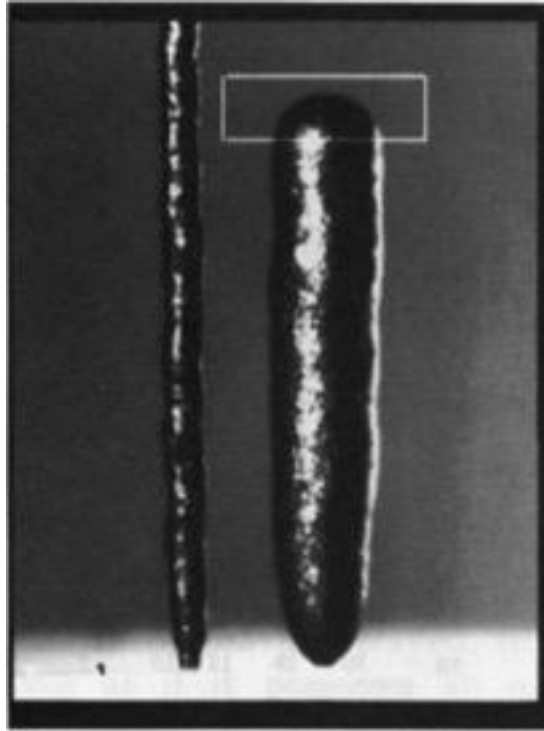


Figure 12 The formation of a blended interface between deposited droplets during phase change on the formation of columns (Gao and Sonin)

The combination of phase change reversal and the effect of spatial pinning by the previous solidified droplet, can produce a self-smoothing effect between the frozen droplets (as is shown in Figure 12 with an image taken from the seminal experimental work of Gao and Sonin), where it can be noted that the boundaries between deposited droplets are well blended and cannot be seen.

Gao and Sonin were also able to achieve a strong correlation between predicted droplet geometry and actual droplet geometry (albeit in experimental work with carefully designed and controlled parameters that ensured consistency of the behaviour they sought to measure). Furthermore, their paper provides a solid theoretical analysis for the fundamental dynamic and thermal aspects of the deposition and solidification process of thermal phase change droplets in three dimensions.

In conclusion, it can be seen that whilst the spread of a single thermal phase change droplet in two dimensions is governed by a set of fixed and definable parameters, once considered as part of a three-dimensional fabrication process, at a practical level both the range and the variability of the governing parameters increase significantly whilst the need for uniformity in those very parameters also increases.

Chapter 3 Materials and Apparatus

3.1 Materials

3.1.1 Ink Selection

The choice of a thermal phase change material for the sacrificial structure is governed by the susceptibility of the residual structure (in this case the biocompatible scaffold) to damage or contamination by the methods/materials needed to remove the sacrificial structure. Paraffin wax is considered to be non-cytotoxic in the presence of cells. 2.5D guidance pathways for Schwann cells have been successfully printed using Paraffin wax as the printing ink (Tse, 2015). Wax had also been utilised as a phase change ink for 3D IJP (Gao & Sonin, 1994).

The melting points for commonly available laboratory grades of Paraffin waxes ranges from 53 to 80° C (supplied by Sigma Aldrich), which means that temperatures in excess of these would be required to remove the sacrificial structure from a biocompatible scaffold material. Such temperature values are not suitable for all biocompatible polymers that might be used as a scaffold material. In such cases 'decanes', which are similar to Paraffin wax, as they are alkane hydrocarbons, (indicating that they comprise hydrocarbon chains with the general formula C_nH_{2n+2}), may prove useful candidate materials for the phase change inks as there many different decanes with a wide range of melting points.

However, it is also important to note that while the melting point of the selected phase change material must be suitable for the biocompatible material that will be used, it must also be carefully matched with the degree of undercooling that can be imparted by the environmental controls of the IJP setup. For example, if gelatin (without a crosslinking mechanism, melting point of approximately 35° C) were to be used as the biocompatible material, then a wax such as Octadecane with a melting point of 28 - 30° C could be used as the sacrificial material, since the temperature required for its removal would not melt the gelatin encasing it.

During the course of this research the two aforementioned materials were used as inks. Octadecane (also supplied by Sigma Aldrich) was used for the examination of the principles underpinning droplet actuation (Chapter 4), it was then necessary to change to Paraffin wax in order to undertake the experiments on droplet deposition and the fabrication of sacrificial microvascular facsimiles (Chapter 5).

While control of the temperature of the printing environment was not needed for the investigation of the principles of droplet actuation, it can (depending on the melting point of the material used, see Table 2 below) be essential for assessing droplet deposition and the fabrication of microstructures.

Table 2 Melting Point of Waxes Used and Indication of Undercooling Achieved

	Octadecane	Paraffin Wax
Melting Point (MP)	28 - 30° C	53 - 55° C
Undercooling applied at 20° C ambient	8 - 10° C	33 - 35° C
Undercooling applied at 30° C ambient	-2 - 0° C	23 - 25° C
Z (calculated allowing for a 60 micron diameter aperture printhead at MP+5° C)	12.44 - Printable with satellite droplets From Figure 10	7.34 - Printable without satellite droplets From Figure 10

Indeed, the main reason for the change from Octadecane to Paraffin wax between the two groups of experiments was that there was great difficulty in applying a sufficient degree of undercooling to Octadecane without control of the IJP environment. The melting point of Octadecane is 8 - 10° C above a stable room temperature of say 20° C, therefore imparting a (just) sufficient 8 - 10° C of undercooling. However, it was found that the use of the heated reservoir and printhead within the IJP cabinet would warm the printing environment over time reducing the degree of undercooling toward zero.

In contrast, the use of Paraffin wax (melting point 53 - 55° C) at room temperature imparts 33 - 35° C of undercooling, so fluctuations in the temperature of the inkjet environment had significantly less impact on the degree of undercooling imparted on the deposited droplet. For example, an 8° C rise in the cabinet temperature above room temperature reduces the undercooling imparted to Octadecane' droplets by 100%, while only reducing the undercooling imparted to Paraffin wax' droplets by 24%. The use of Octadecane as an ink to fabricate microstructures would necessitate an IJP cabinet temperature of around 0° C to provide approximately 30° C of undercooling. Furthermore, if the IJP environment was 0° C, then humidity controls would also be required to prevent frost from forming on the substrate surface.

When a Peltier module was introduced into the IJP cabinet to provide a substrate with a consistent degree of undercooling for Octadecane, the fan of the module created a great deal of microturbulence, which was found to disturb the flightpath of the ejected droplets leading to the formation of inconsistent microstructures.

Further advantages may have accrued from the use of Paraffin wax for the fabrication of microstructures beyond that of a more suitable melting point than Octadecane. For instance, from Table 2, it can be seen that the reduction in the dimensionless Z number from 12.44 to 7.34 indicates that droplets can be formed without satellites with Paraffin wax whilst with Octadecane the converse is true. The longer molecular chain of Paraffin wax may also enhance the probability of entanglement at the interface between droplets especially if a blended interface is achieved.

3.1.2 Ink Preparation

Sterile Polytetrafluoroethylene (PTFE) syringe filters were prepared for use by irrigating with 5 ml of Ethanol Absolute to remove any manufacturing debris from the filter production process. The syringe barrel style ink reservoirs (used in the bespoke IJP Setup) were also prepared for use by rinsing through with filtered Ethanol Absolute in order to remove any manufacturing debris and/or dust that had accumulated during storage. The filters and reservoirs were dried in a sealed petri dish for 48 hours at 40° C.

Octadecane was heated to approximately 35° C on a hotplate with the temperature being monitored using a digital thermometer (Signstek 6802 Amazon U.K.). It was then filtered through the prepared sterile 0.5 micron PTFE syringe filter, discarding the first 2 ml of the filtered solution, with the remaining ink being dispensed into the prepared reservoir.

Paraffin wax was heated to approximately 75° C on a hotplate with the wax temperature being monitored using a digital thermometer. Both the syringe and prepared filter were warmed to approximately 40° C, so that the heated Paraffin wax remained liquid (once decanted into the syringe) during the filtration process. It was then filtered through the prepared sterile 0.5 micron PTFE syringe filter, similarly, discarding the first 2 ml of the filtered solution.

3.1.2.1 Solvents – Cleaning Compatibility with Wax and Disposable Reservoir

Ethanol Absolute (supplied by Sigma Aldrich) was chosen as a suitable solvent for cleaning printheads because of its compatibility with the polypropylene reservoirs. Typically, the solvent was heated to approximately 10° C above the melting point of the wax being used and then filtered through a sterile 0.5 micron PTFE syringe filter

(Camlab Ltd, Cambridge, U.K.), discarding the first 2 ml of the filtered solution, prior to attaching the printhead to the syringe filter and flushing the printhead through. The procedure was carried out both before and after printhead use.

3.1.3 Viscosity Tests – Methods and results

Viscosity is an important component in determining the printability of an ink. For many IJP applications, the research emphasis is on adjusting the viscosity of an ink to ensure printability at a specified temperature or range of temperatures (e.g. by altering the solvent to solids ratio or changing the solvent that is being used so that the ink can be printed at room temperature for instance). However, in the case of IJP with phase change inks the emphasis is reversed. The priority is to select a holding temperature for the ink, such that the ink's resulting viscosity ensures the printability of the ink, but not so high that excessive latent heat in each individual ink droplet retards phase change once printed.

Octadecane was heated to approximately 40° C on a hot plate and was then set on a Peltier cooling module set at 10° C. As the Paraffin wax cooled, viscosity and temperature were measured and recorded at 5-second intervals. At 35° C, approximately 5° C above melting point, viscosity was measured at 2.9 mPa.s. The viscosity test was repeated three times with the viscometer being calibrated or recalibrated prior to each test.

The Paraffin wax was heated to approximately 70° C and allowed to cool to room temperature. As the Paraffin wax cooled, viscosity and temperature were measured and recorded at 5-second intervals. At 60° C, approximately 5° C above melting point, viscosity was measured at 5 mPa.s, and at 65° C viscosity was measured at 4.43 mPa.s. The viscosity test was repeated three times with the viscometer being calibrated or recalibrated prior to each test.

In both cases, as one would expect with phase change materials, the viscosity of the ink changed rapidly from a low viscosity liquid to a high viscosity liquid and then to a solid as the ink cooled. Also, the temperatures of phase change were found to be in good agreement with the manufacturers' stated melting point.

3.2 Apparatus

3.2.1 Jetlab 4 Inkjet Printer - Standard Setup

Early experiments were conducted with the MicroFab JetLab 4 “Drop on Demand” printer with JetLab 4 software (MicroFab Technologies Inc., Version 6.3), with backpressure control provided by the MicroFab CT-PT-4 Pressure controller. The drive electronics for the waveform signal are included within the JetLab 4 unit. This was combined with the MicroFab PH-04a style heated reservoir c/w single jet-dispensing device, which maintains thermal phase change inks at suitable temperatures prior to dispensing and complimented with a MJ-SF style Polymer Jet™ high-temperature, drop-on-demand printhead (shown in Figure 13 below).

This approach caused a degree of imprecision, since the temperature inside the IJP cabinet would fluctuate over the course of the day due to thermal effect of the large heated reservoir (typically from 18 to 24° C degree) and in turn create a variance in the degree of undercooling being applied to the deposited droplets. Greater variability was observed over the course of a year, with cabinet temperatures as low as 12° C being seen at the start of the day in winter and temperatures of 28° C and above after a mornings work in the summer. The ambient temperature and humidity of the IJP cabinet was monitored by means of a hygro-thermometer (Maplin Ltd U.K.).

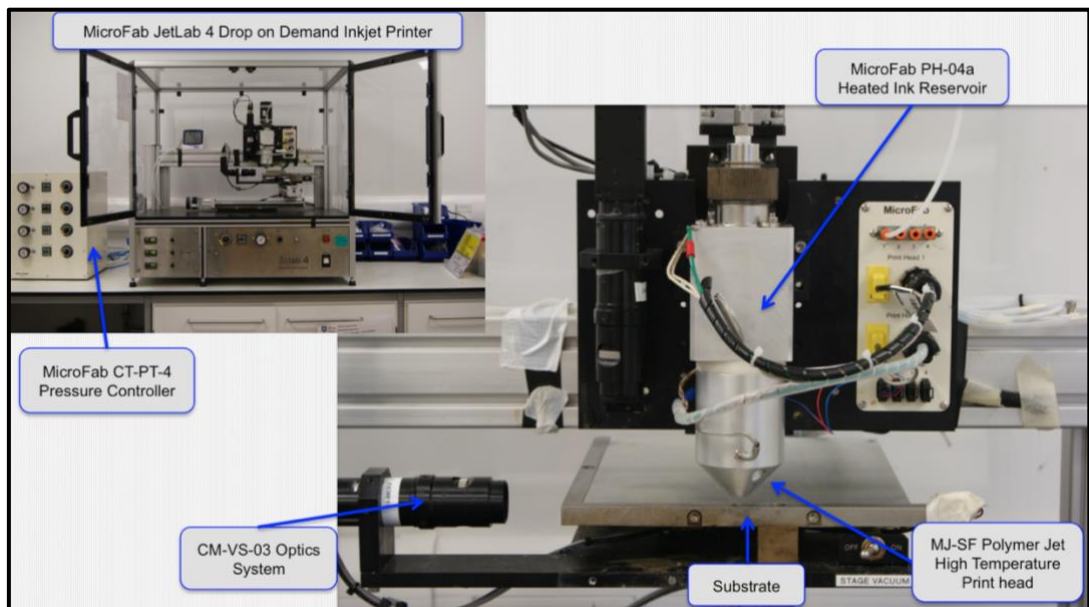


Figure 13 JetLab 4 c/w high temperature reservoir and printhead



Figure 14 The thermal mass of the high temperature printhead.

It was also noted that the proximity of the uppermost point of the printed microstructure to the heated printhead adversely affected the degree of undercooling applied to droplets deposited in close vicinity to the thermal mass of the heated printhead as illustrated by Figure 14 (left).

It was expected that spatial constraints would prevent the formation of consistent columns if droplet deposition is occurring in the immediate vicinity of the printhead. However, it was observed that the effect of the heated printhead was to create a thermal zone around the printhead, which at some point slowed and eventually prevented phase change at a certain clearance between printhead and the top of the deposited column.

3.2.2 Jetlab 4 Inkjet Printer - Bespoke Setup

Due to dissatisfaction with the suitability of the MicroFab PH-04a for the fabrication of thermally sensitive microstructures, it was decided to design and manufacture a bespoke heated reservoir and printhead assembly to use within the JetLab 4 IJP setup.

The design objectives were to:

- Decrease the intensity of the thermal effect near the printhead.
- Reduce the temperature increase of the IJP cabinet over the course of the working day.
- Reduce the z-axis offset required between the printhead and the top of the finished microstructure in order to improve the accuracy of droplet deposition.

The relatively low volume (usually 1-2 ml) and low melting temperatures of the phase change ink being used over the course of a day's experimental work enabled the use of a 3 ml internal disposable polypropylene syringe barrel with 'luer' connection (Fisnar Europe Ltd U.K.), as a reservoir which could be combined with a low temperature MJ-A drop on demand printhead by means of a standard PTFE 'luer to thread' connection, to form a disposable reservoir-printhead assembly as shown in Figure 15 above.

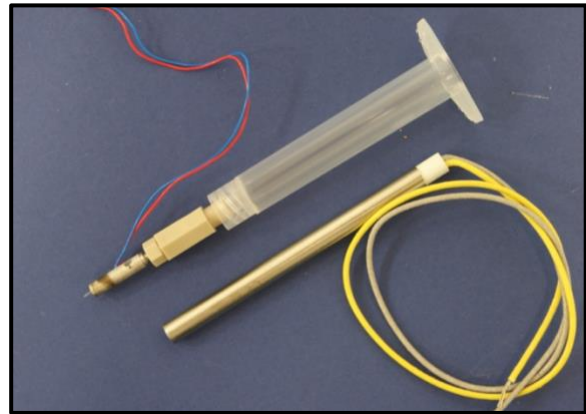


Figure 15 Fisnar 3 ml reservoir with PTFE connector to MJ-A printhead. Ceramic tubular heating rod also shown.

The introduction of the disposable reservoir with a significantly reduced volume (3 ml as compared with 30 ml for the MicroFab PH-04a heated reservoir) then allowed for the dimensions of the encasing aluminium thermal jacket to be reduced. It was decided that a similar ceramic tubular heating rod to that used in the MicroFab PH-04a heated reservoir would be employed in the bespoke design, as it had proven reliable in the past. The dimensions of the ceramic tubular heating rod and the disposable reservoir-printhead module combined to serve as overriding spatial constraints on the dimensions of the bespoke device (also shown in Figure 15).

Those dimensions allowed sufficient leeway for the design of the reservoir's encasing thermal jacket to be refined so that it could function as a modular unit i.e. copies of the 'module' could be made, which would then self-align alongside the first unit. Multiple printheads could then be used in the same fabrication process. It was anticipated that this design feature may eventually be useful for the production of complex sacrificial structures or simply to multiply the achievable production rate of standard structures over an increased area.

Finally, the finished device was further enhanced by incorporating a printhead protection feature (to prevent accidental damage to the printhead). The design was modelled with Solidworks™ software. The assembly of the design (see Figure 16, overleaf) was then tested in Solidworks™, and once finalised, passed to the department's workshop for fabrication.

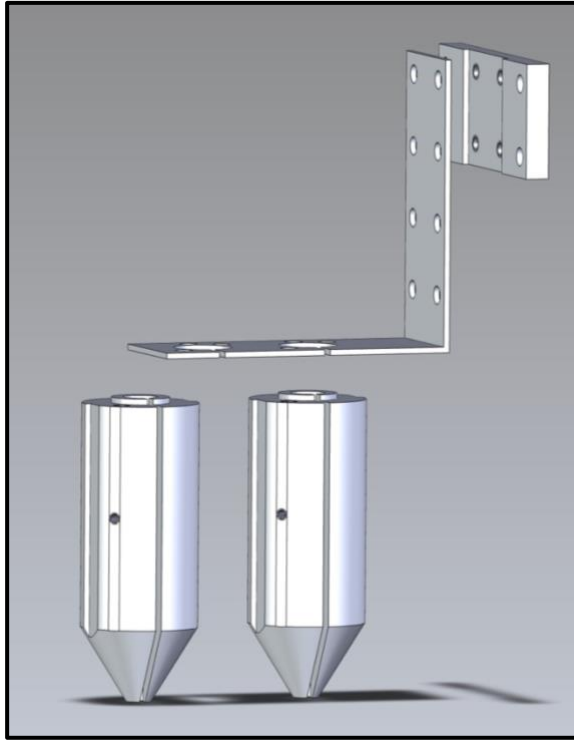


Figure 16 Exploded ‘Solidworks’ assembly of the reservoir’s encasing thermal jacket and relevant connecting fittings.

Comparing the MicroFab PH-04a (Figure 13 previous section) with the bespoke device (Figure 17 overleaf), we find that the MicroFab PH-04a has a total surface area of 0.036 m^2 , and the conical area around the printhead, which emits the primary convective force, has a surface area of 0.004 m^2 . The design of the bespoke device achieved a reduction in total surface area of 64.2% (to 0.013 m^2) and the conical surface area around the printhead was reduced by 23.6% (to 0.003 m^2). The angle of the conical area was increased, thereby reducing the aggregate proximity of the convective face, further reducing the intensity of the thermal gradient between printhead and fabricated microstructure.

The final assembly is shown within the Jetlab 4 cabinet in Figure 17 overleaf. An extension shelf attachment (also shown) was fabricated in order to enable a Peltier thermoelectric cooler module heatsink and fan assembly controlled with a TEC temperature controller unit (Electron Dynamics Ltd, Southampton, U.K.) to be attached to the printing platform of the MicroFab printer. This was done to provide a reliable and controllable degree of undercooling at the substrate level. However, it was found that Peltier module introduced microturbulence into the IJP cabinet and lead to inconsistent droplet deposition.

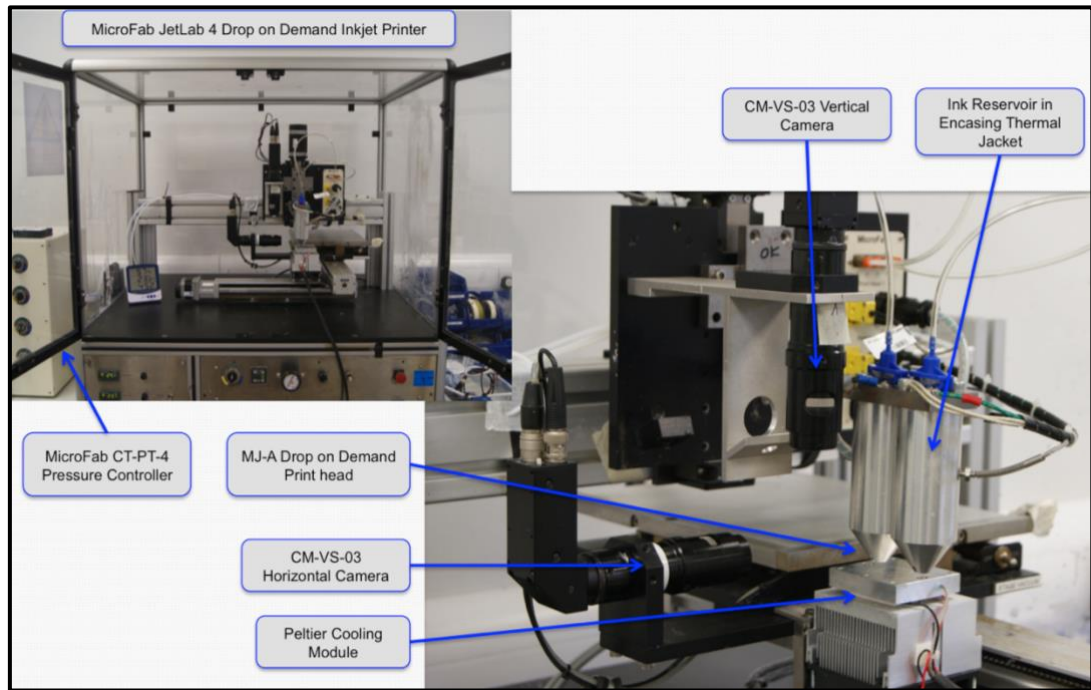


Figure 17 JetLab 4 c/w bespoke heated reservoir and printhead assembly.

3.2.3 Temperature Gradient Tests

Temperature gradient tests were conducted in order to compare the thermal effect of the two heated reservoir printhead assemblies at an offset of 5 mm between substrate and printhead. At the reservoir, thermal input was provided by the heating rod of the MicroFab PH-04a, which was used ‘as is’ for the standard setup, then cannibalised and reused for the bespoke setup. Feedback was provided by the JetLab 4 thermostat, which is mounted in the body of the reservoir. The thermal input at the substrate level (for thermal gradient measurement) was provided by a Peltier thermoelectric cooler module heatsink and fan assembly controlled with a TEC temperature controller unit (Electron Dynamics Ltd, Southampton, U.K.). The JetLab 4 and MicroFab PH-04a setup provides temperature regulation to $\pm 1^{\circ}\text{C}$ of the set temperature, whilst the TEC temperature controller unit enables temperature regulation of the Peltier module to $\pm 0.1^{\circ}\text{C}$ of the set temperature.

Temperature measurements of substrate and printhead were taken using a Signstek 6802 II dual channel digital thermometer with a 2 K-type thermocouple sensor probe (Signstek Ltd U.K.), at two intervals of approximately 1.1 mm (the thickness of a glass slide) of the substrate to capture the area of maximum undercooling, then at the midpoint between temperature (as a reference point) and then at intervals of 1.1 mm from the midpoint to the printhead to capture the thermal effect of the printhead. At each measurement point the sensor was allowed to acclimatise for two minutes, then the temperature range was observed for two minutes. During this period of

observation, the range and direction of temperature fluctuation at substrate and printhead were clearly in accordance with changing temperatures of the substrate and printhead, which were being controlled by independent thermostats. The simple median point of the observed temperature range was therefore selected and recorded.

Further temperature tests were conducted on the bespoke reservoir and printhead to assess the distribution of heat around the body of the reservoir and compare the programmed temperature for the internal heating rod of the reservoir with the actual temperatures. In this instance the tip of the thermocouple was taped to the reservoir at the point of interest then the temperature was observed using the method described above.

3.2.4 Comparison of Thermal Gradients

The Peltier cooling module temperature was set at 5°C for the substrate and the printhead temperature set at 40°C, which gave a 35°C of undercooling between substrate and printhead. The ambient temperature of the IJP cabinet was 21.8°C at the beginning of the experiment and 22.1°C at its conclusion.

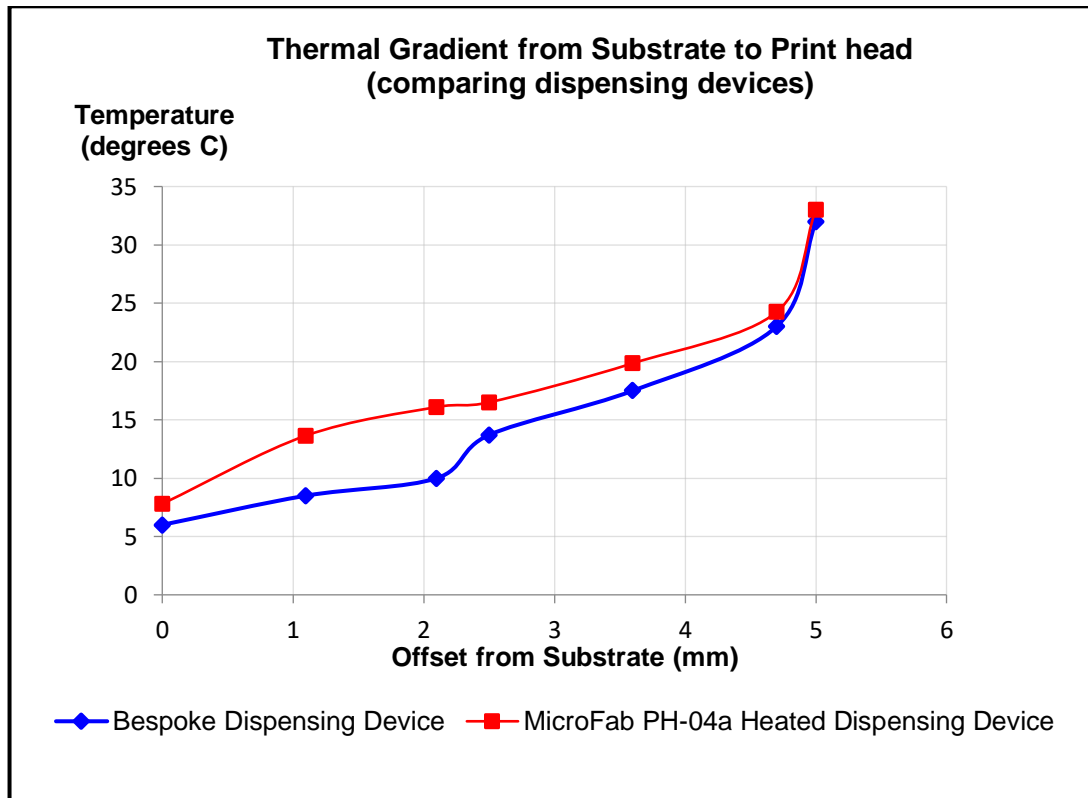


Figure 18 Measurement of the thermal gradient from substrate (at 5°C) to printhead (at 40°C), comparing the MicroFab heated dispensing device to the bespoke dispensing device.

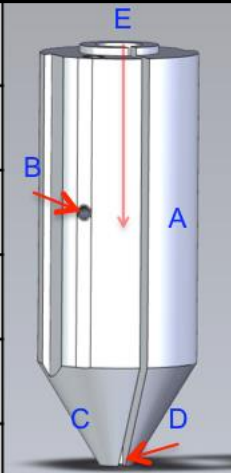
From Figure 18, a clear reduction in the general effect of the bespoke dispensing device is observable over the entire spatial range of the thermal gradient. More importantly, the thermal gradient of the area near the substrate (between 0 - 2 mm offset), offers a more consistent degree of undercooling. This represents an extension of the spatial zone where a high degree of constant undercooling would be applied to the dispensed droplets, which should in turn enable:

- Higher frequencies of droplet deposition thus reducing fabrication time.
- More uniform phase change behaviour leading to greater consistency in the fabricated structures.
- Taller microstructures to be fabricated whilst maintaining the desired degree of consistency.

3.2.5 Measurement of Actual Reservoir and Print Head Temperatures.

Although not directly related to the thermal gradient, temperatures around the reservoir and printhead assembly were then measured, in order to establish the extent to which the temperature of the ink as jetted from the printhead would accurately reflect the temperature as set on the thermal input regulator of the JetLab 4. In this instance, the temperature as set on the JetLab 4 was 40°C, the ambient temperature in the Inkjet cabinet was 21.1°C and the substrate temperature was 19.1°C. The reservoir-printhead assembly was then moved to the maximum offset away from the substrate (35 mm) to minimise the influence of the slightly cooler substrate on the temperature at the tip of the reservoir. The results are shown in Table 3 below.

Table 3 Measurements of the reservoir and printhead temperatures.

	Reservoir Measurement Location	Temperature	
A	External Body – mid-centre	37.1 ⁰ C	
B	Internal Body – at thermocouple location	38.4 ⁰ C	
C	External Tip	33.15 ⁰ C	
D	Internal Tip	37.1 ⁰ C	
E	Octadecane in the Internal Reservoir	40.6 ⁰ C	

It can be seen that there is a good agreement between the set temperature (40°C) and the temperature of the ink within the body of the reservoir. However, it can also be noted that there is a small decrease in the temperature from the internal body location

to the internal tip location, indicating that the heat from the heating rod (contained within the body of the encasing aluminium thermal jacket) is being less effectively conducted to reservoir's furthestmost location. This is important because the viscosity of a phase change ink, an important determinant of 'printability', is closely related to its temperature, particularly if that temperature is close to the melting point of the ink. Although it was not possible to measure the temperature of the ink at this location, it was thought that it would be preferable to err on the side of caution and assume that the temperature of the ink would decrease as it travelled toward the tip. Furthermore, it was though that the temperature at the tip would decrease further still when the tip was located in close proximity to the substrate. For those reasons it was decide that a 'rule of thumb' should be applied, which was that the temperature of the reservoir should be set at 5° C above that which would otherwise be indicated by the results of the viscosity test for the ink.

3.2.6 Imaging

Droplet imaging within the MicroFab JetLab 4 "Drop on Demand" printer is provided by CM-VS-03 optics system (comprising both horizontal and vertical cameras) with 150 mm working distance. Figure 19 below gives an overview of the imaging system.

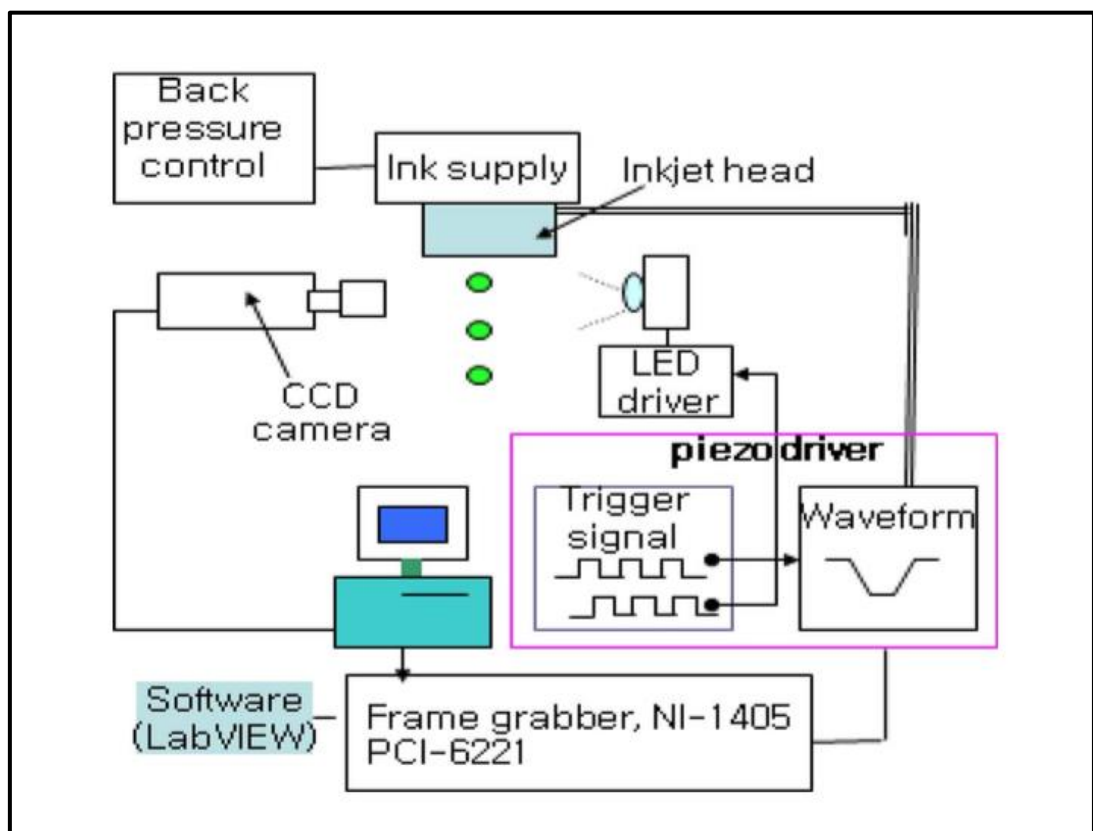


Figure 19 The image capture system for dispensed droplets (Kwon & Lee, 2013).

Figure 19 (previous page), shows the typical setup used for capturing images of dispensed droplets in order to measure velocity and volume for IJP research (Kwon & Lee, 2013). An LED light is situated behind the printhead (relative to the CCD camera). The digital pulse from the signal waveform that drives the piezo in the printhead then in turn drives a second digital pulse that activates the LED light. This in turn creates a timed strobe effect so that the video image of the droplet appears 'frozen' on the screen. Further, the delay between the digital pulse of the signal waveform and that of LED light can be set by the researcher, which enables 'frozen' droplets to be 'captured' at multiple locations over the course of the droplets' flight path.

Subsequent imaging of completed microstructures was undertaken using a MaozuaTM, 5 MP, 20 – 300 x magnification USB microscope (Amazon U.K.), which is processed with proprietary software.

Chapter 4 Enhanced Control of Droplet Actuation by Waveform Manipulation and Optimisation

4.1 Introduction

At the outset of the research, the degree to which fundamental IJP theory and methods would have to be questioned and extended during the course of the investigation was not anticipated. In typical IJP style, it was thought that a 'sufficiently robust' set of waveform parameters for the research would be found by methodical but mechanical alterations to those parameters over the course of a few days' lab work.

However, during the initial exploratory research period, the importance of the conflict between the objectives and methods of conventional IJP research and the objectives of this research began to be fully appreciated.

In conventional 2D IJP (or layer-by-layer 3D approaches) the fabricated macro-structure is typically the result of multiple overlapping and/or blended droplets. Once a single sufficiently robust waveform that generates a consistent droplet has been found, work then moves on to producing repeating patterns of that deposited droplet in order to produce the desired printed macro-structure. The process may be relatively forgiving, in that small errors in individual droplet deposition may be hidden within the resulting macrostructure. In such circumstances the research goal is often to optimise a single waveform, so that IJP may take place at the highest frequencies possible.

In contrast, in this research the critical dimension (i.e. the diameter) of the fabricated macro-structure is reliant on the precise and repeatable deposition of a single jetted droplet. Multiple optimised waveforms are required so that the volume, shape and velocity of individual droplets can be varied in order for the full range of diameters of microvascular conduits to be replicated. Given the objectives of this research the IJP process is unforgiving since small errors in droplet formation (such as the formation of detached satellite droplets) may mean that the resulting macro-structure is no longer a microvascular facsimile.

The fabrication of a full range of precise, predictable and consistent microvascular facsimiles therefore demands optimised waveforms providing an enhanced degree of control over the shape and velocity of the ejected droplets at low deposition frequencies over a wide range of droplet volumes.

It can be clearly seen from Figure 20, that there is an extensive range of input parameters and disturbances that contribute to the droplet creation process. The 8-point waveform input control of the Jetlab 4 gives the researcher access to thousands of possible waveform permutations by which to adapt the droplet creation process to the input parameters and produce a droplet with the desired characteristics.

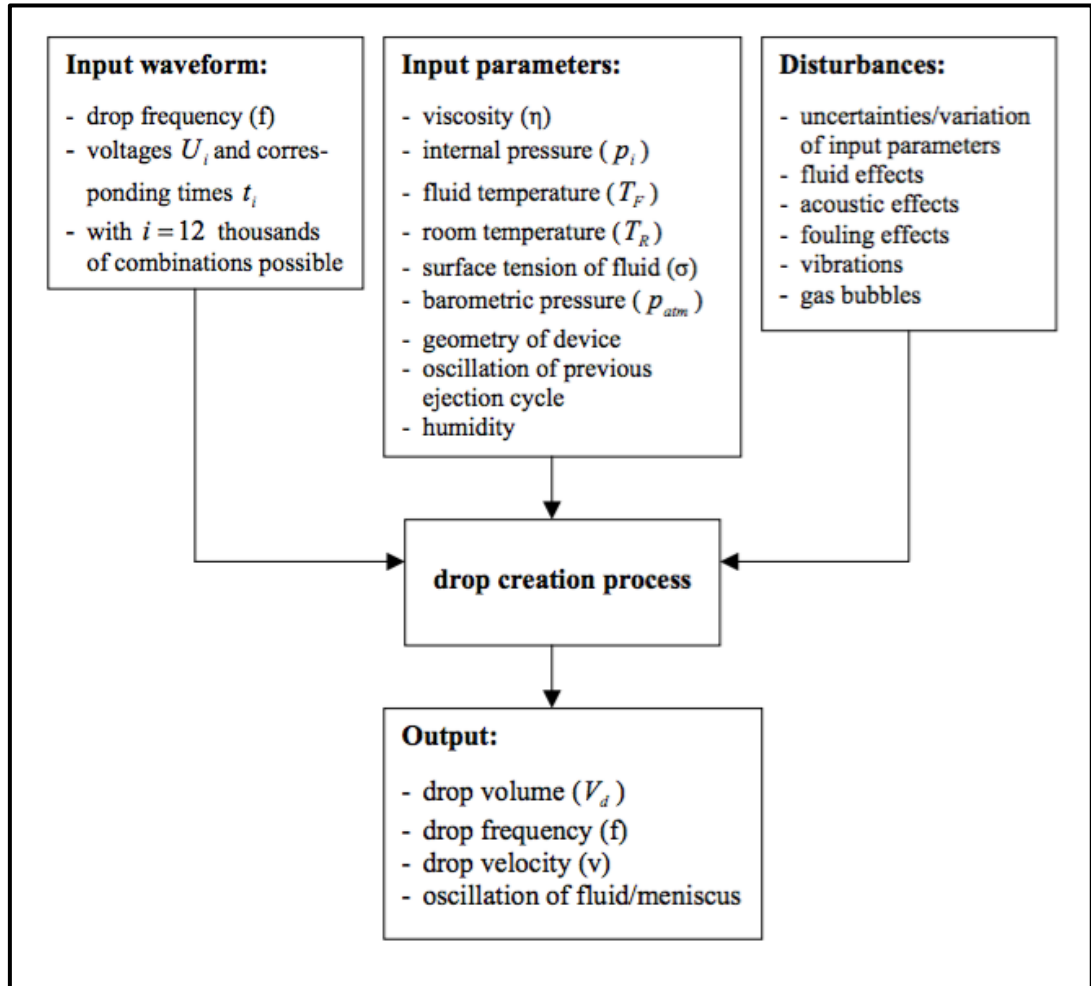


Figure 20 Inputs and outputs in the droplet creation process (Rensch, 2006).

However, (to my knowledge) there is no algorithm available to the IJP community by which a researcher might detail the input parameters and the desired droplet characteristics and in return receive the settings needed for an optimised waveform.

The need to exercise an enhanced degree of control over the ejected droplets in order to produce the wide range of solidified droplet diameters required (in the absence of an algorithm for creating optimised waveforms) meant that a detailed investigation needed to be undertaken into the principles underpinning droplet actuation.

The following series of waveform experiments were performed on IJP setup 3, using octadecane at 40° C (Sigma Aldrich), with a 60-micron aperture MJ-A drop on demand printhead at a droplet deposition frequency of a 1000 Hz. This frequency actuated the piezo for approximately 3.5 % of the programmed printing time, allowing sufficient time for residual oscillations to dampen down prior to the beginning of the next actuation of the printhead. The viscosity of the octadecane within the reservoir was 2.88 mPa.s (at 40° C) but was anticipated to be approximately 2.91 mPa.s (at 35° C) at the printhead. The backpressure was set at -8 m bar (unless otherwise stated).

4.2 Acceleration and Velocity of a Droplet over the Course of its Flightpath

Over many of the early experiments, variations in the velocity of a droplet during the course of its flight had been noted. Although Kwon and Lee (Kwon & Lee, 2013) have developed a method of instantaneously plotting the jetting speed curve of droplets, the software required to produce such results is not readily available and the development of a similar system is outside the scope of this thesis.

However, since droplet velocity and volume were now important determinants in the demonstration of control over the IJP process, the laborious task of replicating the jetting speed curve for each experiment was avoided. Data was needed to inform the point at which, and/or the method by which, velocity measurements would be taken in subsequent experiments. This, in turn, might ensure that the measured velocity used in comparison of droplets would be more indicative of the ‘actual’ velocity of the droplet. The image shown in Figure 21 below, shows that during the moments shortly after ejection the droplet may form a ligand, then that ligand may break and form two (or more) separate droplets, which results in changes in the velocity of the droplet (further explained in the discussion below) making the measurement of acceleration and velocity a nontrivial matter.

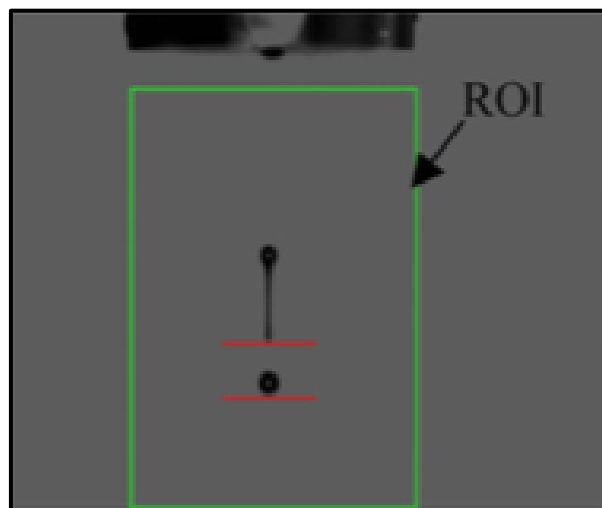


Figure 21 A dispensed droplet showing the formation of a ligand and the break in the ligand as the initially dispensed single droplet separates into two droplets. ROI = Region of Interest. (Kwon & Lee, 2013).

4.2.1 Method, Results and Discussion

The velocity of two contrasting droplets was therefore mapped over their flight paths. Rise and fall times of $6\ \mu\text{s}$, were used with a dwell time of $20\ \mu\text{s}$ (established from the manufacturers post-production quality control tests) to generate the unipolar

waveform. The two different velocities were generated by using amplitudes of 30 and 32 V. The strobe delay was varied for the LED over the course of the droplet's flight and captured by the CCD camera to record the droplet's position at:

1. The moment of ligand break after ejection from the capillary tip (A)
2. The formation of a double droplet (B)
3. The moment when the secondary droplet re-joined with the primary droplet (C)
4. The formation of a single spherical droplet (D)
5. Then at 100 μ s interval until approximately 900 μ s

Screen shots were taken with an image of the dispensed droplet at those points. The distances between the capillary tip and the droplet were measured from the screenshots by means of pixel ruler using the diameter of the printhead as a constant. The droplet's velocity was first calculated (incrementally) over the immediate period prior to each of these measurement points. Velocity was then also calculated (as an average) over the total flight time up until the measurement points. The results are shown in Figure 22 below.

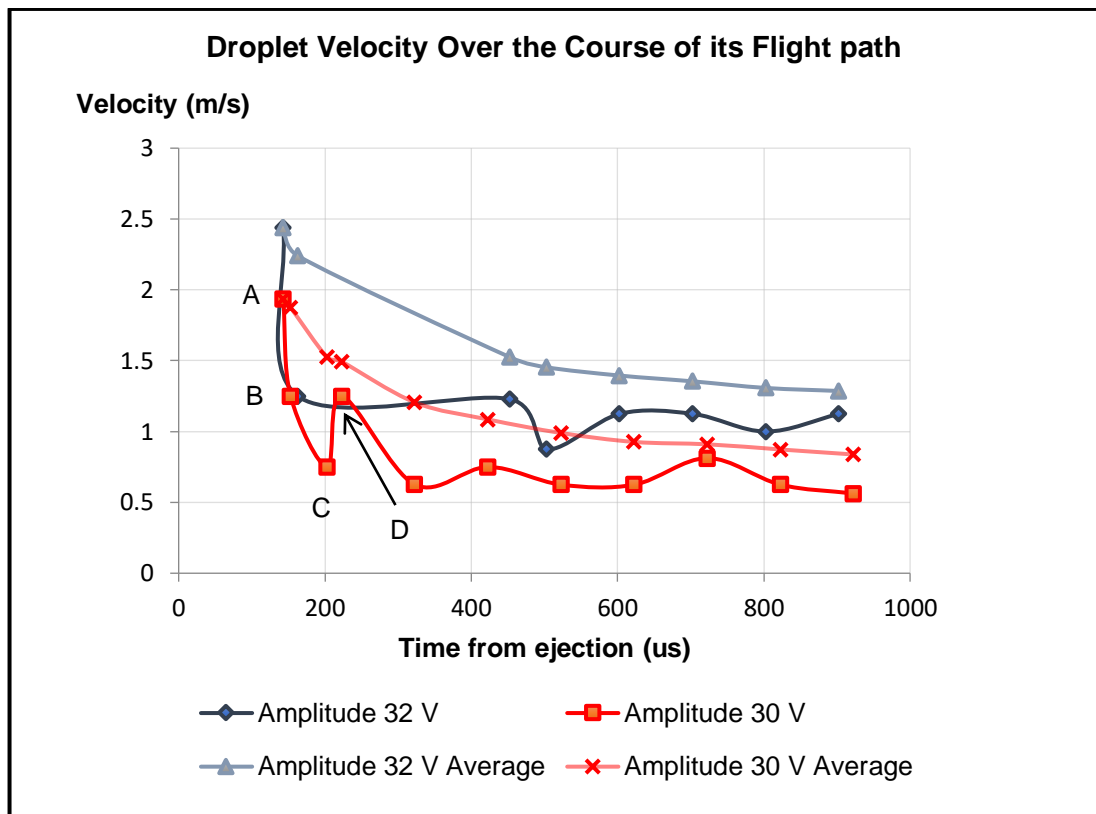


Figure 22 The incremental and average velocities of two droplets ejected at amplitudes of 30 V and 32 V respectively.

Figure 22 on the previous page, shows that the velocities of the droplets, when measured incrementally, have significant variations at ligand break, formation of a double droplet and then reconstitution into a single droplet. In this sequence of events there is an interchange between the energy states of surface tension and velocity. So, for example, at ligand break (point A, Figure 22), the droplet is a longitudinally extended droplet, at point B, the droplet then breaks into two (due to the viscous forces within the ink). In this state, the total surface area of the two droplets is greater than that of the equivalent volume single droplet, which means a greater amount of the total energy generated during the droplet formation and ejection process is captured in the surface tension of the double droplet. In accordance with the principle of conservation of energy, the velocity of the droplet is reduced until point C, where the secondary droplet begins to re-join with the primary droplet. As the two droplets reconstitute into a single spherical droplet, the excess energy previously captured in surface tension is released and velocity increases, as can be seen at point D. A more comprehensive treatment of this subject can also be found in Kwon and Lee's paper as mentioned previously (Kwon & Lee, 2013).

From Figure 22, it can be seen that measuring velocity incrementally can produce highly variable results at any point during the sequence from ligand separation to droplet reconstitution. Furthermore, the comparison between two (or more) similar droplets at a given time point can generate significantly different results simply based on the arbitrary selection of a measurement point. Whilst it may be an accurate reflection of velocity at that point in time, it is clear that velocity at a given time point may not serve as a reliable proxy for velocity over the entirety of the droplet flight time.

Conversely, it can also be seen that the use of a moving average generates less variability (naturally) particularly as the measurement period extends. Whilst this may mask what is happening at a given point in time, it serves as a more accurate reflection of the velocity of the droplet over the course of its flight time.

The implications for droplet velocity measurement are:

- Droplet velocity should be mapped prior to selecting a measurement point/s for an experiment.
- Unless specific experimental needs dictate otherwise, a moving average will provide a more representative result.
- If using a moving average, then measurements taken at an extended time period will further reduce variability.

4.3 The Sensitivity of Jetting Pulse Amplitude to Backpressure Modification and its effect on Droplet Velocity and Volume.

The effect of jetting pulse amplitude on droplet velocity (in the context of increasing rise times using a unipolar waveform) is an area of general agreement within the IJP research community. Indeed, Gerhauser et al's 1983 communication (a precursor to Bogy and Talke's seminal paper in 1984 on fundamental IJP theory) notes the relationship between pulse amplitude and droplet velocity (Gerhauser, Hirschman, Lee, & Talke, 1983) (Bogy & Talke, 1984). Droplet volume is less frequently discussed (more usually within the context of pulse width or waveform type), however Figure 23 below, clearly illustrates the relationship between droplet' velocity/volume and pulse amplitude at an optimised pulse width for a unipolar single pulse waveform.

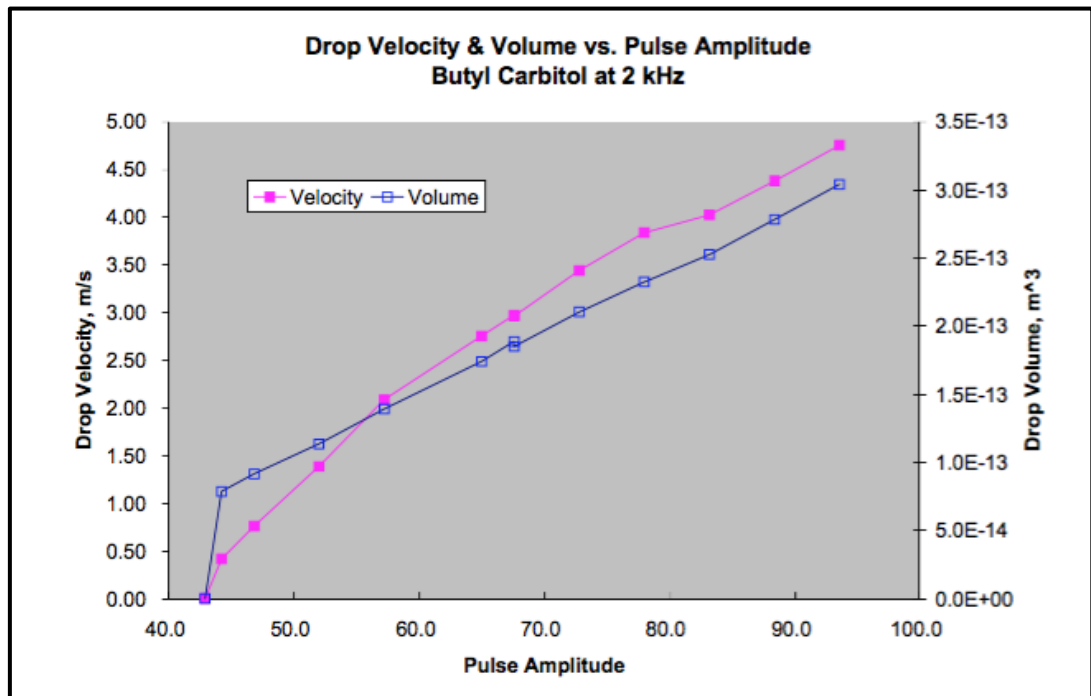


Figure 23 The relationship between jetting pulse amplitude and droplet velocity and volume (Microfab Technologies Inc., 1999).

It can be seen that once pulse amplitude surpasses the threshold resistance value a strong linear relationship quickly develops between pulse amplitude and both droplet volume and velocity.

Typically, in IJP a small amount of backpressure (i.e. a pressure below the atmospheric pressure) is applied to the ink reservoir to prevent ink leaking from the aperture of the capillary when the printer is idle. The application of this pressure leads to the formation of the ‘meniscus’ at the capillary tip. If too large of a backpressure is applied, then air is sucked into the capillary through the aperture. MicroFab’s technical notes (Microfab Technologies Inc., 2007), suggest the use of small adjustments in backpressure for:

- Management of secondary droplets and the elimination of satellite formations.
- Management of frequency effects on droplet formation (as a method of damping or enhancing the effects of residual oscillations).

To the author’s knowledge, consideration of the issue of backpressure goes virtually unnoted in IJP literature.

4.3.1 Methods, Results Discussion

In order to investigate the intensity of this phenomenon further, a simple experiment using the previously optimised waveform was conducted against a range of backpressure settings. The results are shown in Figure 24 below.

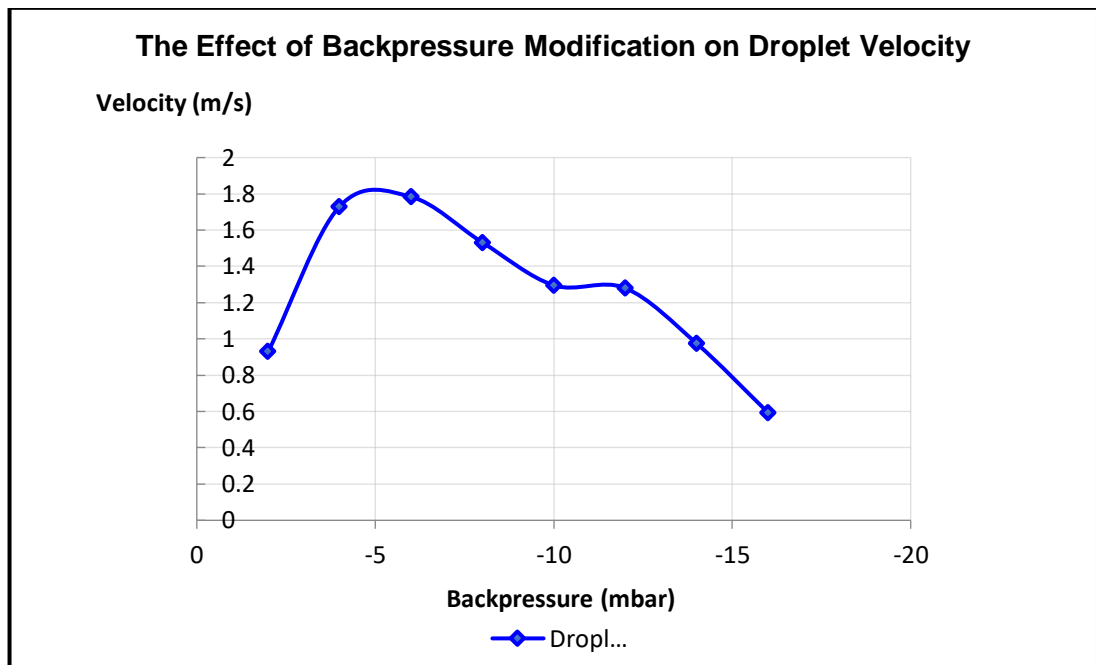


Figure 24 The droplet velocity generated by a jetting pulse amplitude of 32 V (with rise and fall times of 6 μ s with dwell time adjusted to achieve an optimum jetting pulse duration of 29.5 μ s, i.e. $t_{rj} + t_{dj} = T_f/2$) at a range of backpressures from -2 mbar to -16 mbar.

The general trend that can be observed is that as the backpressure being applied increases, the velocity of the droplet decreases. The exception to this trend occurs from 0 mbar to some point between -4 mbar and -6 mbar. Over this range of backpressure, the force provided is insufficient to ensure formation of the meniscus, which allows drips of ink to form at the aperture tip. This, in turn, means that the droplets that are being dispensed must immediately travel through a volume of ink before the visible droplet flight path commences. As the ink provides significantly more resistance than air, the initial acceleration of the droplet is immediately slowed, and aggregate velocity is lowered.

Having mapped the effect of backpressure on droplet velocity, an item of concern on the MicroFab CT-PT₄ Backpressure regulator became apparent. On this model of backpressure regulator, backpressure is measured rather than set. Backpressure is increased or decreased by turning an unmarked dial and the regulator's measurement of backpressure is shown digitally in 2 mbar increments. It is therefore, for instance, equally possible for backpressure to be -4 mbar and the readout to be showing -4 mbar, as it is for backpressure to be -5.9 mbar and be showing -4 mbar. Considering that backpressure had just been demonstrated to be an important determinant of droplet velocity (and therefore droplet volume), and the range of 'useful' backpressures is limited to say between -6 mbar and -10 mbar, a range of -2 mbar in potential measurement error is clearly not optimal. For this reason, four incremental settings, which all showed '-8 mbar', were tested and the velocities for the resultant droplets calculated, which are shown in Table 4 below.

Table 4 Droplet velocities within a range of backpressure settings measured at -8 mbar.

Backpressure	-8 mbar	-8 mbar +	-8 mbar ++	-8 mbar +++
Droplet Velocity	1.53 m/s	1.45 m/s	1.36 m/s	1.33 m/s

The results in Table 4 above show that there was a 13% decrease in the velocity of the droplet at the 'same' backpressure. Figure 23 leads us to anticipate a similarly proportionate increase in droplet volume.

The results shown in Figure 24 and Table 4 show that back pressure is an important determinant of droplet velocity and therefore volume, a determinant that has gone largely unreported in IJP literature. There are three immediate implications from the failure to properly control backpressure:

The measurement of the time of meniscus displacement will vary. The commencement of the measurement of a droplet flightpath is dependent on the emergence of the

droplet from the tip of the capillary printhead. Inadequate back pressure control will cause small variations in the position of the meniscus within the tip of the capillary. These variations will then manifest as variances in the time at which the droplet begins to emerge from the printhead i.e. if the meniscus is set at the tip of the capillary the droplet will emerge immediately, whilst when the meniscus is set back from the tip of the capillary, the droplet will appear a few microseconds later. As meniscus displacement is an important measurement point for calculating pulse width, actual pulse widths may vary from recorded pulse widths.

Actual droplet velocity will vary (as well as the measurement and calculation of it). A number of important experimental methods in IJP research revolve around changing waveform parameters to achieve constant droplet velocity at a timed point during the course of the droplet's flightpath. As the droplet's velocity may be varied by a change in backpressure (from experiment to experiment) rather than changes in waveform parameters, possible correlations between parameters and velocity may become less transparent.

Droplet volume will also vary considerably. Whilst this is an important finding for the objectives of this thesis it also has wider implications. For instance, in the field of reactive IJP where two or more reactive chemicals are deposited on a substrate in order to combine and create a specific chemical reaction, small changes in droplet volume may change the outcome of that reaction.

In general, in IJP research it is often found that applying identical settings on different days, or even at different times on the same day may generate marginally different outcomes. Although this phenomenon has been much discussed, to date there is no settled agreement on the factor/s that might cause this to happen. The theme running through the implications noted above is that without proper control of backpressure the replication of results from day to day and experiment to experiment will be difficult and provides a clear explanation for the difficulties IJP researchers face. Furthermore, as repeatability is a cornerstone of scientific methodology, the importance of the control of backpressure is a significant finding for the IJP community.

4.4 Establishing the Fundamental Resonance Period of the Printhead and the Optimal Jetting Pulse by Varying Dwell Time

The following discussion is generally informed by and adapted from N. Morita et al's chapter 'Inkjet Print Heads' from S. Hoath's book 'The Fundamentals of Inkjet Printing' 2016 (Hoath, 2016), where Morita et al discuss the underlying principles of droplet formation (Morita, Khalate, Buul, & Wijshoff, 2015). Whilst establishing the fundamental resonance period of the printhead is the purpose of this section, it is only a step in Morita et al's procedure, their ultimate objective being to constrain the effect of residual oscillations on droplet deposition¹. Therefore, to better understand the fundamental relationships underpinning waveform optimisation the seminal works of Bogy and Talke (Bogy & Talke, 1984) and Gerhauser et al (Gerhauser et al., 1983) are also used.

As previously discussed, the unipolar single pulse waveform is considered to be the 'jetting' pulse that drives droplet formation and ejection. The 'pulse' is in fact the 'timely culmination' of the negative pressure wave (set up by the expansion of the printhead capillary as voltage is applied to the piezo) and the positive pressure wave (set up by the subsequent contraction of the capillary when that voltage is returned to zero). The effectiveness of this pulse (the kinetic energy produced) is determined by how closely the duration of the waveform is matched to the 'acoustic' properties of the printhead' capillary (schematic Figures 8 & 9), in order to produce the 'timely culmination' of the pressure waves (Bogy & Talke, 1984).

The main determinant of the 'acoustic' properties of the printhead is the length of the printhead capillary, which generates the fundamental resonance mode of the capillary. The fundamental resonance mode is the lowest frequency at which small periodic driving forces have the ability to produce relatively large amplitude oscillations and changes between different modes of energy (e.g. a pendulum changing from potential energy to kinetic energy and back again as it describes an arc). Other determinants, such as the reflection coefficients of the capillary ends and

¹ The capability of the 'JetLab 4' to generate bipolar dual-pulse waveforms is slightly different from that of the apparatus referred to by Morita et al, since the 'idle' period used by Morita et al, cannot be introduced in between the dual pulses with the JetLab 4. Morita et al's approach is therefore adapted and customised with assistance from MicroFab's Technical Note 99-03 'Drive Waveform Effects on Inkjet Device Performance' (Microfab Technologies Inc., 1999) in order to guide the following droplet velocity, volume and shape optimisation experiments

the transmission coefficients of the ‘ink’ (i.e. the sound speed of the ink) are also relevant to establishing the optimum waveform.

‘Morita et al’ assert that it is **not necessary to know** the fundamental resonance frequency of the capillary, since its fundamental resonance period can be quantified by conducting a brief experiment where the droplet velocity is measured as a function of the dwell time of the jetting pulse (t_{dj}). In the case of a printhead capillary, the fundamental resonance period (T_f) is the time taken for a pressure wave to travel the length of the capillary and return. The nomenclature used in the following discussion is summarised in Table 5 below.

Table 5 Nomenclature for ‘fundamental resonance’ period equations.

T_f	The fundamental resonance period of the capillary, equivalent to the time taken for the pressure wave to travel a length of the capillary and return i.e. <u>two lengths</u>
$T_f/2$	The time taken for the pressure wave to travel a <u>single length</u> of the capillary
t_{jp}^o	The total time of the <u>optimal</u> jetting pulse
t_{jp}	The total time of the actual jetting pulse
t_{rj}	The rise time of the jetting pulse – the power applied ramps up
t_{dj}	The dwell time of the jetting pulse – the power applied remains constant
t_{dj}^o	The optimal dwell time
t_{fj}	The fall time of the jetting pulse – the power applied ramps down

Morita et al assert that the droplet velocity will be maximum when the duration of the jetting pulse i.e. ‘ $t_{jp} = t_{rj} + t_{dj} + t_{fj}$ ’ is half that of the fundamental resonance period i.e. ‘ $t_{jp} = T_f/2$ ’.

The reasoning behind this assertion is because the piezo is situated at the centre of the length of the capillary; the negative pressure wave should therefore travel to the end of the capillary and return (equivalent to a single total length of the capillary) before the subsequent positive pressure wave is applied. Furthermore, it then follows that the fundamental resonance period may be derived experimentally simply by varying the dwell time whilst maintaining constant rise and fall times at a given amplitude. The droplet that is ejected at maximum velocity will indicate the optimum dwell time, because the positive pressure wave will be applied at the correct time to map precisely on to the initial negative pressure wave, therefore producing maximum impulse at the capillary tip.

If the total jetting pulse period is optimised in accordance with the capillary's fundamental resonance period, then equal rise and fall times will ensure that pressure waves of equal intensity are generated at correctly timed intervals, ensuring the positive pressure wave maps precisely onto the initial negative pressure wave in order to maximise the intensity of the final combined pressure wave as it moves toward the capillary tip. Varying rise and fall times (against a constant amplitude) introduces significant additional complexity in exchange for limited returns in terms of control of volume and velocity. Unequal rise and fall times will deliver pressure waves of different lengths. The waves will be unmatched, and the positive pressure wave will fail to map precisely onto the initial negative pressure wave, which will result in the final impulse that is generated at the capillary tip being diffused. Whilst these unequal pressure waves may still produce droplets, identical droplets could be produced with equal rise and fall times at a lower amplitude (Wijshoff, 2010).

4.4.1 Methods, Results and Discussion

A unipolar single pulse waveform was generated. The jetting pulse amplitude was set to 32 V. The rise time was set to 6 μs ($t_{rj} = 6 \mu\text{s}$), which was then mirrored by setting the fall time to 6 μs ($t_{fj} = 6 \mu\text{s}$). A 600 μs strobe delay was set for the LED and captured by the CCD camera; screen shots were taken with an image of the dispensed droplet at that point. With these settings in place, jetting dwell times (t_{dj}) were increased from zero in increments of 5 μs until a droplet appeared at 15 μs . These incremental increases were continued up to a setting of 30 μs , whereupon droplet formation and ejection ceased. When the droplet locations were compared on these images; it was found that the greatest distance between droplet and capillary had occurred at settings of 20 and 25 μs .

The jetting dwell time range between 20 and 25 μs was then tested at increments of 1 μs . The time of the initial disturbance of the meniscus (dwell time 20 μs) was measured at 42 μs and then the 600 μs strobe delay was added. The meniscus measurement procedure was repeated as dwell times were increased, and the strobe delay was then adjusted, so that the captured image would more accurately reflect the distance travelled from the tip of the printhead capillary within a constant time period. The distances between the capillary tip and the droplet were measured from the screenshots by means of pixel ruler using the diameter of the printhead as a constant. Velocity was then calculated against the constant 600 μs delay. Results are shown in Figure 25 overleaf.

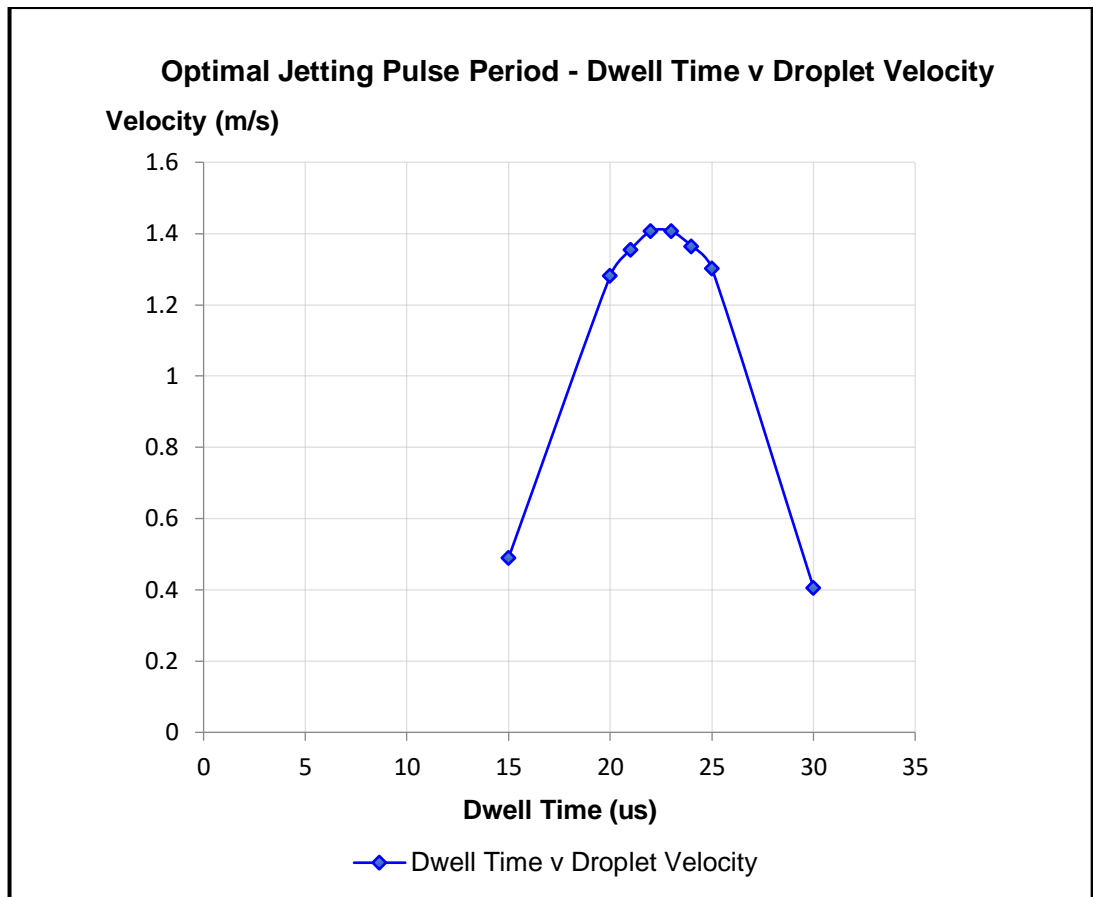


Figure 25 Droplet’s average velocity at 600 μs after droplet ejection, for a jetting pulse of 32 V, rise and fall times both set to 6 μs, dwell times varied from 15 to 30 μs.

The results show that maximum droplet velocity was achieved at a jetting dwell time of between 22 and 23 μs. Although the period between 22 and 23 μs was then tested at 0.1 μs intervals, no significant variation in velocity could be observed. Furthermore, as the strobe delay could not be adjusted in 0.1 μs intervals, if there were any visible variation, the measurement of that velocity may not have been accurate. It was therefore decided that 22.5 μs would suffice as a representative figure for the optimised dwell time.

Completing Morita et al’s formula ‘ $t_{jp} = t_{rj} + t_{dj} + t_{fj}$ ’ (Morita et al., 2015) gives a total jetting pulse time of 34.5 μs, which indicates (from $t_{jp} = T_f/2$) that the fundamental resonance period for the capillary is 69 μs.

If $T_f = 69 \mu s$, then the initial meniscus displacement (i.e. a protrusion of ink from the capillary tip) may have been expected to be seen at $\frac{3}{4} T_f$, i.e. at 51.75 μs, when the leading edge of the pressure wave would have travelled 1.5 lengths of the capillary. The strobe delay was set to 52 μs in order to confirm the expected meniscus displacement. In Figure 26 overleaf, it is clear that at that point in time the droplet

ejection process had already been initiated. The meniscus was then checked at 1 μs intervals and it was observed that the first actual visible sign of meniscus displacement took place at approximately 44 μs .

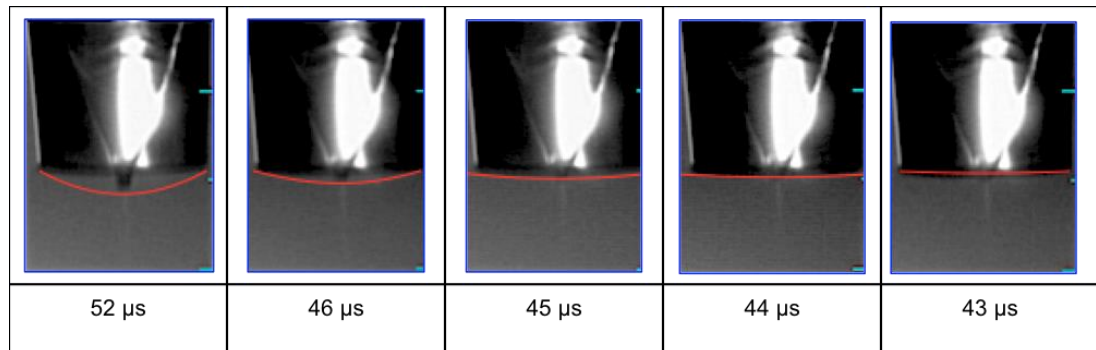


Figure 26 The timing of meniscus displacement for a 32 V amplitude jetting pulse with rise and fall times set at 6 μs and an optimised dwell time of 22.5 μs .

The evidence presented in Figure 26 called Morita et al's assertion that $t_{jp}^{\circ} = t_{rj} + t_{dj} + t_{fj} = T_f/2$ into question. Careful consideration of 'what may actually be happening' over the duration of the jetting pulse (see Figure 27 overleaf) showed that an alternative explanation (and equation) might provide a better fit with the observed phenomenon. Figure 27 shows that the leading edge of the negative pressure wave (propagated over the period t_{rj}) is actuated at the midpoint of the capillary, in theory, at $t \rightarrow 0 \mu\text{s}$. The leading edge will travel to the end of the capillary and return to the midpoint at $T_f/2$.

So, if, $t_{rj} \rightarrow 0$, then the optimal dwell time, $t_{dj}^{\circ} \rightarrow T_f/2$

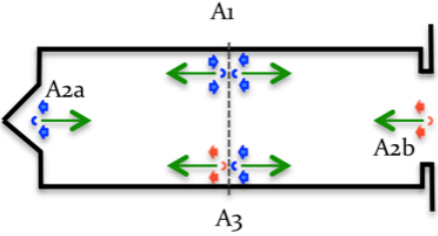
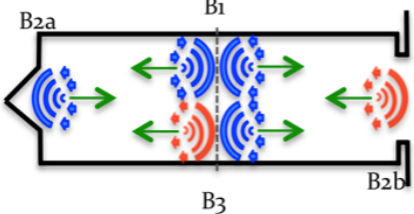
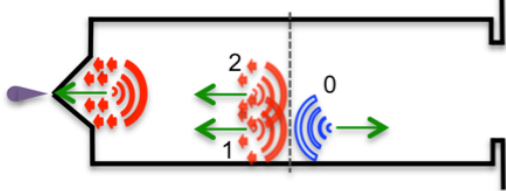
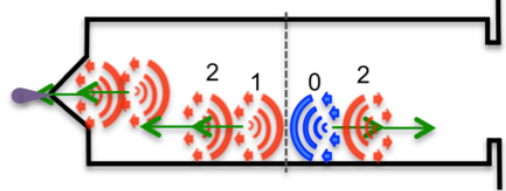
However, since the rise period must have an absolute value and the dwell period is not activated until the rise period is complete, the relationship may be better reordered as:

$$t_{dj}^{\circ} = T_f/2 - t_{rj} \quad \text{or}$$

$$T_f/2 = t_{rj} + t_{dj}^{\circ}$$

Indeed, it can be seen from the equation above that the fall time, 't_{fj}', proposed in Morita et al's equation ' $t_{jp}^{\circ} = t_{rj} + t_{dj} + t_{fj} = T_f/2$ ' is a redundant term in the calculation of optimal waveforms.

Figure 27 The positions of the leading and trailing edge of the pressure wave during printhead actuation relative to the fundamental resonance period.

Leading Edge of Pressure Wave		Trailing Edge Of Pressure wave
A1. At $t \rightarrow 0$, the leading edge of the negative pressure wave is actuated		B1. At $t \rightarrow t_{rj}$, the trailing edge of the negative pressure wave is actuated
A2a. At $t = \frac{1}{4}T_f$, the leading edge of the negative pressure wave reflects from the capillary end		B2a. At $t = \frac{1}{4}T_f + t_{rj}$, the trailing edge of the negative pressure wave reflects from the capillary end
A2b. At $t = \frac{1}{4}T_f$, the leading edge of the negative pressure wave reflects from the capillary end (turning positive)		B2b. At $t = \frac{1}{4}T_f + t_{rj}$, the trailing edge of the negative pressure wave reflects from the capillary end (turning positive)
A3. At $t = \frac{1}{2}T_f$, the leading edge of both pressure waves returns to the midpoint of the capillary		B3. At $t = \frac{1}{2}T_f + t_{rj}$, the trailing edge of both pressure waves return to the midpoint of the capillary
<p>Now consider two scenarios:</p> <p>A, the positive pressure wave is actuated at $t = \frac{1}{2} T_f$ for the duration t_{rj}, or B, the positive pressure wave is actuated at $t = \frac{1}{2} T_f - t_{rj}$ for the duration t_{rj} (in order to satisfy the Morita et al's equation $t_{i0}^0 = \frac{1}{2} T_f = t_{rj} + t_{di} + t_{rj}$)</p>		
A1. The positive pressure wave (2) is actuated at $t = \frac{1}{2} T_f$ for the duration t_{rj} and maps directly onto the existing pressure waves, intensifying the positive pressure wave (1) and cancelling the negative pressure wave (0).	B1. The positive pressure wave (2) is actuated at $t = \frac{1}{2} T_f - t_{rj}$ for the duration t_{rj} , and as it is instigated before the arrival of the existing pressure waves, it therefore fails to intensify the positive pressure wave(1), and fails to cancel the negative pressure wave (0).	
		

Recalculating the optimal waveform using $T_f/2 = t_{jp}^o = t_{rj} + t_{dj}$ gives a fundamental period of $57 \mu\text{s}$ and suggests that initial meniscus displacement will occur at $42.75 \mu\text{s}$ (i.e. at $3/4 T_f$), which is in good agreement with initial meniscus displacement shown as shown at $44 \mu\text{s}$ as shown in Figure 26.

In order to test whether or not this finding was simply an anomaly for which a randomly correlated formula happened to work, a further experiment was undertaken. Using rise times of 3, 6, 9 and $12 \mu\text{s}$, dwell times were optimised in accordance with the procedure set out at the beginning of this section. It was found that the amplitude of the pressure waves had to be increased as the rise times were increased (the rationale for this is explained in Section 4.5 that follows).

The results of the dwell time optimisation process are shown in Figure 28 below and Figure 29 overleaf. The first of the two figures shows the optimised jetting pulse as the sum of dwell times combined with both rise and fall times (as per Morita et al), whilst the second figure shows the optimised jetting pulse as the sum of the dwell times with only the relevant rise times included (as per the posited revision).

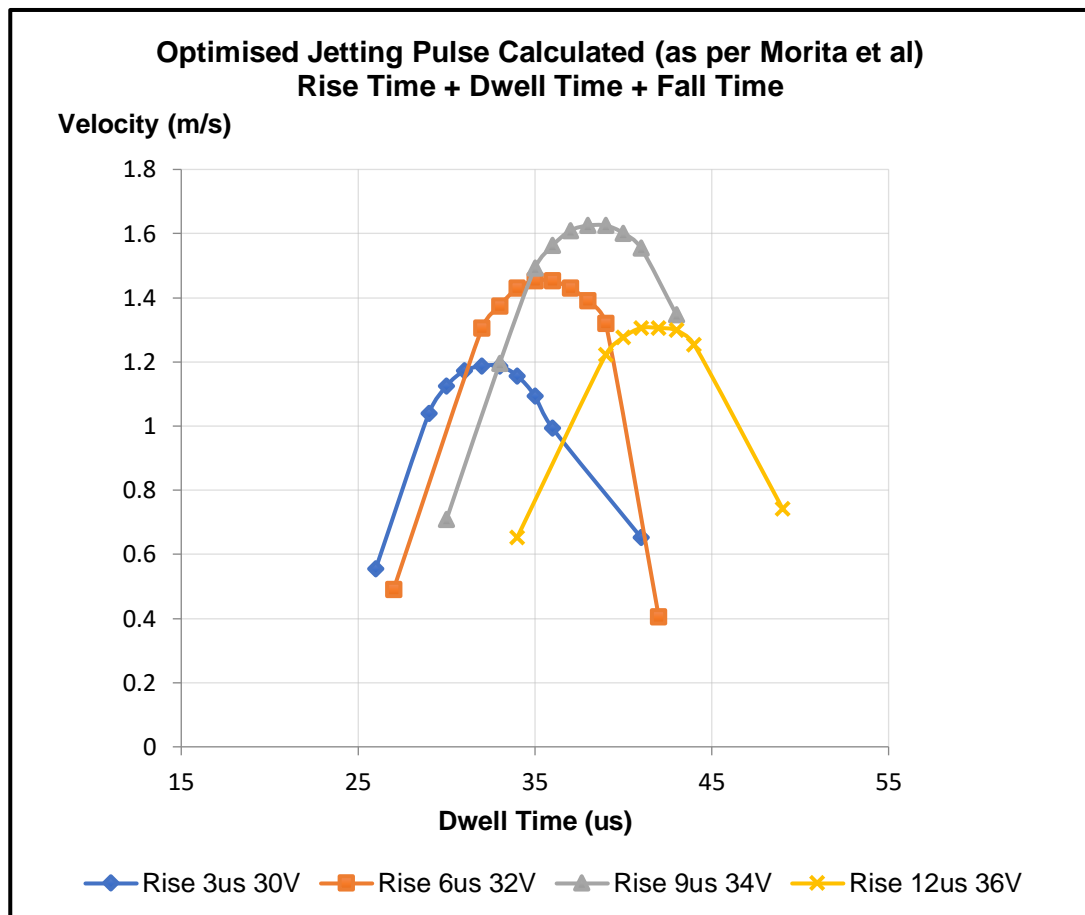


Figure 28 Droplet's average velocity at $600 \mu\text{s}$ after droplet ejection, for a jetting pulses of a, 30 V amplitude and $3 \mu\text{s}$ rise and fall times, then b, 32 V and $6 \mu\text{s}$, c, 34 V and $9 \mu\text{s}$ and d, 36 V and $12 \mu\text{s}$. Dwell times varied from 15 to $30 \mu\text{s}$.

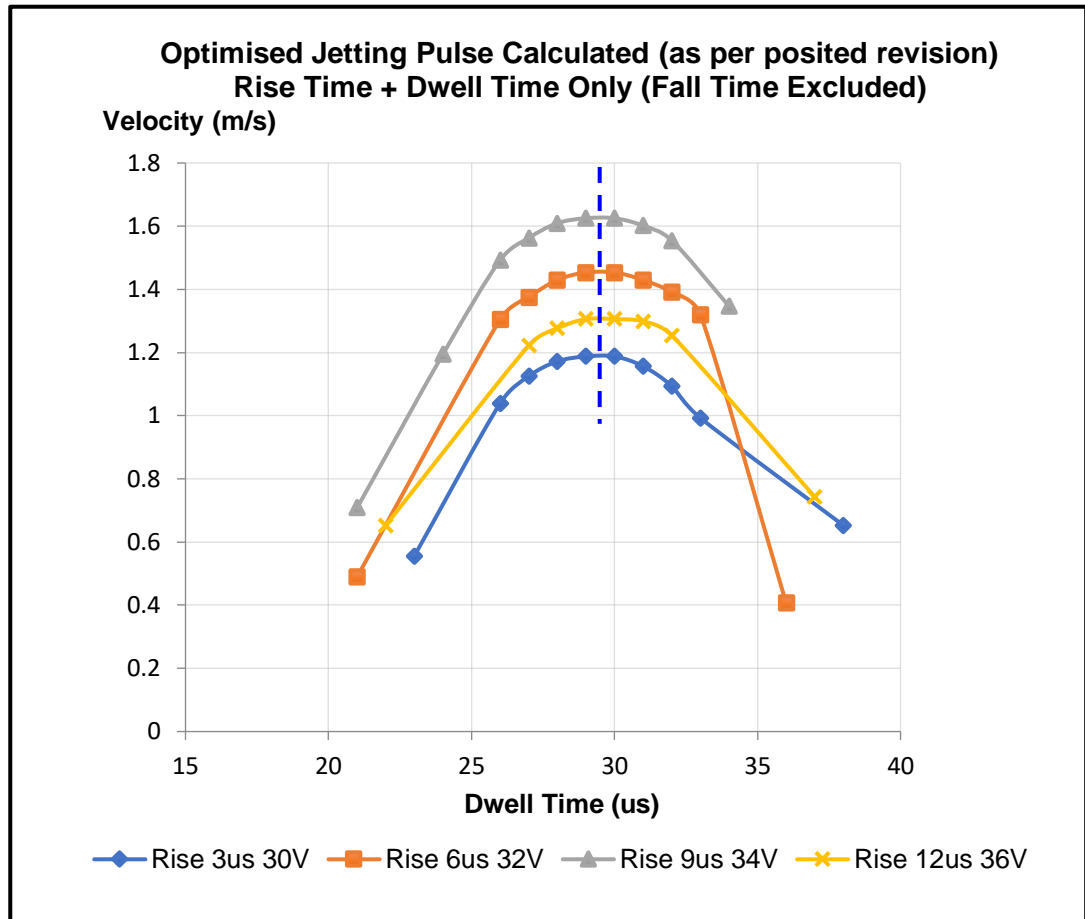


Figure 29 Average droplet velocity at 600 μ s after droplet ejection, for a jetting pulses of a, 30 V amplitude and 3 μ s rise and fall times, then b, 32 V and 6 μ s, c, 34 V and 9 μ s and d, 36 V and 12 μ s. Dwell times varied from 15 to 30 μ s.

From comparison of Figures 28 & 29, it is clear that when only the rise times are combined with the optimised dwell times, the result is a consistent predictor of the fundamental resonance period of the printhead.

It should also be noted that whilst the second experiment was conducted on a different day, in spite of the same settings being used, there has been an approximate 1 μ s increase in the optimised dwell times compared to the first of the dwell time optimisation experiments indicating that there was a minor difference in backpressure.

The capability of Morita et al's formula and the proposed revised formula to predict the timing of meniscus displacement was then assessed. The timing of the initial meniscus displacements for each rise and dwell time combination were measured and compared with the expected anticipated initial meniscus displacement times, using:

- $\frac{3}{4} T_f$, when T_f has been defined by $t_{JP}^o = t_{rj} + t_{dj} + t_{fj} = T_f/2$ following Morita et al.
- $\frac{3}{4} T_f$, when T_f has been defined by $t_{JP}^o = t_{rj} + t_{dj} = T_f/2$ following the posited revision.

The results are shown in Table 6 below.

Table 6 Comparison of actual meniscus displacement times with anticipated meniscus displacement times as per Morita et al and the posited revision

Rise Times	Dwell Times	Fall Times	<u>Morita et al</u> Expected Meniscus Displacement 2 x (Rise + Dwell + Fall) x 0.75	<u>Revised</u> Expected Meniscus Displacement 2 x (Rise + Dwell) x 0.75	<u>Actual</u> Meniscus Displacement (Observed)
3 μs	26.5 μ s	3 μ s	48.75 μ s	44.25 μ s	48 μ s
6 μs	23.5 μ s	6 μ s	53.25 μ s	44.25 μ s	49 μ s
9 μs	20.5 μ s	9 μ s	57.75 μ s	44.25 μ s	50 μ s
12 μs	17.5 μ s	12 μ s	62 μ s	44.25 μ s	52 μ s
Rise Time + Dwell Time + Fall Time gives values from 32.5 to 41.5 μ s					
Rise Time + Dwell Time <u>always</u> gives a value of 29.5 μ s					

From Table 6 above, the first observation that can be made is that actual meniscus displacement of 49 μ s (at a rise time of 6 μ s) is 5 μ s later than that of the previous experiment, where initial meniscus displacement was recorded at 44 μ s, indicating that a slight variance in backpressure had set the meniscus further back from the capillary tip. The data is corrected for the variance of 5 μ s in Table 7, which follows overleaf.

Table 7 Comparison of actual meniscus displacement times and revised meniscus displacement times in view of a correction for backpressure.

Rise Times	Dwell Times	Fall Times	Expected Meniscus Displacement (Morita et al)	Expected Meniscus Displacement (Revised)	Revised Time of Actual Meniscus Displacement
3 μs	26.5 μ s	3 μ s	48.75 μ s Variance 5.75 μ s	44.25 μ s Variance 1.25 μ s	43 μ s
6 μs	23.5 μ s	6 μ s	53.25 μ s Variance 9.25 μ s	44.25 μ s Variance 0.25 μ s	44 μ s
9 μs	20.5 μ s	9 μ s	57.75 μ s Variance 12.75 μ s	44.25 μ s Variance -0.75 μ s	45 μ s
12 μs	17.5 μ s	12 μ s	62.00 μ s Variance 15 μ s	44.25 μ s Variance -2.75 μ s	47 μ s

It can be seen that Morita et al's expected displacement is in reasonable agreement with the actual displacement observed when the rise time is at its minimum (3 μ s). However as rise times increase, it can be seen that the droplet ejection process has been initiated increasingly in advance of Morita et al's expected displacement times. It is clear that Morita et al's formula $t_{jp}^{\circ} = t_{rj} + t_{dj} + t_{\theta} = T_f/2$ is not an accurate representation of the relationship of an optimised jetting period to the fundamental resonance period of the printhead.

It must also be noted that the suggested revised formula $t_{jp}^{\circ} = t_{rj} + t_{dj} = T_f/2$ maintains good general agreement with meniscus displacement times and is well supported by the evidence shown in Figure 29. However, that said, it can also be seen from Table 7 above that the formula predicts a fixed meniscus displacement time and does not account for the fact that measured meniscus displacement time appears to increase in some proportion to the increase in rise time.

The suggested refinement of Morita et al's formula is also has practical implications for the IJP community. At present, maximum theoretical jetting frequencies are calculated using Morita et al's equation, which overstates the duration of the fundamental resonance period. The use of the revised fundamental resonance period (indicative of a shorter duration) shows that theoretical maximum jetting frequencies can be increased.

Morita et al's formula also overweighs the importance of rise and fall times, this may lead to these times being unnecessarily minimised and in turn may adversely impact the shape of the dispensed droplet (discussed further in the following section).

Finally, a significant proportion of jetting time is devoted to damping 'residual oscillations'; it is possible that these residual oscillations are being mischaracterised (due to the overstated duration of the fundamental resonance period) and are in fact harmonic oscillations, which should be harnessed to increase jetting frequencies at lower amplitudes.

4.5 The Effect of Varying Rise Times on Droplet Actuation.

Morita et al suggest that for ink viscosity of 3 – 15 mPa.s a rise/fall time equal to $T_f/8$ is a ‘fairly good choice’ (irrespective of amplitude) whereas in an ‘illustrative’ MicroFab’ experiment (Microfab Technologies Inc., 1999), the jetting pulse amplitude is changed whilst the differing rise and fall times remain constant. The combined implication appears to be that the issue of rise and fall times is somewhat trivial but should be addressed as a function of the duration of the total jetting pulse. In light of the results in the previous section and since the advice set out above is neither specific nor consistent, it was decided that the matter should be investigated.

4.5.1 Method, Results and Discussion

A jetting pulse amplitude of 33 V was used in conjunction with the optimum jetting pulse duration of 29.5 μs (i.e. $t_{rj} + t_{dj} = T_f/2$). Rise times of 3, 6, 9, 12, 15 and 18 μs were used and dwell times were then adjusted in accordance with the revision posited for Morita et al’s optimal jetting period formula. Fall times were set to match rise times in order to ensure the propagation of matching pressure waves (Wijshoff, 2010). Velocity was measured over the first 600 μs of the droplet flight time. The results are shown in Table 8, which follows.

Table 8 The effect of varied rise times within an optimised jetting pulse period on droplet velocity for a jetting pulse amplitude of 33 V.

Rise/Fall Times	Dwell Time	Droplet Velocity	Rate of Increase in Application of Voltage
3 μs	26.5 μs	1.53 m/s	11 V/ μs
6 μs	23.5 μs	1.375 m/s	5.5 V/ μs
9 μs	20.5 μs	1.208 m/s	3.67 V/ μs
12 μs	17.5 μs	1.10417 m/s	2.75 V/ μs
15 μs	14.5 μs	0.542 m/s	2.2 V/ μs
18 μs	11.5 μs	0.271 m/s	1.83 V/ μs

The first observation is that Morita et al's suggested value of rise and fall times being set to approximately $T_f/8$ ($8.625 \mu\text{s}$ using Morita et al's optimum jetting pulse formula or $7.7 \mu\text{s}$ using the proposed revision to the optimum jetting pulse formula) may be a valuable piece of generic advice when it is considered that using a rise time of $3 \mu\text{s}$ generated a suboptimal droplet shape, whilst droplet shape was satisfactory at $6 \mu\text{s}$ and above i.e. the secondary droplet was seen to reattach to the primary droplet over the visible course of the flightpath.

However, the results from Table 8 show that an increasing rise time i.e. the speed at which the power to the piezo is ramped up, is also a predictor of the velocity of the dispensed droplets. The results are also illustrated in Figure 30 below.

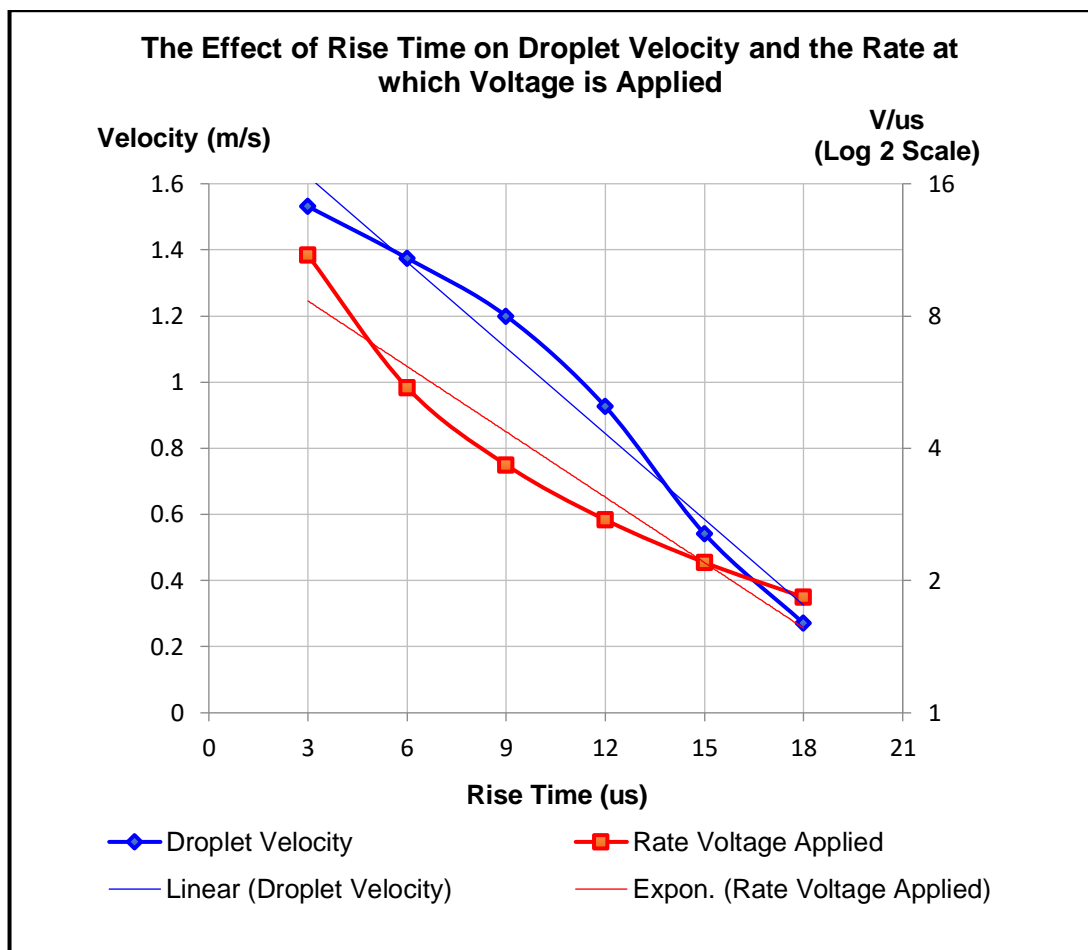


Figure 30 Droplet velocities of jetting pulses with rise times of 3, 6, 9, 12, 15 and 18 μs (with dwell times adjusted to achieve an optimum jetting pulse duration of $29.5 \mu\text{s}$, i.e. $t_{rj} + t_{dj} = T_f/2$) at a jetting pulse amplitude of 33 V are compared with the rate of increase in the jetting pulse amplitude (i.e. the steepness of the 'ramp up' in applied voltage).

It can be clearly seen from Figure 30 (previous page) that as the rate at which power is applied decreases, velocity droplet decreases. This is a novel finding. At present, IJP literature only describes a relationship between absolute pulse amplitude and droplet velocity (Derby et al 2005). Indeed, it was noted in the introduction to this section that general IJP opinion is that rise times should be addressed as a function of the duration of the total jetting pulse not pulse amplitude (as the results of this experiment would indicate).

IJP literature acknowledges that there is a ‘threshold value’ that piezo expansion must surpass to successfully generate a droplet (Derby et al 2005), although in line with current thinking, that threshold value is thought of as a constant (since rise times aren’t considered to contribute to droplet velocity). It was therefore thought that this value should be isolated first and tested to ascertain if it was in fact a constant. At each rise time the applied voltage was decreased from 33 V in 1 V increments until droplet ejection ceased (in order to quantify the ‘threshold voltage’), as shown in Table 9 below.

Table 9 Jetting pulse amplitudes adjusted against jetting pulses with rise times of 3, 6, 9, 12,15 and 18 μ s (with dwell times adjusted to achieve an optimum jetting pulse duration of 29.5 μ s, i.e. $t_{rj} + t_{df} = T_f / 2$) to achieve a constant droplet velocity of 0 m/s.

Rise/Fall Time	Dwell Time	Droplet Velocity	Threshold Voltage	Delta V
3 μs	26.5 μ s	0 m/s	26 V	NA
6 μs	23.5 μ s	0 m/s	27 V	1 V
9 μs	20.5 μ s	0 m/s	28 V	2 V
12 μs	17.5 μ s	0 m/s	29 V	3 V
15 μs	14.5 μ s	0 m/s	30 V	4 V
18 μs	11.5 μ s	0 m/s	31 V	5 V

Table 9 shows a lineal increase in the voltage value (i.e. it is increasing at the rate of 1 V per 3 μ s) indicating that the threshold value is in fact a variable that is clearly correlated with rise times. To anyone who works with a research grade IJP, this should be an uncontroversial proposition, since IJP researchers will almost certainly be familiar with at least one of the ‘inefficiencies’ of the IJP process, namely the acoustic losses (the constant mosquito-like buzz) from the printhead. Therefore, it

should be unsurprising that the threshold voltage value will increase at a constant rate due to the increasing dissipation of energy from the system over the extended duration of the rise time.

In order to test if this 'threshold variable' accounted for the change in droplet velocity, it was decided to conduct a follow up experiment in order to find out what amplitudes were required at the predetermined rise times in order to generate droplets at a constant velocity as seen in Table 10 below.

Table 10 Jetting pulse amplitudes adjusted against jetting pulses with rise times of 3, 6, 9, 12,15 and 18 μ s (with dwell times adjusted to achieve an optimum jetting pulse duration of 29.5 μ s, i.e. $t_{rj} + t_{dj} = T_f/2$) to achieve a constant droplet velocity of 1.53 m/s.

Rise/Fall Times	Dwell Time	Constant Droplet Velocity	Voltage to Achieve Constant Droplet Velocity	Delta V
3 μs	26.5 μ s	1.53 m/s	33 V	NA
6 μs	23.5 μ s	1.53 m/s	34 V	1 V
9 μs	20.5 μ s	1.53 m/s	35 V	2 V
12 μs	17.5 μ s	1.53 m/s	37 V	4 V
15 μs	14.5 μ s	1.53 m/s	39 V	6 V
18 μs	11.5 μ s	1.53 m/s	41 V	8 V

As Table 10 shows, only relatively small increases in the absolute amplitude of the voltage applied are needed to maintain equal droplet velocity, which also of course means that the change in the average increase in voltage (per micro second) applied is also proportionately small. The question then is; does this result negate the previous working hypothesis or inform it? A comparison of the threshold and constant velocity droplet change in voltage values is shown overleaf.

Table 11 A Comparison of the Change in Threshold and Constant Droplet Velocity Voltage Values for Rise Times of 3, 6, 9, 12,15 and 18 μ s

Rise/Fall Time	Dwell Time	Threshold Delta V	Constant Droplet Velocity Delta V	Difference Between Threshold Delta V and Constant Velocity Delta V
3 μs	26.5 μ s	NA	NA	NA
6 μs	23.5 μ s	1 V	1 V	0 V
9 μs	20.5 μ s	2 V	2 V	0 V
12 μs	17.5 μ s	3 V	4 V	1 V
15 μs	14.5 μ s	4 V	6 V	2 V
18 μs	11.5 μ s	5 V	8 V	3 V

It is clear from Table 11 that whilst the dissipation of energy offered an explanation for the increase in voltage required to maintain constant droplet velocity for the rise times of 3, 6 and 9 μ s , it certainly didn't account for the full increase in voltage required to maintain constant droplet velocity for the longer rise times. The result indicates that a further variable beyond that of the threshold voltage value must exist. The following causal mechanism is suggested:

The application of a current to the piezo drives its expansion. The maximum amplitude of the applied current defines the total change in the area of the piezo (from rest state to expanded state), which in turn governs the total energy of the resultant pressure waves within the capillary. The time taken to apply the current to the piezo governs the physical length of the pressure wave as well. The combination of both the amplitude of the pressure wave and the duration of the wave, govern the intensity of the pressure wave i.e. given a constant displacement of the piezo, a shorter rise time (sharp transition) will generate a more intense pressure wave, whilst a longer rise time (gradual transition) will generate a less intense pressure wave. The capillary aperture through which the droplet is ejected may then create a secondary threshold or boundary condition. The longer pressure waves associated with longer rise times may therefore lack the intensity to surmount the threshold value or may take a longer time to do so.

As testing this hypothesis was at the limits of the scope of this enquiry and the limitations of the Jetlab 4 were already apparent (insufficient voltage sensitivity and limited meniscus imaging) further research couldn't be justified.

However, although the causal mechanism cannot be proven at the moment, it remains clear that the combination of extended rise times and threshold values that vary with those rise times means that there is a period when the waveform has been activated, but a sufficient pressure wave has not yet begun to propagate.

The definition of the fundamental acoustic period T_f can therefore be refined in light of the observations from this section to the following equation:

$$T_{f\text{ IJP}} = t_{\text{zero}} + 2(t_{\text{adjr}} + t_{\text{dj}}) = 2t_{\text{jp}}^{\circ}$$

Where:

t_{zero} = the period of delay between waveform activation and actual pressure wave propagation

t_{adjr} = the actual effective period of the rise time (i.e. adjusted for t_{zero} above)

t_{dj} = the actual travel period of the pressure wave

Furthermore, the existence of this period ' t_{zero} ' opens an avenue for research into the explanation for the delayed meniscus displacement seen in the previous section.

In this section it has been established that the issue of rise times is a nontrivial matter. The research has revealed a novel finding. At present, IJP literature only describes a relationship between absolute pulse amplitude and droplet velocity, but it has been clearly demonstrated that as the rate at which power is applied decreases, velocity droplet decreases.

Although further research is required in order to precisely determine the actual drivers of rise time's influence, it is initially clear that:

There is a period described as ' T_{zero} ' when although the waveform has been activated, pressure waves in the ink do not begin to propagate. As rise times increase ' T_{zero} ' increases, so an allowance for this period must be considered in order to avoid overstating the fundamental resonance period. Although the correlating mechanism is suggested (the presence of a threshold value), at present the causal mechanism cannot be stated, much less its effect be calculated. However, it is possible that an approximate allowance for the effect may be derived by experiment.

' T_{zero} ' may address the problem that the proposed revision to Morita et al's formula predicts a fixed meniscus displacement time but does not account for the fact that the measured meniscus displacement time increases in proportion to the rise time. Altering rise times offers a useful secondary method of controlling droplet velocity (and possibly volume) beyond that of simply adjusting pulse amplitude.

It has also been shown that neither the use of a generalised rule of thumb, such as ' $t_{\text{rj}} = t_{\text{fj}} = T_{\text{f}}/8$ ', nor the use of optimised dwell times that have been tuned iteratively to a given set of rise and fall times (but are then applied indiscriminately to other rise and fall times) appear to be appropriate approaches to optimising rise times. The selection of rise times should be better considered as a function of jetting pulse amplitude to ensure that the droplet has the desired shape

4.6 The Use of Extended Dwell Times to Increase Droplet Volume.

IJP research is usually focused toward achieving minimum duration waveforms so that droplet deposition frequency can be maximised. There is little literature that considers dwell times in excess of $T_i/2$, except to acknowledge that these will produce sub optimal droplet velocities and frequencies. However, Bogy and Talke suggest that the use of the residual positive pressure wave oscillation after the first droplet has been dispensed can then be used to produce the subsequent droplet of a greater volume. (Bogy & Talke, 1984).

Furthermore, Gerhauser et al describe in a communication that the use of extended dwell times can produce variations in the volume of droplets if accompanied by adjustments of pulse amplitude to maintain constant droplet velocity although there is no discussion of what the causal mechanism could be (Gerhauser et al., 1983). Their results are shown in Figure 31 below, where dwell times and amplitude are varied to achieve equal velocity droplets, and the volume of those droplets is then measured.

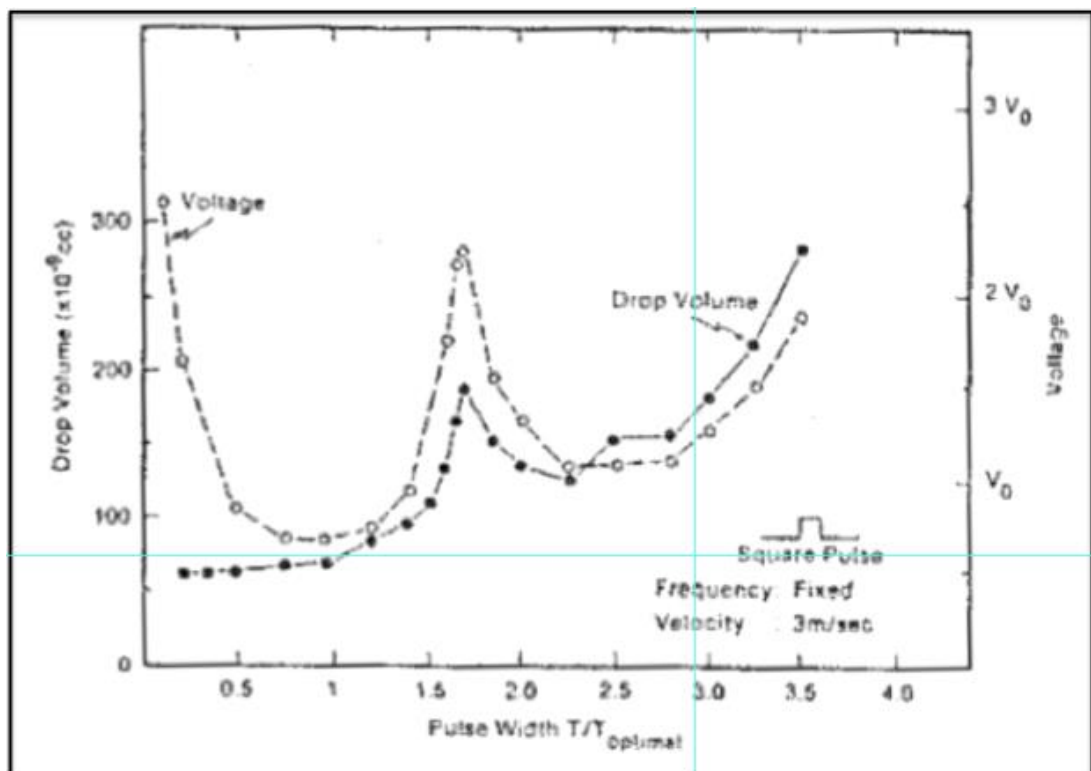


Figure 31 The figure from Gerhauser et al shows droplet volumes generated by jetting pulse amplitudes that have been adjusted against extended dwell times to achieve a constant droplet velocity of 3 m/s (Gerhauser et al., 1983).

The combination of these two observations provided a starting point for the research into the previously unexamined use of greatly extended dwell times in order to

expand the range of droplet volumes that can be deposited from a single printhead. This was undertaken so that the size and complexity of sacrificial microvascular facsimiles that can be fabricated while avoiding the time consuming and error inducing process of changing printhead could be increased.

In order to understand the causal mechanism behind this process, it is important to carefully consider how the negative pressure waves that are propagated by the initial expansion of the capillary might continue on if the subsequent contraction of the capillary is delayed beyond its first optimal point ($T_f/2$). Figure 32 below shows how the pressure waves would continue to propagate until $t = 2 \frac{1}{2} T_f$, after which the sequence then repeats itself (returning to $\frac{1}{2} T_f$).

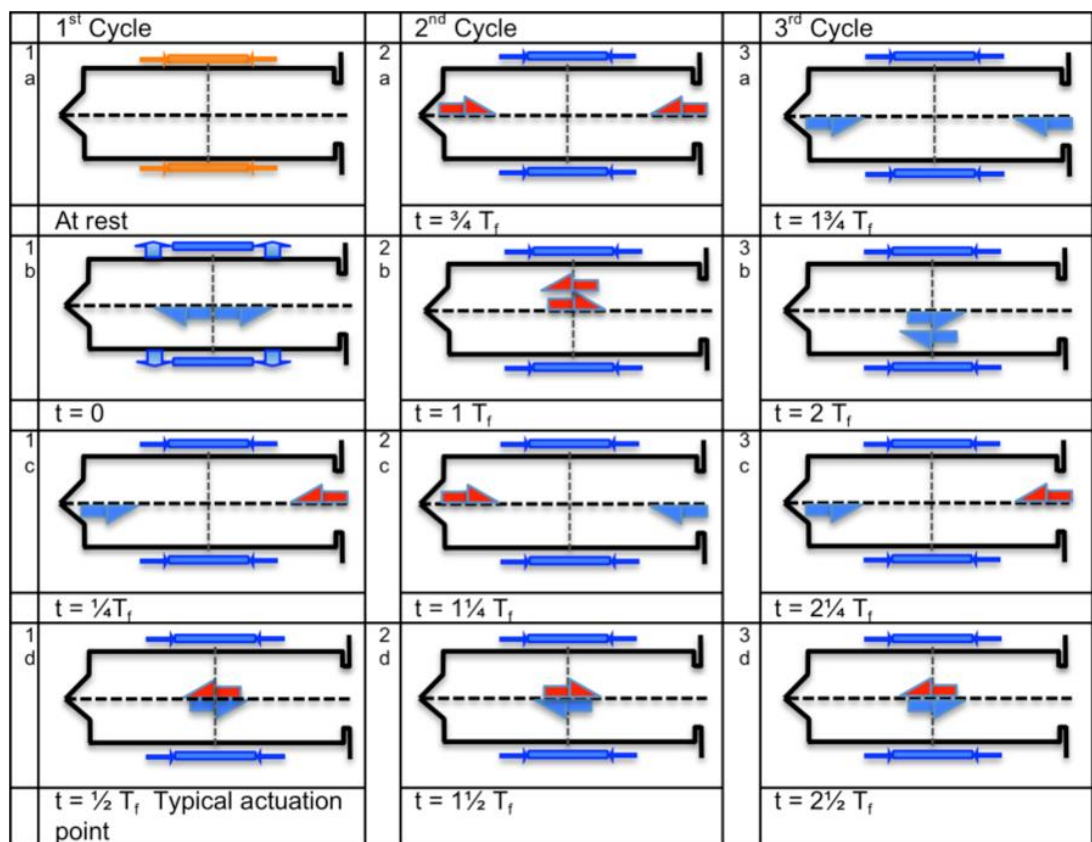


Figure 32 The propagation of pressure waves in the printhead capillary during extended dwell time periods. Negative pressure wave = blue arrow. Positive pressure wave = red arrow.

It can be seen that there are a number of obvious time-points that are of interest for the application of the delayed positive pressure wave. The first, for instance being frames 2d and 3d, where initially, the reverse combination of pressure waves (2d) of those that exist at the traditional actuation point can be seen, then in frame 3d, when the identical combination of those that exist at the traditional actuation point return.

Of further interest are frames 2b and 3b. In Frame 2b, a double amplitude positive pressure wave exists at the midpoint of the capillary at $t = 1 T_f$. Conversely, in frame 3b a double amplitude negative pressure wave is shown $t = 2 T_f$.

4.6.1 Methods, Results and Discussion

A jetting pulse amplitude of 32 V was used in conjunction with a rise time of 6 μs with fall times set to match the rise time. The dwell time was increased from 0.5 μs in 2 μs intervals until droplet deposition began at 4.5 μs . Meniscus displacement was checked and found to take place at 28 μs . The droplet flight path was assessed, and it was found that a strobe delay of 700 μs of flight path allowed sufficient time for the droplet velocity to achieve a steady velocity. Therefore, the strobe delay was initially set at 728 μs , but was then increased in 2 μs increments in line with the subsequent increases in dwell time.

Average velocity was measured over the first 700 μs of the droplet flight time at 1.47 m/s. As dwell times were increased in 2 μs increments thereafter, the jetting pulse amplitude was increased or decreased in order to maintain constant droplet velocity. At each point a screenshot was taken to capture an image of the droplet for subsequent diameter measurement and volume calculation. This procedure was continued until a dwell time of 162.5 μs had been achieved (80 data points), whereupon it was estimated that the 4th cycle of wave propagation had begun (see Figure 32) and it was thought that a repeating pattern would be seen thereafter, although this assumption remains to be tested.

Figure 33 on the following page, reflects the effect of extended dwell time on droplet volume and the jetting pulse amplitude that is required to maintain constant droplet velocity. The yellow and green 'locator' bars relate the 'points of interest' identified in Figure 32 to the data shown in Figure 33 (although further discussion of their precise location follows).

The initial pattern of the data presented in Figure 33 is in overall agreement with the data presented by Gerhauser et al in Figure 31. A number of further general observations can be made about the trends within the data.

The jetting pulse amplitude required to maintain a constant velocity shows a good degree of synchronicity with the variations in droplet volume. Overall this is to be expected, as the amplitude of the jetting pulse needed to maintain constant velocity would need to be increased for larger droplets and decreased for smaller droplets. However, it can also be seen that the jetting pulse amplitude (relative to the droplet volume) required to propel larger droplets is significantly reducing as the series

progresses, whilst the jetting pulse amplitude required to propel the smaller droplets is increasing in proportion with droplet volume.

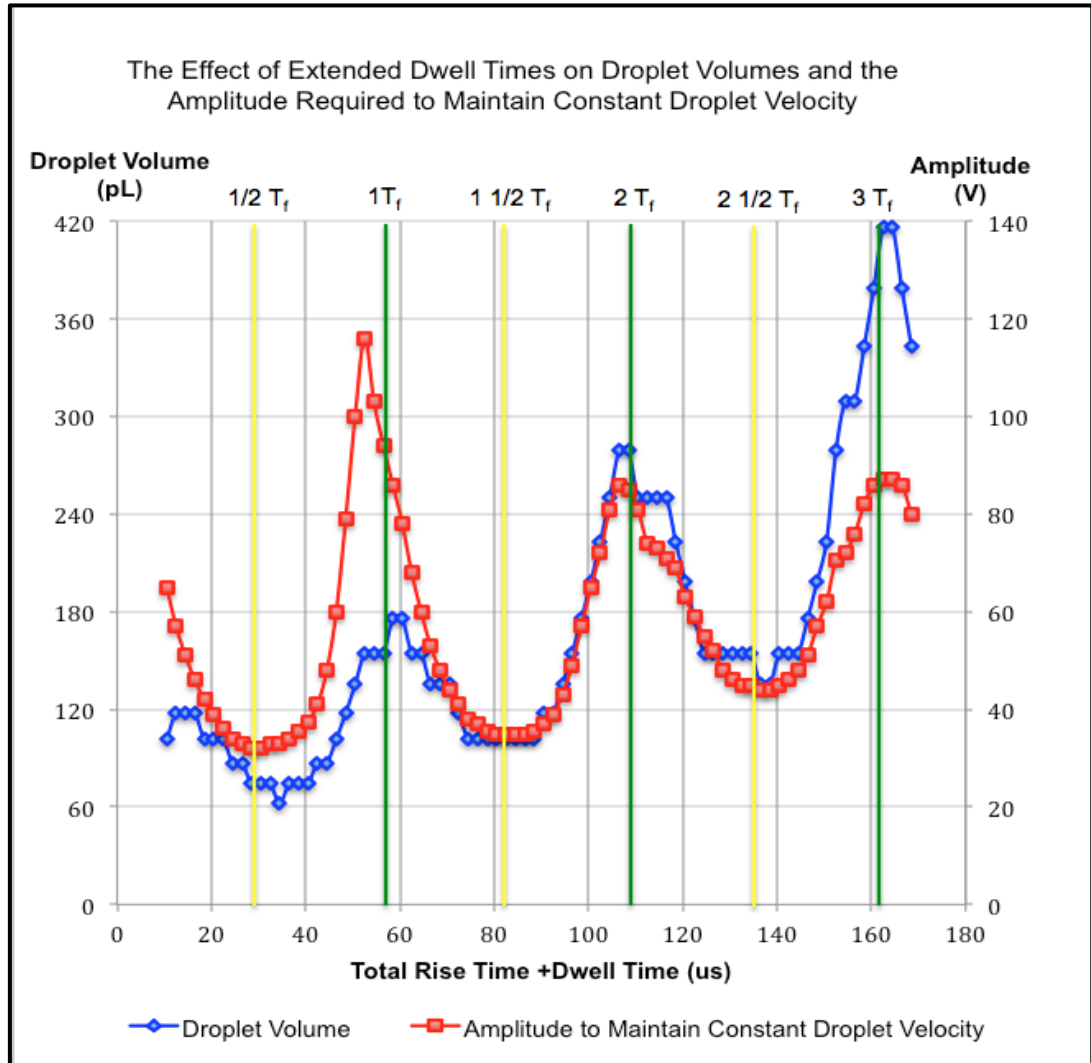


Figure 33 The droplet volumes generated by jetting pulse amplitudes that have been adjusted against extended dwell times to achieve a constant droplet velocity of 1.47 m/s

It can also be seen that the average droplet volume is increasing as the series is progressing, and furthermore, that the difference in droplet volume between the cyclic peaks and troughs is increasing. A slightly different pattern for jetting pulse amplitude can be observed, with the difference between the cyclic peaks and troughs decreasing as the series progresses, whilst the average jetting pulse amplitude is increasing, albeit at a slower rate than that of the droplet volume.

The working hypothesis linking these general trends is that with each oscillation of a negative pressure wave at the reservoir (when the negative pressure wave returns as a positive pressure wave) more ink is drawn into the capillary. However, with each

oscillation of a positive pressure wave at the reservoir a smaller volume of ink is expelled from the capillary. The reason for the occurrence may well be as simple as the orientation of the capillary (below the reservoir) and the force of gravity, which ensures that less energy is required to draw a volume of ink down into the capillary than is required to expel the same volume of ink up and out into the reservoir.

Addressing the timing of peaks and troughs in droplet volume and jetting pulse amplitude; it can be noted that the troughs in both droplet volume and jetting pulse amplitude occur at $\frac{1}{2} T_f$, $1\frac{1}{2} T_f$, and $2\frac{1}{2} T_f$, whilst the peaks occur at $1 T_f$, $2 T_f$, and $3 T_f$. The troughs correspond with oscillation sequences where a negative and a positive pressure wave coexist at the centre of the capillary when the contraction of the capillary is actuated. The peaks correspond with oscillation sequences where either a double positive or a double negative pressure wave coexists at the centre of the capillary when the contraction of the capillary is actuated. In all cases, the direction of the waves i.e. toward the capillary tip or toward the reservoir, whether positive or negative, does not appear to have a discernible impact on the volume of the deposited droplet.

Table 12 below, compares the actual time of each peak and trough with the projected time of each peak and trough using the previously established formula for the optimum jetting pulse duration of ' $t_{jp}^o = t_{tj} + t_{dj} = T_f/2$ ' as shown on Figure 33 by the yellow and green locator bars.

Table 12 Comparison of the actual timing of peaks and troughs in droplet volume and jetting pulse amplitude from Figure 33 with those anticipated by the waveform propagation theory advanced in Figure 32.

Time in Cycle	$\frac{1}{2} T_f$	$1 T_f$	$1\frac{1}{2} T_f$	$2 T_f$	$2\frac{1}{2} T_f$	$3 T_f$
Jetting Amplitude Peak/Trough (μs)	28.5	52.5	82.5	106.5	136.5- 138.5	162.5
Droplet Volume Peak/Trough (μs)	34.5	58.5	82.5	106.5	136.5- 138.5	162.5
Range of Droplet Volume and Jetting Amplitude Peak/Trough (μs)	28.5- 34.5	52.5- 58.5	82.5	106.5	136.5- 138.5	162.5
Projected Time of Peak/Trough (μs) $t_{jp}^o = 28.5 \mu s$	28.5	57	85.5	114	142.5	171
Discrepancy (μs)	Nil	Nil	3	7.5	4.5- 6.5	8.5

It can be seen from Table 12 that the use of the formula ' $t_{jp}^{\circ} = t_{rj} + t_{dj} = T_f/2$ ' to project the timing of peaks and troughs leads to increasing discrepancies between the projected peak/trough times and the time of their actual occurrence. The observed discrepancy led to a reconsideration of the formula ' $t_{jp}^{\circ} = t_{rj} + t_{dj} = T_f/2$ '.

To recap, the fundamental acoustic period of the capillary is a measure of the time taken for the pressure wave to travel the length of the capillary, and then reflect from the end of the capillary and return. However, both the application of the concept of the fundamental period and what is actually happening during that period of time may neither be accurately captured in the equation ' $t_{jp}^{\circ} = t_{rj} + t_{dj} = T_f/2$ ' nor be what is actually measured when the optimum jetting pulse width is derived by experiment.

In section 4.5 the concept of ' T_{Zero} ' was introduced, which stated that there is a period between waveform being initiated and the actuation of the corresponding pressure wave. This will occur because the capillary material has a threshold value that must be exceeded before the material is deformed sufficiently by the force applied by the piezo for a pressure wave to begin to be propagated. If this is the case, then the stated rise time is an overstatement of the actual rise time, and consequently the optimum jetting pulse width is also an overstatement of the time it actually took for the pressure wave to travel the length of capillary, be reflected, and then return. However, applying the previously proposed formula:

$$T_{f IJP} = t_{zero} + 2(t_{adjr} + t_{dj}) = 2t_{jp}^{\circ}$$

which only accounts for a single incidence of ' T_{Zero} ' over repeated cycles of reflecting pressure waves would not produce the pattern of discrepancy shown in Table 12 (previous page).

So, let us consider the application of the concept of the fundamental acoustic period and how precisely it applies to the actual travel of the pressure waves within a capillary.

For the optimal jetting pulse width, subsequent to actuation, the pressure wave travels half the length of the capillary, is reflected and then travels half the length of the capillary on return, with ' t_{jp}° ' being considered to be equivalent to $T_f/2$. However, if dwell time is increased by delaying piezo expansion, the pressure wave continues another half capillary length, is reflected again, and then returns a further half capillary length. At this point, the time taken for the pressure wave to travel a total of two lengths of the capillary is equated to the fundamental acoustic period.

This is a false equivalence, because the fundamental acoustic period allows for a single reflection of the pressure wave, however, when the reality of the precise movement of the pressure waves within the capillary is considered, it is clear that there are two reflections of the pressure wave within what had otherwise been considered as the fundamental acoustic period.

If the time taken for the reflection of a pressure wave was instantaneous, then the above observation may be interesting but not significant. However, it is improbable that either the open reservoir at one end of the capillary or the capillary tip (with an aperture and a moving meniscus) at the other end are 'ideal' conditions for the optimum reflection of a pressure wave and therefore the reflective coefficient may need to be considered .

If allowances are made to the formula ' $t_{jp}^{\circ} = t_{rj} + t_{dj} = T_f/2$ ', in order to allow for extended dwell times, both the actual rise time (i.e. allowing for the delay before the pressure waves actually propagate) and an additional (and imperfect) reflection of the pressure wave at the capillary ends would be included. The formula may then be revised as follows:

If general acoustic theory is now carefully applied to the specific IJP use case to define the fundamental acoustic period, which is now described as T_{fIJP} , and:

t_{zero} = the period of delay before actual pressure wave propagation commences

t_{adjr} = the actual effective period of the rise time (i.e. adjusted for t_{zero} above)

t_r = the additional time taken for one reflection of the pressure wave, then

t_{adjd} = the actual travel period of the pressure wave (i.e. the dwell time adjusted to exclude the reflection period).

Then the following equation may be applied:

$$T_{fIJP} = t_{zero} + 2(t_{adjr} + t_{adjd} + t_r) = 2t_{jp}^{\circ}$$

If values of

$t_{zero} = 1.5 \mu s$, and

$t_r = 0.5 \mu s$ (per pressure wave reflection),

are applied, and t_{adjr} and t_{adjd} are adjusted accordingly, then the previous table (Table 12) can be revised in the manner shown in Table 13 overleaf.

Table 13 Comparison of the actual timing of peaks and troughs in droplet volume and jetting pulse amplitude from Figure 33 with those anticipated by the waveform propagation theory advanced in Figure 32 incorporating the proposed revisions to fundamental acoustic period theory (for extended dwell times).

Time in Cycle	$\frac{1}{2} T_f$	$1 T_f$	$1\frac{1}{2} T_f$	$2 T_f$	$2\frac{1}{2} T_f$	$3 T_f$
Range of Droplet Volume and Jetting Amplitude Peaks/Troughs (μs)	28.5-34.5	52.5-58.5	82.5	106.5	136.5-138.5	162.5
t_{zero} (μs)	1.5	1.5	1.5	1.5	1.5	1.5
$t_{\text{arj}} + t_{\text{adj}}$ (μs)	26.25	52.5	78.75	103	131.25	157.5
t_r (μs)	0.5	1	1.5	2	2.5	3
Projected Time of Peaks/Troughs (μs)	28.25	55	81.75	106.5	135.25	162
Discrepancy (μs)	0.25	0	0.75	0	0.75	0.5

It can be seen from Table 13 that the projected timing of the peaks and troughs is now in good agreement with the actual timing of the peaks and troughs.

It is noted that the values used may seem arbitrary, however it can be seen that there are significant variations in MicroFab’s specified optimum jetting pulse widths for each individual printhead that is supplied. A copy of a MicroFab’ delivery note is included in the appendix, where it can be clearly seen that there is substantial variance in jetting pulse width for capillaries of identical length and aperture size (suggesting that pressure wave reflection time may be highly variable). It will therefore be of interest to test this working hypothesis by comparing the performance of a number of different capillaries in future research.

Whilst discussion of the relationship between the fundamental resonance period and the optimum jetting pulse is of great interest to the IJP community, it must be remembered that the original objective of the experiment was to ascertain if droplet volume may be controlled by the extension of dwell times.

The minimum droplet size that was deposited was measured at 49 μm diameter, giving a volume of 62 pL, whilst the maximum droplet volume that was achieved was measured at 93 μm diameter giving a droplet volume of 416 pL. This result means that a 6.7 fold range of droplet volumes may be produced from a single printhead,

which allows controlled deposition of a wide range of specified volumes of ink and is significantly beyond the typical range of droplet volumes and diameters (1 - 100 pL and 10 - 60 micron) previously cited (Saunders & Derby, 2014). Applying this novel IJP technique across a range of commonly available printhead aperture sizes, e.g. from say 20 μm to 100 μm , will enable the IJP researcher to precisely fabricate a representative range of microvascular facsimiles.

4.7 The Effect of the Transition from Unipolar Single Pulse Waveforms to Bipolar Dual Pulse Waveforms on Droplet Actuation

Within IJP literature, the second pulse (or quenching pulse) is added to a single pulse waveform in order to 'quench' residual oscillations, thereby ensuring undisrupted propagation of subsequent droplets. For this purpose, in conjunction with bipolar dual pulse waveforms, Morita et al. recommend a brief period of idle time equivalent to that of the jetting pulse time (i.e. $T_f/2$, which allows residual pressure waves to reflect from the capillary ends to the capillary centre), before the second 'quenching pulse' is applied. Naturally, the duration of the quenching pulse is also equivalent to that of the jetting pulse, to avoid inadvertently setting up further oscillations in the ink. However, the amplitude of the quenching pulse must be tuned iteratively until consistent droplet formation and flight characteristics are observed.

Alternatively, but to the same end, MicroFab's technical note recommends that the quenching pulse is applied immediately after the cessation of the jetting pulse and that the duration of the quenching pulse be twice that of the jetting pulse.

Furthermore, the amplitude of the quenching pulse should be equivalent to the amplitude of the jetting pulse. MicroFab's ideal bipolar pulse is shown in Figure 34 below.

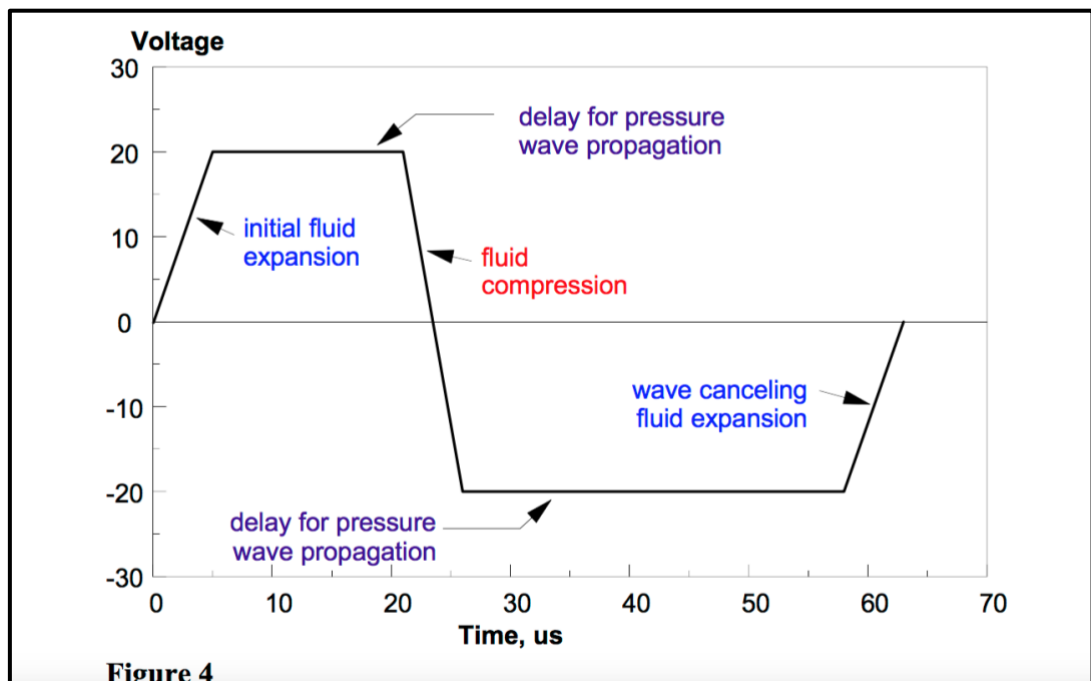


Figure 34 The bipolar double-pulse trapezoidal waveform of the JetLab 4 (Microfab Technologies Inc., 1999).

At this stage, it would have been ideal to have been able to directly compare Morita et al's recommendation with that of MicroFab's technical note, however the JetLab 4 does not have the capacity to generate Morita's suggested dual pulse waveform (Morita et al., 2015). It was therefore decided to compare the output of the optimised unipolar single pulse waveform with the output generated from following the guidance in MicroFab's technical note. The unipolar waveform droplet was created with settings of 6 μ s rise/fall time and 23.5 μ s dwell time, using a dwell voltage of 32 V, whilst the bipolar waveform droplet was generated as per the unipolar droplet, with additional settings of 47 μ s for the echo time (second dwell time) and 6 μ s for the second rise time. Echo amplitude mimicked dwell amplitude at -32 V. The images were captured at a 120 μ s strobe delay after meniscus deformation. The waveforms and associated droplets are shown in Figure 35 below.

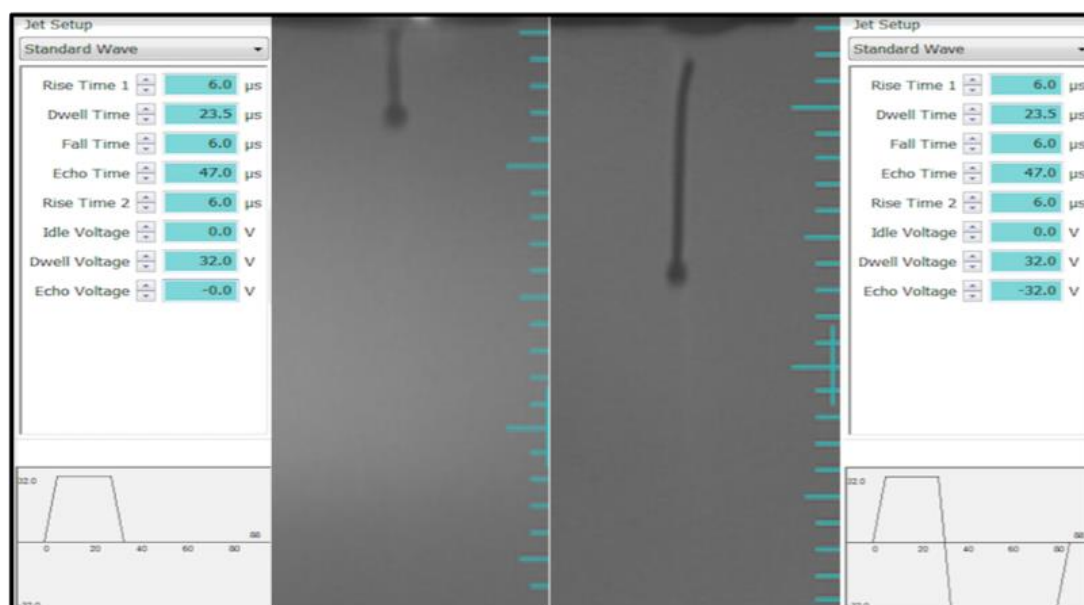


Figure 35 Comparison of the unipolar waveform (6 μ s rise/fall time and 23.5 μ s dwell time, dwell voltage of 32 V), with the bipolar waveform (in accordance with MicroFab's suggested bipolar waveform) having additional settings of 47 μ s for the echo time (second dwell time) and 6 μ s for the second rise time. Echo amplitude mimicked dwell amplitude at -32 V.

It can be observed that there is an increase in velocity and volume, as well as a lengthening of the droplets' ligand. A general observation in previous IJP experiments had been that the greater the length of the droplet tail the greater the probability that a secondary droplet may be formed (and then fail to reattach to the primary droplet) thereby becoming a satellite droplet, which are prone to greater droplet deposition inaccuracy than single droplets. Indeed, following the droplet over the length of its flight path revealed that the droplet soon separated into three separate droplets that failed to re-join.

More importantly, the observation of increased volume and velocity was a contraindication that the application of the quenching pulse had only had the effect of dampening residual oscillations. It was therefore important to ascertain if the ‘quenching pulse’ could in fact generate droplet output, which may have added to droplet volume and velocity.

4.7.1 Negative Unipolar Waveforms contribute to Droplet Volume and Velocity

A negative unipolar single pulse waveform was generated, equivalent to the negative portion (or secondary pulse) of the bipolar waveform that had been used in Figure 68 (previous page), albeit with the Echo voltage increased from -32 V to -64 V. The output is shown in Figure 36 below. It can be observed from Figure 36 that the use of the negative single pulse waveform alone has caused a droplet to be ejected, indicating that the reversed propagation of pressure waves at a higher intensity is also a suitable method for generating droplets. The droplet volume is approximately

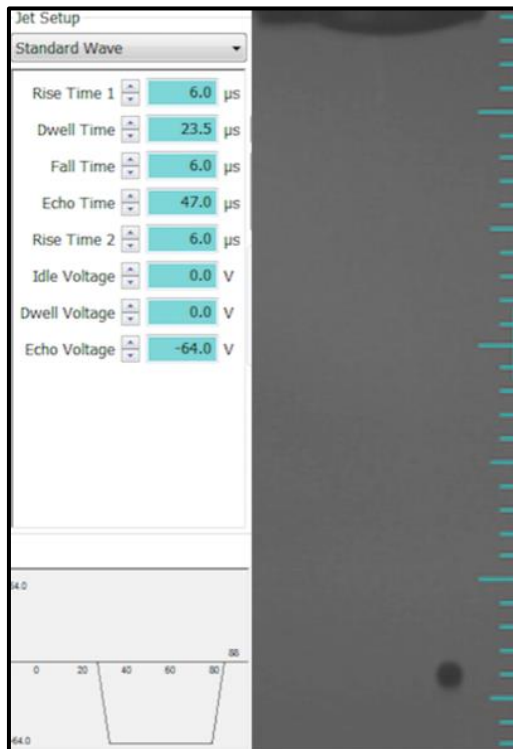


Figure 36 Droplet formation generated by a negative unipolar waveform (replicating the negative portion of the previous bipolar waveform)

135 pL and its velocity is 2.1 m/s. Indeed, the total volume of ink of this droplet may well be comparable to the droplet generated by the bipolar dual-pulse waveform shown in Figure 35, although a direct comparison is difficult to make because of the extended droplet ligand. It is therefore clear that the use of the bipolar dual-pulse waveform generated using the MicroFab' template, had added both volume and velocity to the dispensed droplet rather than simply quenching residual oscillations.

Whilst the application of the ‘quenching’ pulse had created the unexpected opportunity of adding volume and velocity to the droplet, further research was required in order to control the shape of the dispensed droplet in order to avoid the formation of unwanted satellite droplets.

4.7.2 The Effect of Amplitude and Amplitude Split on Bipolar Waveforms.

In order to examine how the bipolar waveform may be used to generate a greater range of ‘useful’ droplets (i.e. free from the formation of satellite droplets), the initial enquiry focused on producing bipolar waveform droplets that were equivalent to the optimised unipolar droplets.

The maximum amplitude of 34 V (consistent with a ‘useful’ droplet) was applied to the optimised unipolar 6 μ s rise time waveform, and the average velocity of the droplet was measured with an 870 μ s strobe delay at 1.92 m/s. Bipolar waveforms were then generated with the total amplitude of positive and negative waveforms split proportionately between each pulse. The amplitude splits used were 75/25 (i.e. 75% of the total amplitude was applied to the dwell voltage and 25% to the echo voltage), 50/50, 25/75 and also 0/100. The amplitudes were then adjusted until the generated droplet achieved the same average velocity as the maximised unipolar droplet.

The results are summarised in Table 14. Figure 37, which follows Table 14, shows the total amplitude required to dispense equal velocity droplets across the varying amplitude splits.

Table 14 Jetting pulse amplitudes – split between ‘dwell’ amplitude (the positive portion of the bipolar waveform) and echo amplitude (the negative portion of the bipolar waveform) required to achieve a constant droplet velocity of 1.92 m/s.

Amplitude Split between Dwell and Echo	Dwell V	Echo V	Total Amplitude	Velocity
100/0	34 V	N/A	34 V	1.92 m/s
75/25	28 V	-9.3 V	37.3 V	1.92 m/s
50/50	21 – 22 V	21 – 22 V	43 V	1.92 m/s
25/75	12 V	-37 V	49 V	1.92 m/s
0/100	N/A	-57 V	57 V	1.92 m/s

Figure 37 shows that the total amplitude that is applied to the waveform must be increased as the split in amplitude toward the echo voltage increases.

Whilst the experiment was being undertaken, it was also observed that small increases in droplet velocity could be achieved as the amplitude split between dwell and echo settings increased, by increasing total pulse amplitude beyond that required to maintain constant velocity, whilst the droplet retained its ‘usefulness’. However, the causal mechanism for this was unclear and the effect on droplet velocity was small so the phenomenon remains a topic for further research

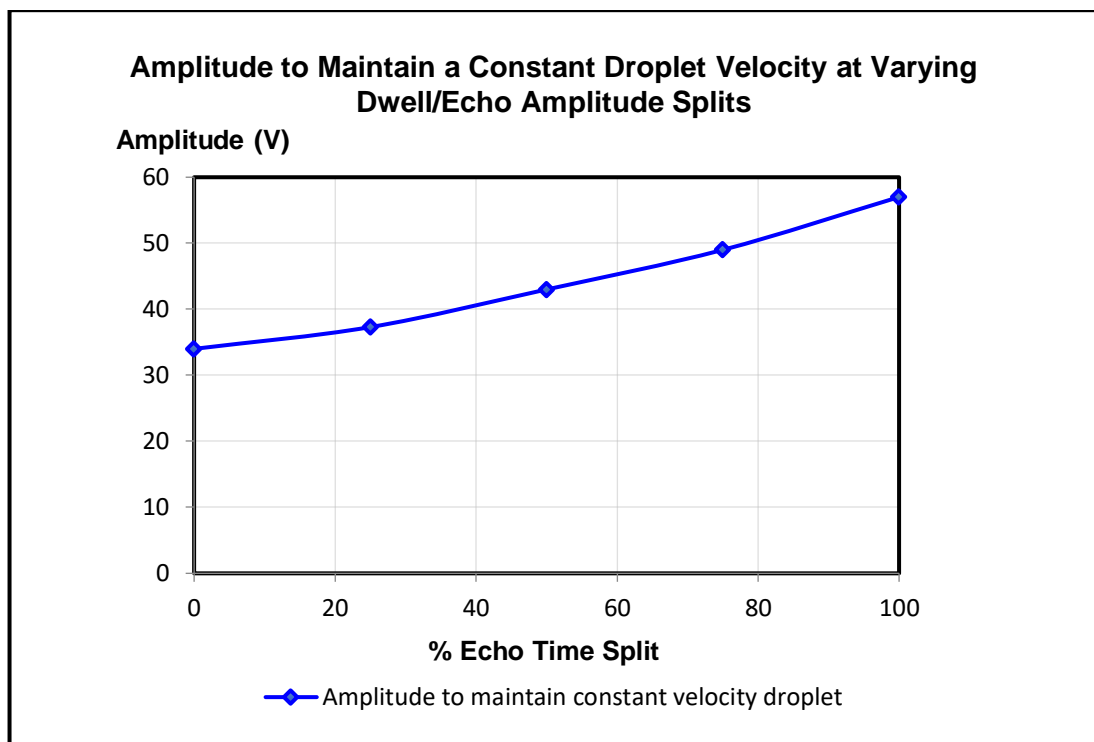


Figure 37 Total jetting pulse amplitudes – combining ‘dwell’ amplitude (the positive portion of the bipolar waveform) and echo amplitude (the negative portion of the bipolar waveform) required to achieve a constant droplet velocity of 1.92 m/s.

4.7.3 Reduction in Echo Duration

The transition from unipolar to bipolar waveform had raised concern over the suitability of MicroFab’s bipolar waveform template for the purposes of this research. It is acknowledged that the purpose of MicroFab’s advice is to quench residual oscillations, while the objective of this research is control over droplet volume, shape and velocity.

In Section 4.4 considerable attention was paid to defining the optimal jetting pulse, and it was noted that droplet ejection should be expected at approximately $\frac{3}{4} T_f$.

MicroFab's long echo time (twice that of the optimised dwell time), which extends the total waveform well beyond the point of droplet ejection is clearly intended to 'quench' residual oscillations, by the delayed application of the final capillary expansion as the capillary's geometry returns to its resting state, which produces a negative pressure wave.

As quenching residual oscillations wasn't a requirement of this research, the echo time was reduced from 47 μs , in increments of 1 μs . No difference in dispensed droplets was observable until the echo time had been reduced to below 14 μs , whereupon droplet ejection became unstable. It should be noted that at 15 μs the duration of the echo period is approximately equivalent to $\frac{1}{4} T_f$, and therefore means that the application of the final capillary expansion (and associated pressure wave) was in good agreement with the theoretical droplet ejection time.

4.7.4 Discussion

Microfab's suggested bipolar waveform was found to increase droplet velocity and volume. The results showed that a negative unipolar waveform can itself actuate a droplet (although the pressure waves will propagate in reverse). It is therefore thought that the use of a bipolar waveform means that there is a timely application of a higher intensity 'squeeze' just prior to droplet ejection. The effect of amplitude split between the negative and positive portions of the bipolar waveform tended to confirm this hypothesis, showing that whilst the positive portion of the bipolar waveform was the main contributor to pressure wave intensity, the negative portion provided additional impetus to droplet velocity.

The fact that the echo dwell time can be reduced to a time that coincides with droplet ejection further compliments this theory. This aforementioned reduction in echo dwell time also indicates that the 'quenching' part of the bipolar pulse is not a cancellation of residual oscillations but actually an extended period to allow oscillations to dissipate. In practise, pulse amplitude can be increased, then split between the positive and negative sections of the bipolar waveform to produce a higher velocity and volume droplet whilst maintaining better control over the shape of the droplet.

Although untested, Morita et al's recommendation of a brief period of idle time equivalent to that of the jetting pulse time, before the second 'quenching pulse' is applied appears to be more consistent with the concept of actually quenching residual oscillations rather than simply allowing additional time for their dissipation.

4.8 Summary

A detailed investigation was undertaken into the principles underpinning droplet actuation in order to exercise an enhanced degree of control over the ejected droplets. The research surpassed the stated objective of optimising actuation parameters by redefining and adding to fundamental IJP theory.

Of particular note was the finding that while Morita et al's theory relating the optimal jetting pulse period to the fundamental resonance period is correct, it is not accurately represented by Morita et al's equation. It was found that inclusion of fall time in the equation is unwarranted and that two additional components to the jetting pulse are required, a, to represent the delay between waveform activation and propagation and b, to compensate for the fact that there are two reflections of the pressure wave (not one) within what had otherwise been considered as the fundamental acoustic period. The proposed revisions to the equation have wide ranging practical implications for IJP research and development.

Rise times have been shown to be an important waveform parameter and that present approaches to the matter are inappropriate. Rise times should be considered as a function of pulse amplitude, not as a function of the duration of the fundamental resonance period. Unnecessarily brief rise times may lead to increased perturbations in the inflow of ink into the printhead. Most importantly, the results gave a clear and novel indication that the rate at which voltage is applied to the printhead is an additional driver of droplet velocity to that of pulse amplitude.

Backpressure was shown to have a direct effect on the amplitude parameter of the waveform, although it is not considered to be an explicit waveform parameter. Without proper control of backpressure, the day to day replication of results for IJP researchers will continue to be problematic.

It was found that there are three methods by which droplets of varying volume can be generated while maintaining control over droplet velocity and shape. Standard unipolar waveforms can be used with an optimised jetting pulse period and rise times adjusted in accordance with jetting pulse amplitude. Bipolar waveforms can be used with the positive waveform optimised at the jetting pulse period and the negative waveform set to coincide with droplet ejection. Finally, the novel use of extended dwell times meant that a 6.7 fold range of droplet volumes may be produced from a single printhead. Applying these methods across the range of readily available printhead aperture sizes will enable the fabrication of a wide range of sacrificial microvascular facsimile diameters.

Chapter 5 The Control of Droplet Deposition and the Fabrication of 3D Sacrificial Microvascular Facsimiles

5.1 Introduction

The purpose of this chapter is to investigate the principles underpinning the control of droplet deposition and then apply the combined principles of actuation (Chp. 4) and deposition to the fabrication of sacrificial microvascular facsimiles. A summary of the experiments undertaken in this chapter is set out in Table 15 overleaf. The first group of experiments, 'Control of Droplet Deposition' consider important droplet deposition parameters in order to optimise the consistency of the microstructures that are fabricated. The limitations of that control are noted due to performance constraints of the Microfab 4 setup and further discussion of those constraints takes place in the Chapter 6.

The second set of experiments are designed to test 3D IJP with phase change ink as a suitable additive manufacturing method for the fabrication of sacrificial microvascular facsimiles. The process must be able to fabricate the components and features of a vascular network (columns with lumen-like dimensions i.e. 50 micron to 0.5 mm, bifurcations and capillary arches) but must also be able to fabricate them at a density that is similar to that of the human body. Additionally, for these microstructures to fulfil their purpose i.e. be coated with a biocompatible material before being sacrificed, they must be freestanding with an 'aspect ratio' (ratio of a structure's height to its diameter) similar to that of microvascular networks, and further, the overhanging structures must be able to be fabricated without the use of support materials.

The dynamic viscosity of Paraffin wax was tested. The wax was heated to approximately 70°C and allowed to cool to room temperature. As the Paraffin wax cooled, viscosity and temperature were measured and recorded at 5-second intervals (as per the method set out in Section 3.4.3). At 65°C viscosity was measured at 4.43 mPa.s. At 60°C, approximately 5°C above the melting point, viscosity was measured at 5 mPa.s. Z was calculated using the viscosity at 60°C and was found to be 7.34, which being in agreement with $1 < Z < 14$ (Derby, 2011; Jang et al., 2009) indicated that the ink should be printable. In Section 2.2.5 (dealing with the measurement of actual reservoir and printhead temperatures) it had been seen that there was a variance of approximately 5°C between reservoir temperature and printhead temperature. Taking this variance into account, the reservoir temperature was set at 70°C, in order to ensure that a temperature of at least 60°C would be generated at the external tip of the reservoir (the point of meniscus formation and droplet ejection).

Table 15 The sequence of experiments and objectives for Chapter 5.

Experiment/Activity	Objective
Control of Droplet Deposition	
Frequency of Droplet Deposition	Explore the relationship between the degree of undercooling and the frequency of droplet deposition consistent with the fabrication of a constant solidified column
Offsets and Deposition Frequency Consistent with Accurate Droplet Deposition	Explore the relationship between the offset between printhead and microstructure, and the droplet deposition frequency consistent with accurate droplet deposition
Fabrication of Microvascular Facsimiles	
Multi-Droplet Layered Columns for Higher Diameter Lumen-like Column Diameter Dimensions	Demonstrate the fabrication of columns with higher diameter lumen dimensions (from 50 micron to a theoretical target of 0.5 mm).
Fabrication of Biomimetic Bifurcating Capillary Structures	Fabricate bifurcating structures incorporating a reduction in 'lumen' dimensions from the single parent incoming arteriole to the dual daughter outgoing capillaries <u>in agreement with 'Murray's law'</u> .
Fabrication of Bifurcating Arches	Join two bifurcating structures by fabricating connecting arches - <u>without support materials</u> - to assemble a complete microvascular facsimile.
Column Spacing	Establish a definitive minimum achievable spacing between column centres and the perimeters of two columns
Column Height	Fabricate freestanding structures with a minimum 100 : 1 aspect ratio

This series of fabrication experiments were performed on the bespoke IJP setup (Section 2.2.2) with 40, 60 and 80 micron diameter aperture, MJ-A 'drop on demand' printheads.

5.2 Frequency of Droplet Deposition

A healthy vascular system exhibits fairly constant lumen diameters at each level of the vascular hierarchy. Over many of the early experiments it had been noted that ‘droplet deposition frequency’ appeared to be one of the many parameters that influenced the consistency of the spread of deposited droplets and thus the formation of column-like sacrificial microstructures that would serve as acceptable microvascular facsimiles.

Using a 60 micron aperture diameter printhead droplet deposition frequencies of 1, 2, 4, 8, 16, 32 and 64 Hz were applied to 30 droplet columns, which were located at 1 mm spacings between column centres (shown in Figure 38 below). As formation of consistent columns could be seen to deteriorate between 8 Hz and 16 Hz, the range of droplet deposition frequencies of 9 to 15 Hz (increasing in 1 Hz increments) were then applied, as shown in Figure 39 overleaf. The experiment was then repeated using a 40 micron aperture diameter printhead (Figure 40 also overleaf). The unipolar single pulse waveform for the jetting period of both printheads were optimised in the manner set out in Section 4.4

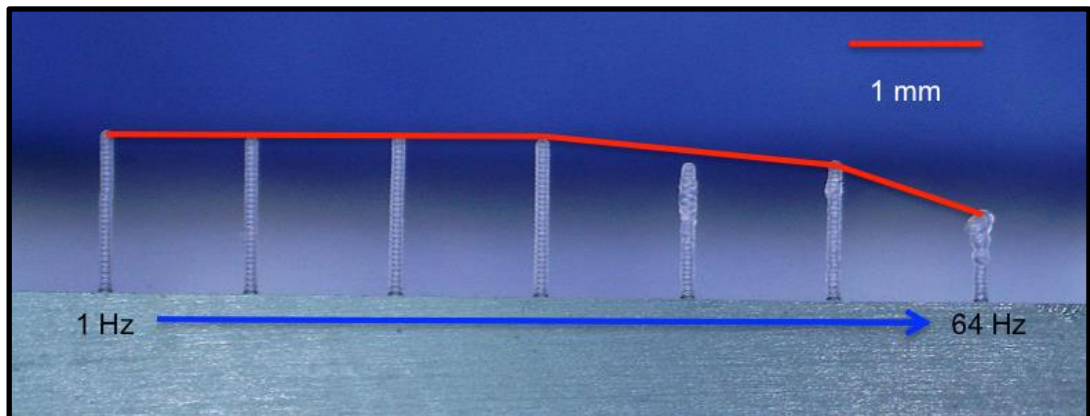


Figure 38; 7 30-droplet columns, fabricated at 1, 2, 4, 8, 16, 32 and 64 Hz, at an offset between printhead and substrate of 5 mm.

It can be seen from Figure 38 above, that droplet deposition frequencies of 1, 2, 4 and 8 Hz lead to the formation of columns with consistent diameters, which indicates that there is sufficient time before the arrival of an ejected droplet, for the phase change of the previously deposited droplet to be completed. However, as droplet deposition frequency increases beyond 8 Hz, the consistency of column formation decreases, until at 64 Hz the appearance of the bulbous column head clearly signifies that there was insufficient time between the deposition of droplets for the phase change of the previously deposited droplet to be completed.

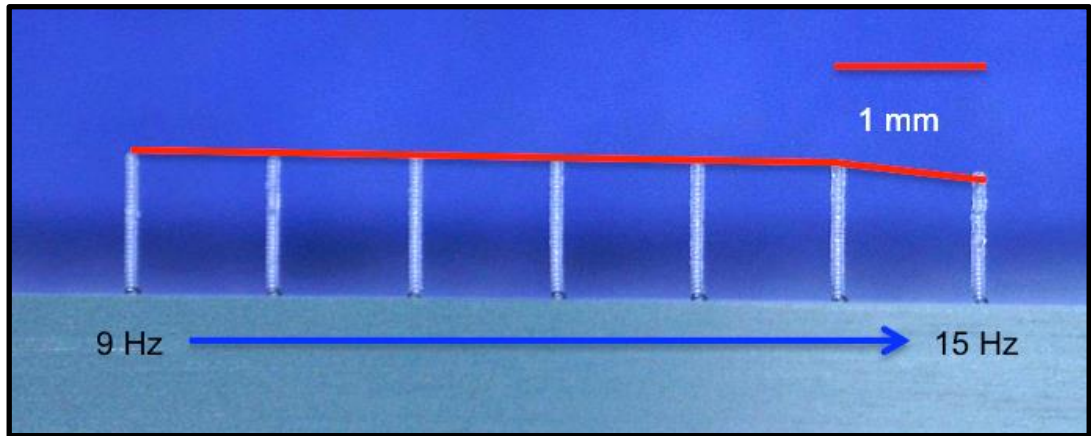


Figure 39; 7 30-droplet columns, fabricated at 9, 10, 11, 12, 13, 14 and 15 Hz, at an offset between printhead and substrate of 5 mm, using a 60 μm printhead.

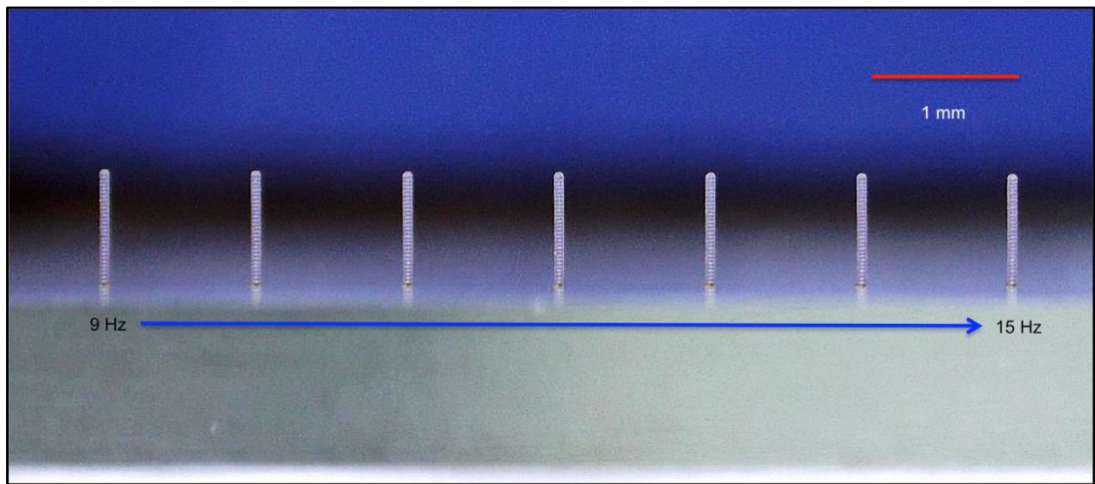


Figure 40; 7 30-droplet columns, fabricated at 9, 10, 11, 12, 13, 14 and 15 Hz, at an offset between printhead and substrate of 5 mm, using a 40 μm printhead

From Figure 39 above, consistent formation of columns can be observed up to and including a droplet deposition frequency of 13 Hz. The columns printed with droplet deposition frequencies of 12, 13 and 14 Hz are shown more clearly in Figure 41 below.

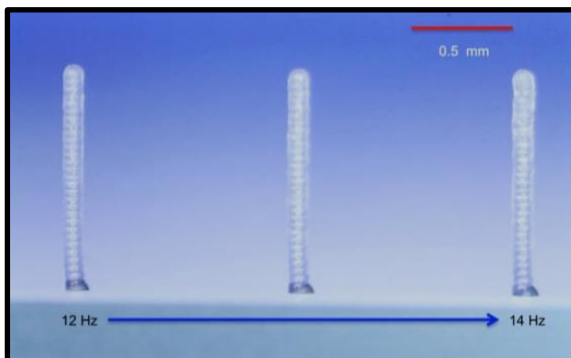


Figure 41 Inset of the 12, 13 and 14 Hz columns fabricated in Figure 39

It can be seen that there are marginal decreases in the height and consistency of overall form of the fabricated columns as droplet deposition frequency progresses from 12 to 14 Hz; therefore 12 Hz was selected as a guide to the optimal droplet deposition frequency for future fabrication.

Looking more closely at the individual columns in Figure 41 (previous page), it can be seen that the diameter and height of the deposited droplet varies from the base of the column to the tip. Gao and Sonin state that the deposited droplet arrives at the target zone largely in its superheated state i.e. there is negligible heat lost from the molten wax droplet during the time of its flightpath. The subsequent cooling can then be broken down into three categories

The loss of superheat - the heat above the melting point of the wax

The loss of the latent heat of fusion - the heat associated with the phase change of the wax from liquid to solid, and

The remaining time it then takes for the solidified wax droplet to cool down to the ambient temperature of the IJP cabinet.

Of these three categories, Gao and Sonin state that the total cooldown time is dominated by the time taken for the latent heat of fusion to be removed. More specifically, the cooldown time is governed by heat transfer to the contact area of the droplet, with a negligible amount of heat being transferred to the surrounding air. Consequently, for consistent column formation to be achieved, the cooldown time for all droplets must be sufficient to allow the droplet to spread to its thermal equilibrium (where capillary-driven creep is balanced by the surface tension of the droplet) prior to solidification.

From examination of the lower regions of the columns shown in Figure 41 on the previous page, it can be seen that the aforementioned condition has not been met. The likely explanation is that the heat of latent fusion is conducted away more swiftly for the droplets nearer the highly conductive substrate (glass slide on a steel plate) and are unable to spread to their thermal equilibrium. In contrast, the condition is met for droplets deposited further up the column, where the substrate is effectively the less conductive previously deposited droplet, which is still in the process of transmitting its remaining heat (cooling to ambient temperature) via the less conductive solidified wax column below, thus allowing the deposited droplet to spread to its thermal equilibrium.

It can be seen from Figure 40, that consistent column formation is being achieved across all frequencies with the lower diameter aperture printhead. When Figure 40 is compared to Figure 39, it is clear that higher droplet deposition frequencies may be obtainable with smaller volume droplets. The observation, that faster droplet deposition frequencies may be obtainable with smaller volume droplets, is consistent with the reduction in the thermal mass of the droplet.

There are four main conclusions demonstrated by the experiments on droplet deposition frequency.

1. There is an upper boundary on droplet deposition frequency. There must be a sufficient 'wait' period between the deposition of one droplet and the arrival of the next droplet to allow phase change to occur. Naturally the wait period between droplet deposition can be minimised by increasing the degree of undercooling that is being applied.
2. However, there is also an upper boundary on the degree of under cooling that can be applied to a droplet, or the droplet will fail to spread to its thermal equilibrium.
3. A consistent degree of undercooling needs to be applied to the microstructure over the course of its fabrication, however excessive conductivity between the first deposited droplet and the substrate acts like an increase in the degree of undercooling and may prevent the spread of the droplet to its thermal equilibrium.
4. If the thermal mass (volume) of the droplets change, then the degree of undercooling applied, and the deposition frequency must be altered to align with the change in thermal mass.

Although the first two conclusions concur with those of Gao and Sonin, the implication of those combined conclusions is not noted by Gao and Sonin i.e. there is a fundamental limitation to the ultimate productivity per printhead for a given ink. Droplet deposition frequency cannot be ever increased simply by increasing the rate of undercooling applied to the deposited droplet. This constraint on the viability of 3D IJP for the fabrication of sacrificial microvascular facsimiles is examined further in the following chapter.

5.3 Offsets and Frequencies Consistent with Accurate Droplet Deposition

A fixed offset between printhead and substrate is used during fabrication due to the discontinuous nature of z-axis printhead motion. Additionally, the thermal effect of the heated printhead on the fabricated microstructures means that a clearance between printhead and microstructure was needed. Early experiments indicated that increased clearances between printhead and the fabricated microstructure led to increasing droplet deposition inaccuracy. As it was clear that discontinuous Z axis motion was creating a trade-off between the thermal effects of the printhead (reduced deposition frequency due to decreased undercooling) and the accuracy of droplet deposition, the mechanism underpinning that trade-off required further consideration.

Two alternative causes are appraised in the following subsections. The first hypothesis is that with low frequency droplet deposition the time between ejected droplets is relatively lengthy so that each droplet will be exposed to turbulent forces from differing angles. The second is that increasing offsets resulted in large proportional increases in the flight-time of the droplet from the printhead to the substrate, this in turn means that the droplet will be exposed to turbulent forces for an increased time period.

5.3.1 The Effect of Droplet Deposition Frequency on Consistent Column Formation.

A script was written for the fabrication of seven 10-droplet columns, spaced at 1 mm intervals, at droplet deposition frequencies of 1, 2, 4, 8, 16, 32 and 64 Hz. This atypical column height was used, so that the deposited droplets would benefit from the enhanced degree of undercooling that occurs near the substrate where a high degree of thermal conductivity from the deposited droplet to the substrate is maintained. This enabled faster droplet deposition frequencies than those that would usually be used for typical columns to be tested. The offset between printhead and substrate was set at 5 mm. The results are shown in Figure 42 overleaf.

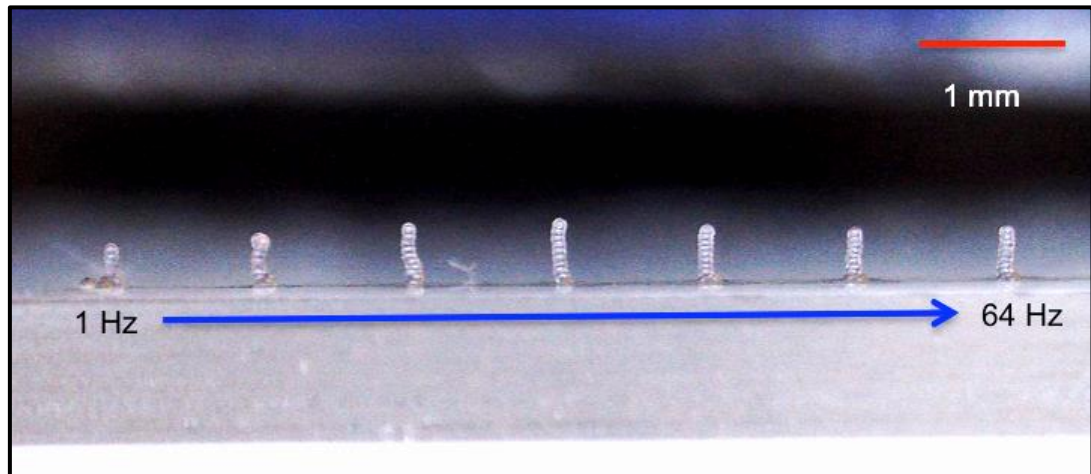


Figure 42; 7 10-droplet columns, fabricated at 1, 2, 4, 8, 16, 32 and 64 Hz, at an offset between printhead and substrate of 5 mm showing the effect of micro turbulence (created by adjacent Peltier cooling module)

It can be clearly observed from Figure 42 above, that the use of increasing frequencies of droplet deposition leads to increasingly consistent column formation. The 10-droplet column deposited at a frequency of 1 Hz, of course took 10 s, whereas the column fabricated at a rate of 64 Hz took 0.156 s to be completed.

During the 10 s fabrication period, there is a high probability that micro turbulence would have led to each individual droplet being subject to the turbulent force from a differing angle as compared to the angles that the other droplets were subject to.

Naturally, during the 0.0156 s taken to fabricate the column at a frequency of 64 Hz, the aforementioned probability is greatly diminished. Indeed, it can be assumed from the consistency of that column that all the deposited droplets were subject to a similar magnitude and direction of force from the micro turbulence. This also tends to confirm the hypothesis that the droplets are being exposed to turbulent forces from differing angles for increased period of times.

5.3.2 The Effect of Offset Distances on Consistent Column Formation

In order to examine the effect of increased offset distances on the consistency of column formation, a script was written to fabricate seven 50 droplet columns at a droplet deposition frequency of 12 Hz, with 1 mm spacings between column' centres, at an initial offset between substrate and printhead of 5 mm, graduating to 11 mm in 1 mm increments. The results are then shown in Figure 43, which follows.

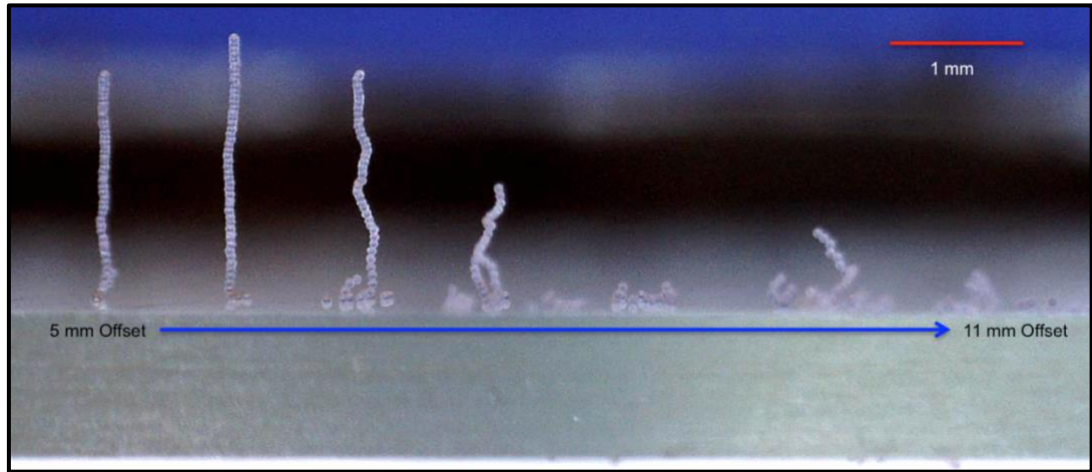


Figure 43; 7 50-droplet columns, fabricated at 12 Hz, at a range of offsets between printhead and substrate from 5 mm to 11 mm – increasing in 1 mm increments - showing the effect of micro turbulence (created by the adjacent Peltier cooling module)

It can be clearly observed from Figure 43 above, that the use of increasing offsets leads to increasingly inconsistent column formation, which also tends to confirm that the droplets are being exposed to turbulent forces from differing angles for increased period of times.

Table 16 (below) calculates the theoretical flight time of droplets at the varying offsets used in the experiment (assuming a droplet velocity of 2 m/s).

Table 16 Calculation of flight time at the offsets shown in Figure 43 above

Offset (mm)	5	6	7	8	9	10	11
Flight time ($\times 10^{-3}$ s)	2.5	3	3.5	4	4.5	5	5.5

It can be seen that the longest flight time, producing the most discontinuous column (at the 11 mm offset) is 0.0055 s. This is a significantly shorter duration than the 0.156 s taken to fabricate the most continuous 10 droplet column at a droplet deposition frequency of 64 Hz (shown in Figure 42).

This being the case, it cannot be true that the reason for discontinuous column formation is that the droplet is being exposed to turbulent forces for an increased period of time.

However, once it is considered that the droplet deposition frequency of 12 Hz gives a 0.083 s delay between each individual droplet' deposition, and furthermore, that the fabrication of a 50 droplet column at that frequency will take 4.2 s, the mechanisms underpinning the increasing inconsistency of column formation are clearer.

Increased delay between the deposition of droplets means that although each droplet is subject to a force of similar magnitude from the micro turbulence, there is an increased probability that each droplet will experience that force from a different direction. Therefore, the initial observation that ‘inaccuracy increases as offsets increase’ derives not from increased turbulence over the increased length of an individual droplets flight, but from the fact that the increased length of the droplet’s trajectory means that the small changes in the angle of droplet trajectory manifest themselves as greater inaccuracies on contact with the substrate.

This conclusion implies that there is less need to focus on offset distances as the driving force behind the inaccuracy of droplet deposition, and conversely a greater need to minimise the fabrication time of microstructures by increasing droplet deposition frequency and also eliminating sources of turbulence, where possible. These implications are borne out by the results of the column height experiment conducted in Section 5.8.

5.4 'Multi-Droplet' Layered Columns for Higher Diameter Lumen-like Column Diameter Dimensions

The reproduction of lumen-like features with dimensions ranging from 50 micron to 0.5 mm was identified as a key objective in Chapter 1 in order to replicate the 'useful' 'arteriole – capillary – veinule' configuration of the microvascular system. The capability for production of a wide range of droplet volumes had been demonstrated from a 60 micron printhead in Section 4.6. Although droplet volumes from 62 pL to 416 pL had been generated, the range of droplet diameters was limited to between 49 μm and 93 μm (the larger volume droplets froze into thicker discs). A novel technique - beyond that of actuating a super-size droplet - was therefore needed if an attempt to generate a 0.5 mm diameter frozen droplet was to be undertaken.

As previously stated, a droplet's eventual diameter at thermal equilibrium is constrained by the balance between capillary-driven creep and the surface tension of the droplet. If large diameter frozen droplets were to be fabricated this constraint would have to be overcome. It has also been noted that the initial inertial forces of the droplet contacting the substrate are quickly dissipated by the viscous forces of the ink and add little force to the spread of the droplet.

However, it was thought that, if, during the period between first droplet contact with the substrate and that droplet's spread to its thermal equilibrium, additional inertial force, thermal mass and volume could be added to the spread of that droplet by the deposition of a second droplet, then the combined effects of additional inertial forces and delayed phase change may extend the droplet's spread beyond that of the typical thermal equilibrium for a droplet.

Put simply, a number of small droplets deposited on the substrate in quick succession (i.e. in a 'burst') then followed by a longer wait period before the delivery of the next 'burst' might create a single frozen droplet of wider diameter, rather than simply fabricating inconsistent columns.

Before this hypothesis could be tested, two questions needed to be addressed:

- What frequency of droplet deposition should be used for the 'burst' of droplets?
- What 'wait' time should be applied between the deposition of one layer (i.e. a 'burst' of droplets) and the deposition of the next layer?

The first question was answered using a quick 'finger in the wind' experiment. The largest aperture diameter printhead available in the lab was selected (80 micron) in

order to gauge the magnitude of diameter increase that this novel technique might generate. A 'wait' time of 5 s between droplet bursts was applied, so that phase change would be certain to be completed before the deposition of the next burst of droplets. A burst size of 4 droplets was defined in the script and 'burst' frequencies ranging from 32 Hz to 1024 Hz for 6 columns (so, doubling up from 32 Hz, 6 times) were set. It was found that burst frequencies of 128 Hz, 256 Hz and 512 Hz all led to the fabrication of consistent columns.

512 Hz was chosen as an appropriate rate of droplet deposition for the 4 droplet bursts, and the specification of wait time between bursts of droplets was then tested as shown in Figure 44 below. Wait times of 0.001 s, 0.01 s, 0.02 s, 0.025 s, 0.033 s, 0.05 s, 0.1 s, 1 s and 5 s were selected for the columns.

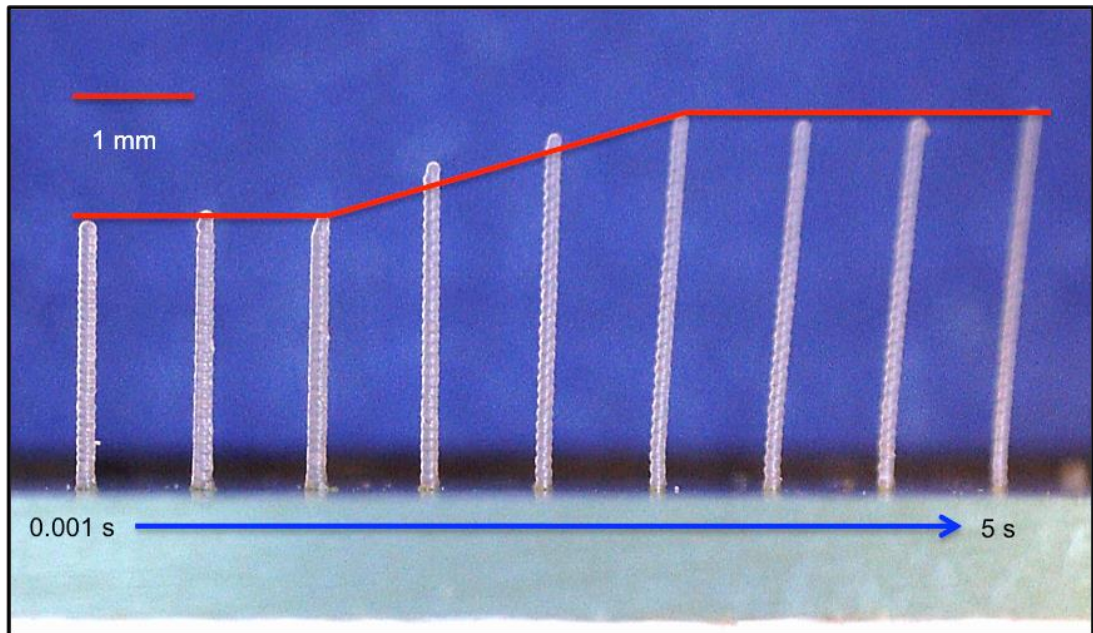


Figure 44; 9 30-layer columns, each layer consisting of four droplets deposited in a 'burst' at 512 Hz, with a delay between the deposition of each layer ranging from 0.001 s to 5 s (0.001 s, 0.01 s, 0.02 s, 0.025 s, 0.033 s, 0.05 s, 0.1 s, 1 s and 5s). Offset between substrate and printhead of 7.5 mm. Print head 80 micron.

The average measured diameters of the three consistent columns (i.e. wait times of 0.001 s, 0.01 s and 0.02 s) was approximately 140 micron, which represented a significant increase in column diameter as compared to previous research in this thesis.

Figure 44 also shows an interesting and unexpected result. It had been thought that the column with a wait time of 0.001 s would exhibit a bulbous column head (as first seen in Figure 38, for instance), since a wait time of 0.001 s is equivalent to a droplet deposition frequency of 1000 Hz, which is considerably greater than the optimal

droplet deposition frequency discussed in Section 5.2 of 12 Hz. Theoretically, in this case, phase change couldn't have had time to occur, so the fact that the use of that particular wait time had led to the fabrication of the most consistent and widest diameter column was atypical. Furthermore, there is little difference between that column and the two that follow (0.01 s and 0.02 s). Once again, a bulbous column head was expected since these wait times are effectively equivalent to droplet deposition frequencies of 100 Hz and 50 Hz respectively. In the period between this experiment and the next, the analysis that informs the discussion of wait times and 'trigger start' command delays was undertaken, which revealed that there were real-time delays in actioning 'wait' commands (further discussion Section 6.2.2). This meant that the minimum actual wait time for the aforementioned columns was in fact 0.25 s, which clearly explained the absence of the expected bulbous column head.

In the second experiment a printhead of 40 micron diameter aperture was selected in order to allow comparison with Figure 40. The number of droplets in each burst of droplets was reduced from four to three (so that further experiments could be conducted comparing multiples of droplets in each burst e.g. 3, 6, 9, etc.). The resultant columns are shown in Figure 45 below. The range of wait times used was restricted to zero seconds, (just using the delay of approximately 0.25 s, which is automatically induced by the use of the 'trigger start' command), then scripting wait times of 0.25 s, 0.5 s and 0.75 s, giving a range of effective total wait times of 0.25 s, 0.5 s, 0.75 s and 1 s.

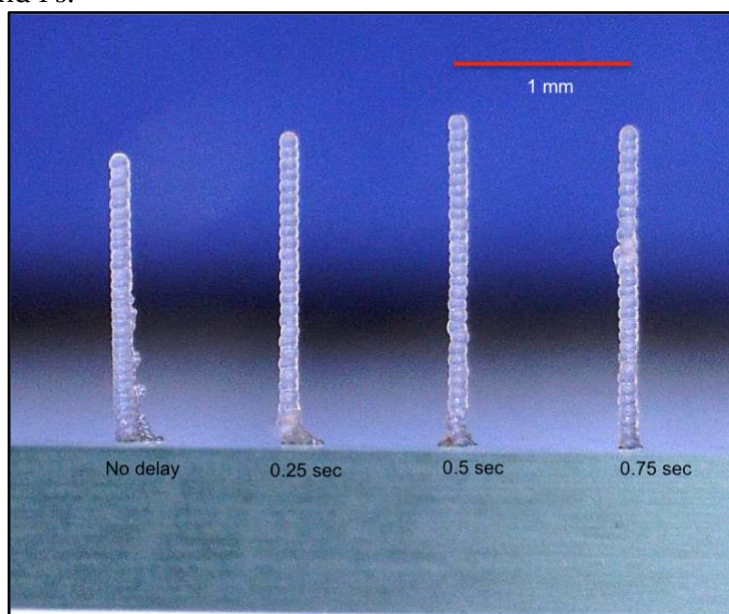


Figure 45 Four 30-layer columns, each layer consisting of three droplets deposited in a 'burst' at 512 Hz, with a delay between the deposition of each layer ranging from 0 s to 0.75 s. Offset between substrate and printhead of 7.5 mm

The columns exhibited in Figure 45, are somewhat as anticipated. The widest diameter column has been printed with an effective wait time of 0.25 s and has a diameter of approximately 120 micron. It can then be seen that the column heights increase as the delay between the deposition of layers of droplets increases. The final column (with the 0.75 s wait time) appears shorter than the column to its left, however, there seems to have been some perturbation in droplet deposition during the fabrication of the column, which would explain the reduction in height.

The experiment was repeated with a 6 droplet burst, producing similar results and larger diameter columns. The experiment was then repeated with a 9 droplet burst, at which point it was found that columns exhibited a ‘stacked snowball’ effect (apparent in Figure 46 overleaf). It appeared that phase change had begun taking place in the first deposited droplets before the final droplets in the burst had been deposited. Three parameters were tested in quick succession in an attempt to rectify the inconsistent column formation. In the first instance the delay between layers was reduced as shown in Table 17 below in order to explore the lower droplet deposition frequencies in more detail.

Table 17 Calculation of Effective Wait Time between Burst Deposition

Delay between Deposition of Bursts				
Programmed Delay	0	0.1	0.2	0.3
Trigger Start Delay	0.25	0.25	0.25	0.25
Effective Wait Time	0.25	0.35	0.45	0.55

The next alteration was to increase the frequency of droplet deposition within each layer from 512 Hz to 1024 Hz, (effectively decreasing the time taken to deposit a burst of droplets by 50%) in order to slow the relative spread of phase change through the burst of droplets

The final change was to increase the substrate temperature from room temperature to 30° C in order to reduce the thermal gradient between the substrate and printhead.

The individual parameter alterations failed to produce a discernible improvement in the consistency of column fabrication, suggesting that there was an upper limit to the number of droplets that could be used in a burst. It was therefore decided to alter all three parameters at once and the results are shown in Figure 46 overleaf.

It can be seen that the stacked snowball effect is still apparent at the base of each column, however, it can also be seen that as the fabrication transitions from the substrate's zone of thermal influence into the intermediate thermal zone that the 'stacked snowball' effect dissipates and the 'frozen discs' (readily apparent in the left-most column for example) that are associated with consistent column formation reappear.

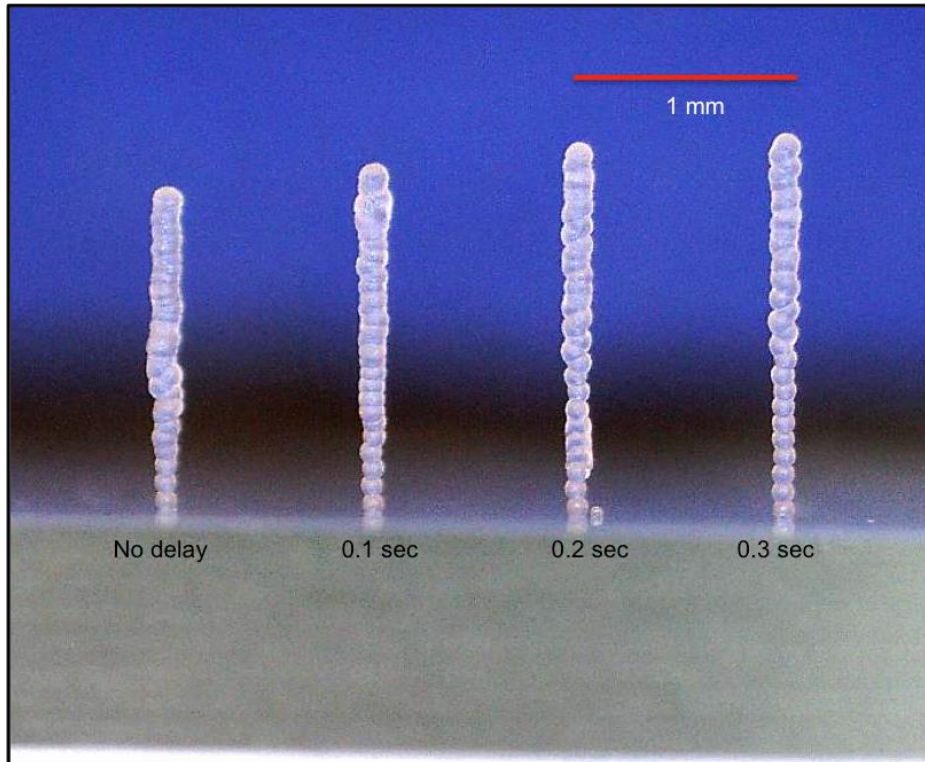


Figure 46; 4 30-layer columns, each layer consisting of nine droplets deposited in a 'burst' at 1024 Hz, with a delay between the deposition of each layer ranging from 0 s to 0.3 s. The substrate temperature set at 30° C with an offset between substrate and printhead of 7.5 mm.

Furthermore, it appears that the transition (from 'stacked snowballs' to 'frozen discs') in the columns fabricated with 'no delay' and a 0.1 s delay between the bursts of droplets. Although the experiment could be deemed to be inconclusive, since adequately consistent column fabrication has not been attained, the results indicated that if sufficient control/manipulation could be exerted over the parameters noted in the introduction to this experiment, then the deposition of larger multiples of droplets might be feasible.

As a final test of parameter manipulation for the 'multi-droplet' layered columns fabrication method it was decided to alter the waveform to generate droplets with increased volume by using the dual pulse bipolar waveform with an extended dwell time, which ejected a 75 micron diameter droplet. This was undertaken in order to

test the importance of the additional thermal mass added by subsequent droplets (leading to delayed phase change) on column formation. The results can be seen in Figure 47 below.

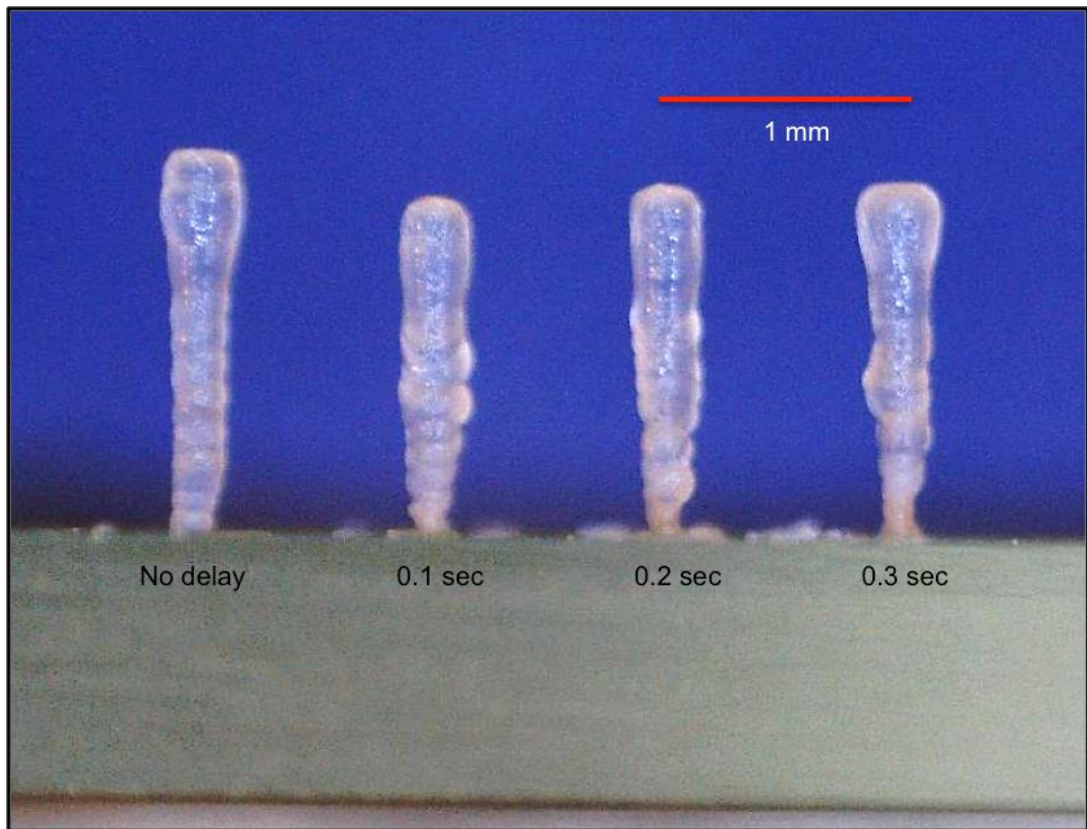


Figure 47; 4 30-layer columns, each layer consisting of nine droplets (increased droplet diameter of $75\ \mu\text{m}$) deposited in a 'burst' at $1024\ \text{Hz}$, with a delay between the deposition of each layer ranging from $0\ \text{s}$ to $0.3\ \text{s}$. The substrate temperature was set at $30^\circ\ \text{C}$ with an offset between substrate and printhead of $7.5\ \text{mm}$.

Naturally, the increase in droplet diameter, from $50\ \mu\text{m}$ to $75\ \mu\text{m}$, led to the fabrication of columns with increased diameters. However, although the increase in diameter is 50% , the increase in droplet volume from $65\ \text{pL}$ to $220\ \text{pL}$ is 337.5% , which represented a significant increase in the thermal mass present in each layer of deposited droplets.

In contrast with Figure 46, it can be seen that the 'stacked snowball' effect is now only visible at the boundary of the substrate level before the transition to 'frozen discs' is immediately visible, although that transition occurs at a later stage in the fabrication of columns with longer delays between the deposition of bursts of droplets. Furthermore, as the fabrication of each column progresses a new phenomenon appears, which is reminiscent of the columns fabricated by Gao and

Sonin (Section 2.3.3.3) and that is the transition from ‘frozen discs’ to a ‘blended interface’ between each layer or burst of droplets.

The fact that this new phenomenon is not visible in Figure 46, but is visible in Figure 47, where the only variable to be altered is the thermal mass of the droplet, indicates that the thermal mass of the droplet (and the rate of its application) is a key determinant in the formation of the blended interface between the multi-droplet layers. Existence of other determinants, such as the temperature of the previously deposited layer of droplets (now the new substrate layer), and the (related) thermal gradient between substrate and printhead, is also clear and these effects are visible over the course of the fabrication of the columns.

It is also interesting to note that there are small zones of consistent column formation visible on the columns with 0.1 and 0.2 s of delay between the deposition of each layer of droplets (actual effective delay 0.35 and 0.45 s, if the time of the trigger start delay is allowed for). The diameter of these zones of consistent column formation is approximately 320 micron. These zones of consistent column formation within a ‘blended interface’ column, might be replicated and extended over a range of combinations of droplet numbers and volumes, if precise control could be exerted over:

- The actual effective delay between the deposition of each layer of droplets
- The continuity of printhead movement on the z axis
- The thermal gradients between ‘the substrate and microstructure’ and ‘the substrate and printhead’

Table 18 summarises the diameters of the columns fabricated over the course of this section.

Table 18 Column diameters fabricated using a 40 micron aperture’ diameter printhead using waveform control of droplet volume and ‘multi-droplet’ fabrication techniques.

Output from the 40 µm Printhead	Number of Droplets	Droplet Diameter	Column Diameter
Figure 40	1	50 µm	60 µm
Figure 45	3	50 µm	120 µm
Figure 46	9	50 µm	155 µm
Figure 47	9	75 µm	320 µm

From Table 18 (previous page), it can be seen that column diameters of 60 to 320 micron have been produced using a single 40 micron diameter aperture printhead. It is therefore reasonable to assume that the range of column diameters could be further extended, by combinations of:

- The use of printhead diameter aperture ranging from 20 – 100 micron
- Manipulation of the waveform to produce an extensive range of droplet volumes
- Varying the number of droplets used within a burst of droplets for the ‘multi-droplet’ layered column fabrication

In the preamble to this section, dimensions of the ‘useful’ ‘arteriole – capillary – veinule’ configuration of the microvascular system ‘ranging from 50 micron to 0.5 mm were identified as key objectives. The range of column diameters fabricated above (60 to 320 micron) from a single 40 micron printhead indicate that this important objective could clearly be achieved by a combination of printhead selection, waveform manipulation, improvements to the apparatus and the use of the novel multi-droplet deposition technique advanced in this section.

5.5 Fabrication of Biomimetic Bifurcating Capillary Structures

Diameter 'Daughter' Capillaries (µm)	Diameter 'Parent' Arteriole (µm)
10	12.6
12.6	15.8
15.8	20.0
20.0	25.2
25.2	30.2
30.2	40.0
40.0	50.4
50.4	63.5
63.5	80.0
80.0	100.8
100.8	127.0
127.0	160.0
160.0	201.6
201.6	254.0
254.0	320.0
320.0	403.2
403.2	508.0
508.0	640.0
640.0	806.3
806.3	1015.9

An essential feature of the vascular system is its bifurcating structures. These structures must incorporate a reduction in their lumen dimensions from the 'single parent' incoming arteriole to the 'dual daughter' outgoing capillaries in order to satisfy the physiological principle of minimum work, which is embodied within 'Murray's law'. Murray's law states that when a parent blood vessel branches into daughter vessels, the cube of the radius of the parent vessel is equal to the sum of the cubes of the radii of daughter blood vessels and is shown in Equation 3 below (Murray, 1926).

Equation 3

$$r_p^3 = r_1^3 + r_2^3$$

Where r_p represents the incoming parent arteriole and r_1 and r_2 represent the outgoing, 'daughter' arterioles.

In order to ascertain the number of 'levels' of branching that might theoretically be required within a microvascular system (consistent with Murray's law) that encompasses a range of spatial values from a capillary with a 10 micron diameter to an artery or vein with a 1 mm diameter, Table 19 (to the left) was prepared. Table 19 shows the diameters of the outgoing 'daughter' capillaries (from a diameter of 10 micron) and calculates the corresponding diameter for the incoming parent arteriole, until an incoming arteriole diameter of 1 mm is attained. The highlighted section shows the 'region of interest' for the purposes of this research (50 micron to 0.5 mm) It can be seen that there are 9 levels of bifurcation in the aforementioned range.

Table 19 Levels of Bifurcation in Microvasculature

5.5.1 Fabrication of Bifurcating Microstructures.

In the first instance, a number of 30 droplet columns were fabricated with the 40 micron aperture diameter printhead, utilising the unipolar single pulse waveform that had previously been used to generate the 50 micron diameter droplet corresponding with the 60 micron diameter columns.

These 30 droplet columns were imaged and measured for height and diameter in order to calculate the droplet volume that the waveform was generating (at that particular backpressure). The dimensions of the 'frozen discs' (from each deposited droplet) were calculated to be 52 micron in diameter and 19 micron in height. Using Equation 3, it was calculated that if the outgoing daughter capillary had a radius of 26 micron then the incoming parent arteriole should have a radius of 33 micron or 66 micron in diameter.

It was also calculated that if a droplet of twice the volume (i.e. a double droplet) were to spread to the same height (19 micron) as the single volume droplet, it would spread to a diameter of 71.7 micron, approximately 6 micron greater than the optimum spread of 66 micron. However, given the fact that phase change and pinning would most likely prevent the 'double droplet' from spreading sufficiently far to maintain the same height as the single frozen droplet, it was thought worthwhile to test the applicability of a simple 2 droplet 'multi-droplet' layered column as a 'rule of thumb' for fabricating bifurcating structures in compliance with Murray's law.

A script for a 30 layer, 2-droplet 'multi-droplet' layered column was written using a droplet deposition frequency of 1024 Hz, and an effective wait time between bursts of droplets of 0.25 s (i.e. the 'trigger start' command delay). The substrate was heated to 35° C in order to minimise the probability of accelerated phase change at the substrate causing the occurrence of the 'stacked snowball effect' at the base of the column. The results are shown in Figure 48 overleaf.

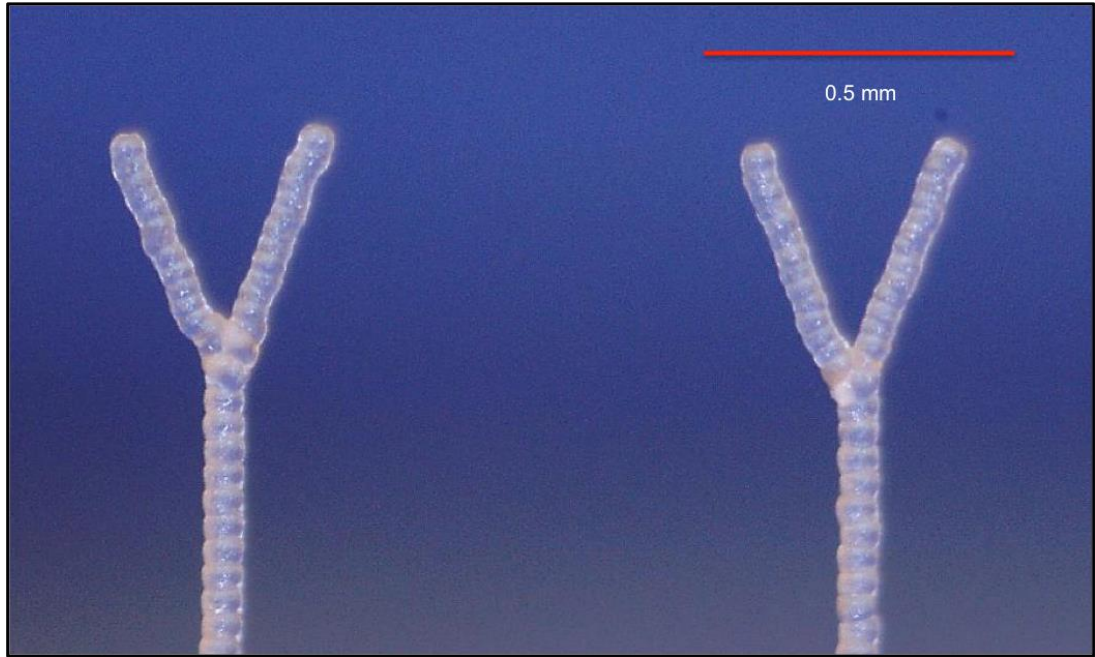


Figure 48; Two 30-layer multi-droplet columns supporting four 15-droplet angled columns. Multi-droplet columns consist of 30 layers of 2 droplets deposited in a burst at 1024 Hz, with an effective delay between droplet bursts of 0.25 s. Angled columns consist of 15 droplets deposited in accordance with the speed of the substrate movement (moving in 10 micron increments per deposited droplet from the point of bifurcation).

The microstructures shown in Figure 48 above were imaged and measured by pixel ruler. The diameter of the multi-droplet columns is approximately 66 micron and is in excellent agreement with the targeted column diameter.

Gao and Sonin describe the spread of the droplet to its thermal equilibrium as being governed by the following equation:

$$\frac{r_d}{a_d} = \left(\frac{4 \sin^3 \theta}{(1 - \cos\theta)^2 (2 + \cos\theta)} \right)^{\frac{1}{3}}$$

Where r_d is the radius of the solidified daughter droplet and a_d is the radius of the ejected droplet.

The ratio $r : a$ will therefore be a constant if θ (the contact angle of the solidified droplet at its thermal equilibrium) remains constant, so:

$$\frac{r_p}{a_p} = \frac{r_d}{a_d}$$

Where r_p is the radius of the solidified parent droplet and a_p is the radius of the ejected droplet.

The radius of the solidified parent and daughter droplets are clearly driven by the volumes of the ejected droplets so the ratio $a_p : a_d$ is of prime importance

and in this case:

$$V_p = 2 \times V_d ,$$

since the 'parent' droplet is a double 'daughter' droplet, and in this case

$$V_p = 2 \times \frac{4\pi a_d^3}{3}$$

So:

$$\frac{4\pi a_p^3}{3} = \frac{4\pi a_d^3}{3} + \frac{4\pi a_d^3}{3}$$

Dividing through by $\frac{4\pi}{3}$ gives

$$a_p^3 = a_d^3 + a_d^3$$

Which is equivalent to Murrays Law

$$r_p^3 = r_d^3 + r_d^3$$

Since both parent and daughter droplet spreads are governed by the constant ratio

$$\frac{r_p}{a_p} = \frac{r_d}{a_d}$$

The combination of the mathematical explanation shown above, and the result shown in Figure 48 indicates that if strict control over all environmental parameters can be maintained, 3D IJP using multi-droplet deposition technique is a natural fit with the fabrication of sacrificial microvascular facsimiles which comply with Murray's law.

However, it must also be noted that the diameter of the angled daughter columns in Figure 48 is now 56 microns, having increased by 4 micron (from 52 micron) from the initial tests that were conducted to establish the dimensions of the frozen droplet. The increased diameters of the deposited droplets of the angled columns may be due to the increase in ambient IJP cabinet temperatures whilst the experiment was being conducted, or the fact that the angled columns' spatial location within the thermal gradient had changed (previously deposited directly on the substrate), exposing the deposited droplets to higher temperatures, thus slowing phase change. The angle of droplet deposition may have also influenced the diameter of the spreading droplet.

5.6 Fabrication of Arches to Join Bifurcating Microstructures

Having completed the fabrication of the bifurcating structures, the next task was to join the two structures with an arch (the essential vascular 'return' feature) and in doing so complete a single 3D pseudo microvascular module. The results are shown in Figure 49 below.



Figure 49 Two 30-layer multi-droplet columns, positioned with 300 micron between column' centres, supporting four 15-droplet angled columns. Multi-droplet columns consist of 30 layers of 2 droplets, deposited in a burst at 1024 Hz, with an effective delay between droplet bursts of 0.25 s. Angled columns: consist of 15 droplets deposited in accordance with the speed of the substrate movement (moving in 10 micron increments per deposited droplet from the point of bifurcation). Arch: decrease gap between the uppermost point of each column from 300 micron to 30 micron, in increments of 10 - 20-micron, then add 'keystone'.

It is important to note that the arch was fabricated without the use of support materials. This is an important benefit of using 3D IJP with high speed phase change materials, since it eliminates the need for the further potential processing step that would otherwise exist i.e. the removal of support materials (a possible cause of damage or source of contamination).

It can be seen from Figure 49 above, that the result of the 'assembly experiment' was technically successful (the component parts join to assemble a single module). It also appears to be a novel outcome. To the author's knowledge, certainly in the field of microfluidics, no 3d microscale device exhibiting both bifurcation and biomimetic tortuosity has yet been fabricated.

Further research will be required to optimise the process to ensure the completed module is as consistent as the components. It can be seen that the effects of small individual imperfections have the tendency to compound over the course of fabrication. Whilst 3D IJP appears to offer a degree of tolerance, it must be noted that many attempts at assembling this module failed, and comparison of those that were

technically successful showed that they weren't identical. At present, there is insufficient control over all of the fabrication parameters for the process to deliver the repeatability needed for its proposed use in Tissue Engineering and Regenerative Medicine

Additionally, the fabrication of a true 3D microstructure has revealed the limitations of the imaging equipment, which had otherwise proven to be effective. A review of suitable imaging equipment for true 3D microstructures must be undertaken in order to improve the quality of images captured and thereby remove the limitations on the analysis that can be undertaken.

5.7 Column Spacing

The spacing between capillaries in the human body is typically described as being in the range of 100 - 200 micron (Folkman 1973). However, close examination of Figure 1 shows that whilst individual capillaries may be spaced at those recognised intervals, the actual spacing of the component parts of each capillary may be significantly closer. The purpose of the column spacing experiment is to establish both the density at which capillaries may be spaced and the minimum spacing that may be achieved between the perimeter walls of each capillary (in order to mimic the closer spacing of the capillary components).

Clusters of three 30-droplet columns were fabricated with spacing of 1 mm being maintained between the centre columns in each cluster of columns. The spacings between the centre points of each column, within a cluster, were varied from 100 micron to 150 micron in increments of 10 micron. The thirty droplet columns were fabricated at a droplet deposition frequency of 12 Hz and are shown in Figure 50 below.

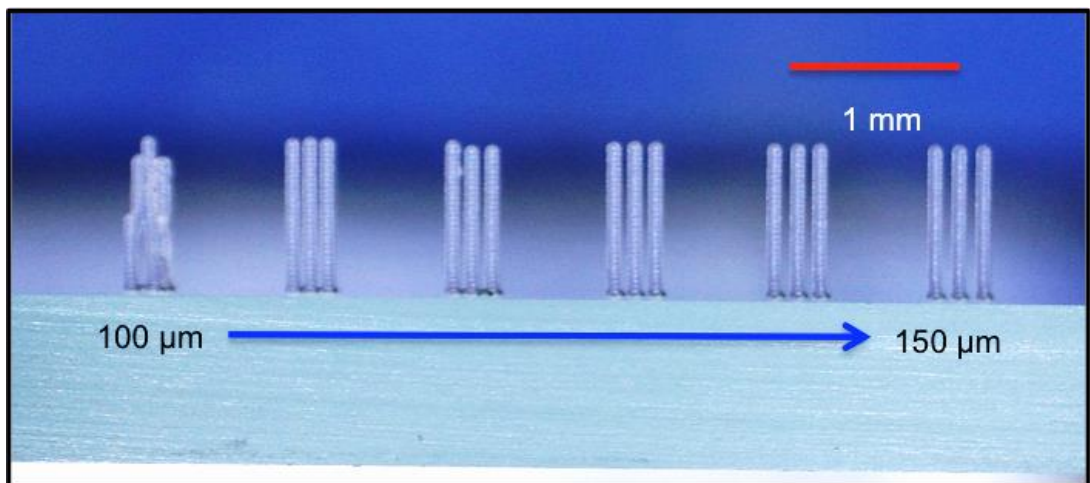


Figure 50; 30-droplet columns at 12 Hz. Spacing between individual columns increasing from 100 micron to 150 micron (in 10 micron intervals). Clusters of columns centred at 1 mm intervals.

The columns, as shown in Figure 50 above, average approximately 95 micron in diameter. It can be seen that the formation of the cluster of columns with spacings between column centres of 100 micron is chaotic. However, order is restored in the clusters of columns with spacings between column centres of 110 micron and above, which means that microvascular facsimiles can be fabricated at the same density at which they occur in the human body.

Column diameters of 95 micron, equate to spacings between column' perimeters of 10 micron and 20 micron, for the clusters at 100 micron centres and 110 micron centres respectively. It can therefore be seen that spacings between column perimeters of 20 micron are achievable, which could be suitable for the spacing between the arteriole section of a capillary and the venule section of a capillary.

5.8 Column Height and Aspect Ratio

In the human body, microvasculature is closely supported by the extracellular matrix (ECM). However, fabricating microvascular facsimiles in the lab must be able to be undertaken without such support. The microstructures must therefore be able to be freestanding at an aspect ratio similar to that of the length of a capillary in comparison with the diameter of a capillary.

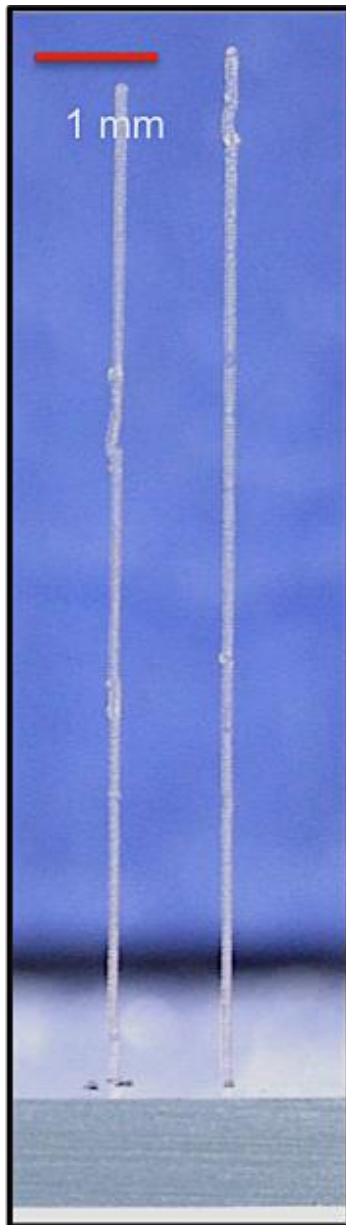


Figure 51; 2 1280-droplet columns fabricated at a frequency of 12 Hz.

In Section 5.3 it was noted that a decreasing droplet deposition frequency and an increasing offset between the printhead and substrate may both contribute to droplet deposition inaccuracy. Demonstrating a self-supporting structure with an aspect ratio of 100:1 (assuming a column diameter of approximately 100 micron), required a challenging offset between substrate and printhead of a minimum of 12 mm (allowing 10 mm for the structure with 2 mm clearance below the printhead). The number of droplets to be deposited per column was set at 1280 (allowing for a frozen droplet height of 78 micron) in the program script, with spacing between column centres of 1 mm and the result is shown in Figure 51 (to the left).

From an examination of the columns in Figure 51, it can be seen that there is a small variance in column height between the two columns, however this may be attributed to the perturbations that may have occurred when printing with an exceptional offset between substrate and printhead. Indeed, the results of said perturbations are visible over the course of the column.

The columns were imaged, and the dimensions checked by pixel ruler. The column diameters average approximately 94 micron. The taller of the two columns is approximately 9.5 mm giving an aspect ratio marginally exceeding 100:1.

5.9 Summary

The first set of experiments sought to understand the principles underpinning the control of droplet deposition. It was found that to optimise control, the wait period between the deposition of each droplet should be minimised by applying the maximum degree of undercooling consistent with maintaining droplet spread to its thermal equilibrium. Furthermore, undercooling should be applied evenly to the complete microstructure with special allowance to be made for the increased conductivity between the base of the microstructure and the substrate, while also minimising sources of microturbulence within the IJP cabinet.

The second set of experiments sought to combine the principles of actuation and deposition and then apply them to the fabrication of the components of sacrificial microvascular facsimiles. It was shown that a single 40 micron diameter aperture printhead could produce column or lumen diameters in the range of 60 to 320 micron using waveform manipulation techniques and the novel 'multi-droplet burst' droplet deposition technique. This result indicated that the desired lumen diameter range of 50 micron to 0.5 mm might easily be achieved using the full range of printhead aperture diameters (10 – 100 micron diameter).

Bifurcating microstructures were fabricated using the 'multi-droplet burst' technique and demonstrated good agreement with the precise dimensions demanded by Murray's law. The result was shown to be the natural mathematical outcome of the relationship between the double-droplet volume of the parent arteriole and the single-droplet volumes of the daughter arterioles. The bifurcating structures were then connected by overhanging arches (without the use of support materials) producing a novel sacrificial microvascular facsimile.

Spacings between column perimeters of 20 micron and between column centres of 110 micron were fabricated mimicking the density at which they occur in the human body. Freestanding columns with heights in excess of 9 mm were also produced, proving that aspect ratios of 100: 1 are achievable without the use of support materials.

In conclusion, the experiments illustrated that the core technological capabilities of 3D IJP with thermal phase change inks are well aligned with the requirements for fabricating sacrificial microvascular facsimiles. However, it was noted that at present there is insufficient control over all of the fabrication parameters for the process to deliver the repeatability needed for its intended use in Tissue Engineering.

Chapter 6 Benchmarking the IJP Apparatus and Assessing the Scalability of 3D IJP as a Technological Platform

6.1 Introduction

The proposed use of 3D IJP with phase change inks within Tissue Engineering and Regenerative Medicine means that a high standard of quality and consistency in the fabricated microstructures is demanded. Attaining resolution, accuracy and repeatability are the paramount considerations.

While the ‘assembly’ experiment (component parts of column, bifurcation and arch into a single module) was technically successful, it was found that due to the accumulation of a variety of small errors in each component, the assembled module was not consistent, nor was it repeatable. In retrospect, performance gaps between the desired control over critical parameters and the actual control achieved are clearly evident, so it is easy to conclude that this outcome was predictable.

The aim of this chapter is therefore to assess those performance gaps and discuss the development pathway that would be required to transform the apparatus used into a hypothetically feasible platform for the fabrication of sacrificial microvascular facsimiles at a research level, effectively benchmarking the existing apparatus against a future ideal. Then the degree to which it might serve as a viable ‘technological platform’ for medical devices in the future is considered. For the purposes of this discussion the term ‘technological platform’ describes the combination of both apparatus (consisting of software and hardware) and know how.

The terms ‘feasible’ and ‘viable’ are frequently used interchangeably, so for clarity and context, in this discussion:

- ‘Feasible’ will be taken to mean ‘the state or degree of being easily or conveniently done’ in the context of fabricating sacrificial microvascular facsimiles for use in experimental devices for Tissue Engineering.
- ‘Viable’ will be considered as the ‘ability to work successfully’ in the context of fabricating sacrificial microvascular facsimiles for use in medical devices.

6.2 The Performance Gaps of the Apparatus as a Platform for 3D IJP

In order to be considered as a technically feasible platform for fabricating sacrificial microvascular facsimiles a number of important objectives must be attained. These are:

- consistency of actuated droplet volumes and velocities
- droplet deposition accuracy
- optimisation of droplet deposition frequency
- optimisation of droplet deposition continuity
- consistent phase change of deposited droplets

The attainment of these objectives is largely governed by the performance of the hardware and software components of the apparatus, while the know how component governs the efficiency with which those objectives can be achieved.

6.2.1 Hardware Limitations

6.2.1.1 Inaccurate Backpressure Regulation

Section 4.3 revealed that backpressure is an important waveform parameter. Without proper control of backpressure, the replication of results from day to day and experiment to experiment will be difficult and the repeatability needed for the fabrication of experimental devices for Tissue Engineering will be elusive. Backpressure should be able to be set to previously determined values (within tolerances of say $1/10^{\text{th}}$ of a mbar), rather than manually regulated as it is at present.

6.2.1.2 Discontinuity of Z-axis (printhead) Motion.

On the Jetlab 4, Z-axis movement is discontinuous, which means that the height of the printhead cannot be altered whilst a microstructure is being fabricated, without causing a change in the continuity of droplet deposition and therefore inconsistency in the microstructure. The Z axis coordinate is therefore set at a single predetermined offset between the tip of the capillary aperture and the uppermost point of the structure to be fabricated. The size of the offset is set to ensure that the thermal effect of the heated printhead does not delay phase change (if the deposited droplet is too close to the heated printhead it will result in the formation of bulbous tops to the fabricated microstructures). This in turn means that there can be a considerable difference in the distance in droplet flightpath between the first droplets deposited (at the base of the structure) and the final droplets deposited at the top of the microstructure. A minor deflection to the course of the droplet over a longer flightpath leads to increased inaccuracy in the deposition of droplets.

Continuous Z axis motion is therefore required to ensure a minimal but consistent distance between the tip of the capillary aperture and the top of the fabricated microstructure. This feature will ensure that both the thermal effect of the printhead and the accuracy of the deposited droplet are constant.

6.2.1.3 Inaccurate Printhead Mounting and Alignment

Although not mentioned previously in this thesis, it was frequently found that errors in printed microstructures were the result of poor alignment between the printhead and substrate, i.e. the printhead was not perfectly perpendicular to the substrate. A simple but effective mounting mechanism and alignment testing method must be devised to facilitate quick but accurate printhead setup.

6.2.1.4 Absence of Appropriate Environmental Controls

The experiments on droplet deposition frequency (Section 5.2) demonstrated the importance of delivering controlled undercooling in order to fabricate consistent columns. There is a maximum degree of undercooling that can be applied to ensure that the droplet is able to spread to its thermal equilibrium. The maximum degree of undercooling then sets the upper boundary on the frequency of droplet deposition. If the thermal mass (volume) of the droplets change, then the degree of undercooling applied and/or the deposition frequency must be altered to align with the change in thermal mass. Therefore, sensitive and responsive environmental controls are required for the IJP cabinet, so that droplet deposition frequency can be optimised and quickly adjusted to accommodate changing droplet volumes and frequencies.

The addition of environmental controls would also give the apparatus the flexibility to use waxes with different melting points in the fabrication of sacrificial microvascular facsimiles. It was noted that it is important that the melting point of the sacrificial material is carefully matched to the thermal sensitivity of the biocompatible material that will eventually surround the microstructure, so that the biocompatible material is not damaged by the temperatures used in the sacrificial procedure. The addition of environmental controls would therefore extend the range of biocompatible materials that could be used to encase the sacrificial microstructures.

6.2.1.5 Further Reduction in the Thermal Mass of the Printhead Reservoir Component

The use of thermal phase change inks necessitates the use of a heated printhead-reservoir component. As the printhead-reservoir component will always be at a higher temperature than that of the IJP cabinet, the occurrence of microturbulence in the IJP cabinet cannot be avoided. However, microturbulence may be further

minimised by reducing the thermal mass of the printhead-reservoir assembly, thus increasing the consistency of droplet deposition.

6.2.1.6 Limited Imaging Capabilities

The Jetlab 4 imaging capabilities only allow the monitoring of the droplet volumes and velocity prior to the actual fabrication of the microstructure. The consistency of the microstructure is then inspected after fabrication is complete. In this way quality is ‘inspected into’ the microstructure after the fact. Realtime observation of droplet deposition accuracy, continuity and phase change consistency is required over the course of the fabrication period. Continuous monitoring would mean that deviations from optimal consistency could be observed and the relevant setting and script changes needed to rectify those deviations could be immediately noted. By this method quality could be built into the microstructure rather than being ‘inspected into’ the microstructure, which would improve the consistency and repeatability of the fabricated microstructures.

6.2.2 Software

Whilst the achievement of optimum droplet deposition frequency is primarily driven by its direct input as an IJP parameter, it is also a function of the efficiency of the program or ‘script’ that drives the electromechanical movements of the IJP substrate. Inefficiencies in the script reveal themselves as inconsistencies in the continuity of the deposited droplets, resulting in irregularities in phase change and therefore the shape of the frozen droplet. Delays in the motion of the substrate had been observed over the course of many experiments. The uncharacteristic column formation behaviour for the ‘multi-droplet layer’ columns (Section 4.4) was also cause for further concern, since it indicated that there may be a significant delay in the execution of scripted commands. These delays were investigated and quantified. The results are shown in the sub-sections that follow.

6.2.2.1 Scope of Command Execution Delays

In order to identify the scope of this investigation, a comparison between the actual execution time for a script used in Section 5.4, was made with a calculation of the theoretical execution time for that fabrication script (excluding time for substrate movement). The calculation and comparison are summarized in Table 20 overleaf.

Table 20 Comparison of the theoretical script execution time with the actual script execution time.

Description: 9 columns of 30 layers, each layer comprised of 4 droplets deposited at 256 Hz. A 'wait' command was used between the deposition of each layer. The 'wait' command was reduced for each column, commencing with 5 s delays on the first column, reducing to 0.0001 s for the final column.		
Actual total print time		252.185 s
Theoretical total print time (see breakdown below)		185.149 s
Discrepancy		67.036 s
Scripted element	Description	Theoretical time taken
Droplet deposition	1080 droplets at 256 Hz	4.218 s
Wait times	29 wait times per column (5, 1, 0.1, 0.05, 0.033, 0.025, 0.02, 0.01 and 0.001 s)	180.931 s

The discrepancy between actual total print time and the theoretical total print time, of 67.036 s (as shown in Table 20) represented 26.6% of the actual total print time. This represented a significant delay, so the various programmed elements of the fabrication script were investigated.

6.2.2.2 Analysis of Scripting Execution Delays

Consideration of the small range of commands used in the formulation of a script revealed three elements that needed to be isolated in order to be evaluated:

- 'Set up' delay – the first lines of code in any fabrication script are used to prepare the Inkjet printer electromechanically to execute the script;
 - selecting which printhead/s that the waveform will be driven through to actuate the deposition of droplets.
 - setting the number of droplets that are to be deposited.
 - setting the frequency at which the droplets are to be deposited.
- 'Trigger start' delay – the delay between the programmed start time of the piezo and its actual start time.

- ‘Moveto’ and/or ‘Moveby’ command delays, i.e. the delay in the execution of the script that activates substrate movement (excluding the actual time of substrate movement).

Naturally every line of code used would incorporate an element of ‘code reading delay’, which is the time taken for the computer to ‘read’ a scripted line of code and translate it into ‘machine code’ and send it to the Inkjet Printer. Whilst the delay is different in nature from the electromechanical delays noted above, it was thought that this element would be fairly consistent across the range of commands used and also be very difficult to isolate. It was decided that ‘code reading delay’ would be assumed to form part of the measured delay.

6.2.2.3 Accuracy of Reported Measurements

It was decided that the first assessment to be made should be a comparison of the reported run time of the script by the computer with the execution time of the script by the Inkjet printer. In order to test this component, three single line scripts incorporating the wait command were written and run (as shown in Table 21 below). The experiment was repeated three times and the results averaged.

Table 21 Comparison of reported script execution times with actual execution times by the Inkjet printer.

Scripted Wait Time	1 s	50 s	100 s
Reported Execution Time	1.388 s	50.074 s	99.746 s

Whilst the first result (1 s: 1.388 s) was somewhat expected, since it was anticipated that there would be a time lag in the execution of the single line of script, the final result provided cause for concern. The ‘wait 100 s’ command was read and executed in 99.746 s, which indicated that the Inkjet printer’s internal timing mechanism was running faster than real time, and therefore that the following measurements should be taken as indicative rather than accurate.

6.2.2.4 Set up Delay

The three standard lines of code for the setup (printhead selection, droplet frequency and droplet quantity) were written using nominal values (printhead 1 (of 4), 10 droplets and 10 Hz) for the required set up elements. A further line of code, ‘wait 1 s’ was then added. The script was run three times and the reported execution times recorded and averaged. The result of 2.263 s was compared with the value reported for the single line ‘wait 1 s’ command from Table 21 above of 1.388 s, showing that the additional time to execute the setup code was 0.875 s

6.2.2.5 'Trigger start' Delay

The three standard lines of code for the setup, which were used above, were repeated and the command 'trigger start' was substituted for the 'wait' command, so that 10 droplets would be dispensed at 10 Hz (i.e. within 0.9 seconds). The script was run three times and then the results were averaged, as shown in Table 22 below.

Table 22 Isolation of the 'trigger start' command delay.

Reported Execution Time	Theoretical Droplet Deposition Time	Setup Time	'Trigger Start' Command Delay
2.012 s	0.9 s	0.875 s	0.237 s

6.2.2.6 'Moveto' and 'Moveby' Delays

In order to test the delay in the execution of the 'moveto' and 'moveby' commands the previous 'setup up' delay script was used again, however after the 'trigger start' command, the 'moveto o,o' command was then added. The combination of 'moveto o,o' and 'trigger start' was then repeated 30 times. The position of the substrate was then adjusted so that the printhead was located directly over the substrate's (o,o) x and y coordinates. This was done so that the substrate would not move during the course of executing the script and the actual delay associated with the command (as opposed to the delay associated with substrate movement) could be isolated. The trial was also repeated using the 'moveby o,o' command in order to establish if any variance existed between the delays associated with the two commands. Each trial was repeated three times and then the results were averaged, as shown in Table 23 below.

Table 23 Isolation of 'moveto'/'moveby' command delays.

	Moveto Command	Moveby Command
Reported Execution Time	25.974 s	29.718 s
Setup Time	0.875 s	0.875 s
Delay Associated with 'Trigger Start' (30)	7.11 s	7.11 s
Total Time Attributed to 'Moveto'/'Moveby' Command (30)	17.989 s	21.733 s
Execution Time per 'Moveto'/'Moveby' Command	0.599 s	0.724 s

The command execution times generated in Table 23 were then compared to the reported movement times of the substrate, in order to generate a time for the actual movement of the substrate in 1 mm increments (i.e. thereby allowing isolation of the actual substrate movement). Two scripts that programmed the substrate to move in 10 x 1 mm increments and 20 x 1 mm increments were generated (thus removing travel time from the substrate maintenance position to its origin coordinates). The times were compared, and it was found that the final series of 10 x 1 mm incremental movements (when the 20 x 1 mm script was executed) were completed in 9.985 s, which theoretically equated to 5.99 s of ‘moveto’ command delay and 3.995 s of actual substrate movement time.

6.2.2.7 Application to the Original Comparison (Section 6.2.2.1)

In order to provide a level of validation to the calculated delays and movement times, these times were introduced into the original comparison between theoretical printing times and actual printing times, which was summarised in Table 20. Table 24 below, reproduces the aforementioned table and then introduces the relevant calculations for the delays and movement times inherent in the IJP process.

Table 24 Revised comparison of the theoretical script execution time with the actual script execution time

Actual total print time	252.185 s	
Theoretical total print time including command execution delays and movement (see breakdown below)	256.863 s (previously 185.149 s)	
Discrepancy	- 4.678 s (previously 67.036 s)	
Scripted element	Description	Theoretical time taken
Droplet deposition	1080 droplets at 256 Hz	4.218 s
Wait times	29 wait times per column (5, 1, 0.1, 0.05, 0.033, 0.025, 0.02, 0.01 and 0.001 s)	180.931 s
Set up delay	1 x setup delay	0.875 s
Substrate movement	9 movements	3.591 s
‘Moveto’ command delay	9 ‘moveto’ command delays	5.391 s
‘Trigger Start’ command delay	261 ‘trigger start’ command delays	61.857 s

It can be seen from Table 24 that the discrepancy between theoretical print time and actual print has reduced from 67.036 s to - 4.678 s, meaning that the delays and movements have been somewhat over accounted for. However, when it is considered that there is a total of 280 of these delay/ movement events to account for, the discrepancy is 0.016 s per event, and may therefore be the result of accumulated rounding errors.

The knowledge gleaned from the research in this section was applied to the original experiment in Section 5.4, which spurred the research, and found to provide a clear explanation for the uncharacteristic column formation behaviour for the ‘multi-droplet layer’ columns is found. Although the ‘wait’ times (ranging from 5 s to 0.001 s) between the deposition of each individual layer of droplets were defined by the script, each ‘wait time’ command is then followed by a ‘trigger start’ command, that is known to have a delay of 0.237 s associated with it. This means that the actual ‘wait’ times, which were effectively being applied between each layer of droplets actually ranged from 5.237 s to 0.238 s, and since the effective layer deposition frequency failed to increase above approximately 4 Hz (1 layer deposited each 0.238 s), thus the anticipated bulbous column formation failed to materialise.

An explanation for these command delays was sought from ‘MicroFab Technologies’, the manufacturers of the Jetlab 4 system. They explained that the Jetlab 4 is controlled by a regular operating system, so each command line introduced a ‘yield’ time to allow the operating system time to allocate resources to the execution of the command (since multiple programs are kept running in parallel) in order to keep the Jetlab 4 from ‘locking up’. The resolution to this problem would therefore be found by switching to a dedicated real-time operating system (RTOS), which would minimise the lag between command and execution. If such a change were undertaken, it would greatly improve the continuity of deposited droplets and enhance the consistency of the final microstructure. Furthermore, the change would also eliminate a significant amount of downtime from the total fabrication time.

6.2.3 Know How

In the introduction to Chapter 4 it was noted that the traditional IJP style of methodical but mechanical alterations to waveform parameters is clearly a time consuming and impractical approach in the search for the multiple optimised waveforms needed in this research. ‘Know how’ therefore forms a key component in the discussion of the feasibility of 3D IJP as a technological platform for fabricating sacrificial microvascular facsimiles.

The research undertaken into droplet actuation and deposition in Chapters 4 & 5 has contributed toward a clearer understanding into the principles underpinning droplet actuation and deposition. A modest amount of further research will be needed to reveal the precise relationships between the fundamental period, the influence of rise times, changes in pulse amplitude (relative to rise times) and expected meniscus displacement. Once these principles are fully understood, research should become increasingly goal directed rather than an elaborate exercise in trial and error.

To ensure technical feasibility, the performance gap between the actual and desired monitoring and control of the droplet actuation process must be overcome. The incorporation of the following features would be essential:

- Instantaneous droplet volume and velocity measurement and display
- Nano second (ns) waveform control and strobe delay settings for image capture
- Milli volt (mV) amplitude settings

In Section 5.2 & 5.4, it was found that the thermal mass of a droplet was a key determinant of optimum droplet deposition frequency and also the formation of a blended interface between the multi-droplet layers. In order to better understand the application of this principle in real time fabrication and how it may be used to maximum advantage, a thermal imaging device should also be included in the required upgrades.

6.3 Apparatus Performance Gaps: Summary

The process of adopting and adapting any technology to a novel application often reveals the limitations of that technology. The lack of consistency and repeatability of the fabricated microstructures spurred investigation into the performance gaps between the existing apparatus and a hypothesised ideal apparatus representing a feasible technological platform.

Important hardware limitations need to be addressed, principally inaccurate backpressure regulation, discontinuity of Z axis (printhead) motion and the lack of appropriate environmental controls. It was also found that the continuity of droplet deposition is an important contributor to overall droplet deposition frequency. The delays caused by program inefficiencies were investigated and quantified. The matter was discussed with the manufacturers of the Jetlab 4 and a change to a dedicated real-time operating system was recommended as the only viable solution to the current software limitation. Finally, it was noted that the accumulation of know-how is an essential component for the efficient implementation of any new technological platform. Upgrades such as ‘instantaneous droplet volume and velocity measurement’ have been recommended, in order to be able to monitor and control the droplet actuation process in real time.

Figure 52 overleaf, summarises the required upgrades as ‘elements’, and then (where applicable) indicates the ‘method’ by which these elements contribute to the achievement of the ‘objectives’ needed to ensure technical feasibility. The figure also shows that in many cases the upgrades combine synergistically. It can be seen that although some of the suggested ‘elements’ are technically advanced or potentially expensive, they do not require any fundamental research to be undertaken. Indeed, some of the suggested adaptations have been published (e.g. instantaneous jetting speed curves (Kwon, 2010), millivolt jetting pulse amplitude control (Cibis & Krüger, 2007)), whilst other adaptations such as environmental controls over temperature and humidity are already commercially available from MicroFab Technologies Inc.

Comparing the outputs shown in Chapter 5 against the limitations in hardware, software and knowhow detailed in this chapter, it is clear that the best achievable results were extracted from a resource with considerable limitations. However, it is not difficult to envisage how the technical improvements that have been described will facilitate the removal or mitigation of these limitations, nor is it difficult to imagine the impact that an enhanced 3D IJP will bring to the consistency and repeatability of the fabricated microstructures.

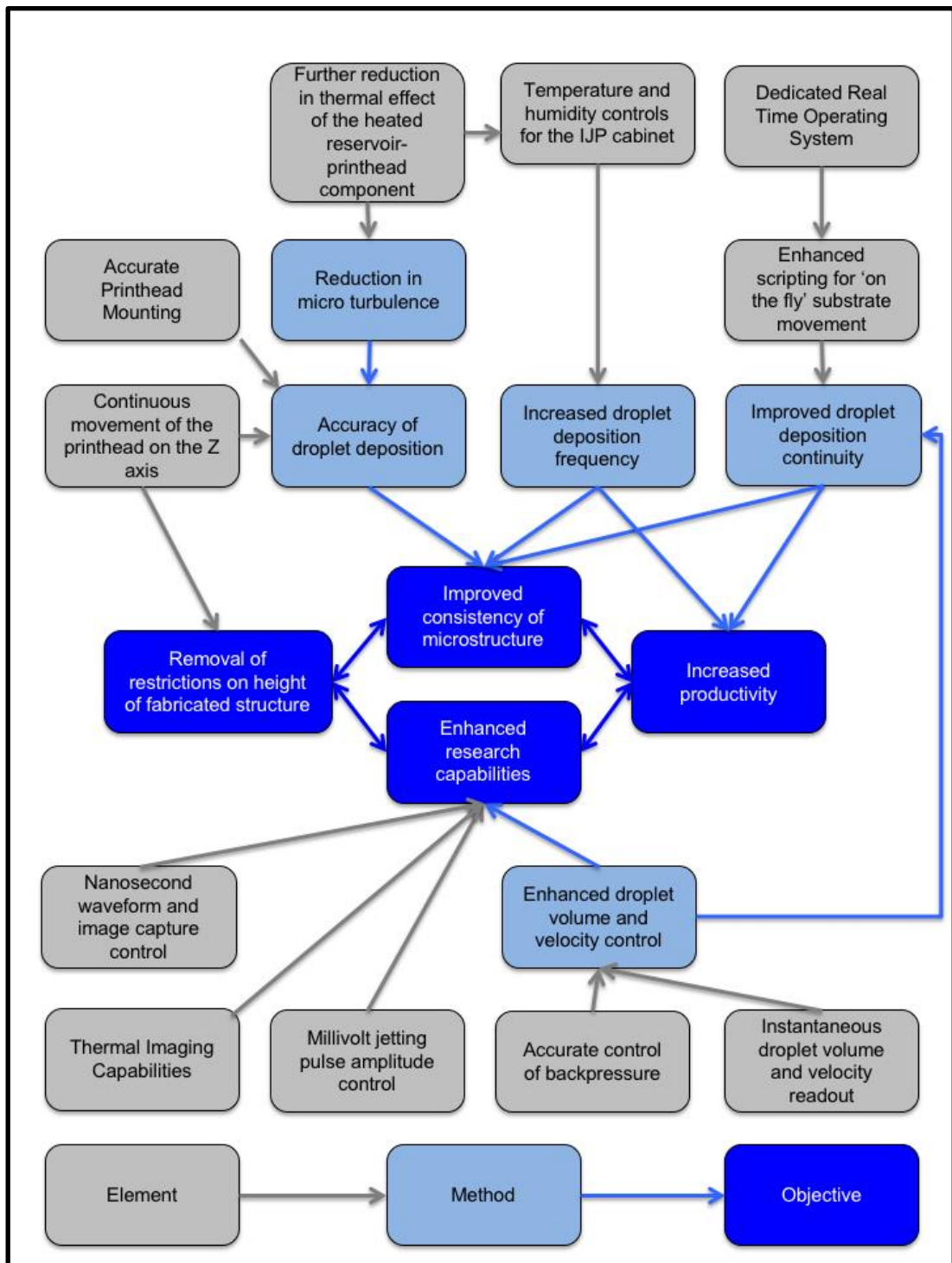


Figure 52 An assessment of the upgrades required to extend the capabilities of the Jetlab 4, in order to be able to fabricate consistent and repeatable sacrificial microvascular facsimiles.

6.4 The Viability of 3D IJP as a Technological Platform

Assuming that the 3D IJP apparatus has been upgraded to the level of feasibility needed for fabricating research grade experimental devices, then the viability of 3D IJP as a technological platform within the context of medical devices can be considered.

The significant step up from feasibility for experimental devices to viability for medical devices requires attention to two interlinked issues, the first being productivity and the second being scalability. The relevant metric for productivity would be a measured output of sacrificial microvascular facsimile per printhead per unit of time. Such a metric may invite comment on 'return on investment' but since the medical devices in question would be highly valuable engineered tissue for the repair or replacement of human organs, it will be assumed (for the purpose of this discussion) that the return on investment will be positive. Therefore, the main question this section seeks to answer is, will the productivity per printhead per unit of time be sufficient to fabricate the sacrificial microvasculature needed to generate clinically meaningful volumes of tissue?

In the introductory chapter, the challenge of scaling from lab to clinic was introduced and the volumes of some common organs were given. The following sections will consider three different fabrication strategies for a small organ, such as the thyroid. The first strategy simply replicates the current fabrication method with allowances made for the increased efficiency that would be gained from the upgrades that were previously suggested. The second and third are 'On the Fly' layer-by-layer printing and 'Vector Motion' printing respectively. 'On the Fly' printing is a 2D IJP technique, so the printing of 3D structures with a 2D technique necessitates that a 'layer by layer' approach must be utilized. The concept of 'Vector Motion' printing assumes that the substrate and printhead are engineered to engage freely in true 3D movement, so that the path of the printhead relative to the substrate follows a continuous vector that describes the 3D position of the microstructure, with the benefit that droplet deposition continuity can be maximised during fabrication of a structure.

Assumptions in the comparison of fabrication strategies

In the previous section, the upgrades required to achieve technical feasibility were set out, which if completed would result in: continuous z axis motion, the optimisation of droplet deposition frequency and the elimination (or reduction toward zero) of command execution delays. As 12 Hz was a well-used deposition frequency under

suboptimal printing conditions, we will assume (for simplicity) that a frequency of 20 Hz can be achieved under optimal conditions.

Although command execution delays are theoretically eliminated, an allowance must still be made for substrate motion. A substrate velocity of 20 mm/s (excluding deceleration/acceleration times) has been a commonly used setting for previously undertaken lab work, and the same allowance will be applied to z axis velocity. In Section 5.8 a droplet height of 78 micron was measured, again for simplicity this will be rounded to an 80 micron. The deposition of an 80 micron droplet at 20 Hz will fabricate 1 mm of structure in 0.625 s and therefore require a minimum z axis velocity of 1.6 mm per second (which is well within the assumed z axis velocity limit of 20 mm/s).

As a brief and simplified comparison, the apparatus used for the two-photon polymerisation fabrication strategy shown in Figure 5 was able to polymerise a 3 micron layer at a rate of 20 mm/s. If used to produce 1 mm of the sacrificial structure shown in Section 5.8 (94 micron diameter so 295 micron circumference) it would require 333 layers giving a fabrication pathway of approx. 98 mm requiring 4.9 s of production time. In this simple example 3D IJP is over 7 times faster than two-photon polymerisation.

The total length of capillaries needed to perfuse a relatively small organ such as the thyroid was calculated at approximately 500 m. However, we will assume 550 m of capillaries and assign a 'complexity ratio' so that 500 m of straight capillaries and 50 m of bifurcations/arches are to be printed.

There is no available biological data on the 'composition' of microvasculature to support any particular value for a complexity ratio, so the 10:1 ratio assigned is clearly arbitrary. However, to illustrate the importance of composition in the calculation of fabrication times, the time taken to fabricate the overhanging arch structure shown in Section 5.6 will be assessed using the current fabrication method, but assuming that 3D IJP performance has been upgraded to the level of technical feasibility.

The 'arch' structure comprised two thirty droplet columns, then 14 droplets deposited alternately on each column (i.e. 7 per column) followed by a keystone at the apex in order to join the demi-arch structures (total 75 droplets). The micro-movement between the deposition of each alternate droplet has been observed to reduce droplet deposition frequency to approximately 1 Hz. At an assumed 20 Hz, the deposition of the two 30 droplet columns would take 1.5 s each, with an added allowance of 1 s for substrate motion from the first column position to the second (sub-total 4 s). The

deposition of the arch and keystone would take 15 s, giving a total fabrication time of 19 s.

At the 10:1 ratio, the example shows a near perfect illustration of pareto distribution. 21% of fabrication time is applied to the columns, which represent 80% of the structure, and conversely, 79% of the fabrication time is devoted to the arch, which represents 20% of the structure. This in turn shows how the complexity ratio and the fabrication rate for bifurcations and arches will be key determinants of the most viable fabrication strategy.

6.4.1 Fabrication Times for the Current Deposition Method

In the case of the sacrificial microvascular facsimile of the hypothetical thyroid; if the 500 m of straight capillaries are produced at 1.6 mm/s (80 micron at 20 Hz) the fabrication time is 312,500 s. The alternate droplet deposition technique may also be used for the fabrication of bifurcating structures at a deposition rate of 1 Hz. The 50 m of bifurcations/arches at 80 micron/s (80 micron at 1 Hz) would take 625,000 s giving an approximate fabrication time of 260 hours. The average droplet deposition frequency for the printhead is 7.3 Hz.

6.4.2 Fabrication Times for 'On the Fly' Layer-by-Layer Printing

When IJP is used for traditional 2D printing tasks, it is common practice for the printer to be instructed to print 'on the fly', which means that substrate movement is continuous on both the X and Y-axis, and each individual droplet of ink is dispensed by the printhead at a calculated interval before the substrate passes the anticipated (or programmed) deposition location of the droplet. Printing 'on the fly' can significantly increase productivity, as the substrate no longer stops at each deposition point, so the stationary time at the deposition point and the acceleration/deceleration periods for the substrate between deposition points are eliminated. A 'layer by layer' approach, the most common production technique used by the AM industry, can then be used for the fabrication of 3D structures.

Figure 53 on the following page shows a small array of overhanging arch structures fabricated 'on-the-fly' at a fixed z axis offset of the printhead. If microstructures were fabricated at a 'biomimetic' interval of 200 micron (spacing between capillaries in vivo), at the given substrate velocity of 20 mm/s, the droplet deposition frequency would be 100 Hz. At 100 Hz, the 6,875,000 droplets that make up the sacrificial microvascular facsimiles for the thyroid would be deposited in 19 hours (net of acceleration/deceleration times).

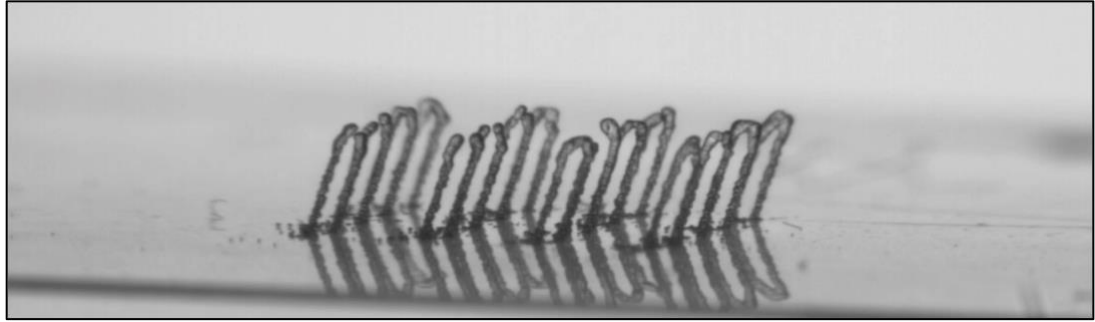


Figure 53 ‘On the fly’ layer-by-layer fabrication of arch-like features: A 4 x 4 Array. Two 30-droplet columns with a 250-micron spacing between centres. Arch: decrease gap to 0.075 mm in increments of 10 - 20-micron, then add ‘keystone’.

However, three relevant observations about the effects of printing ‘on the fly’ layer-by-layer can be made:

1. The microstructures have a noticeable lean to the right.
2. The deposition of the final droplets toward the top of the arch (the keystone) appears to be inaccurate and is indeed missing on a number of the arches.
3. Arches (and therefore bifurcations) must be oriented to the x axis

It is thought that the lean to the right was caused by the relative lateral momentum imparted into the droplet by the motion of the substrate moving ‘on the fly’ from left to right, which effectively angled the trajectory of deposition. However, the lean of the micro structures could be counteracted by making discrete adjustments to the printhead on the Z-axis as each layer was completed, thereby ensuring that the printhead would maintain a fixed offset relative to the uppermost point of the column during fabrication.

The angled trajectory of the droplet offered an explanation for the inaccuracy in the deposition of the final droplets (e.g. the keystones of the arches). Minor degrees of inaccuracy caused by the angled trajectory may be acceptable during column formation, since the droplets are being deposited at the centre of the column. However, during arch fabrication, droplets are deposited toward the perimeter of the column (where there is an increasing spatial restriction) so the acceptable tolerances diminish.

6.4.3 Fabrication Times for a Hybrid ‘On the Fly’ Layer-by-Layer Solution

At present, the relative lateral momentum imparted to the droplet as it is deposited ‘on the fly’ appears to be a hindrance to attaining uniformly fabricated microstructures. However, if considered carefully it could be used to improve the consistency of the fabricated structures as shown in Figure 54 overleaf.

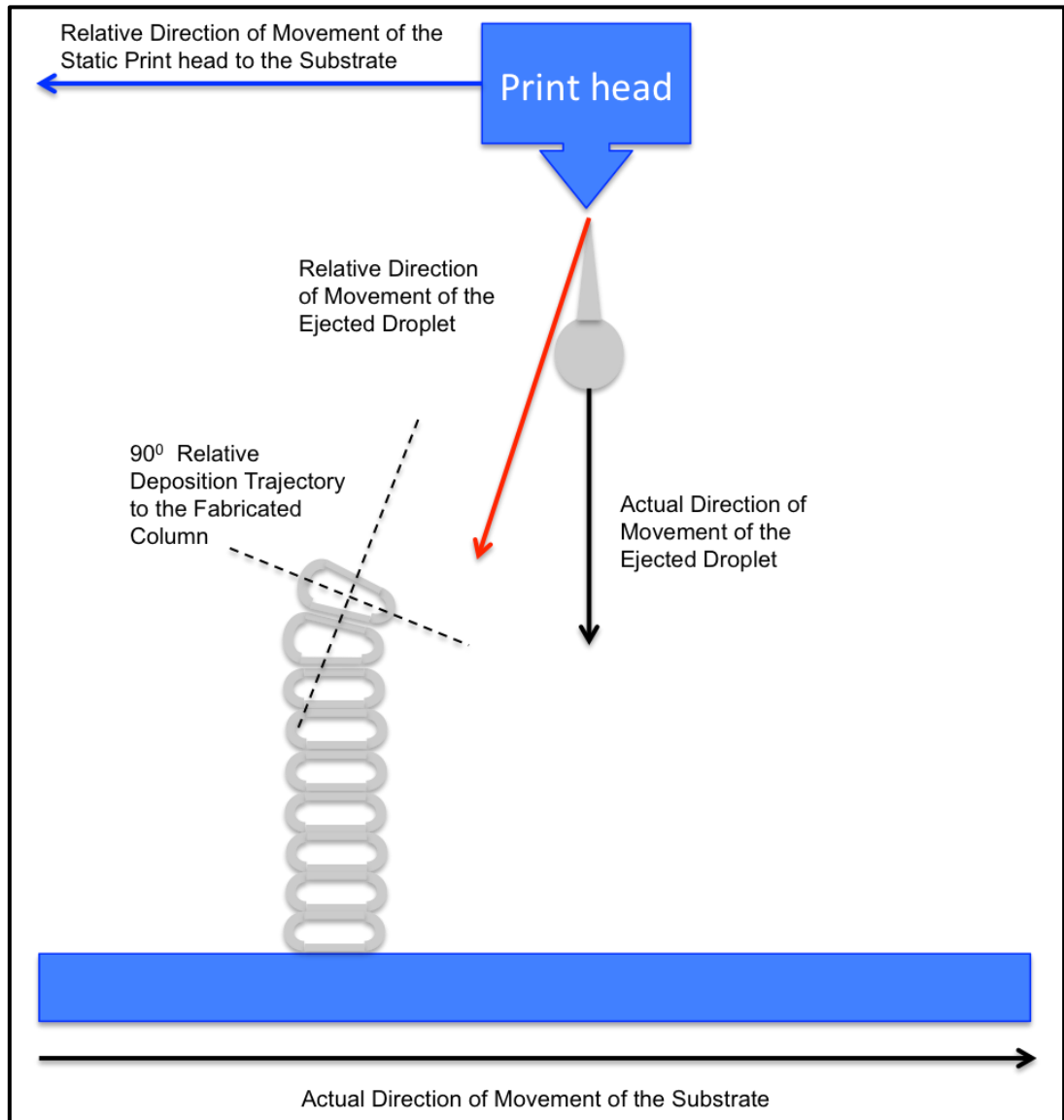


Figure 54 The use of the lateral movement of the substrate to enhance the fabrication quality of 3D microstructures.

It can be seen in Figure 54, that as the fabrication of the arch (or other 3D component) progresses, then the optimum deposition trajectory of the dispensed droplet remains at 90° relative to the last deposited substrate droplet, but relative to the printhead the optimum deposition trajectory of the dispensed droplet progressively decreases from 90° toward 0° . This condition may be (partially) satisfied by using the relative lateral momentum imparted to the droplet as it is deposited 'on the fly'. So, as the fabrication of the arch commences, a low substrate velocity setting is used so that a near 90° relative deposition trajectory is achieved. As fabrication progresses and the optimum droplet trajectory angle decreases, the velocity of the substrate is progressively increased so that the relative lateral momentum imparted by the substrate decreases the effective droplet trajectory

angle. Unfortunately, the scripting limitations of the JetLab 4 prevented this novel method from being tested.

It should be noted that the use of such a technique would immediately halve the effective droplet deposition frequency, since droplets could only be deposited on one half of the arch as the substrate moved in one direction and then the other half of the arch structure as the substrate moved in the opposite direction. Further reductions in efficiency would result from the slow movement of the substrate as arch fabrication commenced. However, these reductions would be somewhat offset by the increased velocity of the substrate as the arch neared completion. The deposition of the final keystone to the 'arch' would of course have to be deposited as a singular droplet under 2.5D printing conditions.

Furthermore, a hybrid of the current method and the 'on the fly' method could be used. Columns could be printed using the traditional substrate and printhead movement to ensure uniformity. The 'true 3D' components such as bifurcations and arches would then be printed 'on the fly'. If the 100 Hz droplet deposition frequency associated with on the fly printing is reduced in accordance with the inefficiencies detailed in the preceding paragraph, a theoretical droplet deposition frequency of approximately 50 Hz could be achieved.

If the droplets for the columns are deposited at the rate of 20 Hz and the droplets for the arches/bifurcations are deposited at 50 Hz, then the theoretical droplet deposition time if the 500 m of straight capillaries are produced at 1.6 mm/s (80 micron at 20 Hz) the fabrication time is 312,500 s. The 50 m of bifurcations/arches at 4 mm/s (80 micron at 50 Hz) would take 12,500 s. This gives a total approximate fabrication time of 90 hours, with an average droplet deposition frequency of 21 Hz. The fabrication time of this hybrid method is significantly longer than that of the 'on the fly' method (19 hours), however it would directly address the fabrication inadequacies observed in Figure 53.

Whilst this hybrid method seems to be an obvious solution a number of caveats remain. It was noted that arches and bifurcations must be oriented to the x axis. At the most fundamental level, it is highly questionable if such a microvascular layout could be considered biomimetic.

At a more practical level:

- machine code would have to be rewritten in order to remove the scripting limitations previously.

- droplet deposition frequencies relative to the individual column (as opposed to the printhead) while printing on the fly will be in the order of 0 to 0.1 Hz. To ensure uniform adhesion between the substrate droplet and the deposited droplet the temperature of the substrate droplet will have to be maintained just below phase change temperature.

6.4.4 Fabrication Times for '3D Vector-Motion' Printing.

Further research into the principles underpinning the structure and spatial arrangement of the microvascular hierarchy will inevitably lead to the need to fabricate increasingly sophisticated structures, incorporating varied permutations of lumen diameter changes, bifurcations and overhanging arches, in order to create truly biomimetic facsimiles of the microvascular structures found in *in vivo* tissue and organs.

To respond to that need, the development of a 3D Inkjet printer where the printhead and substrate can be engaged in true 3D movement i.e. sharing six degrees of freedom between the motion of the printhead and substrate will be required (as opposed to the 3 degrees of freedom shared between printhead and substrate at present). One might imagine a reservoir-printhead module attached to a robotic arm, so that the path of the printhead will follow a continuous line or curve smoothly through three dimensions (e.g. mimicking the shape of a capillary arch) that will be described by a vector in the script controlling the movement path of the robotic arm. Droplet deposition would therefore be at optimal frequency and as close to continuous as an optimised movement path could allow. The corollary of developing an advanced system is of course that an advanced level of know how would have to be developed to operate the system effectively.

For the purposes of calculation an allowance of 50% is made for inefficiency in the optimised movement path, reflecting the time taken to move from the end point of fabrication of one component to the start point of the fabrication of the next (the assumed 20 Hz frequency is therefore reduced to 10 Hz). For vector motion 3D IJP, the theoretical droplet deposition frequency for straight capillaries and bifurcations/arches would be the same. The 550 m of capillaries are produced at 0.8 mm/s (80 micron at 10 Hz) The total approximate fabrication time is 191 hours, with an average droplet deposition frequency of 10 Hz.

6.5 The Viability of 3D IJP: Summary

Although there has been extensive discussion about alternative fabrication methods, their productivity, and their key advantages and disadvantages, the main finding of this chapter has gone virtually unremarked upon and that is: If 3D IJP is upgraded beyond the level that ensures technical feasibility, it immediately delivers scalability and therefore viability.

In the hybrid 'on the fly' method, the sacrificial microvascular facsimiles for a small organ such as the thyroid could be fabricated at a reasonable level of quality in approximately 3.75 days. Clearly there are additional processing steps required after the fabrication of the facsimile such as coating with a biocompatible material and removal of the sacrificial structures, in order to produce the final scaffold ready for cellularisation. However, 3D IJP as a technological platform for the fabrication of sacrificial microvascular facsimiles has the potential to provide a scalable solution to the challenge of vascularisation in Tissue Engineering.

The results of the comparison of the various fabrication strategies are summarised in Table 25 below.

Table 25 An evaluation of fabrication strategies to produce the sacrificial microvascular facsimiles required for a hypothetical small organ.

	Printhead Productivity	Total Fabrication Time	Investment Level Estimate (100 as Base)	Key Benefits	Key Limitations
Upgraded Standard 3D IJP	7.3 HZ	260 Hours	100	Least Expensive Good Consistency	Comparatively Low Productivity Modest Biomimicry
Standard 'On the Fly' 3D IJP	100 Hz	19 Hours	100	Highest Productivity	Poor Consistency and Biomimicry Intra-droplet Adhesion?
Hybrid 'On the Fly' IJP	21 Hz	90 Hours	110	Value for Money Good Consistency	Poor Biomimicry Intra-droplet Adhesion?
Vector Motion IJP	10 Hz	191 Hours	300 - 500	Optimal Biomimicry Consistency and Repeatability	Expensive Extensive Development of Know How Required

Average droplet deposition frequencies using the current fabrication strategy were limited by the 1 Hz deposition frequency that can be achieved while fabricating bifurcations and arches. This compared poorly against the deposition frequency of 100 Hz for the 'on the fly' layer-by-layer fabrication process, however observations regarding the consistency of these microstructures led to the suggestion of a novel 'hybrid on the fly' solution. The layer-by-layer fabrication process also raises the question of intra-droplet adhesion at low deposition frequencies, which requires further research to reveal a, if it is in fact a problem and b, how such a problem might be mitigated. Whilst the proposed solution would address the problem of consistency of a microstructure (with a reduction in average deposition frequency to 21 Hz), the need to align all bifurcations and arches to either the x or y axis means that the fabrication strategy may create a microvascular structure that may not function biomimetically.

Biomimicry may only be achieved by constructing a 3D Inkjet printer where the printhead and substrate can be engaged in true 3D movement i.e. sharing six degrees of freedom between the motion of the printhead and substrate. The construction of such a 3D inkjet printer would be expensive and require significant research to achieve the know how needed to operate it effectively and efficiently. It would probably deliver a relatively modest average deposition frequency of 10 Hz and be capable of fabricating the hypothetical thyroid in 8 days. However, 3D 'Vector Motion' printing is probably the fabrication strategy that is best positioned to deliver consistency, repeatability and most importantly the elusive quality of biomimicry.

Chapter 7 Applications of 3D IJP to Aid Enabling Technologies

In anticipation of establishing the technical feasibility of the 3D IJP fabrication process for sacrificial microvascular facsimiles three potential applications that may be used to assist the development of 'enabling technologies' were forward tested. As consistency and repeatability in the fabricated microvascular facsimiles had not been achieved, these experiments were limited to short proof of principle trials.

7.1 Fabricating Three Dimensional Microvascular Networks within Microfluidic Devices for use in the Validation of '*in silico*' Models.

Extracted from 'The Use of Inkjet Printing and Thermal Phase Change Inks to Create Sacrificial Prevascular Networks'. Peer reviewed and presented at IS&T Printing for Fabrication Conference, Manchester, Sept. 2016

7.1.1 Introduction

Although the hemodynamic principles and physiological structures of the microvascular system are well understood, designing a spatial layout for a physiologically relevant 3D microvascular network remains beyond the capabilities of tissue engineers. The design of the network must be physiologically relevant to be effective, i.e. it must account for pressures and flows within the network so that at maturity the tissue replacement construct is well perfused and allows sufficient 'mass transfer' to occur. Previously, 2D 'vascular tree' *in silico* models had begun to be validated with the use of 2D microfluidic devices. These devices were typically fabricated using stereo lithographic or micro-moulding processes (Janakiraman, Kienitz, & Baskaran, 2007a). However, such fabrication processes do not lend themselves well to the replication of complex 3D micro-dimensioned structures that attempt to replicate the tortuosity of three-dimensional microvasculature.

Physiologically relevant 3D designs are needed for tissue engineered microvascular networks to ensure that the networks are able to provide efficient 'mass transfer' to surrounding cells. At present, there is a dearth of 3D '*in silico*' models for microvascular networks that may be correlated to the absence of suitable 3D microfluidic devices for use as validation tools.

The study of vascular patterning that is fundamental to the study of hemodynamics was founded on the seminal work of Cecil Murray published in 1926 (Murray, 1926). Murray proposed that the self-organisation of the anatomical vascular system is underpinned by the principle of minimum dissipation of energy so that the metabolic operating costs of the circulatory system are minimised. This hypothesis was

enshrined in the equation known as Murray's Law, which proscribed the optimal radii of two daughter vessels resulting from a bifurcation to that of the radius of the parent vessel. Murray's Law still holds when bifurcations from a parent channel to two symmetric daughter channels are being considered on a two-dimensional plane. Furthermore, it has been used to optimize mass transport within a 2D network while similar studies have validated the underlying principles of these 2D in-silico models using microfluidic devices (Janakiraman et al., 2007a) (J. Y. Lee & Lee, 2009). The fabrication of microfluidic devices for validating 2D in silico models is well served by current AM technologies (e.g. micro-stereolithography). The maximum resolution of the device is ultimately bounded by the minimum layer thickness of the AM technology. However, there are many reported uses of microchannels with pseudo microvascular dimensions (albeit with rectangular channels) e.g. Grogan et al 2013 making 20 μm features with a 100 μm layer thickness, Gauvin et al 2012 making 100 μm features with 100 μm layers, Fozdar et al 2011 40 μm features with 100 μm layers (Grogan et al., 2013) (Gauvin et al., 2012) (Fozdar, Soman, Lee, Han, & Chen, 2011).

Murray's Law has held sway in the field of vascular patterning even though hemodynamic behaviour in three dimensions has started to be investigated. In three dimensions, asymmetric branching is clearly a natural anatomical feature. Our own vasculature does not 'optimally' arrange itself into rows of symmetrical conduits that might be found for instance in a modern heat exchanger. Kim et al telegraph the emerging interest in three dimensional structures by applying 'constructal law' most commonly found in the thermodynamics of non-equilibrium systems to vascular patterning (S. Kim, Lorente, Bejan, Miller, & Morse, 2008) (Bejan, 1997) (Bejan, 2000). Constructal law states that,

For a flow system to persist in time to live it must evolve in such a way that it provides easier and easier access to the currents that flow through it.

By the application of constructal law to 3D vascular patterning Kim et al are able to demonstrate that stacked optimal 2D networks produce a sub-optimal outcome in the 3D construct as a whole.

The work of Mondy et al in 2009, where micro CT scanning was used as a tool to reverse engineer whole vascular trees added further momentum to the investigations (Mondy & Piegler, 2009). The growing interest in biomimetic 3D pseudo vascular structures quickly spawned a number of important revisions to the hegemony of Murray's law. In 2010, Savage et al hypothesised that the trade-off between 'effective space filling' and 'hydraulic costs' was a better predictor of vascular structure in plants than the Murrays' original principle of minimal dissipation (Savage, Bentley, &

Enquist, 2010). In 2012, Yang and Wang demonstrated that an out of plane angle between parent and daughter vessels was a necessary condition for efficient 3D volume filling (J. Yang & Wang, 2012). Most recently the revisions have closed in on Murray's original premise. In 2016, A. Miguel expounded a novel hypothesis regarding networks that showed that asymmetric branching in daughter tubes if combined with optimised but unequal vessel lengths (i.e. the larger daughter tube must have a longer length than the smaller daughter tube) was a viable outcome for an optimised total network in terms of both geometry and flow resistance (Miguel, 2016). Finally Stephenson and Lockerby 2016 showed that Murray's law is only optimal for symmetrical bifurcating networks when considered over the entire network, but suboptimal for asymmetric bifurcations when considered over the entire network (Stephenson & Lockerby, 2016). Stephenson and Lockerby then proceeded to present a general law for the design of complete symmetric and asymmetric networks.

It is clear that the field of vascular patterning is in a state of flux at present, as researchers have started to consider the importance and implications of three-dimensional asymmetric vascular networks in nature and anatomy. For researchers who wish to apply vascular patterning knowledge to the design of 3D microvascular networks, it is important to note that the research is dominated by a top down modelling approach i.e. the work is modelled from the macro to the micro. Furthermore, few of the 3D *in silico* models described in recent literature have been validated. Validation may be of marginal relevance at the macro scale of vascular patterning since there is limited physiological interaction between the engineered construct and the surrounding tissue. However, at the micro scale the interaction between the engineered microvascular construct and the tissue that it serves is of the utmost importance.

The rapid emergence of the theoretical principles underpinning three-dimensional biomimetic vascular patterning, means the absence of suitable tools to validate *in silico* models (that embody these principles) is a non-trivial matter. It was noted that prior to the recent emergence of 3D microvascular tree models, 2D vascular tree networks were being validated with 2D microfluidic devices. It is therefore not unreasonable to consider that the provision 3D microfluidic devices will enable 3D microvascular tree models to be validated.

The comprehensive review of microfluidic techniques for development of 3D vascularised tissue (Hasan, A. et al, 2014) considers a plethora of fabrication techniques from simple needle-based moulding to advanced direct and indirect microfabrication techniques. Whilst the reviewed techniques now produce a range of

cylindrical conduits in a variety of dimensions, all conduits were situated on a two-dimensional plane. The exception to this rule was the omnidirectional direct ink writing strategy developed by Wu et al, which was able to demonstrate a bifurcating hierarchy of cylindrical microchannels across three dimensions but was limited to a minimum 200 micron diameter conduit. Whilst the formation of encapsulated three dimensional non planar circular channels is now achievable, the conduit's diameter and the tortuosity do not yet approach that needed to replicate a microvascular network (Hasan et al., 2014).

Most recently a novel protocol has been published by Heintz et al, which demonstrates a procedure for laser based hydrogel degradation to create three dimensional encapsulated conduits for microfluidic experiments that significantly enhances the minimum conduit diameter that may be fabricated (Heintz, Mayerich, & Slater, 2017). The technique relies on 'layer by layer' degradation of the hydrogel, but it is unclear from the literature what the minimum layer thickness that can be achieved is, and furthermore whether the geometry of a conduit remains constant if it diagonally transverses multiple fabrication layers on the z axis. Furthermore, the equipment has x, y and z axis limitations of 450 micron, 450 micron and 1.5 mm respectively, which limits its use as a method for fabricating microfluidic devices of sufficient size to be used to validate in silico models of clinically relevant tissue volumes (see <https://www-jove.com.sheffield.idm.oclc.org/video/55101/image-guided-laser-based-fabrication-vascular-derived-microfluidic>).

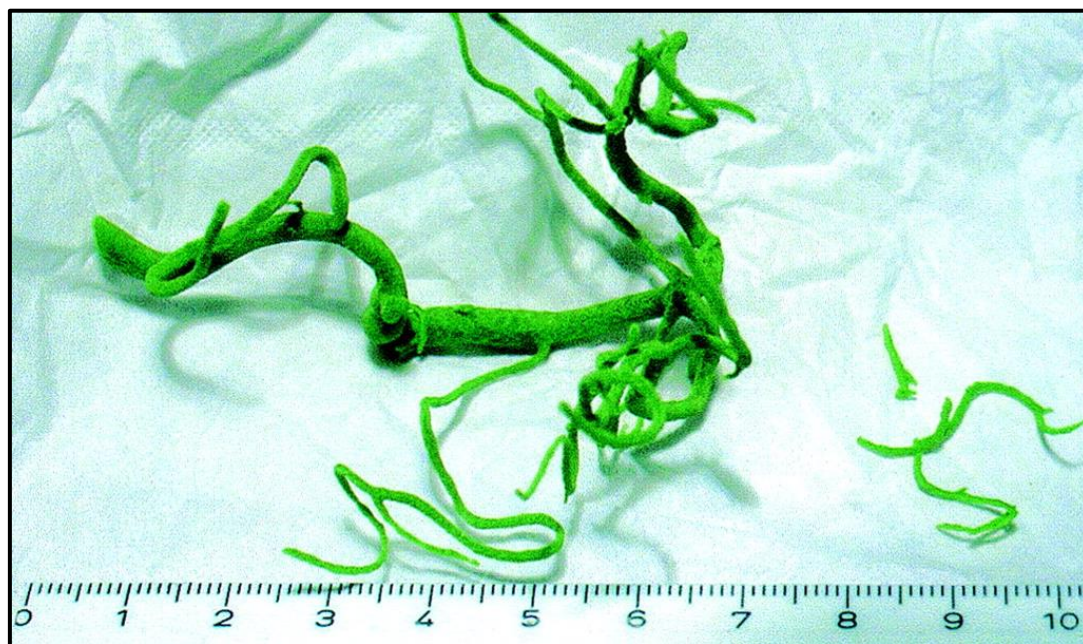


Figure 55 Model of cerebral vasculature prior to encapsulation in PDMS, (Wetzel et al., 2005).

The use of sacrificial or ‘lost-wax’ processes has become commonplace in replicating a wide range of macro scale vascular features such as that shown in Figure 55. On the micro scale, Dr C. Tse has recently replicated an aneurism within a 2.5D microfluidic device using a lost wax process with the wax being deposited by Inkjet printer, and then encapsulated in PDMS prior to the wax being sacrificed (Tse, 2015).

7.1.2 Fabrication Procedure

Recent advances in the use of IJP as a 3D AM technique have enabled the fabrication of sacrificial 3D microvascular facsimiles (without the use of support material for overhanging structures), in conjunction with a traditional 2.5 D microfluidic substrate. The use of thermal phase change inks allows the microstructures to be constructed and encapsulated in Polydimethylsiloxane (PDMS), before being sacrificed without damage to the PDMS as shown in Figure 56 below.

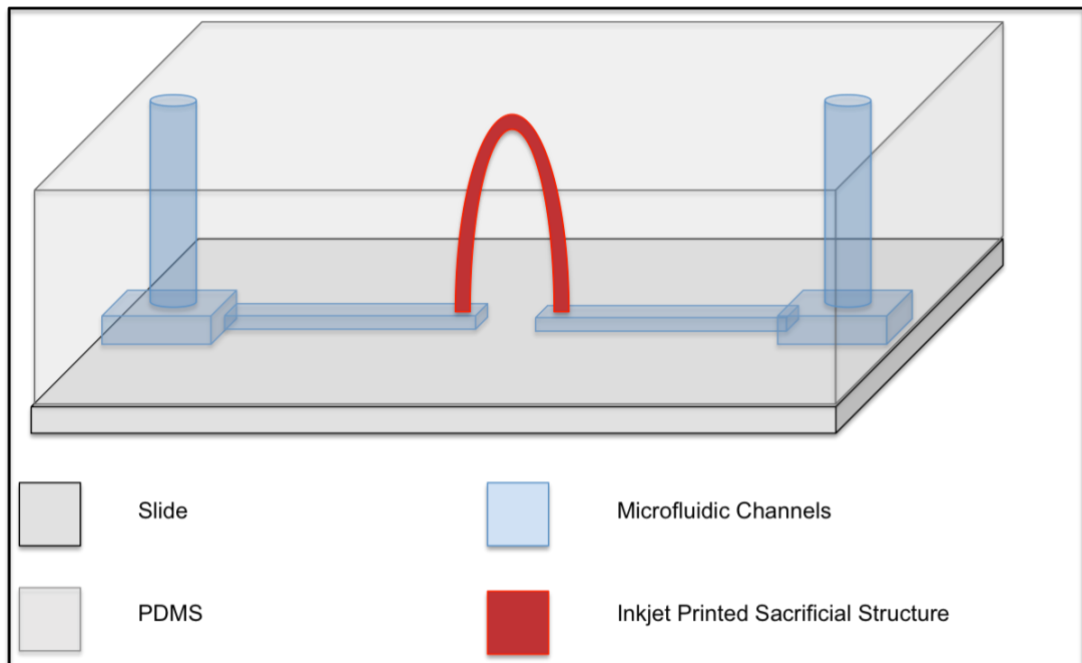


Figure 56 Schematic representation of an Inkjet printed 3D microfluidic device

The 2.5 D microfluidic channels (350 μm in width) were designed with ‘Inkscape’ software (open-source vector graphics editor), then converted into ‘*dxg*.’ files and fabricated with a ‘Graphtec Craft Robo Pro’ vinyl cutter (Graphtec Corp. California U.S.A.) using a double layer of 50 μm thickness cast matt self-adhesive vinyl film (total thickness of 100 μm) (KPMF Ltd. Newport, U.K.), creating conduits with a cross sectional area of 3500 μm^2 . The film was applied to a glass slide, then the negative portion of the film was removed, leaving the 2.5D microchannels intact on the slide as shown in Figure 57 overleaf.

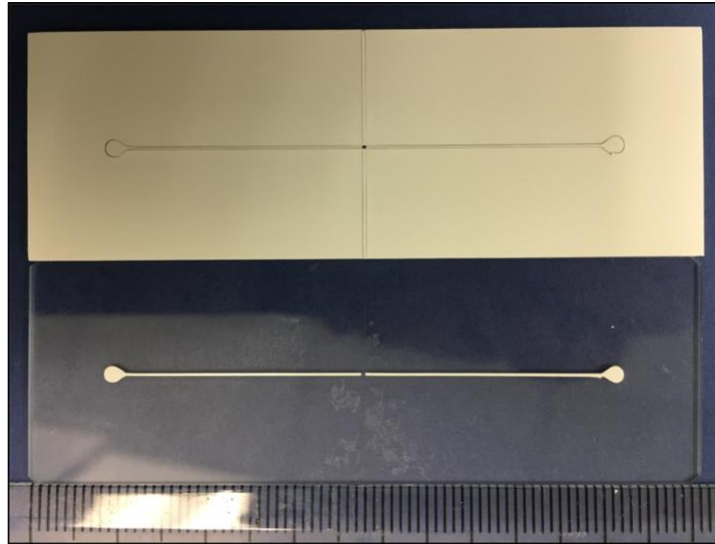


Figure 57 2.5D vinyl microfluidic channels cut using the 'Graphtec Craft Robo Pro' and applied to a glass slide (channel cross-sectional area of $3500 \mu\text{m}^2$)

The 3D sacrificial microvascular facsimile (of an arteriole bifurcating into two capillaries before reconnecting to a veinule) was then Inkjet printed in Paraffin wax to connect the terminals of the 2.5D microfluidic channels as shown in Figure 58.

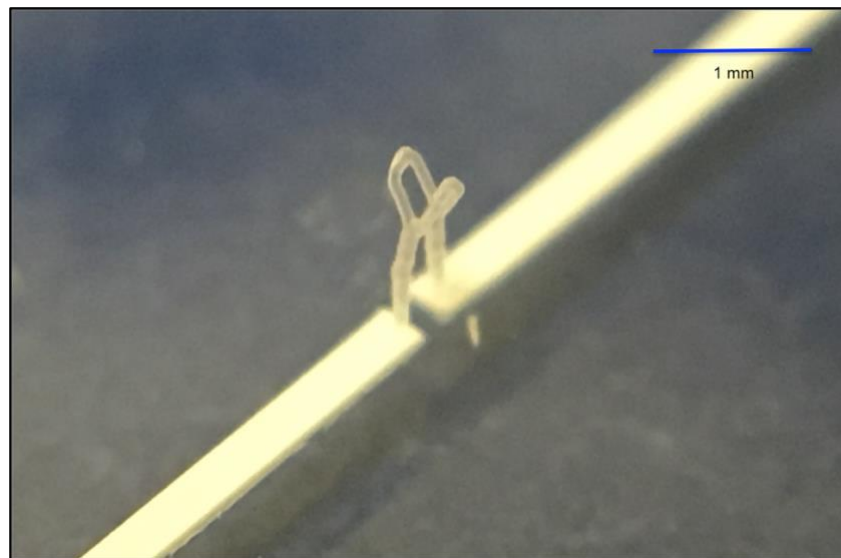


Figure 58 The 3D sacrificial facsimile printed to connect the terminals of the 2.5D microfluidic channels

The complete structure was then placed in a petri dish, and PDMS was carefully dispensed into the dish by syringe until the structure was submerged. The PDMS was then allowed to cure at room temperature for 48 hours (allowing sufficient time for air bubbles to escape). Once cured, the PDMS encapsulated structure was removed from the petri dish.

The PDMS was then trimmed to match the dimensions of the glass slide (as shown in Figure 59 below), then it was removed from the glass slide and the glass slide (complete with the sacrificial vinyl microfluidic channels) was discarded.

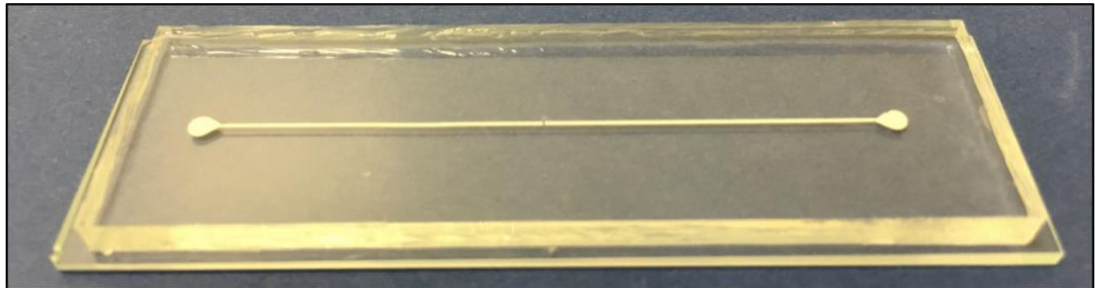


Figure 59 The 3D microfluidic device encapsulated in PDMS.

In order to remove the sacrificial paraffin wax structure from the PDMS, the PDMS was submerged in water heated to 80 °C and sonicated for 5 minutes. Whilst the PDMS was still submerged, a syringe was applied to the terminal ends of the 2.5D microfluidic conduits and a gentle negative pressure was manually applied until water flow through the 3D conduits was evident. The device was allowed to dry overnight.

The PDMS structure and a secondary glass slide were then plasma treated using a 'Zepto' plasma system (Diener Electronic, Ebhausen, Germany) and carefully placed together until bonded. After the plasma bonding treatment of the PDMS, holes (1 mm diameter) were punched into the circular terminals of the microfluidic channels and matching diameter tubing was attached, as shown in Figure 60 below.

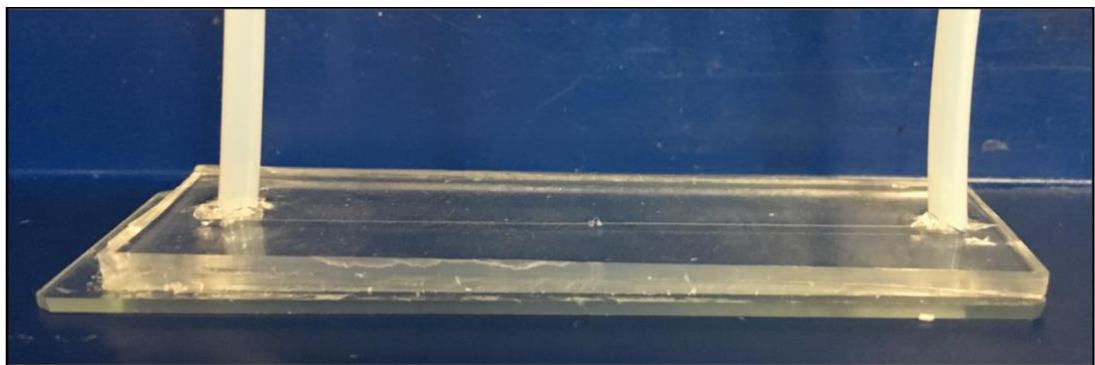


Figure 60 Completed microfluidic device

7.1.3 Conclusion

Validated three-dimensional in silico models for microvascular networks are needed to provide the platform for designing physiologically relevant microvascular networks. New theoretical principles, which underpin three-dimensional biomimetic vascular patterning show that asymmetric networks are needed to efficiently perfuse

irregular 3D volumes. In the past 2.5 D in silico models of vascular tree networks were validated with 2.5 D microfluidic devices. Therefore, the absence of 3D microfluidic devices to validate 3D in silico models is a non-trivial matter.

In this instance, 3D Inkjet printing and thermal phase change 'inks' have been used to make sacrificial 3D microvascular facsimiles that are initially employed in the production of the biomimetic 3D microfluidic devices. A 3D bifurcating capillary arch facsimile was printed onto 2.5 D microfluidic channels, thereby providing the basis for a novel 3D microfluidic platform. The cross-sectional area of the 3D printed parent arteriole ($3421 \mu\text{m}^2$) was in good agreement with the cross-sectional area of 2.5D microfluidic device ($3500 \mu\text{m}^2$). The reduction in lumen diameter from the parent arteriole (66 micron) to the daughter capillary (52 micron) is compliant with Murray's law. This fabrication technique enabled structurally sound three-dimensional microstructures to be constructed (without the need for support material) and encapsulated in PDMS to form a microfluidic device, prior to being sacrificed without damage to the PDMS.

The resulting microfluidic device represents an improvement on current microfluidic technology in terms of the minimum conduit diameters that can be achieved in 3D. Furthermore, the device exhibits accurate reproductions of bifurcations and approaches the degree of tortuosity that may be found in capillaries. The microfluidic device is not only inexpensive but further improvements are possible. Standard printheads are available with aperture sizes to a minimum of 20 micron are available, so further reductions in conduit diameter may be achieved. This novel microfluidic device may prove useful in analysing aspects of flow through conduits that reproduce the hierarchical structure, dimensions and tortuosity found in microvasculature, thus assisting in the validation of future 3D in silico models for the design of physiologically relevant microvascular networks for use in Tissue Engineering.

7.2 Co-fabrication of a Primary Engineered Tissue Scaffold in Conjunction with a Microvascular Scaffold

7.2.1 Introduction

Microvascular networks have a symbiotic relationship with surrounding tissues, relying on those tissues for physical support whilst providing the tissues with biological support. The microvascular network (and the scaffold for it) must be designed so that it adequately perfuses the primary engineered tissue, providing the mass transfer needed for cells to thrive, whilst the extra cellular matrix (ECM) of the engineered tissue provides mechanical support to the microvascular network.

The fact that it is not currently feasible to insert or 'retrofit' a three-dimensional microvascular network into the primary engineered tissue, nor is it possible to engineer a tissue around an unsupported (but fully functional) microvascular network, has a significant implication for TE researchers pursuing the objective of engineering complex vascularised tissue. The implication is that the 'symbiotic relationship' may well necessitate the co-fabrication of the primary engineered tissue scaffold in conjunction with the microvascular scaffold in order to provide it with mechanical support.

Having fabricated 3D sacrificial microvascular facsimiles with high aspect ratios and without the use of support materials, which might be dipped or coated with a suitable biocompatible material before the microstructures are removed to create microvascular scaffolds, encouraged consideration of complimentary (or at least non-conflicting) materials and methods that might be used to fabricate the scaffold to accommodate the cells for the primary engineered tissue. Figure 61 (following page), outlines the relationships between the fabrication techniques and materials that must be considered and resolved, in order to undertake the coproduction of a microvascular scaffold with a scaffold for the primary engineered tissue in order to successfully engineer a complex vascularised tissue.

The research question in this case is two-fold a, is there a complimentary combination of materials and processes to produce a microvascular scaffold and then fabricate the primary engineered tissue scaffold, and b, will the primary engineered scaffold provide support to the microvascular scaffold?

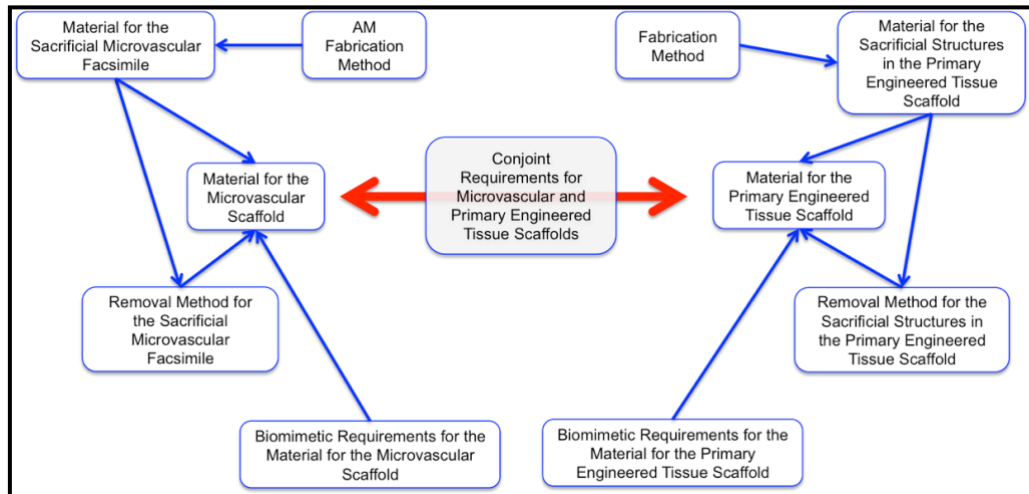


Figure 61 The relationships between material selection and fabrication method for a ‘coproduced scaffold’ for complex vascularised tissue

In this case, gelatin (denatured collagen) was thought to be an appropriate biocompatible material for the microvascular scaffolds, since the smooth surface of gelatin provides a biomimetic surface that facilitates cell attachment, proliferation and migration of endothelial cells (Golden & Tien, 2007). Collagen (the precursor to gelatin) is the major component in the ECM and may therefore be considered an ideal scaffold material for the primary engineered scaffold. Figure 62 below, shows the residual collagen structure from the decellularised dermis. Cells see collagen as ‘self’ and fibroblasts attach to a collagen scaffold, proliferate and migrate readily, providing the structure has appropriate porosity and interconnectedness.

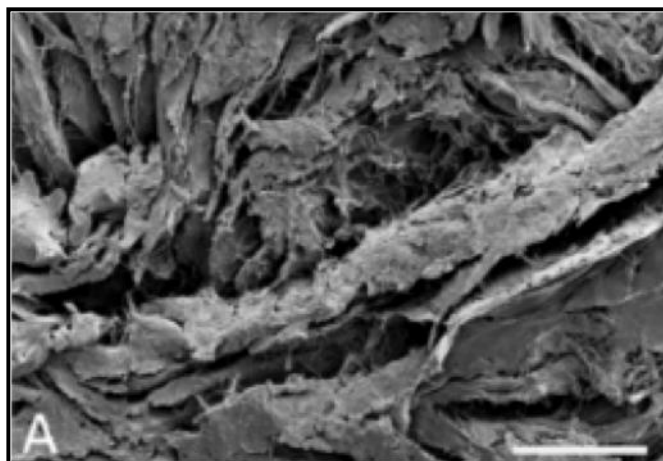


Figure 62 SEM of decellularised dermis (Wessels, 2014)

Freeze drying is a frequently used technique for introducing micro scale porosity into a collagen scaffold. In the seminal work of Yannas et al, micro scale porosity was fabricated by means of freeze drying and pore sizes ranging from 25 to 125 micron were found to be appropriate for fibroblast seeding and migration (Yannas, Lee,

Orgill, & Skrabut, 1989), although Chang found that pore sizes in the region of 160 μm were suitable (C. C. Chang et al., 2011). However, excessive porosity decreases scaffold strength, decreases the available scaffold surface area for cell and increases the distances required for cell migration.

7.2.2 Apparatus, Materials and Methods

7.2.2.1 Collagen

Collagen is the major component in the ECM and may therefore be considered an ideal scaffold material for the primary engineered scaffold. There are 29 genetically distinct types of collagen, however if the human dermis is used as a fairly generic example, Collagen Type I (80%) represents the largest component with Type III (15%) and Type IV forming the remainder. Collagen Type I (prepared from Bovine neck ligament) was selected as an appropriate material for the primary engineered tissue scaffold (Sigma – Aldrich U.K.).

Figure 62 shows the residual collagen structure remaining after decellularization of the dermis, which illustrates the form of the collagen structure in its functional state as an ECM. There is a need to endeavour to replicate that form in a TE scaffold for a primary engineered tissue, in order to minimise the extent to which the TE scaffold will need to be remodelled by fibroblasts and collagenases to create a functional ECM (Wessels, 2014). However, sufficient porosity must remain in the structure to enable cell seeding.

Comparing the freeze-dried collagen scaffold shown in Figure 63 (following page) with the decellularised ECM shown in Figure 62 (previous page), highlights the similarities in form that can be achieved by using the freeze-drying process. The use of freeze-drying to form collagen based TE scaffolds was initially proposed in the seminal works of Burke et al, and Yannas et al, which led to the first commercially available product (Integra™) for the treatment of burn wounds (Burke, Yannas, Quinby, Bondoc, & Jung, 1981) (Yannas, 1980). More recent developments in the field of burn care include Matriderm™, (now considered to be the fastest vascularizing dermal substitute), which also incorporates a freeze-dried collagen structure (Rnjak, Wise, Mithieux, & Weiss, 2011).

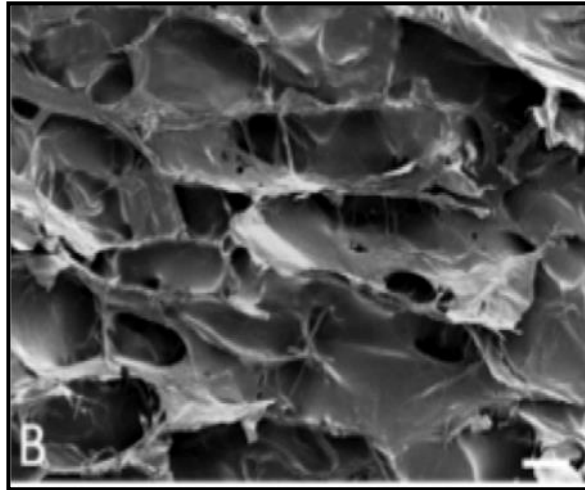


Figure 63 SEM of a freeze dried collagen scaffold (Wessels, 2014)

As the TE scaffold required for the primary engineered tissue will be subject to the forces of perfusion, it was considered appropriate to mimic the concentrations of commercially available collagen scaffolds that are sufficiently robust for clinical use. A sample of Matriderm™ was procured to act as a standard for the preparation of the collagen scaffolds presented in this research.

7.2.2.2 Elastin

Burke et al established the need for the freeze dried collagen scaffold to remain substantially intact during cellularization for a period of not less than 21 days for ‘neocollagenesis’ (remodelling) to take place, so that the mechanically superior ECM is formed prior to the collagen scaffold becoming structurally unstable through degradation (Burke et al., 1981). For this reason, secondary biomolecules are often used within commercially produced collagen based TE constructs. Elastin is favoured as a secondary biomolecule since it is produced extremely slowly by fibroblasts, with the majority being created during neonatal development and the first five years of life. Elastin has a half-life of approximately 70 years so is turned over very slowly, indeed elastin expression in grafted wounds can take up five years to return to normal levels (Jones, Currie, & Martin, 2002). The ratio of collagen to elastin in the dermis varies from 2% to 4% (Rosenbloom, Abrams, & Mecham, 1993) depending on the local requirements for flexibility in the dermis. On average the ratio is approximately 3%. Matriderm™ is cited as containing 3% elastin (Rnjak et al., 2011) and has been used successfully in many demanding clinical applications.

The use of insoluble elastin in scaffolds has been shown to cause calcification whereas the use of an soluble elastin has been shown not to (Daamen et al., 2008; 2006). Elastin hydrolysate (E6527 from bovine neck ligament Sigma Aldrich U.K.)

was selected as it is a soluble elastin formulation dissolving readily in water and combining conveniently with Collagen I during the homogenising process.

7.2.2.3 Method for the Preparation of Collagen-Elastin Solutions

The base collagen solutions were prepared in the first instance using a method described in many papers that appears to be founded in the pioneering work of Yannas albeit using a blend of collagen and glycosaminoglycan (Dagalakis, Flink, Stasikelis, Burke, & Yannas, 1980a; 1980b). It appears that most methods for the preparation of collagen – elastin solutions are a variation on this method although the recent availability of a soluble elastin hydrolysate simplifies previous techniques.

Collagen Type 1 is mixed with a weak (0.5 M) solution of acetic acid (also Sigma). The solution is blended with a high shear, high-speed homogeniser (IKA, Staufen, Germany) at 15,000 rpm for 20 minutes. The use of a high shear mixer enables more concentrated mixes of collagen to be blended than mechanical stirring. To prevent the temperature increasing and denaturing the collagen, the mixing takes place in an ice bath. After the initial twenty minutes mixing soluble elastin (Sigma) is added at a pre-determined rate to achieve the required concentration and the solution is re-blended for a further twenty minutes. The solution is then carefully neutralised to pH 7, using a strong solution of Sodium hydroxide (Sigma) so that dilution of the concentration of collagen elastin in the solution is minimised. The solution is refrigerated pending ultracentrifugation.

In order to improve the mechanical properties of the collagen, the solution was concentrated by ultra-centrifugation. The prepared solution was divided into aliquots and centrifuged on a Beckman Coulter Optima L90K high-speed centrifuge at 20,000 rpm on a Type 45 Ti rotor (relative centrifugal force or r.c.f. = 46377.8 x g) for 30 minutes at 40° C. Upon completion a volume of the supernatant equivalent to half the initial quantity of solvent was removed from the vessel and discarded. The pellet and remaining supernatant were then re-blended prior to refrigeration.

The process of homogenising, ultra-centrifugation and freeze-drying presents three opportunities to alter the structural properties of the scaffold by tuning the dimensions of the C-E structures, the total volume of pores, pore size and the alignment and interconnectedness of the pores. On initial inspection, concerns over the weight of the scaffold – measured as weight per unit of surface area - may appear to be somewhat academic. Altering the volume of solution to be freeze-dried relative to the area the solution is to be freeze dried on, can accommodate the use of varying concentrations and still produce a similar result for weight by surface area (as opposed to density by volume) because the freeze-drying process will of course

eventually reveal the total solids content of the formulation as related to the surface area of the vessel. To enable simple and straightforward comparisons between solutions the target weight per area of the final finished scaffold for all experiments has been set at 26 g/m² to match the MatridermTM samples and concentrations and volumes have been adjusted to achieve this.

7.2.2.4 Freeze Drying

Freezing

The process of freezing the C-E solution leads to the propagation of ice crystals; collagen and elastin fibres in the solution are squeezed in between the growing ice crystals in the freezing solution. The final pore structure that is revealed after sublimation depends on the underlying thermodynamic processes governing the propagation of the ice crystals during the freezing process. These underlying processes are the rate of nucleation i.e. the number and speed at which the ice crystals form, and the rate of diffusion i.e. the speed at which the cooling moves away from the propagating crystal and diffuses through the protein structure defining the size of the crystal. Put simply, the colder or faster the freezing process the greater the speed of nucleation, similarly the faster the rate of diffusion the greater the size of the crystal. In general, the variables to be controlled during the process are well known and documented (Madaghiele, Sannino, Yannas, & Spector, 2008).

Concentration of the solution and the weight per area of solution - gives the total fibre density and porosity. The concentration of the solution also affects the speed of diffusion. More concentrated solutions slow the rate of diffusion and tend to lead to the formation of smaller crystals. Less concentrated solutions increase the speed of diffusion resulting in larger pore sizes. However overly porous scaffolds that appear to maintain their volume in a vacuum may quickly self-compact giving way to the effect of atmospheric pressure once removed from the vacuum.

The samples were frozen at -80° C overnight in single sample size moulds that comprised a stainless-steel base and thick PDMS walls. The following morning the samples were quickly demoulded on freezer packs and returned to the freezer for storage.

Lyophilisation / Sublimation

The process of lyophilisation or freeze-drying relies on the phenomena of sublimation where the material changes from a solid phase directly to a gas phase without passing through the liquid phase. For the sublimation process to work, water must be frozen (e.g. -20° C and 1 bar) then placed in a vacuum so that the pressure

drops and takes the solid through to the vapour phase at 1 mbar. At this point the ice crystals will begin to sublime to vapour and providing there is a colder surface nearby that the vapour can condense on the vacuum will be adequately maintained until the process is complete.

The samples were freeze-dried for a period of 24 hours (in individual flasks) at 0.05 mbar, with the condenser running at -50°C ('Modulyo' freeze dryer, no longer produced).

7.2.2.5 Cross Linking

The mechanical properties of a freeze-dried collagen scaffold can be improved by cross-linking. Although elastin hydrolysate is itself a cross-linking material (Skopinska-Wisniewska et al., 2009), the necessary additional cross-linking of collagen helices typically relies on the modification of amine and carboxyl groups within the collagen molecules, to allow the formation of covalent bonds. Cross-linking can be achieved by chemical, enzymatic or physical processes. In general chemical and enzymatic processes used to cross-link collagen scaffolds are cytotoxic, such as glutaraldehyde or formaldehyde (as for gelatin based scaffolds) (Sionkowska, Skopinska-Wisniewska, Gawron, Kozłowska, & Planecka, 2010) and can be discounted.

Ultra-violet irradiation (UV) and dehydrothermal treatment (DHT) are physical cross-linking processes and both produce similar results, in terms of cross-link density (Haugh, Jaasma, & O'Brien, 2009). Of the thermal processes, DHT is generally more effective with the longest crosslinking cycles causing the least denaturation of the collagen. DHT has a marginal advantage over UV by further reducing the residual water or water-ethanol that remains in the construct after the freeze-drying.

Thermal crosslinking tends to lead to an improvement in the mechanical properties of collagen elastin compounds. The duration and temperatures achieved during the process can affect the number and strength of bonds. Short periods of modest temperatures e.g. two hours at 60°C lead to significant increases in the Young's modulus of the scaffold. The prepared samples were cross linked by DHT at 60°C for 12 hours. After removal the samples were placed in Petri dishes and vacuum packed, complete with desiccants and moisture indicator cards, then placed in the refrigerator.

7.2.2.6 Characterisation Techniques

Scanning Electron Microscopy SEM

Samples of the dry scaffold were prepared by cutting two sections, approximately 2 mm by 2 mm, from the centre of the dry scaffold and mounting them face up and face down respectively on the self-adhesive stub. A further strip, of approximately 4 mm in length and 1 mm width, was cut from the edge of the scaffold and the divided in two. One is mounted with the moulded side face exposed and the other mounted with the cut face exposed. The samples were prepared for the electron intense environment of the SEM imaging chamber by means of the See Vac Auto 'conductavac' sputter coater.

Once a sample was placed in the imaging chamber, representative images for the surfaces of the scaffold were taken at magnifications of 3200, 1600, 800, 400, 200 and 100. This enabled the sequential identification of CE strands, pore size and interconnectedness, the existence of 'collagen - elastin sheets', pore orientation and general topography.

Mechanical Testing

Mechanical testing was undertaken using the Bose Electroforce 3000. For the purposes of the collagen-elastin tests the Bose is operated with a micro-force load cell, capable of handling forces of 2 n to 40 n. All samples for mechanical testing were cut to an ASTM standard 'dog-bone' patterns using the Epilog Laser Mini. A test piece was cut prior to use, to check the laser settings, in order to ensure that the samples would not be damaged during the preparation procedure.

If samples were to be tested 'wet' they were hydrated in deionised water for one hour in an incubator, then excess moisture was removed by resting the sample on a paper towel (5 minutes each side).

Prepared samples (dog-bone) are applied in to the grips of the Bose so that they are secure. The sample is pre-tensioned by increasing the distance between grips until a small amount of force registers on the load cell. The force and strain are then tared off. The test follows the pattern of force as programmed over the test time and the displacement is recorded. The data was transferred to Excel for analysis. Stress is calculated as Force/Area. Strain is calculated as the Change in length/Original Length. Young's modulus is calculated as Stress/Strain at the desired point in the test.

7.2.3 Results and Discussion

SEM images comparing Matriderm, the decellularised dermis and collagen-elastin concentrations of 1, 5 & 10% were produced. It can be seen from Figure 64 following that as the elastin content increases, the porosity of the freeze-dried constructs reduces as the elastin begins to create a sheet like coating over the collagen structures.

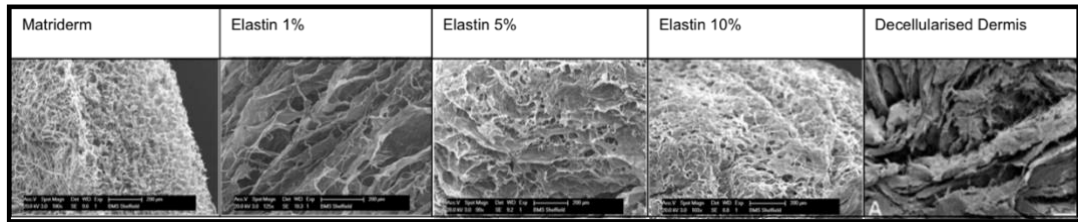


Figure 64 SEM comparison of freeze-dried collagen - elastin ratios with Matriderm and the decellularised dermis

It can also be seen from Figure 64 that the strong sheet like formation of the decellularised dermis is not matched by the structures of either the Matriderm or any of the other collagen-elastin samples.

It was found that a collagen solution prepared to a 1.25 % concentration (prior to freeze drying) gave a scaffold density and thickness similar to that of MatridermTM and presented near identical mechanical properties when tested for tensile strength. The ultimate tensile strength of Matriderm was tested using the Bose Electroforce 3000. The results are shown in Figure 65 overleaf gave a Young's modulus of 7.5 kPa.

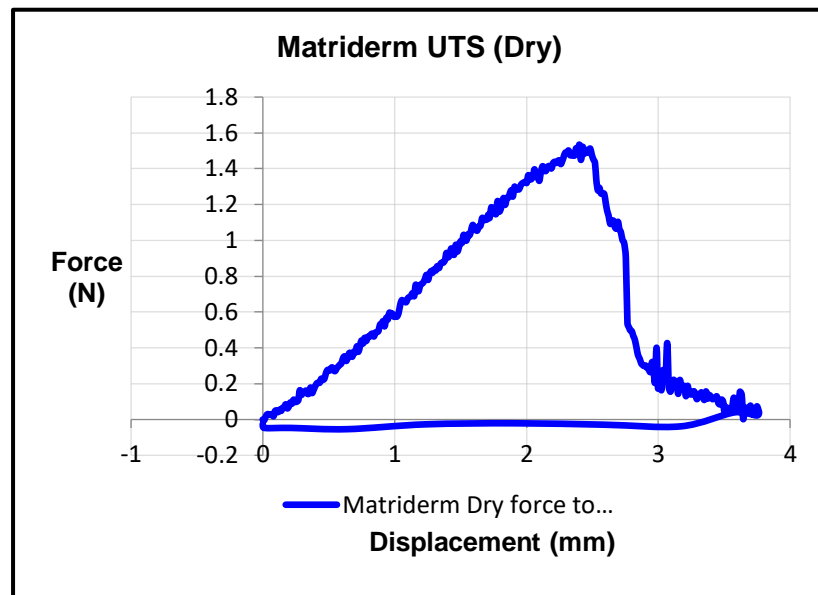


Figure 65 The ultimate tensile strength of Matriderm measured using the Bose Electro force 3000 with 2 – 40 N load cell.

The Young’s modulus value is in good agreement with literature (Varley et al., 2016). The subsequent measurement using hydrated Matriderm failed to give a result. Four samples (dog bone shape) were then placed together and hydrated en masse, prior to being tensioned within the grips, producing the result seen in Figure 66 below.

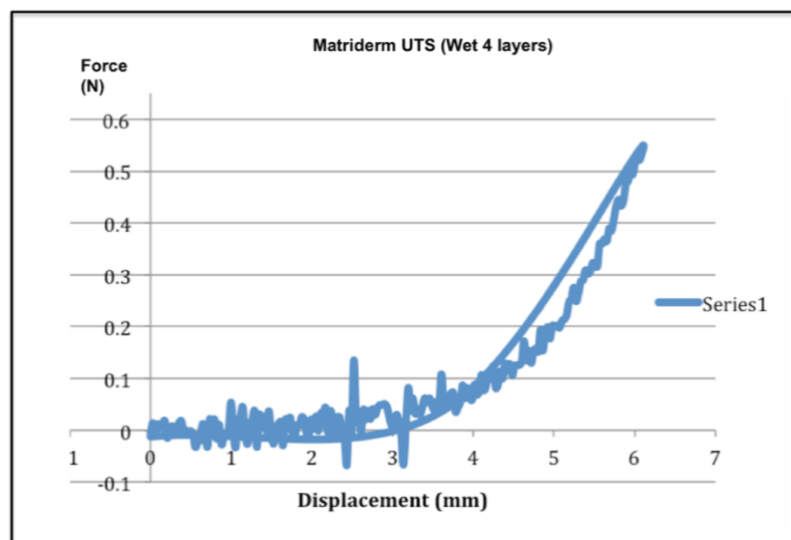


Figure 66 The ultimate tensile strength of four layers of hydrated Matriderm as measured by Bose Electro force using 2 – 40 N load cell.

From Figure 66 above that the peak force applied was approximately 0.55 N as compared with 1.5 N as applied in Figure 65; additionally it is noted that the sample thickness in Figure 66 was four times that of the sample thickness in Figure 65, indicating a significant reduction (factor of 10) in load bearing capacity. Additionally, careful observation of the unloading curve show that it has a small but negative value

between 3 and 0 mm of displacement, which indicates that the curve is not the traditional J curve associated with many biomaterials (as the tested material recovers its neutral state subsequent to hysteresis). Close observation of the test revealed that the material had permanently lengthened, suggesting the bulk properties (particularly the porous structure) of the sample had been deformed.

7.2.4 Interim Conclusion

The result was not in good agreement with literature since the vast majority of literature cites ultimate tensile strength as measured with dry collagen samples.

Furthermore, it indicates that the practise of measuring the UTS of freeze-dried collagen in a unhydrated state may produce erroneous or even irrelevant results if the engineered construct is going to be used in a hydrated state e.g. in vivo. Varley et al. have now published a comprehensive assessment of this phenomena (Varley et al., 2016)

The poor mechanical performance of the hydrated collagen-elastin scaffold suggests that this approach to the coproduction of the microvascular scaffold and the primary engineered tissue scaffold must be adapted or abandoned.

7.2.5 Further Research Opportunities

Further attention might be paid to increasing the effectiveness of the cross-linking strategy for the freeze-dried constructs. Recent literature suggests that the use of genipin as a cross linking agent for collagen leads to significantly improved mechanical performance; although, as with the majority of literature, the mechanical testing is undertaken with the scaffold in its dehydrated state (X. Zhang et al., 2014).

Alternatively, a different source of mechanical support for the collagen-elastin scaffold could be provided by the gelatin of the microvascular scaffold. Freeze dried gelatin exhibits a degree of stiffness that is not anticipated from the mechanical properties that it displays in its set or solid state. If the microvascular scaffold were to provide a source of mechanical support to the collagen-elastin scaffold, a bonded interface between the two scaffolds would be needed. A number of permutations for achieving a bonded interface between collagen-elastin and gelatin were tested in order to inform the sequencing of operations in future fabrication experiments. It was found that applying a collagen elastin solution onto previously freeze dried gelatin, produced a distinct but bonded interface as shown in Figure 67. However, the converse did not apply. It can be seen from the sample on the right of the Figure below, that the gelatin has dissipated into the freeze-dried collagen structure and while there is a clearly a bonded structure the interface is not delineated.

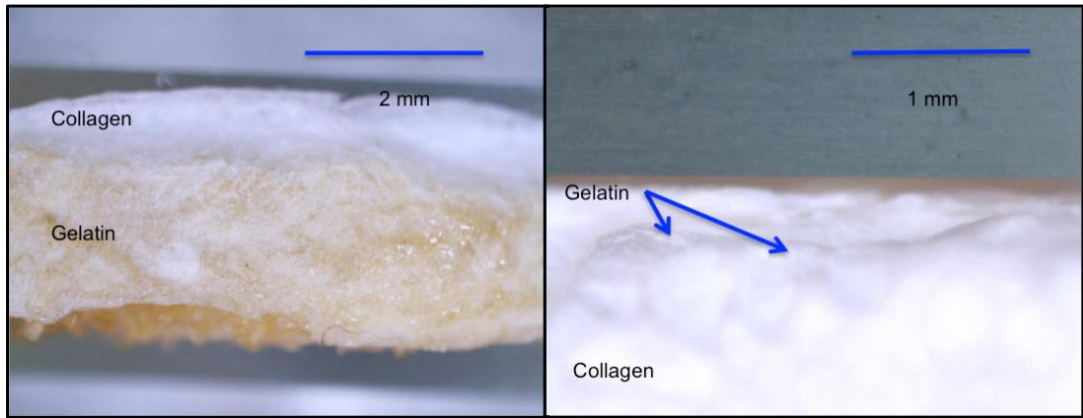


Figure 67 Left, Collagen–elastin solution applied to freeze dried gelatin and subsequently freeze dried. Right, gelatin solution applied to freeze dried collagen and subsequently freeze dried.

This could indicate that if the sacrificial microstructure were fabricated using a phase change material that could be removed by freeze drying (e.g. water), then the structure could be coated with gelatin and the freeze-drying process would remove both the sacrificial structure and alter the mechanical properties of the gelatin. Naturally, further research is required. Alternatively, as Bioprinting/bio-fabrication is primarily focussed on the rapid deposition of scaffolds and cells for the primary engineered tissue, a collaboration with a bioprinting group to further research into Tissue Replacement suggests itself.

7.3 Enhancing Cellularisation in Microvasculature

The fundamental function of a bioreactor is to provide a stable, supportive and protected environment for cells to adhere, proliferate and migrate on the experimental scaffold. In practice, 'stability' translates as control of pH, temperature and humidity, 'supportive' as enabling the mass transfer of oxygen and nutrients to the cells and removal of waste from the cells, and 'protected' as the prevention and detection of contamination (I. Martin, Wendt, & Heberer, 2004). However, practical experimental demands invite the consideration of the requirements for the tissue samples, cell seeding methods, inspection and monitoring techniques, and cell/scaffold stimulation by mechanical or bio-chemical means as further requirements to be catered for in the design of an ideal bioreactor.

Numerous perfusing bioreactors have been engineered to improve cellular responses in a wide range of TE constructs with low or intermediate vascular needs, such as bone and cartilage, but few have targeted highly vascularized, three-dimensional, multi-cellular tissues. Endothelializing a complex branching 3D microvascular network by direct cell seeding techniques also presents significant difficulties. So far, the direct seeding method has failed to produce micro-vessels with an exterior diameter of less than 30 micron for 'capillary' scale vessels (Zheng, Chen, Craven, & Stroock, 2012) (Chrobak, Potter, & Tien, 2006). This is because endothelial cells have a diameter of approximately 10 – 15 micron, which means that even the most minor agglomeration of two or three cells can cause a blockage in conduits that are approaching capillary-like dimensions. More recently Linville et al succeeded in refining the seeding and flow techniques to enhance cellular migration through 20-micron capillary channels (Linville et al., 2016). However, it must be noted that the demonstration of their novel method was limited to a simple single, short, straight conduit.

Establishing appropriate flow rates has been shown to be an important determinant of experimental outcomes. For instance, the flow of the cell suspension over or through the scaffold in the bioreactor during the critical cell-seeding phase is influential on the distribution of cells during the seeding phase. The flow patterns are also usually reproduced in the mass transfer rates achieved during the culture period when media replaces seeding solution. This two-fold effect in seeding density and mass transfer compounds the effects on the proliferation rate of the cells. Flow also provides mechanical stimulation of cells; activating cell-signalling mechanisms thereby further encouraging proliferation and migration. Flow can therefore be seen to have a three-fold effect in determining experimental outcomes (Melchels et al., 2011).

Although it is easy to envisage using optimised flow rates for enhancing cellular migration for the endothelialisation of a single capillary, the probability of agglomeration of endothelial cells during the seeding process ensures that translation from a single capillary to a network may be significantly more demanding.

It is thought that if a bioreactor were designed to maintain low seeding densities for extended periods of time, at physiologically relevant pressures and flows for micro vasculature, the frequency of agglomerations might be minimised, and cellular migration may be further facilitated. Furthermore, if the perfusive flows of the bioreactor could be periodically reversed for a short period of time, small blockages might be removed from the capillary size conduits.

If the microvascular network is re-imagined as a spatial arrangement of ‘apertures’ rather than a series of ‘leaky conduits’, it is then analogous to a macro scale semi-permeable membrane, and the technical difficulties of micro scale seeding may be reassessed from a new perspective. In 2014, publication of a novel dual-flow bioreactor was released (shown in Figure 68 below) (Giusti et al., 2014).

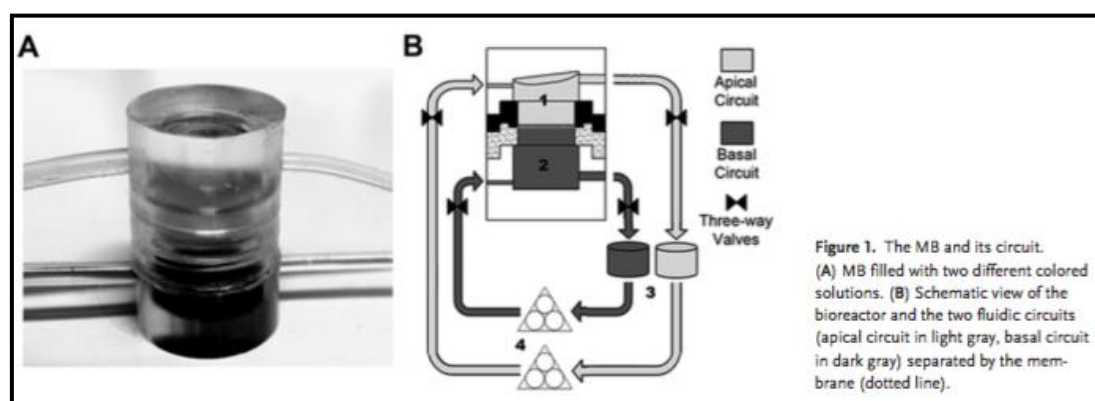


Figure 68 The ‘Dual flow’ bioreactor – utilising flow to produce a pressure differential across an epithelial membrane (Giusti et al., 2014).

The design of the bioreactor was formulated to provide an in vitro model of the permeability in epithelial tissue barriers. As such the novel element of the bioreactor was that flow through the epithelial membrane was affected by establishing a pressure differential between the two sides of the membrane, as opposed to the flow being directed through the membrane and a pressure differential being the result of the flow. It is interesting to note that in vivo, capillaries function in a somewhat similar ‘dual-pressure’ environment (see Figure 2).

The capacity of Giusti et al’s bioreactor to produce a distinct and controllable pressure differential, might be utilised in the design of a novel bioreactor suitable for

perfusing a microvascular network i.e. by providing physiologically relevant pressures at both ends of the capillary. This may also provide mechanical cues for cellular proliferation and migration, perhaps even reducing the frequency or severity of agglomerations. With such a bioreactor design, the pressure differentials might be easily and quickly reversed if agglomerations were found to be causing capillary blockages or even to enable cellularization from both ends of the capillary.

This hypothesis was tested by adapting an air-liquid interface bioreactor (QV 600, Kirkstall Ltd, Sheffield UK) to create a dual flow bioreactor enabling a pressure differential to be maintained across a 'capillary' membrane (thus ensuring that physiologically relevant flow rates and pressure differentials are maintained). The 'capillary' membrane is fabricated using 3D IJP in conjunction with thermal phase change inks to make sacrificial microvascular facsimiles which are then encapsulated in PDMS. Once the sacrificial microstructures have been removed from the encapsulating material (leaving capillary dimensioned conduits in the material) the resulting construct functions as a 'capillary' membrane.

7.3.1 Adaptation of the Bioreactor

The QV 600 bioreactor (Figure 69 overleaf) is typically used for dermo-epidermal research since its design facilitates the positioning of an air liquid interface in the middle of the bioreactor. This means that the keratinocytes of the epidermis can be positioned above the interface whilst the fibroblasts of the dermis can be perfused by serum below the interface.

In order to replicate the capacity of Giusti et al's bioreactor to produce a distinct and controllable pressure differential, it was necessary to adapt the QV 600 to provide a mechanical barrier to separate the single chamber into two chambers whilst ensuring that flow through bioreactor could be maintained via the four inlet/ outlet ports on the bioreactor. Acrylic tube was acquired, then laser cut to fabricate a 'stand' that the barrier could rest on, with apertures cut into the tube so that flow could be maintained via the ports. In order to make initial tests to establish the relationship between flow and pressure differential within the bioreactor a membrane with a reliable mesh size was needed to provide a quantifiable semi permeable barrier. Whilst the 'Millicell' membrane satisfied this criterion, the height of the complete component led to the lower ports being blocked when the membrane was centred in the chamber. The base of the Millipore component was milled until there was just sufficient material left to locate a nitrile 'o' ring on the Millicell component. The complete assembly fits tightly within the QV 600 chamber.

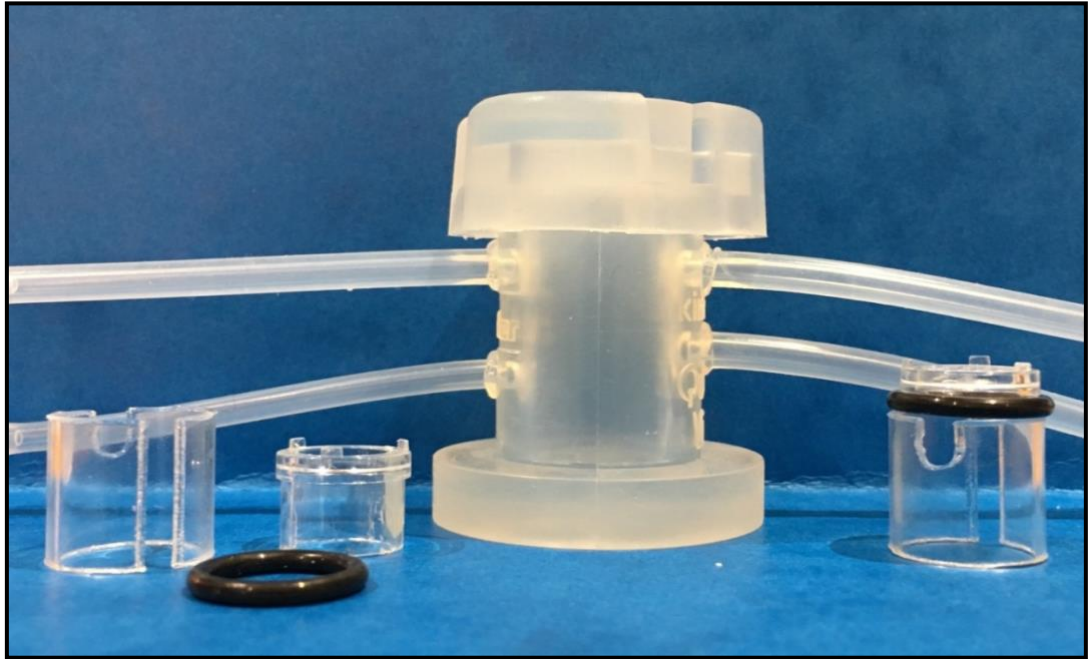


Figure 69 Adaptation kit for the QV 600 air –liquid interface bioreactor (Kirkstall Ltd, Sheffield U.K.). From left: 1, Acrylic tube (13 mm internal diameter 1 mm wall thickness) laser cut to shape. 2, Nitrile ‘o’ ring (13 mm internal diameter) Millicell 0.4. micron semi permeable membrane (EMD Millipore Ltd U.K.) prior to reduction in height by milling 4, QV 600 air – liquid interface bioreactor (empty) 5, Complete assembly.

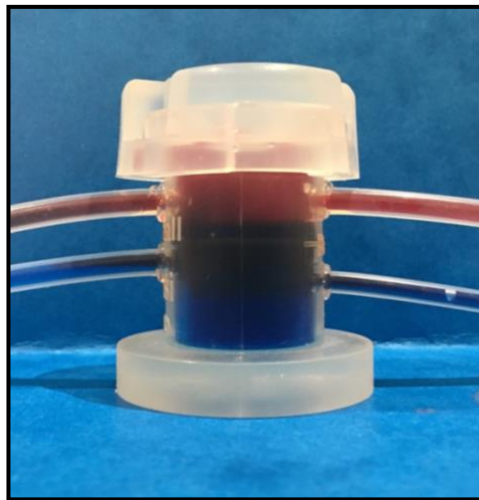


Figure 70 QV 600 air – liquid interface bioreactor (Kirkstall Ltd, Sheffield U.K.) adapted to a ‘dual flow’ and ‘dual pressure’ bioreactor

The adapted QV 600 chamber was tested by syringe pump. Two syringes were used (with coloured water) so that the two chambers were exposed to equal flow and no pressure differential between the two chambers would exist. The fact that no mixing of the two streams of coloured water could be seen, served as a clear indication that the mechanical barrier between the two chambers was effective and that the Millicell membrane would provide a quantifiable semi permeable barrier for further research.

Pump

Flow is provided by a Parker PF22X0103 pump, which has two independent channels, each with Vernier dials. Each pump head provides fine control of the flow rate at low ranges whilst enabling separate flow rates to be established for the upper and lower chambers, which is ideal for providing biomimetic flow and pressure rates for a 'capillary' membrane.

7.3.2 Fabrication of the 'Capillary Membrane'

An Inkjet printing script for the fabrication of a 20 x 20 array of 100 droplet micro columns, spaced at intervals of 200 micron was written (producing 400 columns approximately 2 mm in height). Once fabrication of the sacrificial Paraffin wax microstructures was complete, the slide (c/w microstructures) was then placed in a petri dish, and PDMS was carefully dispensed into the dish by syringe until the structure was submerged. The PDMS was then allowed to cure at room temperature for 48 hours (allowing sufficient time for air bubbles to escape). Once cured, the PDMS encapsulated structure was removed from the petri dish. The PDMS was then trimmed to match the dimensions of the inkjet printed sample, then it was removed from the glass slide and the glass slide was discarded. In order to remove the sacrificial paraffin wax structure from the PDMS, the PDMS was submerged in water heated to 800 C and sonicated for 5 minutes. The device was allowed to dry overnight.

An accurate encapsulation of the sacrificial microstructures in PDMS is required, since the data from the expected flow through the PDMS structure is to be compared to the data from the flow through the Millicell membrane. The fabricated sample shown in Figure 71 (overleaf) does not compare well with the 3D microfluidic devices fabricated previously (Chapter 5).

Close observation of the movement of the PDMS once dispensed into the petri dish showed that the closely spaced columns provided greater resistance to the spread of the dispensed PDMS than had been observed during the fabrication of the microfluidic devices. It was thought that the mechanism underpinning this was the significant increase in surface tension relative to the area of PDMS spread caused by the closely spaced structures relative to the highly viscous nature of the PDMS.



Figure 71 Paraffin wax microstructures encapsulated in PDMS

7.3.3 Interim Conclusion

A novel dual-flow bioreactor for capillary-like conduits, which produces flow by pressure differential has been inexpensively fabricated. It will be used to test the hypothesis that endothelialisation of microvascular sized conduits may be accelerated by recreating the physiologically relevant pressures and flows that endothelial cells experience in vivo.

The process of encapsulating the sacrificial microstructures in PDMS has revealed that modest revisions to the fabrication approach are required. In the first instance, a low viscosity PDMS should be sourced, in order to encapsulate the sacrificial microstructures without causing distortion. If that is insufficient then Microcrystalline wax (with its longer molecular chain lengths), which is both more adhesive and more ductile than Paraffin wax can also be considered for the sacrificial microstructures. The enhanced mechanical properties may ensure that the microstructures can withstand the forces created by the encapsulation process. However, the lowest melting point for readily available laminating grades (adhesive properties) of microcrystalline wax is 60 to 65° C, and 80 to 85° C for the toughening grades (improvement in ductility), which would require the ink to be maintained at approximately 70° C or 90° C, some 10° C and 30° C respectively in excess of the suggested maximum operating temperature for the printhead. Microcrystalline wax (if used in conjunction with a suitable high temperature printhead) does, however, remain an avenue for further investigation should improvements in mechanical properties beyond that of Paraffin wax be required.

Chapter 8 Conclusion

The disadvantages of surgical repair to diseased/damaged organs or of ongoing medical management (combined with an ever-increasing clinical need) have inspired increasing research in the fields of Tissue Engineering and Regenerative Medicine. ‘Tissue Replacement Technologies’ which rely on an ex vivo/in vitro bioreactor for cellular proliferation are sought to enable like-for-like replacement of tissue. One of the greatest challenges in developing a Tissue Replacement Technology is providing perfusion through an engineered tissue and diffusion of essential oxygen and nutrients to the cells in the primary engineered tissue.

Three key evaluative criteria were advanced to assess current attempts to provide perfusion and diffusion to an engineered tissue via an engineered vascular/microvascular network. These were *i, replication* - emphasising the exceptionally demanding spatial specifications that must be met to fabricate a biomimetic vascular/microvascular network *ii, co-fabrication* - considering the need to co-fabricate the scaffold for the primary engineered tissue around the scaffold for the vascular/microvascular network and *iii, scalability* - discussing the need to provide perfusion/diffusion to whole organ size scaffolds.

These evaluative criteria were applied to the many and varied existing research approaches currently being pursued to resolve the challenge of vascularisation (utilising the framework of Novosel et al). It was found that the Pre-vascularisation and Synthetic Scaffold approaches may provide suitable avenues to resolve the vascularisation challenge. It was noted that the Pre-vascularisation approach is unlikely to provide clinically meaningful volumes of tissue unless the clinician’s requirements are exceptionally small. Of the many Additive Manufacturing technologies, micro-stereo lithography shows promise in the direct fabrication of synthetic scaffolds, it is as yet unable to perfuse surrounding engineered tissue.

Additive Manufacturing technologies were then reconsidered for the indirect fabrication of synthetic scaffolds i.e. the fabrication of sacrificial microvascular facsimiles around which a synthetic scaffold could be formed prior to the microvascular facsimile being removed. Amongst others, IJP with its proven scalability, stood out as a candidate technology, primarily due to the good agreement between the size and circular output from the printhead with the size and cross section of microvasculature’ lumen. Thermal phase change inks could be used to create sacrificial 3D microstructures thus overcoming the disadvantage of the low viscosity inks that are usually associated with IJP.

8.1 Primary Aims and Objectives

In this thesis 'first of a kind' 3D sacrificial microvascular facsimiles have been fabricated, which demonstrate the potential to meet the evaluative criteria of replication, co-fabrication and scalability. The 'replication' criterion of this demanding 'tissue replacement' application means that the critical dimensions of the fabricated facsimile are reliant on the precise and repeatable deposition of every single ejected droplet. A detailed investigation was therefore undertaken into a, the principles underpinning droplet actuation and b, the principles underpinning droplet deposition in order to exercise an enhanced degree of control over the IJP process, prior to c, applying those principles to the fabrication of sacrificial microvascular facsimiles.

Droplet Actuation

The research surpassed the stated objective of identifying actuation parameters by redefining and adding to fundamental IJP theory. Otherwise, it was found that there are three methods by which droplets of varying volume can be generated while maintaining control over droplet velocity and shape, although the novel use of extended dwell times meant that a 6.7 fold range of droplet volumes may be produced from a single printhead, thus enabling the fabrication of a wide range of sacrificial microvascular facsimile diameters from the range of readily available printhead aperture sizes.

The more significant findings were that a, Morita et al's equation relating the optimal jetting pulse period to the fundamental resonance period is inaccurate and incomplete and that b, present approaches to rise times are inappropriate since rise times are an overlooked but important additional driver of droplet velocity. Additionally, backpressure, although not considered to be an explicit waveform parameter, was shown to have a direct effect on the amplitude parameter of the waveform. The proposed revisions to Morita et al's equation and an updated treatment of the issue of rise times will have wide ranging theoretical implications for IJP research and development, while improved control of backpressure will facilitate the day to day replication of results for IJP researchers in the lab.

Droplet Deposition

The investigation of droplet deposition parameters focussed on the frequency of droplet deposition and the offset between the printhead and the fabricated microstructure. It was found that to optimise both the consistency of column formation and the accuracy of droplet deposition (against a background of

microturbulence), the wait period between the deposition of each droplet should be minimised by applying the maximum degree of undercooling consistent with maintaining droplet spread to its thermal equilibrium. However, both constant column formation and accuracy of droplet deposition were demonstrably hindered by the discontinuous nature of z -axis printhead motion and the existence of microturbulence within the IJP cabinet caused by the heated reservoir and printhead assembly. While this effect was somewhat mitigated in the subsequent fabrication experiments it could not be entirely overcome.

Sacrificial Microvascular Facsimile Fabrication

Spacings between column perimeters of 20 micron and between column centres of 110 micron were fabricated mimicking the density at which capillaries occur in the human body.

A novel 'multi-droplet burst' droplet deposition technique was introduced, which demonstrated that a single 40 micron diameter aperture printhead could produce column or lumen diameters in the range of 60 to 320 micron, indicating that the desired lumen diameter range of 50 micron to 0.5 mm might easily be achieved. More importantly, bifurcating microstructures were fabricated using this technique that were in good agreement with the precise dimensions demanded by Murray's law. The result was shown to be the natural mathematical outcome of the relationship between the double-droplet volume of the parent arteriole and the single-droplet volumes of the daughter arterioles.

The bifurcating structures were then connected by overhanging arches (without the use of support materials) producing a novel sacrificial microvascular facsimile. Freestanding columns with heights in excess of 9 mm were produced also without the use of support materials, proving that aspect ratios of 100: 1 are achievable. These two results demonstrated that the sacrificial microvascular facsimiles are suitable candidates for co-fabrication.

In conclusion, the experiments illustrated that the core technological capabilities of 3D IJP with thermal phase change inks are generally well aligned with the replication and co-fabrication requirements for sacrificial microvascular facsimiles. However, there is insufficient control over the deposition parameters for the process to deliver the consistency and repeatability needed for its intended use in TE.

Benchmarking the IJP Apparatus and Assessing the Viability of 3D IJP as a Technological Platform

This lack of consistency and repeatability of the fabricated microstructures spurred an investigation into the performance gaps between the existing apparatus and a hypothesised ideal apparatus that would be able to consistently satisfy the replication criterion. The key hardware limitations are identified, principally, inaccurate backpressure regulation, discontinuity of Z axis (printhead) motion and the lack of appropriate environmental controls. It was also found that program inefficiencies effect the continuity of droplet deposition and are an important contributor to overall droplet deposition frequency. A change to a dedicated real-time operating system is recommended as the only viable solution to the current software limitation. Finally, to further the accumulation of process know-how, specific upgrades are recommended in order to better monitor and control the droplet actuation and ejection process in real time.

If the aforementioned idealised IJP apparatus was created, it would mean that 3D IJP with thermal phase change inks would be a technologically feasible platform for the fabrication of sacrificial microvascular facsimiles. The ability of such a platform to provide vascular/microvascular scaffolds for clinically meaningful volumes of tissue was then addressed. Using a small organ such as a thyroid as an example, a range of fabrication strategies, their productivity, and their key advantages and disadvantages were considered. The key finding of the investigation of scalability was that if 3D IJP is upgraded beyond the level that ensures technical feasibility, it immediately delivers scalability and therefore viability. It was found that using the hybrid 'on the fly' fabrication strategy (moderate investment and good fabrication consistency) the hypothetical thyroid could be fabricated in approximately 3.75 days. In contrast, a high investment alternative (3D Vector Motion Printing) could produce the same structure with the highest degree of biomimicry in approximately 8 days. Clearly there are additional processing steps required after the fabrication of the facsimile such as coating with a biocompatible material and removal of the sacrificial structures, in order to produce the final scaffold ready for cellularisation. However, 3D IJP as a technological platform demonstrates the potential to provide a scalable solution to the challenge of vascularisation in Tissue Engineering.

8.2 Ancillary Aims and Objectives

The solution to engineering Tissue Replacement constructs will be advanced but not resolved by fabricating a biomimetic scaffold for a microvascular network. A complete solution to this multi-faceted problem can only be arrived at by considering the broader challenges to engineering complex tissue. At present, the development of key 'enabling technologies' is essential.

Fabricating Three Dimensional Microvascular Networks within Microfluidic Devices for use in the Validation of 'in silico' Models

New theoretical principles, which underpin three-dimensional biomimetic vascular patterning show that asymmetric networks are needed to efficiently perfuse the irregular 3D tissue volumes found in the human body. Three-dimensional in silico models for microvascular networks are needed to provide the platform for designing physiologically relevant microvascular networks for TE. 3D microfluidic devices are needed to spur the development of 3D in silico models and assist in their subsequent validation.

3D IJP and thermal phase change inks have been used to make sacrificial 3D microvascular facsimiles that are initially employed in the production of the biomimetic 3D microfluidic devices. A 3D bifurcating capillary arch facsimile was printed onto 2.5 D microfluidic channels. The reduction in lumen diameter from the parent arteriole to the daughter capillary is compliant with Murray's law. The facsimile was encapsulated in PDMS to form a microfluidic device, prior to being sacrificed without damage to the PDMS.

The resulting device represents an improvement on current microfluidic technology in terms of the minimum conduit diameters, reproduction of bifurcations and degree of tortuosity that can be achieved in 3D. This device should prove useful in analysing aspects of perfusion and diffusion in microvasculature thereby assisting in the creation and validation of 3D in silico models.

Co-fabrication of a Primary Engineered Tissue Scaffold in Conjunction with a Microvascular Scaffold

Co-fabrication is an important criterion for evaluating the capacity of a vascularisation strategy to become a component part of a TRT. Having fabricated 3D sacrificial microvascular facsimiles with high aspect ratios and without the use of support materials, research was undertaken on a complimentary combination of materials (Gelatin and Collagen-Elastin) to act as microvascular scaffold and primary

engineered tissue scaffold respectively, with freeze-drying as a common fabrication process for both materials. The primary research question was to establish if the primary engineered scaffold could provide mechanical support to the microvascular scaffold thus replicating the symbiotic relationship found in the ECM.

A range of freeze dried Collagen-Elastin scaffolds were prepared, and a method that produced a sample that was in good agreement with Matriderm (a commercially procured C-E scaffold to act as a control) was selected. The ultimate tensile strengths (UTS) of both lab-made sample and Matriderm were measured in both dehydrated and hydrated states. Whilst the UTS of both samples in dehydrated states was in good agreement with literature, in the hydrated state the result indicated poor mechanical properties and was not in good agreement with literature (the vast majority of literature cites UTS as measured in dehydrated samples). The poor performance of the hydrated collagen-elastin scaffolds suggested that it would provide negligible mechanical support to the microvascular scaffold.

Moreover, the result indicates that the practise of measuring the UTS of freeze-dried collagen in a dehydrated state may produce erroneous or even irrelevant results if the engineered construct is going to be used in a hydrated state e.g. in vivo. Whilst the finding was novel at the time of the research, Varley et al have now published a comprehensive assessment of this phenomena (Varley et al., 2016).

Enhancing Cellularisation in Microvasculature

Endothelializing a complex branching 3D microvascular network presents significant difficulties. The direct cell seeding method has failed to produce micro-vessels with an exterior diameter of less than 30 micron for 'capillary' scale vessels. Endothelial cells have a diameter of approximately 10 – 15 micron, so a minor agglomeration of two or three cells can block conduits with capillary-like dimensions. Linville et al recently refined the cellular migration method by enhancing bioreactor flow techniques (Linville et al., 2016). However, demonstration of their novel method was limited to a single, short, straight 20-micron diameter conduit.

An inexpensive novel dual-flow bioreactor (producing flow by pressure differential) was designed and fabricated to maintain physiologically relevant in-vivo pressure differentials for microvasculature whilst maintaining low seeding densities for extended periods of time. An insert for the bioreactor that replicates the diameters and spacings of capillaries has been produced using 3D IJP with thermal phase change inks. With modest revisions to the fabrication of the insert, the bioreactor-insert setup can be used to test the hypothesis that the frequency of agglomerations

could be reduced, and cellular migration accelerated through a complex branching 3D microvascular network by mimicking the flow and pressure differentials endothelial cells experience in the human body.

8.3 Further Research and Development

The capacity for 3D Inkjet printing in conjunction with thermal phase change inks to fabricate sacrificial microvascular facsimiles which are able replicate the components and features necessary to create a physiologically relevant microvascular system has been clearly demonstrated, which in turn opens a number of significant research channels.

A series of technical upgrades for the 3D IJP setup have been recommended to ensure consistency and repeatability in the fabricated microstructures. If developed, 3D IJP will be capable of fabricating microstructures for experimental TE research devices. Furthermore, it has been shown that 3D IJP has the capacity to meet the ‘scalability’ criterion of a Tissue Replacement Technology and the fabrication of medical devices may be considered.

A novel microfluidic device has been fabricated that may enable the development and validation of much needed 3D in silico models of microvasculature. Additionally, a novel dual flow bioreactor-insert has been made to accelerate research into enhanced endothelialisation of capillaries. Further research is required to enhance the mechanical properties of the primary engineered tissue scaffold to enable co-fabrication with the microvascular scaffold. Potential strategies include improving cross linking of the collagen scaffold, altering the co-fabrication method or alternatively, collaborating with a Bioprinting group to access advanced materials and deposition techniques for the scaffold and cells of the primary engineered tissue.

List of References

- Aird, W. C. (2007). Phenotypic heterogeneity of the endothelium: I. Structure, function, and mechanisms. *Circulation Research*, 100(2), 158–173. <http://doi.org/10.1161/01.RES.0000255691.76142.4a>
- Auger, F. A., Gibot, L., & Lacroix, D. (2013). The Pivotal Role of Vascularization in Tissue Engineering. *Annual Review of Biomedical Engineering*, Vol 15, 15(1), 177–200. <http://doi.org/10.1146/annurev-bioeng-071812-152428>
- Barrientos, S., Stojadinovic, O., Golinko, M. S., Brem, H., & Tomic-Canic, M. (2008). Growth factors and cytokines in wound healing. *Wound Repair Regen*, 16(5), 585–601. <http://doi.org/10.1111/j.1524-475X.2008.00410.x>
- Bejan, A. (1997). *Advanced Engineering Thermodynamics*. John Wiley and Sons.
- Bejan, A. (2000). *Shape and Structure, from Engineering to Nature*. Cambridge University Press.
- Ben Utela, Storti, D., Anderson, R., & Ganter, M. (2008). A review of process development steps for new material systems in three-dimensional printing (3DP). *Journal of Manufacturing Processes*, 10(2), 96–104. <http://doi.org/10.1016/j.jmapro.2009.03.002>
- Berne, R. M., & Levy, M. N. (1972). *Cardiovascular Physiology*.
- Bogy, D. B., & Talke, F. E. (1984). Experimental and theoretical study of wave propagation phenomena in drop-on-demand ink jet devices. *IBM Journal of Research and Development*, 28(3), 314–321. <http://doi.org/10.1147/rd.283.0314>
- Boland, T., Mironov, V., Gutowska, A., Roth, E. A., & Markwald, R. R. (2003). Cell and organ printing 2: Fusion of cell aggregates in three-dimensional gels. *Anatomical Record - Part a Discoveries in Molecular, Cellular, and Evolutionary Biology*, 272(2), 497–502.
- Boland, T., Tao, X., Damon, B. J., Manley, B., Kesari, P., Jalota, S., & Bhaduri, S. (2007). Drop-on-demand printing of cells and materials for designer tissue constructs. *Materials Science and Engineering C*, 27(3), 372–376. <http://doi.org/10.1016/j.msec.2006.05.047>
- Braverman, I. M. (1997). The Cutaneous Microcirculation: Ultrastructure and Microanatomical Organization. *Microcirculation*, 4(3), 329–340. <http://doi.org/10.3109/10739689709146797>
- Burke, J. F., Yannas, I. V., Quinby, W. C., Jr., Bondoc, C. C., & Jung, W. K. (1981). Successful Use of a Physiologically Acceptable Artificial Skin in the Treatment of Extensive Burn Injury. *Annals of Surgery*, 194(4), 413–428. <http://doi.org/10.1097/00000658-198110000-00005>
- Castrejón-Pita, J. R., Kubiak, K. J., Castrejón-Pita, A. A., Wilson, M. C. T., & Hutchings, I. M. (2013). Mixing and internal dynamics of droplets impacting and coalescing on a solid surface. *Physical Review E*, 88(2), 768–11. <http://doi.org/10.1103/PhysRevE.88.023023>
- Chang, C. C., Boland, E. D., Williams, S. K., & Hoying, J. B. (2011). Direct-write bioprinting three-dimensional biohybrid systems for future regenerative therapies. *J Biomed Mater Res B Appl Biomater*, 98(1), 160–170. <http://doi.org/10.1002/jbm.b.31831>
- Christensen, K., Xu, C., Chai, W., Zhang, Z., Fu, J., & Huang, Y. (2015). Freeform inkjet printing of cellular structures with bifurcations. *Biotechnology and Bioengineering*, 112(5), 1047–1055. <http://doi.org/10.1002/bit.25501>

- Chrobak, K. M., Potter, D. R., & Tien, J. (2006). Formation of perfused, functional microvascular tubes in vitro. *Microvascular Research*, 71(3), 185–196. <http://doi.org/10.1016/j.mvr.2006.02.005>
- Cibis, D., & Krüger, K. (2007). System Analysis of a DoD Print Head for Direct Writing of Conductive Circuits. *International Journal of Applied Ceramic ...*, 4(5), 428–435. <http://doi.org/10.1111/j.1744-7402.2007.02160.x>
- Daamen, W. F., Nillesen, S. T. M., Wismans, R. G., Reinhardt, D. P., Hafmans, T., Veerkamp, J. H., & van Kuppevelt, T. H. (2008). A Biomaterial Composed of Collagen and Solubilized Elastin Enhances Angiogenesis and Elastic Fiber Formation Without Calcification. *Tissue Engineering - Part a.*, 14(3), 349–360. <http://doi.org/10.1089/tea.2007.0076>
- Daamen, W. F., Nillesen, S. T. M., Wismans, R., Reinhardt, D., Hafmans, T., Veerkamp, J. H., & van Kuppevelt, T. H. (2006). Depots of solubilised elastin promote the formation of blood vessels and elastic fibres in rat. *Journal of Controlled Release*, 116(2), e84–e85. <http://doi.org/10.1016/j.jconrel.2006.09.062>
- Dagalakis, N., Flink, J., Stasikelis, P., Burke, J. F., & Yannas, I. V. (1980a). Design of an artificial skin. Part III. Control of pore structure. *Journal of Biomedical Materials Research*, 14(4), 511–528. <http://doi.org/10.1002/jbm.820140417>
- Dagalakis, N., Flink, J., Stasikelis, P., Burke, J. F., & Yannas, I. V. (1980b). Design of an artificial skin. Part III. Control of pore structure. *Journal of Biomedical Materials Research*, 14(4), 511–528. <http://doi.org/10.1002/jbm.820140417>
- Datta, P., Ayan, B., & Ozbolat, I. T. (2017). Bioprinting for vascular and vascularized tissue biofabrication. *Acta Biomater*, 51, 1–20. <http://doi.org/10.1016/j.actbio.2017.01.035>
- Derby, B. (2011). Inkjet printing ceramics: From drops to solid. *Journal of the European Ceramic Society*, 31(14), 2543–2550. <http://doi.org/10.1016/j.jeurceramsoc.2011.01.016>
- Derby, B., & Reis, N. (2003). Inkjet Printing of Highly Loaded Particulate Suspensions. *Mrs Bulletin*, 28(11), 815–818. <http://doi.org/10.1557/mrs2003.230>
- Fathi, S., Dickens, P., & Hague, R. (2011). Jetting stability of molten caprolactam in an additive inkjet manufacturing process. *International Journal of Advanced Manufacturing Technology*, 59(1-4), 201–212. <http://doi.org/10.1007/s00170-011-3500-6>
- Folkman, J. (1973). Self-regulation of growth in three dimensions. *Journal of Experimental Medicine*, 138(4), 745–753. <http://doi.org/10.1084/jem.138.4.745>
- Fozdar, D. Y., Soman, P., Lee, J. W., Han, L.-H., & Chen, S. (2011). Three-Dimensional Polymer Constructs Exhibiting a Tunable Negative Poisson's Ratio. *Advanced Functional Materials*, 21(14), 2712–2720. <http://doi.org/10.1002/adfm.201002022>
- Fraunhofer. (n.d.). *Artivasc EU*. Retrieved from www.artivasc.eu
- Fromm, J. E. (1983). Numerical Calculation of the Fluid Dynamics of Drop-on-demand Jets.
- Gao, F., & Sonin, A. A. (1994). Precise deposition of molten microdrops: the physics of digital microfabrication. ... *Of the Royal Society of London ...*, 444(1922), 533–554. <http://doi.org/10.1098/rspa.1994.0037>
- Gauvin, R., Chen, Y.-C., Lee, J. W., Soman, P., Zorlutuna, P., Nichol, J. W., et al. (2012). Microfabrication of complex porous tissue engineering scaffolds using 3D projection stereolithography. *Biomaterials*, 33(15), 3824–3834. <http://doi.org/10.1016/j.biomaterials.2012.01.048>
- Gerhauser, H., Hirschman, K. H., Lee, F., & Talke, F. E. (1983). The effect of pulse shape on the drop volume and the frequency response of drop-on-demand ink jet transducers. *SID Dig.*

- Giusti, S., Sbrana, T., La Marca, M., Di Patria, V., Martinucci, V., Tirella, A., et al. (2014). A novel dual-flow bioreactor simulates increased fluorescein permeability in epithelial tissue barriers. *Biotechnol J*, 9(9), 1175–1184. <http://doi.org/10.1002/biot.201400004>
- Golden, A. P., & Tien, J. (2007). Fabrication of microfluidic hydrogels using molded gelatin as a sacrificial element, 7(6), 720. <http://doi.org/10.1039/b618409j>
- Grogan, S. P., Chung, P. H., Soman, P., Chen, P., Lotz, M. K., Chen, S., & D'Lima, D. D. (2013). Digital micromirror device projection printing system for meniscus tissue engineering. *Acta Biomater*, 9(7), 7218–7226. <http://doi.org/10.1016/j.actbio.2013.03.020>
- Han, Y., Wei, C., & Dong, J. (2015). Droplet formation and settlement of phase-change ink in high resolution electrohydrodynamic (EHD) 3D printing. *Journal of Manufacturing Processes*, 20, 485–491. <http://doi.org/10.1016/j.jmapro.2015.06.019>
- Hasan, A., Paul, A., Vrana, N. E., Zhao, X., Memic, A., Hwang, Y.-S., et al. (2014). Microfluidic techniques for development of 3D vascularized tissue. *Biomaterials*, 35(26), 7308–7325. <http://doi.org/10.1016/j.biomaterials.2014.04.091>
- Haugh, M. G., Jaasma, M. J., & O'Brien, F. J. (2009). The effect of dehydrothermal treatment on the mechanical and structural properties of collagen-GAG scaffolds. *J Biomed Mater Res A*, 89(2), 363–369. <http://doi.org/10.1002/jbm.a.31955>
- Heintz, K. A., Mayerich, D., & Slater, J. H. (2017). Image-guided, Laser-based Fabrication of Vascular-derived Microfluidic Networks. *Journal of Visualized Experiments*, (119). <http://doi.org/10.3791/55101>
- Hoath, S. D. (2016). *Fundamentals of Inkjet Printing*. John Wiley & Sons.
- Hoch, E., Tovar, G. E. M., & Borchers, K. (2014). Bioprinting of artificial blood vessels: current approaches towards a demanding goal. *European Journal of Cardio-Thoracic Surgery*, 46(5), 767–778. <http://doi.org/10.1093/ejcts/ezu242>
- Janakiraman, V., Kienitz, B. L., & Baskaran, H. (2007a). Lithography Technique for Topographical Micropatterning of Collagen-Glycosaminoglycan Membranes for Tissue Engineering Applications. *Journal of Medical Devices*, 1(3), 233–237. <http://doi.org/10.1115/1.2775937>
- Janakiraman, V., Mathur, K., & Baskaran, H. (2007b). Optimal Planar Flow Network Designs for Tissue Engineered Constructs with Built-in Vasculature. *Ann Biomed Eng*, 35(3), 337–347. <http://doi.org/10.1007/s10439-006-9235-0>
- Jang, D., Kim, D., & Moon, J. (2009). Influence of Fluid Physical Properties on Ink-Jet Printability. *Langmuir: the ACS Journal of Surfaces and Colloids*, 25(5), 2629–2635. <http://doi.org/10.1021/la900059m>
- Jones, I., Currie, L., & Martin, R. (2002). A guide to biological skin substitutes. *British Journal of Plastic Surgery*, 55(3), 185–193. <http://doi.org/http://dx.doi.org/10.1054/bjps.2002.3800>
- Katstra, W. E., Palazzolo, R. D., controlled, C. R. J. O., 2000. (2000). Oral dosage forms fabricated by Three-Dimensional Printing™. *Elsevier*, 66(1), 1–9. [http://doi.org/10.1016/S0168-3659\(99\)00225-4](http://doi.org/10.1016/S0168-3659(99)00225-4)
- Khatavkar, V. V., Anderson, P. D., Duineveld, P. C., & Meijer, H. E. H. (2007). Diffuse-interface modelling of droplet impact. *Journal of Fluid Mechanics*, 581, 97. <http://doi.org/10.1017/S002211200700554X>
- Kim, S., Lorente, S., Bejan, A., Miller, W., & Morse, J. (2008). The emergence of vascular design in three dimensions. *Journal of Applied Physics*, 103(12), 123511. <http://doi.org/10.1063/1.2936919>
- Kullmann, C., Schirmer, N. C., Lee, M.-T., Ko, S. H., Hotz, N., Grigoropoulos, C. P., & Poulidakos, D. (2012). 3D micro-structures by piezoelectric inkjet printing of gold nanofluids. *Journal of Micromechanics and Microengineering*, 22(5), 055022–12. <http://doi.org/10.1088/0960-1317/22/5/055022>

- Kwon, K.-S. (2010). Experimental analysis of waveform effects on satellite and ligament behavior via in situ measurement of the drop-on-demand drop formation curve and the instantaneous jetting speed curve. *Journal of Micromechanics and Microengineering*, 20(11), 115005. <http://doi.org/10.1088/0960-1317/20/11/115005>
- Kwon, K.-S., & Lee, D.-Y. (2013). Investigation of pulse voltage shape effects on electrohydrodynamic jets using a vision measurement technique. *Journal of Micromechanics and Microengineering*, 23(6), 065018–15. <http://doi.org/10.1088/0960-1317/23/6/065018>
- Langer, R., & Vacanti, J. (1993). Tissue engineering. *Science*, 260(5110), 920–926. <http://doi.org/10.1126/science.8493529>
- Laschke, M. W., Harder, Y., Amon, M., Martin, I., Farhadi, J., Ring, A., et al. (2006). Angiogenesis in Tissue Engineering: Breathing Life into Constructed Tissue Substitutes. *Tissue Eng*, 12(8), 2093–2104. <http://doi.org/10.1089/ten.2006.12.2093>
- Lee, J. Y., & Lee, S. J. (2009). Murray's law and the bifurcation angle in the arterial micro-circulation system and their application to the design of microfluidics. *Microfluidics and Nanofluidics*, 8(1), 85–95. <http://doi.org/10.1007/s10404-009-0454-1>
- Linville, R. M., Boland, N. F., Covarrubias, G., Price, G. M., & Tien, J. (2016). Physical and Chemical Signals That Promote Vascularization of Capillary-Scale Channels. *Cellular and Molecular Bioengineering*, 9(1), 73–84. <http://doi.org/10.1007/s12195-016-0429-8>
- Liu, Y., Markov, D. A., Wikswa, J. P., & McCawley, L. J. (2011). Microfabricated scaffold-guided endothelial morphogenesis in three-dimensional culture. *Biomed Microdevices*, 13(5), 837–846. <http://doi.org/10.1007/s10544-011-9554-2>
- Madaghiele, M., Sannino, A., Yannas, I. V., & Spector, M. (2008). Collagen-based matrices with axially oriented pores. *J Biomed Mater Res A*, 85A(3), 757–767. <http://doi.org/10.1002/jbm.a.31517>
- Martin, I., Wendt, D., & Heberer, M. (2004). The role of bioreactors in tissue engineering. *Trends Biotechnol*, 22(2), 80–86. <http://doi.org/10.1016/j.tibtech.2003.12.001>
- Melchels, F. P. W., Domingos, M. A. N., Klein, T. J., Malda, J., Bartolo, P. J., & Hutmacher, D. W. (2012). Additive manufacturing of tissues and organs. *Progress in Polymer Science*, 37(8), 1079–1104. <http://doi.org/10.1016/j.progpolymsci.2011.11.007>
- Melchels, F. P. W., Tonnarelli, B., Olivares, A. L., Martin, I., Lacroix, D., Feijen, J., et al. (2011). The influence of the scaffold design on the distribution of adhering cells after perfusion cell seeding. *Biomaterials*, 32(11), 2878–2884. <http://doi.org/10.1016/j.biomaterials.2011.01.023>
- Meyer, W., Engelhardt, S., Novosel, E., Elling, B., Wegener, M., & Krüger, H. (2012). Soft Polymers for Building up Small and Smallest Blood Supplying Systems by Stereolithography. *Journal of Functional Biomaterials*, 3(4), 257–268. <http://doi.org/10.3390/jfb3020257>
- Microfab Technologies Inc. (1999). *MicroFab Technote 99-03 Drive Waveform Effects on Ink-Jet Device Performance* (pp. 1–4). Retrieved from <http://www.microfab.com/images/pdfs/technote99-03.pdf>
- Microfab Technologies Inc. (2007). *Satellites occurrence and approaches to eliminate them*. (Microfab Technologies Inc., Ed.). Microfab Technologies Inc. Retrieved from http://www.microfab.com/images/pdfs/Satellites_version_09_26_07.pdf
- Miguel, A. F. (2016). Toward an optimal design principle in symmetric and asymmetric tree flow networks. *Journal of Theoretical Biology*, 389(C), 101–109. <http://doi.org/10.1016/j.jtbi.2015.10.027>

- Mondy, W., & Piegler, L. (2009). Computer-aided design of microvasculature systems for use in vascular scaffold production. *Biofabrication*, 1(3), 035002.
- Morgan, J. P., Delneri, P. F., Zheng, Y., Verbridge, S. S., Chen, J., Craven, M., et al. (2013). Formation of microvascular networks in vitro. *Nature Protocols*, 8(9), 1820–1836. <http://doi.org/10.1038/nprot.2013.110>
- Morita, N., Khalate, A. A., Buul, A. M. V., & Wijshoff, H. (2015). Inkjet Printheads (Vol. 36, pp. 57–92). Weinheim, Germany: Wiley-VCH Verlag GmbH & Co. KGaA. <http://doi.org/10.1002/9783527684724.ch3>
- Murray, C. D. (1926). The Physiological Principle of Minimum Work Applied to The Angle of Branching Of Arteries. *The Journal of General Physiology*, 9(6), 835–841. <http://doi.org/10.1085/jgp.9.6.835>
- Novosel, E. C., Kleinhans, C., & Kluger, P. J. (2011). Vascularization is the key challenge in tissue engineering. *Advanced Drug Delivery Reviews*, 63(4-5), 300–311. <http://doi.org/10.1016/j.addr.2011.03.004>
- Olivares, L., Koshima, I., Teo, T. C., Suominen, S., Masia, J., Olivares, L., et al. (2014). Barcelona Consensus on Supermicrosurgery. *Journal of Reconstructive Microsurgery*, 30(1), 053–058.
- Pataky, K., Braschler, T., Negro, A., Renaud, P., Lutolf, M. P., & Brugger, J. (2011). Microdrop Printing of Hydrogel Bioinks into 3D Tissue-Like Geometries. *Adv Mater*, 24(3), 391–396. <http://doi.org/10.1002/adma.201102800>
- Patan, S. (2001). Vasculogenesis and angiogenesis as mechanisms of vascular network formation, growth and remodeling. *Journal of Neuro-Oncology*, 1–15.
- Raman, R., Bhaduri, B., Mir, M., Shkumatov, A., Lee, M. K., Popescu, G., et al. (2015). High-Resolution Projection Microstereolithography for Patterning of Neovasculature. *Adv Healthc Mater*, 5(5), 610–619. <http://doi.org/10.1002/adhm.201500721>
- Reis, N., & Derby, B. (2000). Ink Jet Deposition of Ceramic Suspensions: Modeling and Experiments of Droplet Formation. *MRS Proceedings*, 624, 65. <http://doi.org/10.1557/PROC-624-65>
- Rensch, C. (2006). Creation of small microdrops. *MicroFab Technologies*.
- Rnjak, J., Wise, S. G., Mithieux, S. M., & Weiss, A. S. (2011). Severe Burn Injuries and the Role of Elastin in the Design of Dermal Substitutes. *Tissue Engineering Part B*, 17(2), 81–91. <http://doi.org/10.1089/ten.teb.2010.0452>
- Rosenbloom, J., Abrams, W. R., & Mecham, R. (1993). Extracellular matrix 4: the elastic fiber. *Faseb J*, 7(13), 1208–1218.
- Roth, E. A., Xu, T., Das, M., Gregory, C., Hickman, J. J., & Boland, T. (2004). Inkjet printing for high-throughput cell patterning. *Biomaterials*, 25(17), 3707–3715. <http://doi.org/10.1016/j.biomaterials.2003.10.052>
- Sachlos, E. (2003). Novel collagen scaffolds with predefined internal morphology made by solid freeform fabrication. *Biomaterials*, 24(8), 1487–1497. [http://doi.org/10.1016/s0142-9612\(02\)00528-8](http://doi.org/10.1016/s0142-9612(02)00528-8)
- Sakaguchi, K., Shimizu, T., Horaguchi, S., Sekine, H., Yamato, M., Umezumi, M., & Okano, T. (2013). In Vitro Engineering of Vascularized Tissue Surrogates. *Scientific Reports*, 3, 1–7. <http://doi.org/10.1038/srep01316>
- Salacinski, H. J., Goldner, S., Giudiceandrea, A., Hamilton, G., Seifalian, A. M., Edwards, A., & Carson, R. J. (2016). The Mechanical Behavior of Vascular Grafts: A Review. *J Biomater Appl*, 15(3), 241–278. <http://doi.org/10.1106/NA5T-J57A-JTDD-FD04>
- Saunders, R. E., & Derby, B. (2014). Inkjet printing biomaterials for tissue engineering: bioprinting. *International Materials Reviews*, 59(8), 430–448. <http://doi.org/10.1179/1743280414Y.0000000040>

- Savage, V., Bentley, L., & Enquist, B. (2010). Hydraulic trade-offs and space filling enable better predictions of vascular structure and function in plants. *Pnas*, 1–6. <http://doi.org/10.1073/pnas.1012194108/-/DCSupplemental>
- Shirazi, F. S., Mehrali, M., Oshkour, A. A., Metselaar, H. S. C., Kadri, N. A., & Abu Osman, N. A. (2013). Characterization and Mechanical Properties of Calcium Silicate/Citric Acid-Based Polymer Composite Materials. *International Journal of Applied Ceramic ...*, 12(2), 371–376. <http://doi.org/10.1111/ijac.12151>
- Silver, F. H., Freeman, J. W., & DeVore, D. (2001). Viscoelastic properties of human skin and processed dermis. *Skin Research and Technology*, 7(1), 18–23. <http://doi.org/10.1034/j.1600-0846.2001.007001018.x>
- Sionkowska, A., Skopinska-Wisniewska, J., Gawron, M., Kozłowska, J., & Planecka, A. (2010). International Journal of Biological Macromolecules. *International Journal of Biological Macromolecules*, 47(4), 570–577. <http://doi.org/10.1016/j.ijbiomac.2010.08.004>
- Skopinska-Wisniewska, J., Sionkowska, A., Kaminska, A., Kaznica, A., Jachimiak, R., & Drewa, T. (2009). Surface characterization of collagen/elastin-based biomaterials for tissue regeneration. *Applied Surface Science*, 255(19), 8286–8292. <http://doi.org/10.1016/j.apsusc.2009.05.127>
- Smith, P. J., & Stringer, J. (2015). Applications in Inkjet Printing (Vol. 9, pp. 397–418). Weinheim, Germany: Wiley-VCH Verlag GmbH & Co. KGaA. <http://doi.org/10.1002/9783527684724.ch15>
- Stephenson, D., & Lockerby, D. A. (2016). A generalized optimization principle for asymmetric branching in fluidic networks. *Proceedings of the Royal Society a: Mathematical, Physical and Engineering Science*, 472(2191), 20160451. <http://doi.org/10.1098/rspa.2016.0451>
- Sun, D., Chang, C., Li, S., & Lin, L. (2006). Near-Field Electrospinning. *Nano Letters*, 6(4), 839–842. <http://doi.org/10.1021/nl0602701>
- Tekin, E., Smith, P. J., & Schubert, U. S. (2008). Inkjet printing as a deposition and patterning tool for polymers and inorganic particles. *Soft Matter*, 4(4), 703. <http://doi.org/10.1039/b711984d>
- Tremblay, P.-L., Hudon, V., Berthod, F., Germain, L., & Auger, F. A. (2005). Inosculation of Tissue-Engineered Capillaries with the Host's Vasculature in a Reconstructed Skin Transplanted on Mice. *American Journal of Transplantation*, 5(5), 1002–1010. <http://doi.org/10.1111/j.1600-6143.2005.00790.x>
- Tse, C. (2015). *Utilising inkjet printing for tissue engineering*. University of Sheffield. U.K.
- Varley, M. C., Neelakantan, S., Clyne, T. W., Dean, J., Brooks, R. A., & Markaki, A. E. (2016). Cell structure, stiffness and permeability of freeze-dried collagen scaffolds in dry and hydrated states. *Acta Biomater*, 33, 166–175. <http://doi.org/10.1016/j.actbio.2016.01.041>
- Wang, T., Patel, R., & Derby, B. (2008). Manufacture of 3-dimensional objects by reactive inkjet printing. *Soft Matter*, 4(12), 2513–6. <http://doi.org/10.1039/b807758d>
- Wessels, Q. (2014). Engineered alternative skin for partial and full-thickness burns. *Bioengineered*, 5(3), 161–164. <http://doi.org/10.4161/bioe.28598>
- Wetzel, S. G., Ohta, M., Handa, A., Auer, J.-M., Lylyk, P., Lovblad, K.-O., et al. (2005). From Patient to Model: Stereolithographic Modeling of the Cerebral Vasculature Based on Rotational Angiography. *American Journal of Neuroradiology*, 26(6), 1425–1427.
- Wijshoff, H. (2010). The dynamics of the piezo inkjet printhead operation. *Physics Reports*, 491(4-5), 77–177. <http://doi.org/10.1016/j.physrep.2010.03.003>

- Wilson, W. C., Jr, & Boland, T. (2003). Cell and organ printing 1: Protein and cell printers. *Anatomical Record - Part a Discoveries in Molecular, Cellular, and Evolutionary Biology*, 272(2), 491–496.
- Xi, T., Chen, L., & Wang, C. (2013). Regulation challenge of tissue engineering and regenerative medicine in China. *Burns & Trauma*, 1(2), 56.
<http://doi.org/10.4103/2321-3868.118927>
- Xu, C., Yang, F., Wang, S., & Ramakrishna, S. (2004). In vitro study of human vascular endothelial cell function on materials with various surface roughness. *J Biomed Mater Res A*, 71(1), 154–161. <http://doi.org/10.1002/jbm.a.30143>
- Yang, J., & Wang, Y. (2012). Design of vascular networks: A mathematical model approach. *International Journal for Numerical Methods in Biomedical Engineering*, 29(4), 515–529. <http://doi.org/10.1002/cnm.2534>
- Yannas, I. V. (1980). Design of an Artificial Skin .1. Basic Design Principles. *Journal of Biomedical Materials Research*, 14(1), 65–81. <http://doi.org/10.1002/jbm.820140108>
- Yannas, I. V., Lee, E., Orgill, D. P., & Skrabut, E. M. (1989). Synthesis and characterization of a model extracellular matrix that induces partial regeneration of adult mammalian skin. *Proc Natl Acad Sci U S A*, 86(3), 933–937.
- Yeong, W.-Y., Chua, C.-K., Leong, K.-F., Chandrasekaran, M., & Lee, M.-W. (2006). Indirect fabrication of collagen scaffold based on inkjet printing technique. *Rapid Prototyping Journal*, 12(4), 229–237. <http://doi.org/10.1108/13552540610682741>
- Zhang, B., He, J., Li, X., Xu, F., & Li, D. (2016). Micro/nanoscale electrohydrodynamic printing: from 2D to 3D. *Nanoscale*, 8(34), 15376–15388.
<http://doi.org/10.1039/C6NR04106J>
- Zhang, X., Chen, X., Yang, T., Zhang, N., Dong, L., Ma, S., et al. (2014). The effects of different crossing-linking conditions of genipin on type I collagen scaffolds: an in vitro evaluation. *Cell and Tissue Banking*, 15(4), 531–541.
<http://doi.org/10.1007/s10561-014-9423-3>
- Zheng, Y., Chen, J. S., Craven, M., & Stroock, A. D. (2012). In vitro microvessels for the study of angiogenesis and thrombosis, 1–6.
http://doi.org/10.1073/pnas.1201240109/-/DCSupplemental/pnas.1201240109_SI.pdf

List of Abbreviations

Acronyms

AM : Additive manufacturing

CIJ : Continuous Inkjet printing

DFU : Diabetic foot ulcer

DOD : Drop on demand

EC : Endothelial cell

ECM : Extra cellular matrix

FDA : Food and Drug Administration (USA)

IJP : Inkjet printer/printing

LED : Light emitting diode

MEMS : Micro-electromechanical system

PDMS : Polydimethylsiloxane

PTHF : Polytetrahydrofuran

TE : Tissue engineering

TERM : Tissue engineering and regenerative medicine

Waveform Nomenclature

T_f = fundamental resonance period, the time taken for the pressure wave to travel a length of the capillary and return i.e. two lengths

$T_f/2$ = time for wave to travel a single length

t_{jp}^o = total time of the optimal jetting pulse

t_{jp} = total time of the actual jetting pulse

t_{rj} = rise time of the jetting pulse

t_{dj}^o = optimal dwell time of the jetting pulse

t_{dj} = actual dwell time of the jetting pulse

t_{fj} = fall time of the jetting pulse

T_{fIJP} = fundamental resonance period redefined for IJP

t_{zero} = period of delay before wave propagation

t_{adjr} = actual effective (adjusted) period of the rise time

t_{adjd} = actual travel period of the pressure wave

t_r = time taken for one reflection of the pressure wave

Units of Measurement

$^{\circ}C$: Degrees Celsius

Hz : Hertz

mbar : Millibar

m/s : Meters per second

mm/s : Millimeters per second

nJ : Nanojoule

mPa.s : Millipascalsecond

pL : Picolitre

μJ : Microjoule

μm : Micron

μs : Microsecond

V : Volt

Z : Dimensionless number reflecting the 'jet-ability' of ink

Appendix A

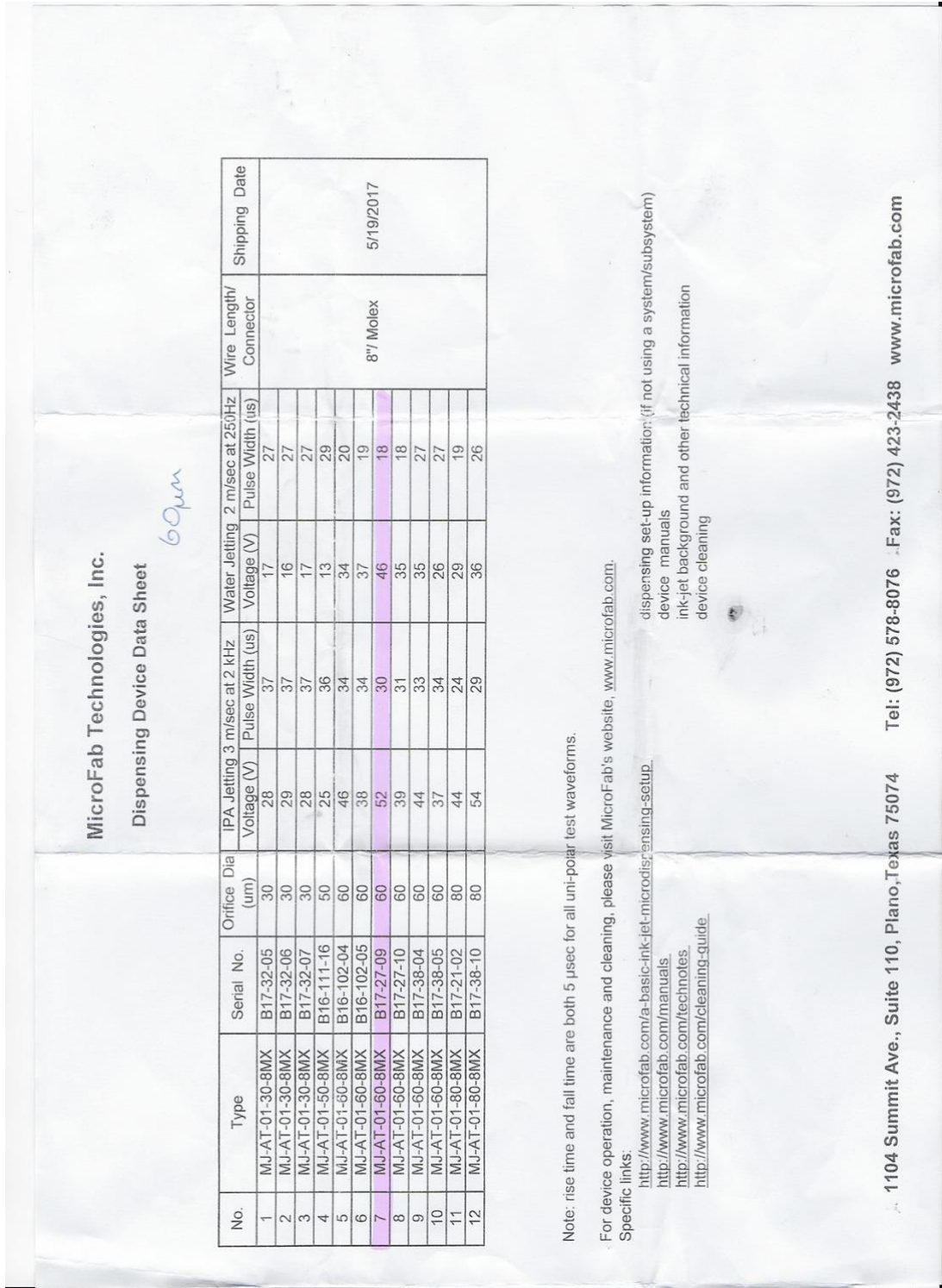


Figure 72 'Microfab' Delivery Note for Print heads; showing the variety of optimum jetting pulse widths and amplitudes for printheads with the same diameter capillary aperture